FINITE ELEMENT MODELING OF BACKWARD EROSION PIPING

by

Bryant A. Robbins

A thesis submitted to the Faculty and the Board of Trustees of the Colorado School of Mines in partial fulfillment of the requirements for the degree of Doctor of Philosophy (Civil and Environmental Engineering).

Golden, Colorado

Date_____

Signed:_____

Bryant A. Robbins

Signed:_____

Dr. D.V. Griffiths

Thesis Advisor

Golden, Colorado

Date_____

Signed:_____

Dr. Junko M. Marr

Professor and Head

Department of Civil and Environmental Engineering

ABSTRACT

Backward erosion piping (BEP) is a type of internal erosion that has caused the failure of many dams and levees and continues to threaten the safety of existing infrastructure. To manage this threat, failure risks are regularly evaluated to prioritize risk reduction measures. Unfortunately, current practice for assessing BEP is limited to simple calculation rules that have large uncertainty and error. While numerical models have been developed for simulating BEP, ambiguity regarding the erosion constitutive model, inconsistencies in the assumed physics, and lack of laboratory tests for measuring model parameters have made it difficult to validate tools for use in practice. No validated, widely accepted model for BEP exists today.

This thesis develops and validates an approach for finite element modeling of BEP by introducing the concept of the critical secant gradient function (CSGF). The CSGF provides a spatial function of the hydraulic gradient upstream of the pipe tip. An analytical expression for the CSGF and a laboratory test for measuring the CSGF are developed. A steady-state finite element model for simulating BEP progression is then developed for both two- and three-dimensional domains. The model and CSGF concept are validated through hindcasting of BEP experiments. Remarkable agreement was obtained between the finite element predictions and the experiments despite the experiments having different scale, configurations, and boundary conditions. These results indicate that the CSGF may provide the needed link between theory, lab testing, and numerical models to reliably predict BEP progression in practice. Additionally, the results indicate that the steady state finite element algorithm proposed is capable of adequately describing the BEP process, and more complex models may not be necessary.

After developing and validating an approach for finite element modeling of BEP progression, the remainder of the thesis demonstrates techniques that can be used to simulate BEP in practice. The use of adaptive meshing is demonstrated in two-dimensions as a means of efficiently simulating BEP progression for field scale problems. Additionally, the random finite element method is applied to demonstrate how to incorporate spatial variability in soil properties into BEP predictions. The results of this study demonstrate how both techniques, in conjunction with the CSGF, offer the potential for transformative improvements in the engineering practice of risk assessment of dams and levees susceptible to BEP progression.

TABLE OF CONTENTS

LIST OF FIGURES

LIST OF TABLES

LIST OF SYMBOLS

a	depth of the erosion pipe [m]
a_e	depth of the erosion pipe in element e [m]
A	cross sectional area of a pipe or surficial area of a boundary [m^2]
$\hat{A}$	pipe cross sectional area represented by chosen finite element discretization of the erosion pipe [m^2]
A_n	Fourier coefficients in Sellmeijer analytical solution for groundwater flow towards the pipe [-]
b_t	depth of ditch at pipe tip in Xiao et al. (2020) conformal mapping solution [m]
c_n	porosity based erosion coefficient [m^2/N s]
c_t	erosion coefficient for erosion of pipe wall [kg/N s]
C	scalar value in the CSGF [$m^{1/2}$] or concentration of particles in fluid phase [-]
C_i	Schmertmann correction factors where i is equal to $D, L, S, k, Z, \gamma, B, G, \alpha$, or R to designate various corrections as indicated in Table 2-5 for use in Schmertmann's prediction method
C_k	constant valued multiplier used to increase soil permeability to represent erosion in previous studies [-]
C_p	volumetric concentration of eroded particles in pore fluid, typically used in suffusion models [-]
C_r	creep ratio or weighted creep ratio proposed as empirical means of predicting piping [-]
C_u	coefficient of uniformity of a soil gradation, equal to the ratio of d_{60}/d_{10} [-]
$C_{u,\mu}$	mean value of C_u for a set of data [-]
d	particle diameter [m]
d_{10}	grain diameter for which 10 percent is finer by mass [m]

d_{50}	grain diameter for which 50 percent is finer by mass [m]
$d_{50,\mu}$	mean value of d_{50} [m]
d_{60}	grain diameter for which 60 percent is finer by mass [m]
D	depth or thickness of soil sample or foundation, or the diameter of cylinder lab experiment [m]
D_h	hydraulic diameter of a pipe, given by $4A/P$ [m]
D_h^*	approximate hydraulic diameter assuming infinite pipe width [m]
D_r	relative density of the soil [-]
e	soil void ratio, or error in the finite element gradient field [-]
e_μ	mean value of soil void ratio for a set of data [-]
f	Darcy-Weisbach friction factor for resistance of flow in a conduit or pipe [-]
F_s	average seepage force per unit volume [N/m^3]
g	gravitational acceleration [m/s^2]
g_m	user defined value that defines the initial depth of the erosion pipe in multiples of d_{50} [-]
h	total hydraulic head at any location [m]
$\hat{h}$	finite element approximation of the hydraulic head across the domain [m]
h_{tip}	total hydraulic head at the upstream tip of the erosion pipe [m]
H	differential total hydraulic head [m]
$\{H\}$	vector of the total head at the finite element nodes [m]
$\{H_e\}$	vector of the total head at the nodes of a single element [m]
H_c	critical value of the differential head at which BEP progresses to failure [m]
i	imaginary number
i	magnitude of the hydraulic gradient [-]

$\hat{\imath}$	finite element approximation of the hydraulic gradient [-]
i^*	estimate of i at FE nodes obtained as average from all elements [-]
i_{cr}	critical value of the hydraulic gradient magnitude at which erosion progresses further [-]
i_{cs}	magnitude of the critical, secant hydraulic gradient in front of the pipe that causes erosion progression [-]
i_h	magnitude of the component of the hydraulic gradient in the horizontal direction [-]
i_s	magnitude of the secant hydraulic gradient in front of the erosion pipe over some distance [-]
i_v	magnitude of the component of the hydraulic gradient in the vertical direction [-]
k_{eq}	equivalent hydraulic conductivity used to represent pipe flow as Darcy flow [m/s]
$[K_e]$	global hydraulic conductivity matrix
$[k_e]$	element conductivity matrix [m/s]
k_h	hydraulic conductivity of the soil [m/s]
k_i	hydraulic conductivity of the soil in the i^{th} coordinate direction [m/s]
k_{pL}	equivalent hydraulic conductivity to represent laminar pipe flow
k_{pT}	equivalent hydraulic conductivity to represent turbulent pipe flow
$k_{s,d}$	depth corrected hydraulic conductivity of the soil for use in two dimensional analysis [m^2/s]
$[k_s]$	soil conductivity matrix [m/s]
$[k_p]$	pipe conductivity matrix [m/s]
K_3	erosion rate constant [m^4/kg]
l_p	length of BEP erosion pipe [m]
$l_{p,c}$	critical length of BEP erosion pipe that occurs at the critical differential head [m]

L	length of domain in direction of flow [m]
L_h	horizontal length along a structure foundation contact [m]
L_s	seepage length along a potential pipe path [m]
L_v	vertical length along a structure foundation contact [m]
n	soil porosity [-]
$\boldsymbol{n}$	unit normal vector [-]
$\{N\}$ or N_i	element shape functions
p	notation for $\partial h/\partial y$ in Sellmeijer's analytical groundwater flow equations
P	fluid pressure or pore pressure [Pa] or perimeter of a pipe [m]
p_f	probability of failure [-]
q	specific discharge [m^2/s]
q	notation for $\partial h/\partial x$ in Sellmeijer's analytical groundwater flow equations
$\{q_e\}$	net flow rate at the nodes of a single element
Q	total flow rate [m^3/s]
$\{Q\}$	net flow rate at the finite element nodes
r	integration variable in Sellmeijer analytical solution
R	w/a is the pipe width to depth ratio [-]
Re^*	particle Reynolds number [-]
$\boldsymbol{S}$	vector of potentially influential soil properties that influence erosion behavior
$t_{(1-\frac{\alpha}{2},n)}$	value of the student's t distribution for significance level α and n degrees of freedom
t	denotes time dimension [-] OR element size [m]
$[T]$	gradient of the finite element shape functions

u	seepage velocity [m/s]
u_c	critical value of seepage velocity at which erosion occurs [m/s]
u^*	hydraulic boundary shear velocity [m/s]
$\boldsymbol{v}$	velocity vector $\{u,v,w\}$ in the *x, y,* and *z* directions [m/s]
V_f	volume of fluidized soils in the pore fluid [m^3]
$\boldsymbol{V_p}$	velocity vector of the erosion pipe tip [m/s]
$\boldsymbol{V_w}$	velocity vector of the erosion pipe walls [m/s]
V_w	volume of water in a soil [m^3]
V_l	volume of liquid in a soil, including V_w and V_f [m^3]
V	total volume of a domain [m^3] OR
V	average flow velocity through a pipe cross section [m/s]
w	width of the erosion pipe [m]
W	width of the soil domain [m]
$\boldsymbol{x}$	vector $\{x,y,z\}$ to a point
x	distance along first coordinate direction or pipe centerline [m]
y	distance along second coordinate direction [m]
z	distance along third coordinate direction or complex coordinate system in conformal mapping solution [m]
$z_{\alpha/2}$	value of the normal distribution corresponding to significance level α
β	friction factor in pipe flow [-]
β_i	regression coefficients
γ_p'	buoyant unit weight of a particle [kN/m^3]
γ_w	unit weight of water [kN/m^3]

Γ	boundary of Ω
δ	height of a pipe element when using parallelepiped or parallelogram approximations [m]
ϵ	average protrusion height, or pipe wall roughness [m]
η	White's constant for hydraulic boundary stress distribution to the particle level
η_e	relative error indicator for adaptive mesh refinement [-]
θ	bedding angle of sand for the rolling resistance of a particle [degrees] OR
θ	volumetric water content of soil given by V_w/V [-]
θ_x	spatial correlation length in the x direction
θ_y	spatial correlation length in the y direction
μ	fluid viscosity [Ns/m^2]
μ_k	mean value of hydraulic conductivity for random field [m/s]
μ_{ics}	mean value of the critical secant gradient for random field [m/s]
ρ	fluid density [kg/m^3]
ρ	correlation coefficient [-]
σ_k	standard deviation of hydraulic conductivity for random field [-]
σ_{ics}	standard deviation of the critical secant gradient for random field [-]
τ	hydraulic shear stress applied on a boundary [Pa]
τ_c	critical value of the hydraulic boundary shear stress for incipient particle motion [Pa]
τ_n	hydraulic shear stress applied on a pore boundary due to seepage through soil [Pa]
τ_{nc}	critical hydraulic pore shear stress at onset of erosion [Pa]
ϕ	seepage potential in conformal mapping [1/s]
ψ	stream function [1/s]

Ψ	Shields parameter for sediment transport
Ψ_c	critical value of the Shields parameter for incipient motion of cohesionless sediments
ω	complex potential in conformal mapping solution [1/s]
Ω	arbitrary domain in two or three dimensions
Ω_s	soil domain
Ω_p	pipe domain

ACKNOWLEDGMENTS

I was introduced to the process of backward erosion piping in 2013 through the training courses *Best Practices in Risk Assessment for Dam and Levee Safety* and *Internal Erosion for Dams and Levees* that were taught jointly by the U.S. Army Corps of Engineers (USACE) Risk Management Center and the U.S. Bureau of Reclamation. It was these courses that sparked my interest in soil erosion in general due to the significance of erosion in engineering practice for dams and levees. In particular, Chuck Redlinger, Tim O'Leary, Scott Shewbridge, Jeff Schaefer, Mark Pabst, and Gregg Scott (all of the USACE Risk Management Center) introduced me to the historical significance and challenges associated with internal erosion. Additionally, many of these individuals influenced my thoughts on the topic for years to come, often reminding me to stay focused on developing solutions we can use to assess erosion risks in practice.

Around this same time, I had the fortunate opportunity to work on a USACE funded research project focused on backward erosion piping at the U.S. Army Engineering Research and Development Center (ERDC) in Vicksburg, Mississippi. John Schmertmann and Frank Townsend of the University of Florida graciously met with me to discuss their experience as part of scoping this new research. I am grateful for their advice and insights, and I still find myself in awe of how well they truly understood the BEP process. The years 2014 and 2015 were full of interesting laboratory investigations that formed my understanding of the BEP process. My ERDC colleagues Isaac Stephens, Axel Montalvo-Bartolomei, Jamie Lopez-Soto, Johannes Wibowo, Dan Leavell, John Murphy and later Samantha Lucker were instrumental in helping to develop and run the many laboratory experiments on BEP conducted, some of which

formed the basis for this thesis. I will be forever grateful for their collaboration, hard work, and shared excitement for investigating the process of BEP. I also had the fortunate opportunity as part of this effort to work with Vera Van Beek, Esther Rosenbrand, Adam Bezuijen, Joost Pol, Sepidah Akrami, John Van Esch, Wim Kanning, and Andre Koelewijn as part of a formal research collaboration between the U.S. and Dutch governments. I greatly appreciated the thought provoking and challenging conversations I've had with all of these individuals. In particular, I had the opportunity to spend significant time working with Vera Van Beek on both experimental and numerical modeling of BEP. In many ways, she charted the path forward with BEP research that I have followed. I am extremely thankful for her mentorship, collaboration, inspiration, and overall friendship.

As this research project was beginning, I approached my advisor D.V. Griffiths in 2015 to inquire about pursuing a Ph.D. on the topic of modeling internal erosion. My experience up to this point was entirely experimental, and I wanted to learn more about numerical modeling. Professor Griffiths taught me everything I know about numerical modeling, programming in Fortran, and the finite element method. I am extremely grateful for his patience, gentle encouragement, and persistent correction on many of the little things I often overlook. From observing him over the years, I have learned the value of having great colleagues, the importance of publishing, and that we should always strive to share research and resources with others.

Lastly, completing this would not have been possible without God and family. I thank God for providing the drive, talents, and support needed to finish. I am forever grateful to my beautiful wife Angela and children Cameron, Ellie, Kaycee, and Abby for the patience and support over the years it took to finish this. While we have always found time for fun, many

nights and weekends were spent working away from them. Without their sacrifice, completing this effort would have never been possible.

CHAPTER 1

INTRODUCTION

One of the greatest threats to the integrity of existing dams and levees is internal erosion (Foster et al., 2000). Backward erosion piping (BEP) is one type of internal erosion that is very common for both dams and levees (Richards & Reddy, 2007; van Beek et al., 2013). This thesis is focused on exploring the use of finite element modeling for predicting the progression of BEP erosion. In this introductory chapter, a brief overview of internal erosion is provided to define the types of internal erosion and design strategies for preventing it. The motivations for this thesis are then described. Finally, the specific research objectives for this work are stated before describing the outline for the remainder of the thesis.

1.1 Overview of Internal Erosion

Internal erosion refers to any process that erodes soil within or beneath an embankment (ICOLD, 2015). Soil erosion can gradually degrade the structure, in many cases leading to catastrophic breach of the embankment as illustrated in Figure 1.1. Historically, internal erosion has accounted for 46 percent of embankment dam failures (Foster et al., 2000). In the United States, internal erosion is also a major issue of concern for levee embankments constructed along rivers to control flooding. A recent report on the national levee portfolio in the U.S. indicated that internal erosion constitutes the second largest risk driver for levee failure after overtopping (Baker, 2018). Given the statistical significance of internal erosion as it pertains to management of the nation's water resource infrastructure, it is critical to develop methods for predicting the

spatial and temporal progression of erosion so that limited financial resources can be efficiently prioritized to minimize failure risks.

Figure 1.1. Photograph of the Teton Dam failure near Rexburg, Idaho in 1977 (USBR, 2020).

The phrase *internal erosion* is a general term that describes all types of erosion that may occur internal to a structure. Experience has shown that erosion can occur by distinctly different mechanisms as illustrated in Figure 1.2. As such, internal erosion has been subdivided into five mechanisms based upon the dominant mechanics of the process driving the erosion progression (e.g., Bonelli, 2013; Fell, 2011; Fry, 2009; Hunter, 2012; ICOLD, 2015). The five internal erosion mechanisms are (1) concentrated leak erosion, (2) backward erosion piping, (3) internal instability, (4) contact erosion, and (5) global backward erosion (also called stoping).

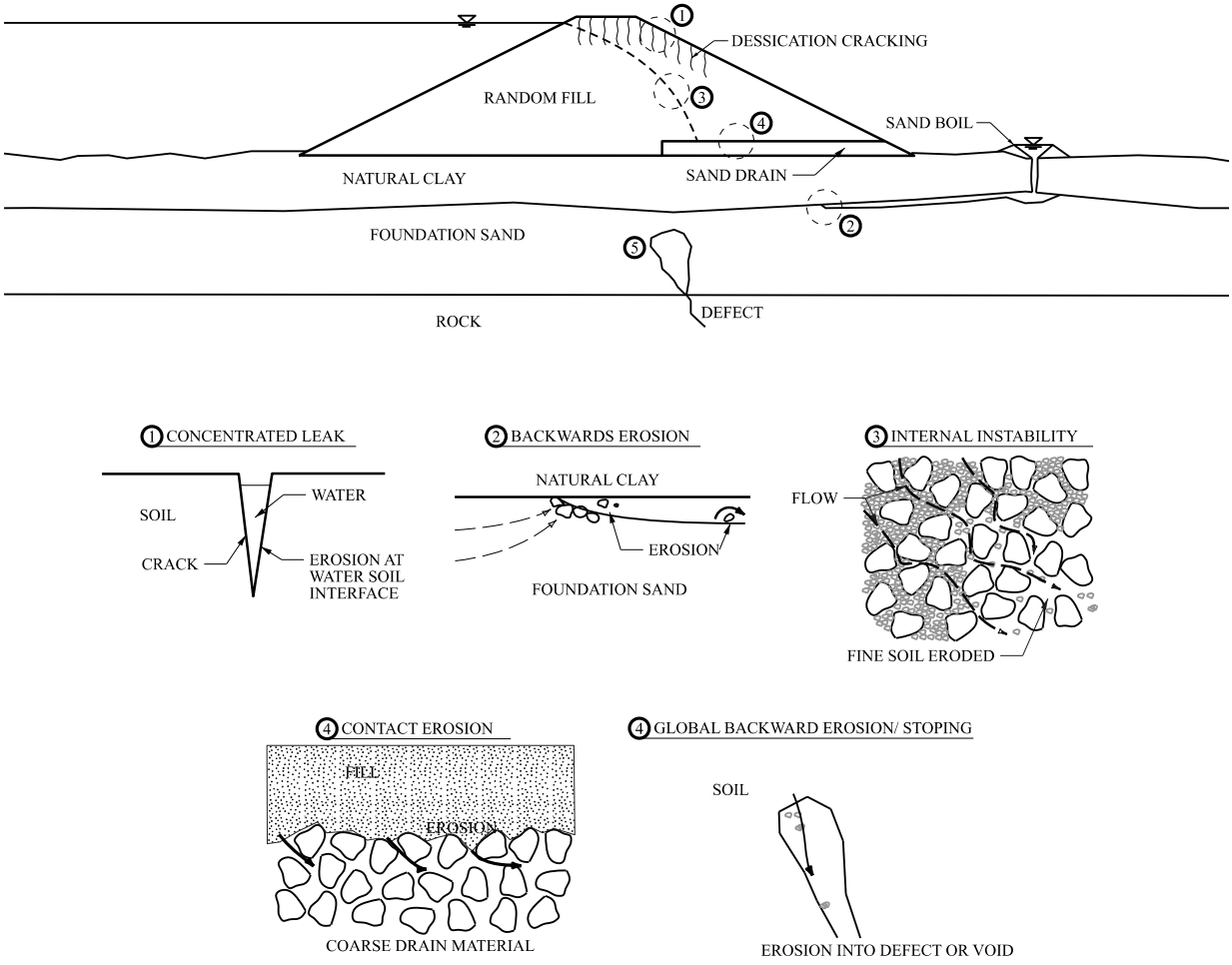

Figure 1.2. Illustration of the 5 types of internal erosion.

With reference to the illustrations in Figure 1.2, each erosion mechanism is defined as follows.

1. Concentrated leak erosion occurs when water flows freely through an opening such as a crack in an embankment and erodes the soil on the walls of the opening. This type of internal erosion is unique as it is the only process driven by freely flowing fluid through an opening. All other IE mechanisms are driven by flow through porous media. Concentrated leaks are the most dangerous internal erosion mechanism as they account for the largest percentage of historical failures (Foster et al., 2000). This is

because leaks occur along common structures through embankments (e.g., outlet works, culverts, interfaces between structural walls and embankments, etc.).

2. Backward erosion piping (BEP) refers to an erosion process by which shallow erosion channels progress upstream, or "backwards", through the foundation sands along the base of a cohesive cover layer as illustrated in Figure 1.2. The eroded foundation sand is often deposited on the ground surface in the form of a sand boil on the downstream side. Backward erosion is driven by the flow through the soil upstream of the pipe, but involves open pipe (conduit) flow through the eroded channels that develop. Additionally, there must be a competent material above the erosion pipe that develops for it to remain open. BEP is the second most dangerous IE mechanism as it has been estimated that approximately 30% of dam failures due to IE are caused by BEP Richards and Reddy (2007).
3. Internal instability refers to all processes by which the fine fraction of a soil matrix is selectively eroded from within the coarser fraction. Internal instability can be further subdivided into the processes of suffusion and suffosion (Fannin & Slangen, 2014) depending on whether or not the erosion causes overall volume change of the soil body. While no significant dam failures have been caused by internal instability, this mechanism has caused costly damage to many structures (Fannin et al., 2011; Garner & Fannin, 2010; Mullens, 1999; Sherard, 1979).
4. Contact erosion refers to erosion of a fine grained soil by water flowing through an adjacent coarse grained soil as illustrated in Figure 1.2. While there is a published case of a potential dam failure due contact erosion (Dounias & Bardanis, 2019), this mechanism is also rarely the cause of failures due to the limited geomorphic

depositional environments capable of producing the conditions for contact erosion to occur.

5. Global backward erosion (or stoping) refers to the process by which open, typically unsaturated, voids progress upwards through the vadose zone in the embankment (Hunter et al., 2012). This type of erosion is usually initiated by dissolution of karstic foundations, filter incompatibility that leads to movement of one dam zone into another, or one of the other IE mechanisms (e.g., internally unstable soils). However, once the void is initiated, the erosion is driven by gravitational forces causing the intermittent collapse of the void in response to changing moisture conditions and corresponding matric suction in the soil surrounding the void. Because this driving mechanism is very different than the other IE mechanisms, it has been listed as a separate category.

Regardless of the type of IE, the design strategy for preventing erosion is the same. All types of internal erosion can be prevented by ensuring properly designed filters and drains are included in the embankment to safely convey seepage out of the dam without removing materials. Fry (2016) reviewed dam failure databases available at the time and discovered that there has not been a single dam failure to date that has included properly designed filters. This clearly indicates that filters are a successful approach to prevent internal erosion. To be considered properly designed, a filter and drain system must (1) be properly graded to prevent erosion and ensure drainage and (2) be placed at all locations where erosion may occur. A cross section with filters meeting these requirements is illustrated in Figure 1.3. When these requirement are met, the filter will prevent material from being removed from the embankment

section due to seepage. If erosion does initiate, it will eventually self-arrest due to material accumulation at the filter interface. For further details on designing against internal erosion with filters and drains, the interested reader is referred to Robbins and Griffiths (2018a) for a summary or FEMA (2011) for a detailed manual on design and construction of embankments with filters.

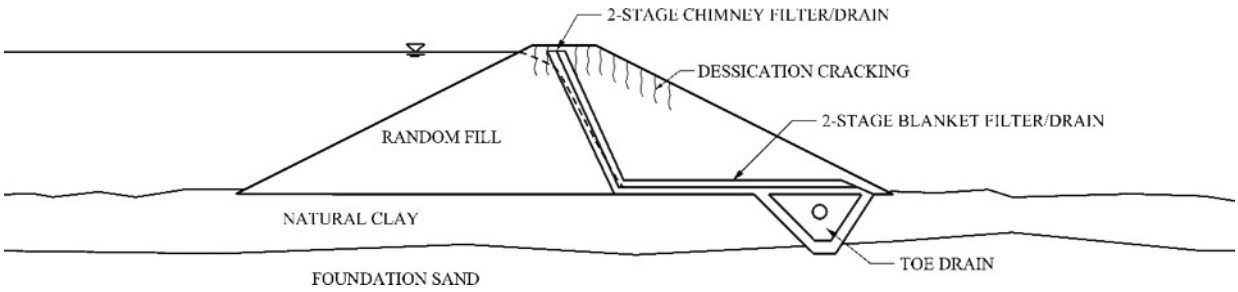

Figure 1.3. Schematic of a modern filter and drain system to prevent IE.

1.2 Motivation: Assessing risks for BEP

While internal erosion can be prevented via properly designed filters, a significant portion of existing dams and levees do not include filters. Many dams were constructed before a proper understanding of filters was developed (Redlinger et al., 2016). There are also many dams and levees for which it was not economically justifiable to include filters in the design during the era of construction. Since these structures have been built, there has been increased development and urbanization in adjacent areas. As a result, these embankments are often a source of high failure risks in terms of potential life loss and economic damages. Wing et al. (2020) demonstrated that these risks will only continue to increase over the next 30 years due to increased development and climate change. Local, state, and federal agencies are tasked with assessing and managing these risks which requires an ability to assess the potential for BEP to

progress to failure. At present, numerical models of BEP progression are not used to assess risks associated with BEP in the United States. Instead, relatively simple calculation rules are used in conjunction with event trees and expert elicitation. This is primarily due to the fact that (1) it has not been demonstrated conclusively that BEP progression can be generally predicted via numerical models and (2) no rationale means of selecting model input parameters based on soil type or laboratory tests has been presented. These issues form the primary motivations for pursuing this research.

1.3 Research Objectives

The objectives of this research are to:

1. Develop finite element (FE) software to model BEP progression in both two- and three-dimensions based on a spatially dependent, local hydraulic criterion near the upstream pipe tip that can be measured in the laboratory.
2. Validate the FE modelling approach, including determination of model parameters, through hindcasting of experimental results.
3. Examine the differences between two- and three-dimensional model predictions.
4. Demonstrate efficient means of assessing BEP for field scale problems through use of adaptive meshing.
5. Develop a means for accounting for soil spatial variability in finite element models for BEP progression.

1.4 Thesis Outline

The remainder of this thesis presents a review of the BEP literature, a description of the finite element model developed for this investigation, a description of laboratory measurements developed for measuring model parameters, and various FE simulation results focused on the research objectives. More details for each chapter are provided in the following paragraphs.

Chapter 2: A review of the literature is provided to present the current state of knowledge regarding the process of BEP, review predictive models commonly used to assess BEP risks in the U.S. today, and summarize the various efforts that have been made to numerically model BEP to date. Issues preventing widespread adoption of numerical models are reviewed.

Chapter 3: Finite element models are developed for simulating the progression of BEP in both two- and three-dimensional domains based upon the head profile in front of the erosion pipe. The governing equations are described along with the various assumptions that can be made regarding discretization of the erosion channel. Additionally, the concept of a Critical, Secant Gradient Function (CSGF) is introduced as a new criterion for pipe progression.

Chapter 4: A novel laboratory experiment is described for measuring the CSGF for pipe progression . A series of 24 laboratory experiments on 7 different sands is conducted to measure the CSGF for various sand types and densities. The results are used to develop equations for predicting the CSGF.

Chapter 5: The finite element modelling approach, simulation algorithm, and concept of the CSGF are validated through three-dimensional simulations of a series of 5 experiments with varying scale, geometry, boundary conditions, and sand types. The sands are the same as the sands for which the CSGF was measured, so the CSGF is applied to the simulations in a predictive manner (no model calibration).

Chapter 6: A thorough understanding of the various source of model errors is critical for understanding which modeling approaches are preferred and overall model reliability. Assessment of the source of errors in the FE solutions for the validation case histories in Chapter 5 is performed by comparing analyses with varying mesh sizes and shape function order.

Chapter 7: Analyses using FE models formulated in both two- and three- dimensions for an example problem are presented to understand the differences between two- and three dimensional model results.

Chapter 8: Because of the small scale at which BEP progression must be assessed, it is difficult to model BEP progression at the field scale using a fixed FE mesh. As such, Chapter 8 describes an approach for modeling BEP progression with adaptive mesh refinement in two-dimensions. The approach is used to demonstrate (1) the influence of turbulent vs. laminar flow assumptions for field scale problems and (2) how FE models for BEP progression can be used to assess the effectiveness of remedial measures used to prevent BEP.

Chapter 9: As BEP is influenced greatly by spatial variability in soil properties, Chapter 8 demonstrates how FE models can be used in a random finite element method (RFEM) framework to assess the influence of soil variability on the probability of pipe progression.

Chapter 10: A summary of the conclusions and primary contributions that can be drawn from this work are presented. Additionally, implications for civil engineering practice and recommendations for future research are also provided.

CHAPTER 2

LITERATURE REVIEW

Erosion due to seepage through dams was recognized as a potential failure mode in the late 19th century by British engineers working on irrigation projects in India (Bligh, 1910; Griffith, 1913; Lane, 1935). Unfortunately, it was not until the last two decades that clarity regarding the different types of IE was achieved. In 2007, a technical working group of the International Committee on Large Dams established the phrase "backward erosion" to refer to BEP (Fell and Fry, 2007). Prior to this time, the terms "piping" and "internal erosion" were used in a generic sense to refer to all types of erosion, and there was significant ambiguity throughout the literature regarding what erosion mechanism was being discussed. Because of this, a thorough literature review was conducted reviewing publications on all types of internal erosion to ensure pertinent studies were not missed by focusing specifically on the phrase "backward erosion piping". This resulted in a compilation of 950 publications from various journals, books, conferences, government institutions, and academic institutions on the topics of internal erosion and design of embankments to prevent internal erosion. The temporal distribution of these publications by publication year is provided in Figure 2.1. Fortunately, it is not necessary to review all of these works as part of this thesis. In recent years, entire books have been published that provide excellent, comprehensive reviews of this body of literature (e.g., Stéphane Bonelli, 2013; ICOLD, 2015). Further, multiple authors have provided detailed reviews of prior studies on BEP as part of their PhD dissertations (Allan, 2018; van Beek, 2015; Vandenboer, 2019). Rather than repeat these extensive works herein, the interested reader is referred to these other studies for detailed overviews of the body of IE literature. Instead, the sections that follow first provide a brief chronology of the evolution of IE/BEP literature to provide overall context. This

is followed by a description of the BEP process and physical characteristics so that a thorough understanding of the process is obtained before examining predictive models. A review of current approaches for predicting BEP progression in practice is then provided. Finally, prior studies on numerical modeling of BEP are reviewed along with a summary of current issues preventing widespread use of models in practice.

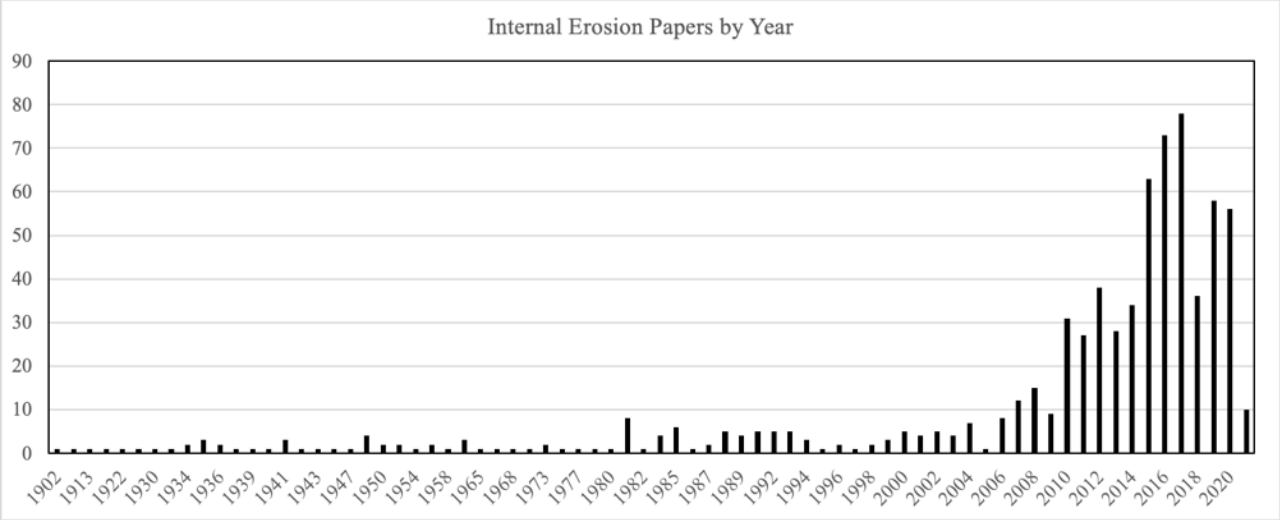

Figure 2.1. Distribution of IE papers by publication year.

2.1 Chronology of Developments

The failure mechanism of BEP became a focal point of discussion in the late 19th century due to irrigation weirs commonly failing due to piping in India. As shown in Figure 2.2, these weirs were relatively low head structures with predominantly horizontal seepage paths. As these structures were often built on river beds of fine sand, they presented ideal conditions for BEP to occur. At this time, methods of analyzing seepage through porous media had not yet been developed, so Bligh (1910) and Griffith (1913) proposed the concept of creep ratios, defined as

$$C_r = \frac{L_h + L_v}{H} \tag{2.1}$$

where L_h denotes the length of the horizontal paths along the structure-soil contact (lines aB and Ef in Figure 2-2c), L_v denotes the length of vertical paths (Lines Aa, BC, DE, and fF in Figure 2.2C), and H is the differential head across the structure.

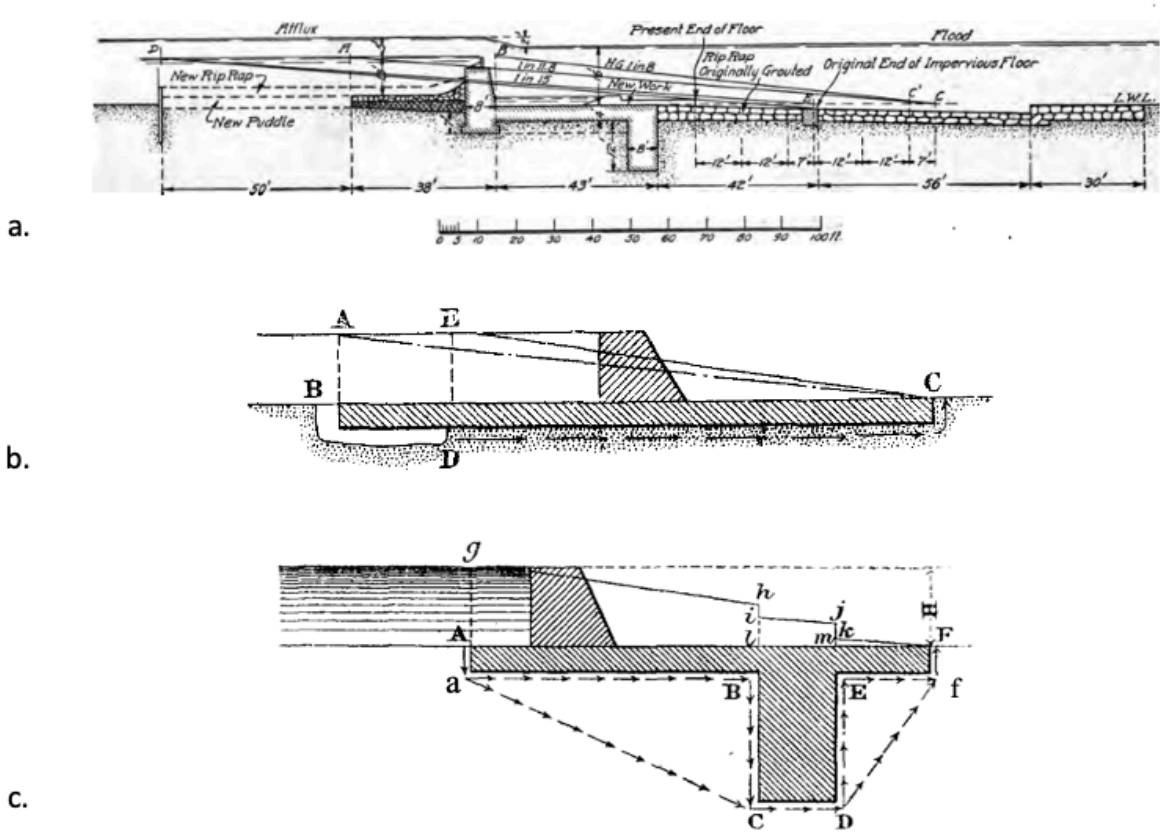

Figure 2.2. Examples weir cross sections illustrating (a) actual cross section of Narora Weir that failed (Bligh, 1915)(b) an example cross section with horizontal seepage path and conceived pipe erosion mechanism (Griffith 1913), and (c) example cross section with vertical seepage path components (Griffith 1913).

Through analysis of unknown case histories, both Bligh and Griffith independently appear to have developed recommended values of safe creep ratios based on foundation materials (Table 2.1). Eventually, the effectiveness of vertical cutoffs was recognized, and Lane (1935) proposed

the weighted creep ratio by giving vertical seepage paths 3 times more weight than horizontal paths. Design values for weighted creep ratios were developed by evaluating 251 concrete and masonry dams, of which only 21 had failed (Lane 1935). Even at the time of publication, there was significant debate over the utility of creep ratios. This was in part because there was not common terminology regarding what type of internal erosion was being referred to, and partly due to the fact that a more scientific approach to design had been developed via the use of flow nets, electrical analogues, and analytical solutions for analyzing flow through porous media (Harr, 1962). Additionally, Terzaghi (1922) had developed the concept of using weighted filters to safely collect seepage and control erosion. Following the publication of Casagrande's treatise on flow nets (1937) and Terzaghi's methods for designing filters (1939), the civil engineering profession widely adopted the use of seepage analysis and filters for designing dams. From 1940 to 1980, the focus of the profession was on using filters to design against internal erosion. Research related to BEP was focused on improved methods of seepage analyses (e.g., Bennett, 1945; Cedergren, 1948), improved filters (e.g.,Casagrande, 1950; Rice & Arthur, 1948; WES, 1941, 1948, 1953), or methods of ensuring prevention of initiation of BEP for cases without filters (e.g., Turnbull & Mansur, 1961b, 1961a). It was not until the 1970's that research into the physical process of BEP began to emerge due to a string of catastrophes.

From 1953 to 1979, many significant dam and levee failures occurred around the world due to erosion. In 1953, the North Sea flood caused a storm surge in the Netherlands 18.4 feet above mean sea level which resulted in the Zeeland dykes breaching in 67 locations, leading to widespread inundation (Figure 2.3). The flooding caused 1,835 fatalities, loss of 47,000 head of livestock, inundation of 47,300 buildings, and $1 billion in damages (Jonkman and Kelman, 2005). Similarly, large floods occurred in Germany in 1954 on the Elbe and Danube rivers, and

in 1965 on the Danube rivers (Hattermann et al. 2012). It is estimated that the 1965 Danube flood alone caused more than $1 billion in damages (NY Times, 1965). In the United States, Teton dam failed in 1976 due to concentrated leak erosion causing 11 fatalities and as much as $2 billion in damages (Reisner, 1986). This catastrophic dam failure led to the U.S. requiring that risk assessment be used as part of federal dam safety programs (FEMA, 1979). Lastly, while a much smaller scale failure, Florida Power and Light Company had a dike fail at the cooling reservoir for Martin Power Plant near Lake Okeechobee, Florida in 1979 due to BEP that caused $20 million in damages and impacted 1,700 people (Kleinberg, 2021).

Figure 2.3. Flooding due to 1953 storm surge in Oude-Tongue, Goeree-Overflakkee, Netherlands. (National Archives photo no. 541705/286-ME-8(1))

Table 2.1. Creep ratios and weighted creep ratios recommended for dam design by Bligh, Griffith, and Lane.

Material	Creep ratio (Bligh)	Creep Ratio (Griffith)	Weighted creep ratio (Lane)
Very fine sand or silt	18	..	8.5
Fine sand (micaceous)	15	14.5-16	7.0
Fine sand (quartz)	..	12.5-14	..
Medium sand	..	..	6.0
Coarse sand	12	..	5.0
Coarse sand (quartz)	..	10-12	..
Fine gravel	..	..	4.0
Medium gravel	..	..	3.5
Shingle	..	8	..
Gravel and sand	9	..	..
Coarse gravel, including cobbles	..	..	3.0
Boulders with some cobbles and gravel	..	..	2.5
Boulders, gravel and sand	4 to 6		..
Boulders	..	4	..
Soft clay	..	..	3.0
Medium clay	..	..	2.0
Hard clay	..	..	1.8
Very hard clay or hardpan	..	..	1.6

Following these disasters, much focus was dedicated to understanding internal erosion, with specific emphasis on BEP. Research programs were initiated at the University of Berlin (Hanses, 1985; Miesel, 1978; Muller-Kirchenbauer, 1978), the Delft Soil Mechanics Laboratory (de Wit, 1984; de Wit, Sellmeijer, & Penning, 1981; Sellmeijer, 1988; Sellmeijer et al. , 1989; Silvis, 1991), and the University of Florida (Schmertmann, 2000; Townsend et al.,

1988; Townsend et al., 1981; Townsend & Shiau, 1986). As a result, an increase in publications was observed from 1980 to 1994 (Figure 2.1). In 1993, the European countries in the International Commission on Large Dams (ICOLD) had delegates meet for the first meeting of what is now known as the European Working Group on Internal Erosion (Brown, 2007). This group has met on nearly an annual basis since that time with members accounting for a significant fraction of the publications shown in Figure 2.1. Additionally, Foster et al. (2000) published their seminal findings that nearly half of embankment failures are due to internal erosion (of all types). Since that time, there has been a significant increase in research focused on understanding internal erosion in order to better assess and manage internal erosion risks. Part of this has included establishing common definitions and terminology to facilitate accurate reporting and communication (Fry and Fell, 2007; Bonelli 2013; ICOLD 2015). In the last two decades, many other researchers around the world have conducted additional laboratory experiments aimed at better understanding the physics of BEP and predictive methods in use today. Additionally, many studies have proposed numerical models for simulating the process. Significant developments from these studies are summarized in the sections that follow.

2.2 The Nature of BEP

Current understanding of the BEP process comes primarily from experimental work conducted by various researchers around the world. These experiments have varied in scale from small, bench scale experiments to full scale embankment prototypes (Figure 2.4). The most significant studies have been those conducted by Miesel (1978), Mueller-Kirchenbauer (1978), Pietrus (1981), de Witt (1984), Hanses (1985), Townsend et al. (1986), van Beek (2008), van Beek (2015), Allan (2018), and Vandenboer (2019). From these studies, a complete description

of the BEP process has been developed. Additionally, the measurements from many of these studies have formed the basis for the predictive methods in use today. Given the significance of these studies, it is imperative to have a general understanding of the experimental configurations, testing procedures, and general results obtained in order to understand some of the issues with current practice. For this reason, the sections that follow will first provide a description of the BEP process before describing typical experiments and results. Following this, physical characteristics of the BEP process will be illustrated based on measurements from the studies mentioned. Vandenboer (2019), Allan (2018), and Van Beek (2015) provide additional details on the experiments described below.

Figure 2.4. Illustration of (a) small scale experiments (0.8m length), (b) medium scale experiments (1.6 m seepage length), and large scale experiments (15 m) (van Beek, 2015).

2.2.1 The Process of BEP

The process of BEP can be broken down into 6 Phases as illustrated in Figure 2.5. These phases are:

Phase 1 – Seepage: Flow of groundwater through the foundation must occur due to an elevated water level on one side of the structure.

Phase 2 – Initiation: Erosion initiates in areas of local flow concentration (van Beek et al., 2014) at unfiltered exit locations where particles can freely mobilize due to high seepage forces. Studies by van Beek et al. (2014) and Montalvo-Bartolomei et al. (2018) have indicated that erosion initiates over groups of grains varying in scale from approximately 10 grains to upwards of 40 grains. Because of the small length scale over which initiation occurs, it cannot be reliably predicted for field scenarios due to natural variability (namely geometry near seepage exits and soil properties). Therefore, prediction of BEP risks has focused primarily on the next phase of the process.

Phase 3 – Progression: Once erosion has initiated, a pipe may form and progress upstream opposite the direction of flow. The pipe that forms is an open channel through which sediment and water flow towards the pipe exit. The eroded material is often deposited on the ground surface near the exit in what is commonly known as a "sand boil" (Figure 2.6). The groundwater flow concentrates severely towards the erosion pipe due to the low resistance to flow in the open pipe that develops (Figure 2.5). The high hydraulic gradients that develop near the pipe tip as a result of this concentrated flow lead to further grain detachment and pipe progression (Hanses, 1985; Van Beek, 2015). Because the locally elevated gradients are responsible for the pipe progression, the erosion near the pipe tip has been called *primary erosion* (Hanses, 1985). As the pipe progresses, more flow is conveyed by the pipe leading to widening and deepening of the pipe along its length. The erosion that enlarges the pipe due to increased flow has been called *secondary erosion* as it influences the overall process but does not directly drive the pipe progression *(Hanses, 1985)*. The terms *primary erosion* and *secondary erosion* will be used

throughout the remainder of this thesis to describe the erosion at the pipe tip and pipe walls, respectively.

Phase 4 – Pipe Enlargement: When the erosion pipe reaches the upstream water source, a significant increase in the flow rate through the pipe is experienced as flow is no longer limited by the soil. The increased flow rate leads to rapid widening and deepening of the erosion pipe, primarily driven by erosion and transport of sand on the bottom of the pipe.

Phase 5 – Dike Failure: As the pipe enlarges, deformations will begin to be observed as the embankment settles due to the foundation being removed by erosion. Eventually, the embankment will collapse into the erosion pipe due to a combination of settlement and slope failure. The initial collapse may only be a partial collapse or may lead to instantaneous breach.

Phase 6 – Breach: In many instances, a partial failure of the embankment will occur prior to breach. In these cases, the partial failure may temporarily block the erosion channels. When this occurs, erosion must undermine the collapsed embankment further for additional failure to occur. Series of failures may take place until the embankment collapses completely leading to full breach of the structure.

Generally speaking, previous studies have focused primarily on Phases 1-3 as these phases are the most pertinent for ruling out risk of failure. The modelling work presented in this thesis is focused on predicting the extent of erosion progression in Phase 3.

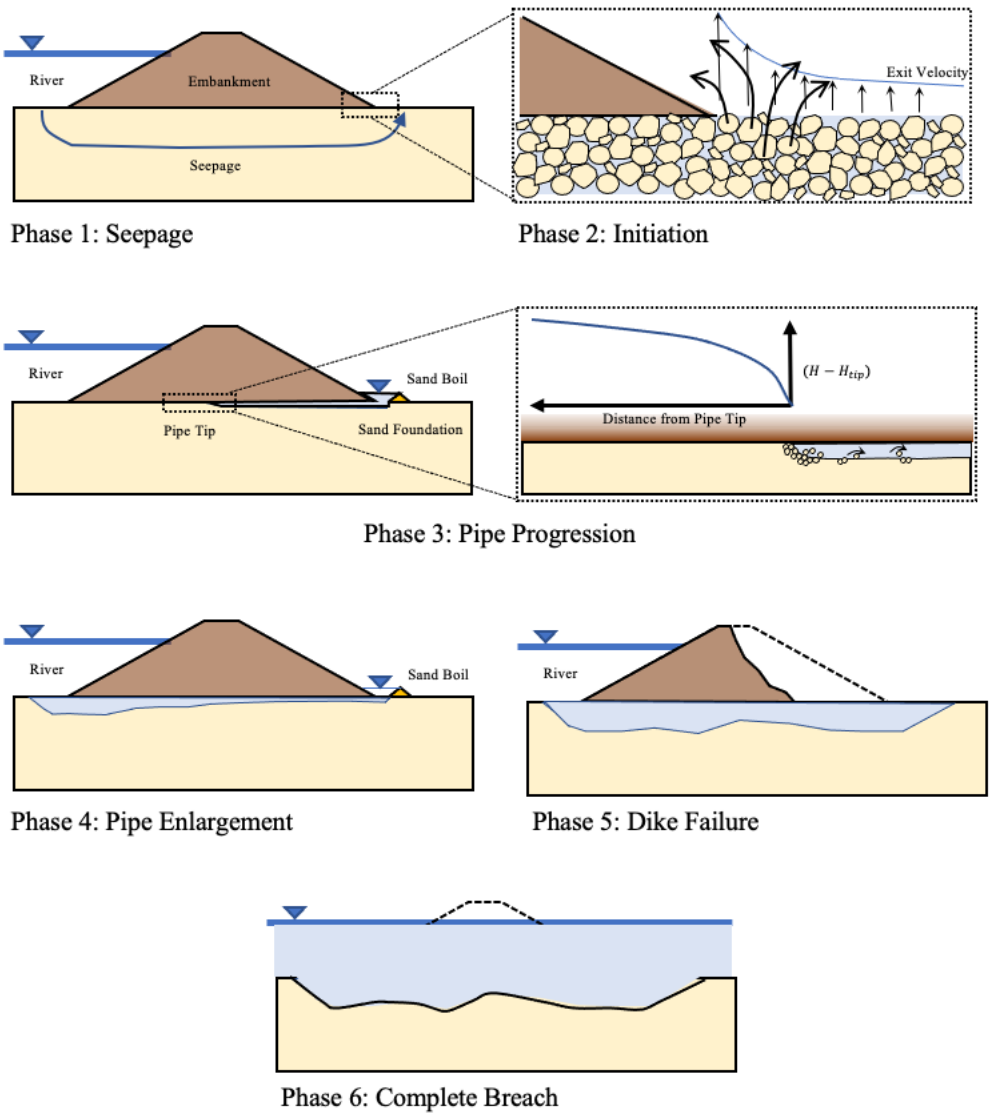

Figure 2.5. Illustration of the BEP process (modified from van Beek 2015, Allan 2018, and Robbins and Griffiths 2022).

Figure 2.6. Large sand boils near Ensley Levee Memphis, TN during the 2011 Mississipi River Flood (Schaefer, et al., 2017)

2.2.2 BEP Experiments

There have been extensive series of BEP experiments conducted by many authors (e.g., (Allan, 2018; de Wit, 1984; Miesel, 1978; Muller-Kirchenbauer, 1978; Pol et al., 2021; Robbins et al., 2020; Robbins et al., 2018; Silvis, 1991; Townsend et al., 1981; Townsend & Shiau, 1986; Van Beek, 2015; Van Beek et al., 2011; Vandenboer, 2019; Yao et al., 2007). While there are subtle differences between test series, the approach for BEP experiments has generally been the same and can be summarized by Figure 2.7. Experiments consist of a soil sample with constant head boundary conditions on the upstream and downstream boundaries. The experiments are run by incrementally increasing the differential head (H) across the soil

sample and observing the progression of BEP erosion channels. The erosion channels may branch and spread into networks of pipes (Figure 2.8a) or progress as a single developing pipe (Figure 2.8b) depending on how concentrated the flow is within the experiment. Because of the meandering nature of the pipes, it is very difficult to measure local pressures precisely near the pipe tip and channel. For this reason, most experiments have only reported the total differential head across the sample (H) at various stages of the experiment.

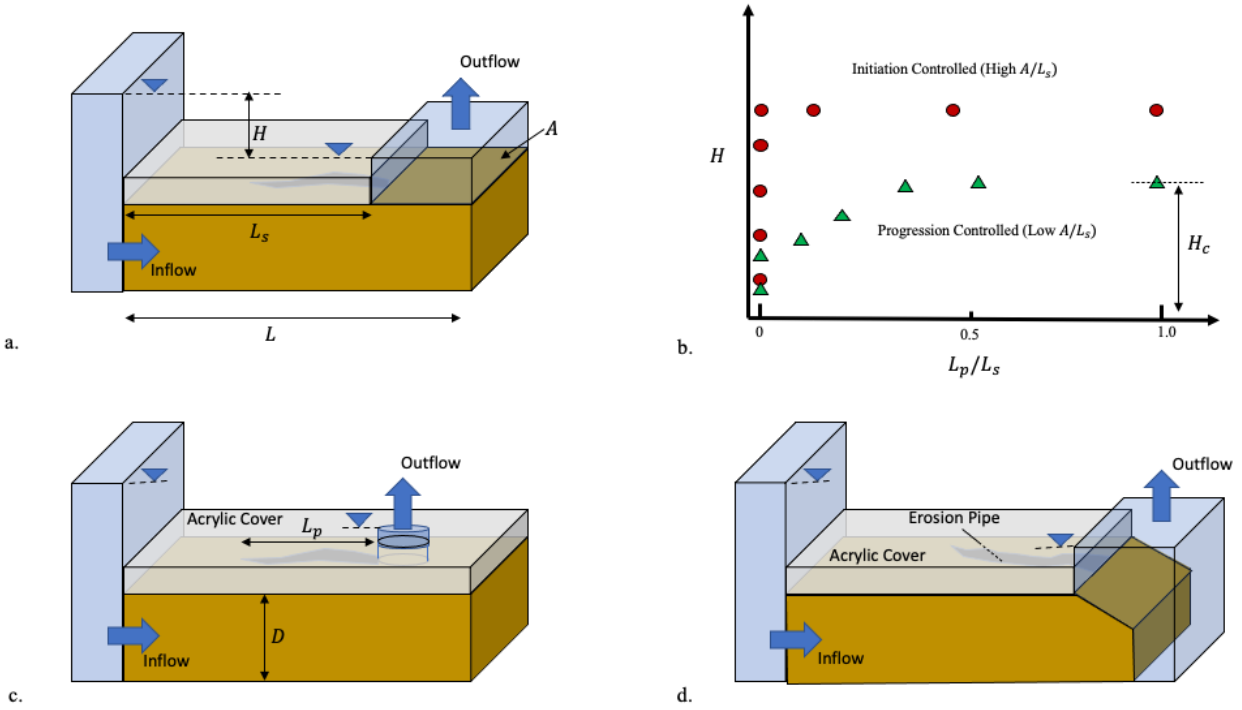

Figure 2.7. Illustration of typical BEP experiments with (a) plane/area exit conditions and (b) typical results showing equilibrium pipe position at different differential head. Exit conditions of (c) hole type exits and (d) sloped type exits are also common. Experiments that concentrate flow are often progression controlled (b) whereas experiments without flow concentration are initiation controlled and often do not provide information regarding progression conditions.

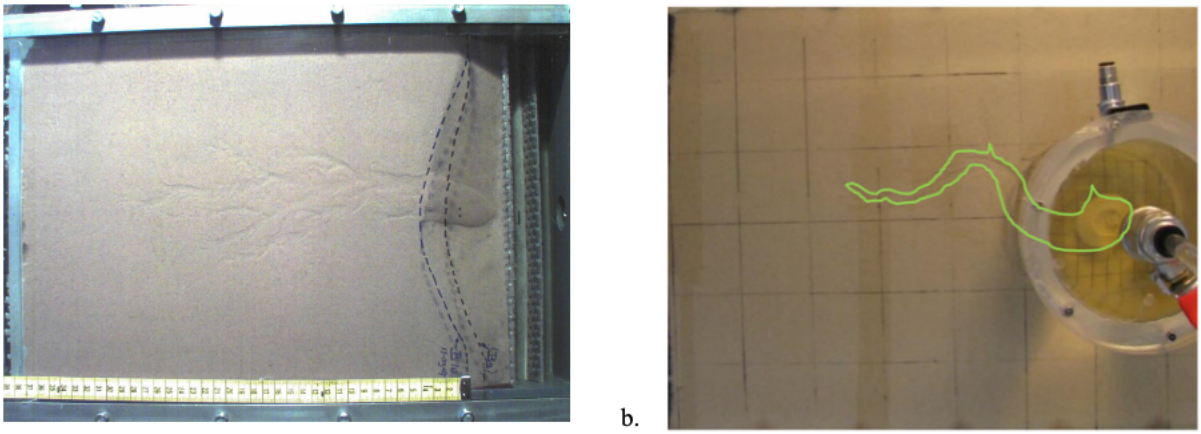

Figure 2.8. Photographs illustrating (a) the meandering and branching nature of erosion pipes (van Beek, 2008) and (b) the meandering nature of a single pipe that develops with more concentrated seepage flow (Vandenboer, 2019).

While the general testing procedure has been similar, there are differences in geometry and boundary conditions between studies. These differences can be summarized primarily by the choice of inflow and outflow boundary geometries. The inflow boundaries have mostly been vertical constant head boundaries as illustrated in Figure 2.7. However, there have been a handful of studies that have used a horizontal inflow boundary similar to what might be the case for an actual dike on a sand foundation (Figure 2.5). The outflow geometries used have mostly been area or plane type exits (Figure 2.7a), hole type exits (Figure 2.7c), and sloped type exits (Figure 2.7d). There have also been a few experiments with ditch type exits in which the downstream portion of the outflow area shown in Figure 2.7a would be covered to concentrate the exiting seepage into a narrow strip.

Experiments are either initiation controlled or progression controlled (Van Beek, 2015). For initiation controlled experiments, the head required to initiate erosion exceeds the critical head for progression. As such, erosion progresses completely upstream once initiation occurs without any further increase in head as indicated conceptually by the relationship between

normalized pipe length and H illustrated in Figure 2.7b. For progression controlled experiments, the erosion pipe initiates at a low value of H and comes to equilibrium. The pipe then progresses a little further with each increase in H until the critical head (H_c) for failure is reached, at which point the pipe progresses to failure without any further increase in H. It is important to recognize the difference between initiation and progression controlled experiments as initiation controlled experiments should not be used for calibrating models of progression. Unfortunately, this has not been the case for many studies in the literature. In general, large scale experiments and experiments with small outflow area (A) have been shown to be progression controlled as these configurations tend to concentrate flow more severely leading to local zones of high hydraulic gradients near the seepage exit at relatively low values of differential head, H.

The experimental studies conducted have reported general trends regarding the critical head for BEP initiation and progression. From these, the following conclusions can be drawn:

- H_c increases as soils become more well graded (increasing coefficient of uniformity) (Schmertmann, 2000; Allan, 2018)
- H_c increases with increasing density (de Wit 1984; Van Beek et al. 2008)
- H_c decreases as the model depth (D) increases (Van Beek 2015)
- H_c/L decreases with increasing experiment scale (Van Beek 2015)

In addition to identifying these general trends, many quantitative observations regarding BEP have been recorded from experiments. The following sections summarize observations pertinent to model development.

2.2.3 Geometry of Erosion Pipes

The erosion pipes due to BEP have been shown to be shallow and wide. This is clearly seen in the photograph and sketch provided by Hanses (1985) and Muller-Kirchenbauer et al. (1993), respectively, shown in Figure 2.9. More recently, Allan (2018) has produced molds of the erosion pipes to measure the channel width and depth (Figure 2.10a), while van Beek (2015) profiled the pipe with a laser (Figure 2.10b). From all of these sources, it is evident that the channels that develop are significantly wider than they are deep. This information is relevant for model development as it informs the cross-sectional shape assumed for the erosion channels. It is readily seen that the channels are best approximated by wide, shallow trapezoidal or rectangular cross sections.

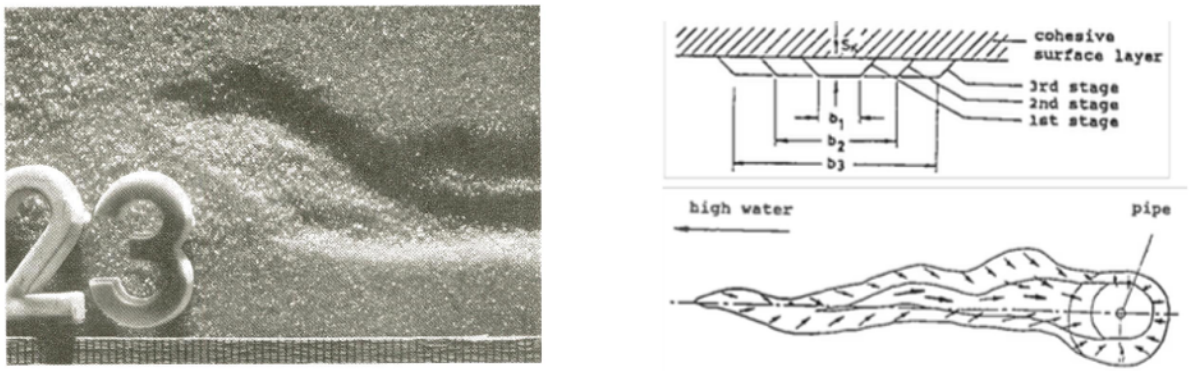

a. b.

Figure 2.9. Erosion pipe geometry illustrated by (a) photograph of a BEP erosion channel for test number 23 (Hanses, 1985) and (b) sketch of erosion pipe dimensions observed in experiments (Mueller-Kirchenbauer, 1993).

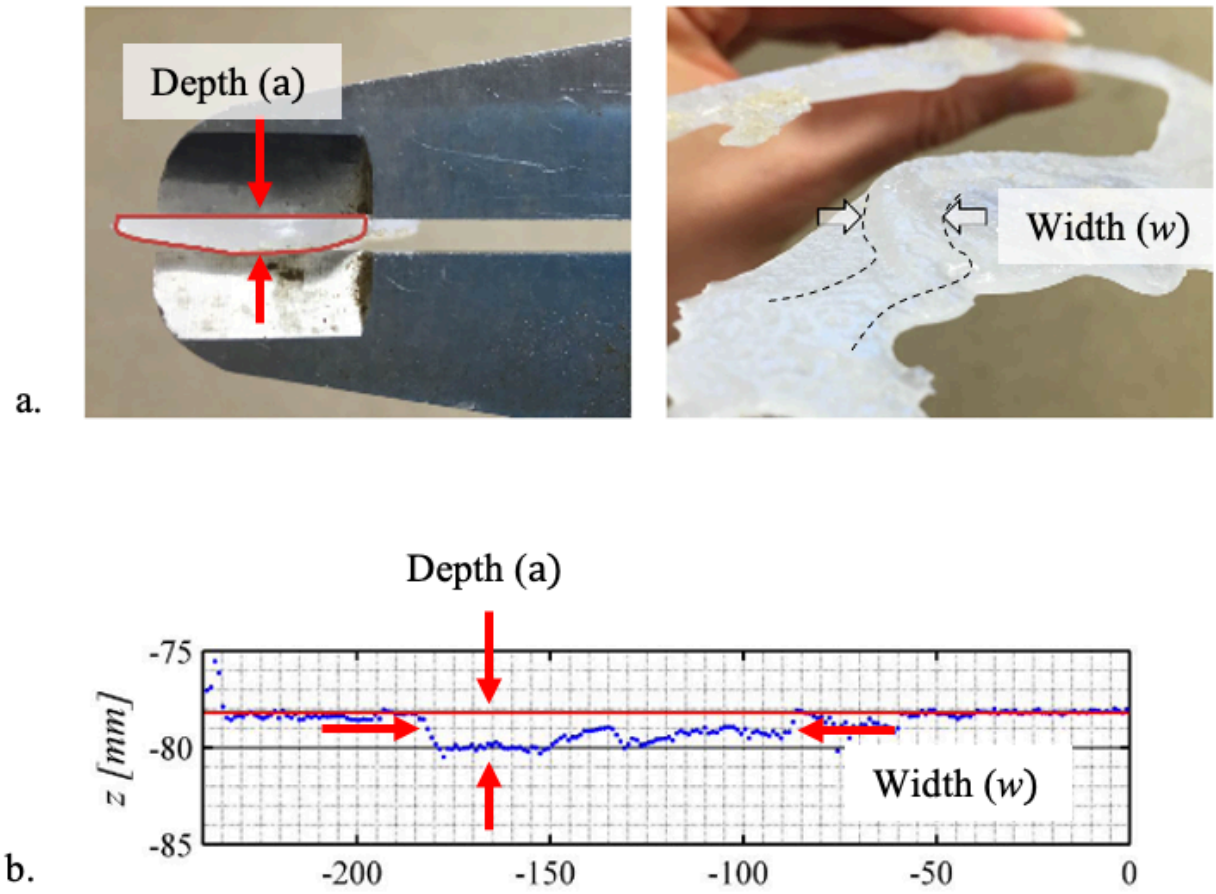

Figure 2.10. Measurements of the pipe depth (denoted by a) and pipe width (denoted by W) based on (a) wax molds of the erosion channels (Allan, 2018) and (b) laser measurements (van Beek, 2015).

The widening of the erosion pipe along the pipe length is also noted in Figure 2.9b. Van Beek (2015) and Vandenboer (2019) measured pipe depth along the pipe profile and demonstrated that the depth increases in addition to the width. As mentioned previously, both the pipe depth and pipe width increase as flow rates increase due to the secondary erosion of the pipe walls. Because these occur together, the erosion channels that develop tend to have channel width (w) to depth (a) ratios that are relatively constant along the erosion pipe. Van Beek (2015) measured channel w/a ratios for two fine sands (Baskarp sand and Enshede Sand) while

Robbins et al. (2018) measured w/a ratios for pipes in fine gravel. The aspect ratio of the channels varied from approximately 10 to 35 (Figure 2.11). The channel aspect ratio will be an important consideration when making choices regarding the flow resistance in the erosion pipes.

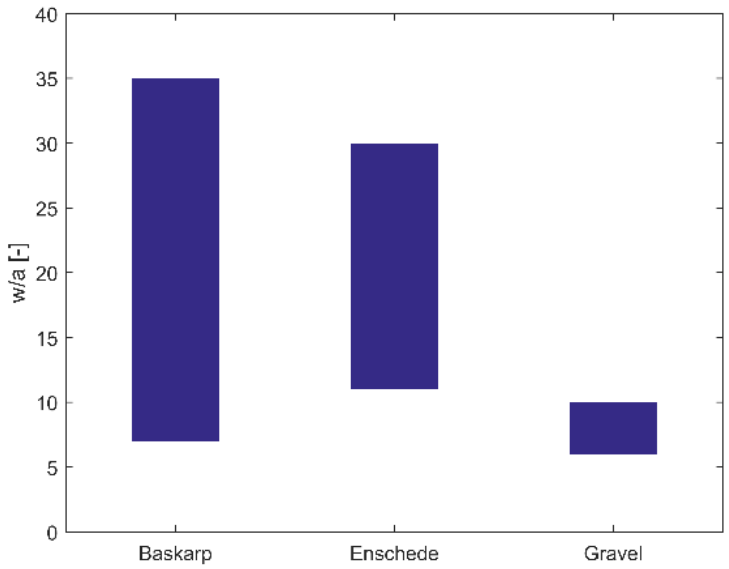

Figure 2.11. Measurements of pipe width (w) to depth (a) ratios for fine sands to gravel (data from van Beek 2015 and Robbins et al. 2018).

Trends have also been observed regarding the width of the pipe tip. Hanses (1985) first observed that the pipe tip was nearly a constant width, regardless of experiment scale and configuration. This observation lead Hanses to the conclusion that there was a primary erosion mechanism at the pipe tip responsible for the pipe progression. Since then, numerous other investigators have examined the dimensions at the pipe tip. Van Beek (2015) found that the pipe tip was equal to approximately 30 times the median grain diameter. Vandenboer (2019) supplemented the measurements by Hanses and Van Beek with additional experiments and confirmed that the pipe width is 30 times the median grain diameter (Figure 2.12). Xiao et al

(2019) also found the pipe tip was approximately 30 times the average grain diameter. Allan (2018), conducted completely independent experiments on a variety of sands covering a broader range of grain sizes and found the pipe tip to be approximately 39 times the median grain diameter (Figure 2.13). It should be noted that the tests by Allan not only include larger grain diameters, but also include much more well graded sands. This may account for the slightly higher widths as broadly graded sands tend to more readily arch due to higher strengths. Nevertheless, it appears that the initial pipe width at the tip can be approximated as 30-40 times the median grain diameter.

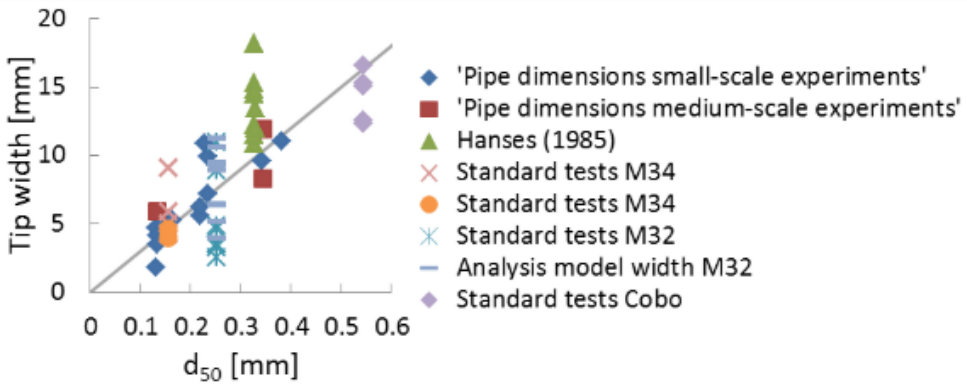

Figure 2.12. Measurements of the pipe tip width as a function of grain size. Line indicates a width of 30 grains. (Vandenboer, 2019)

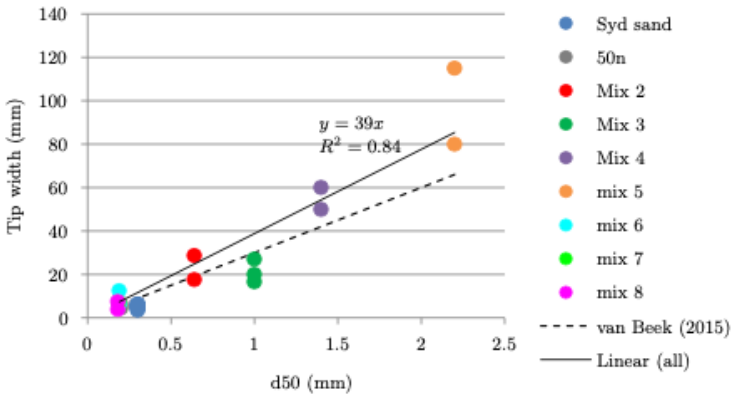

Figure 4.11: Tip width with d_{50}

Figure 2.13. Pipe tip width in various sands as measured by Allan (2018).

The depth of the pipe has also been closely examined. Hanses (1985) found that the pipe had a depth of 1-2 mm (5 times the median grain diameter) near the pipe tip. Van Beek (2015) reported average pipe depths for 4 different sands. The values ranged from 1.6-11 times the median grain size; however, these measurements considered the full pipe length. Vandenboer (2019) reported the depth profile for 3 sands (Figure 2.14). When normalized to grain size, the depth profile for all sands was found to be approximately the same (Figure 2.14b) and could be described by

$$a_{avg} \cong \left(0.53 + 0.11855 \cdot \frac{n^{\frac{3}{2}}}{(1-n)} \sqrt{\frac{\rho g}{\mu}} x\right) d_{50} \tag{2.2}$$

where a_{avg} is the average pipe depth for the cross section, n is the soil porosity, ρ is the water density, μ is the water viscocity, g is the gravitational acceleration, x is the distance from the pipe tip along the length of the pipe, and d_{50} is the median grain size of the sand. From Figure 2.14b, it is observed that the pipe depth near the tip of the erosion pipe is between 0.5 and 1 grain

diameters. Based on the results of Vandenboer and Hanses, it appears that the pipe tip may have an initial depth between 0.5 and 5 times the grain diameter.

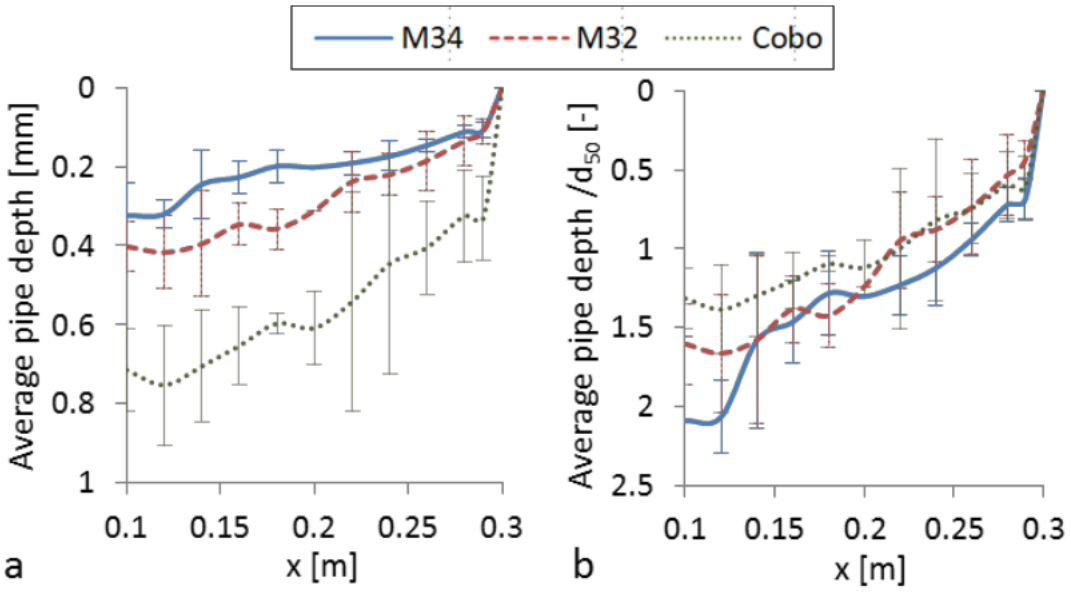

Figure 2.14. Measured (a) pipe depth and (b) pipe depth normalized to grain size for three sands (Vandenboer 2019).

2.2.4 Primary Erosion

The progression of the erosion pipe is driven by the primary erosion at the pipe tip. A criterion for pipe progression is therefore required for simulation of BEP. The particles are detached from the soil matrix when the seepage forces on the particle exceed the frictional forces restraining the particles. The criterion must therefore be representative of the seepage forces on the particles. Various authors have proposed using the hydraulic gradient (Schmertmann, 2000), seepage energy (Richards & Reddy, 2014), or hydraulic shear stress in the pores ((Fujisawa et al., 2010b) as a criterion for progression. Use of the hydraulic gradient appears to be the most common approach in the literature. This is likely because Terzaghi (1922) recognized long ago that the average seepage force per unit volume, F_s, acting on a body of soil is given by

$$F_s = \nabla(h) \cdot g \cdot \rho \tag{2.3}$$

where $h = z + P/(\rho g)$ is the total, piezometric head expressed in terms of the elevation (z), fluid pressure (P), fluid density (ρ), and gravitational acceleration (g). The gradient of h, i.e. the hydraulic gradient, thus became used as a criterion for hydraulically induced failure of soils.

While Equation 2.3 can mathematically be evaluated at a point, it must be recognized that it is only valid over scales for which the soil acts as a continuum. The concept of a representative elementary volume (REV) (Hill, 1963) has been defined to express the smallest volume over which a heterogeneous mixture acts as a continuum. This concept has been regularly applied to analysis of internal erosion (e.g., Abdou et al., 2020; Olsen, 2018; Tran et al., 2017; Wautier, 2018). The REV for sandy soils has been shown to be on the order of 10 to 40 times the median grain diameter (Olsen, 2018). This is similar in scale to the width of the erosion pipes, but is much larger than the depth of the erosion pipes near the pipe tip. Fortunately, the pipe tip is driven primarily by the collapse of arches spanning the pipe width, and quantities calculated over this length scale are quite relevant for BEP. It therefore seems suitable to use the hydraulic gradient as a primary erosion criterion. This is the approach that will be taken in this study.

The upstream tip of the erosion pipe is illustrated in Figure 2.15. The head profile varies nonlinearly with distance away from the pipe tip due to the concentration of flow. Because of this, the average value of the hydraulic gradient in front of the tip is a function of the distance over which it is evaluated. Additionally, the hydraulic gradient can be evaluated from differing directions. Ideally, the hydraulic gradient would be evaluated over the distance associated with the size of the group of grains that collapse under the imposed load in the direction of particle movement. This would allow a traditional limit equilibrium analysis to be conducted by

comparing the driving forces to the resisting forces over the volume of interest. Unfortunately, no clear approach for determining the effective grain group size for BEP progression has been established. As a result, studies have used the hydraulic gradient over arbitrarily chosen distances (in various directions) as the criterion for pipe progression. For this study, we will use the magnitude of the horizontal, hydraulic gradient (i_h) in front of the pipe tip over various distances as illustrated in Figure 2.15. This choice was made as a matter of convenience because all of the laboratory data and example problems in this thesis are oriented horizontally. In a generalized sense, the hydraulic gradient in the direction of the pipe axis should be used.

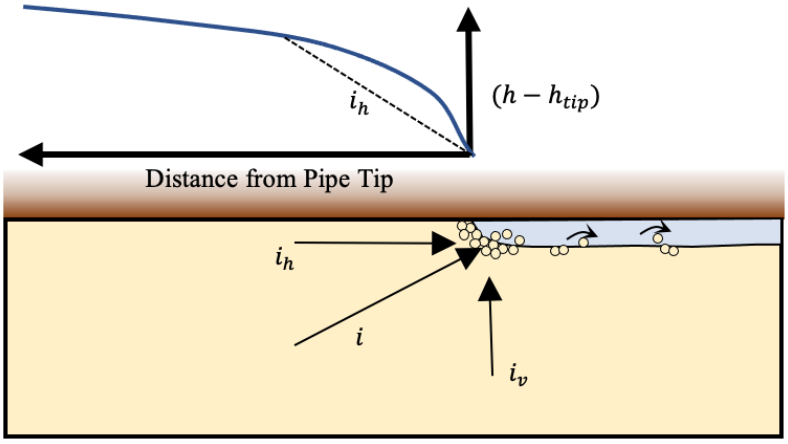

Figure 2.15. Illustration of local hydraulic gradients near the pipe tip.

Unfortunately, the meandering nature of the erosion pipes has made measuring the pore pressures near the pipe tip nearly impossible. As a result, very few studies have successfully made precise measurements near the pipe tip, and it is often necessary to try to determine the conditions near the pipe tip from analytical or numerical calculations of experiments. Table 2.2 summarizes available studies that have measured or analyzed pore pressure and associated horizontal, hydraulic gradients near the pipe tip.

Hanses (1985) made simplifying assumptions regarding the pipe geometry and simulated the head distribution near the pipe tip in his experiments. He concluded that the head increased by approximately 30 mm over a distance of 20 mm in front of the pipe, indicating an average gradient of 1.5 at the pipe tip. Van Beek (2015) visually recorded the position of the pipe tip relative to pressure transducers in an experiment. Using this information along with assumed head values in the erosion pipe, the average hydraulic gradient between the measurement point and the pipe tip was able to be calculated (Figure 2.16). A clear jump in the hydraulic gradient was calculated as the pipe reached the sensor (value of 0 on x-axis) for three of the four sensors. While these measurements provide evidence of a high local gradient driving progression, they did not provide a quantitative value that could be used due to the high variability of the sensors.

Table 2.2. Measured or estimated horizontal hydraulic gradients near the pipe tip.

Study	d_{50}	C_u	n_{min}	n_{max}	n	i_{cr}	**d, m**	**Method**
Hanses (1985)	0.325	1.3	0.41	0.51		1.5	0.02	Modelled
Robbins et al (2018)	0.3	1.42	0.36	0.44	varied	0.35-0.43	0.1	Measured
Vandenboer et al (2019)	0.155-0.544	1.29-2.61	-	-	-	1	unknown	Modeled
Xiao et al. (2020)	0.35	1.65	0.40	0.50		0.6-1.4	0.002	Both
	0.75	1.45	0.39	0.47		0.7-1.8	0.002	Both
Pol et al. (2021)	0.185	1.59	0.36	0.49	0.383	0.28-0.30	0.8	Measured
Rosenbrand et al. (2021)	-	-	-	-	-	1-1.8	0.05	Modelled

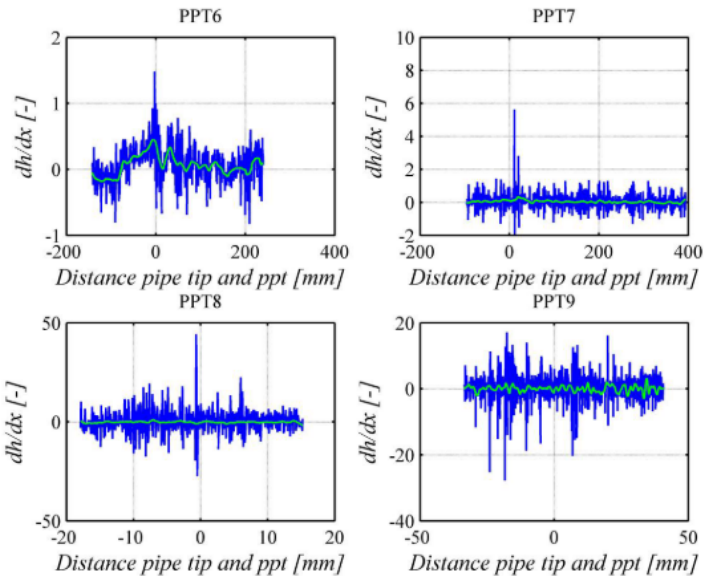

Figure 2.16. Measured hydraulic gradients from pore pressure measurements near the pipe tip in experiments (van Beek 2015).

Robbins et al. (2018) developed the first laboratory test for intentionally measuring the local gradient upstream of the erosion pipe. This device was a cylindrical flume as shown in Figure 2.17. Because of the cylindrical shape, the BEP pipe that developed was forced to pass below the sensors thereby enabling a clear measurement of the elevated gradients in front of the pipe tip (Figure 2.18). Using this device, values of the critical hydraulic gradient for a single sand were measured over a distance of 10 cm. These laboratory tests will be discussed further in Chapter 4 as one potential means of measuring the primary erosion criterion.

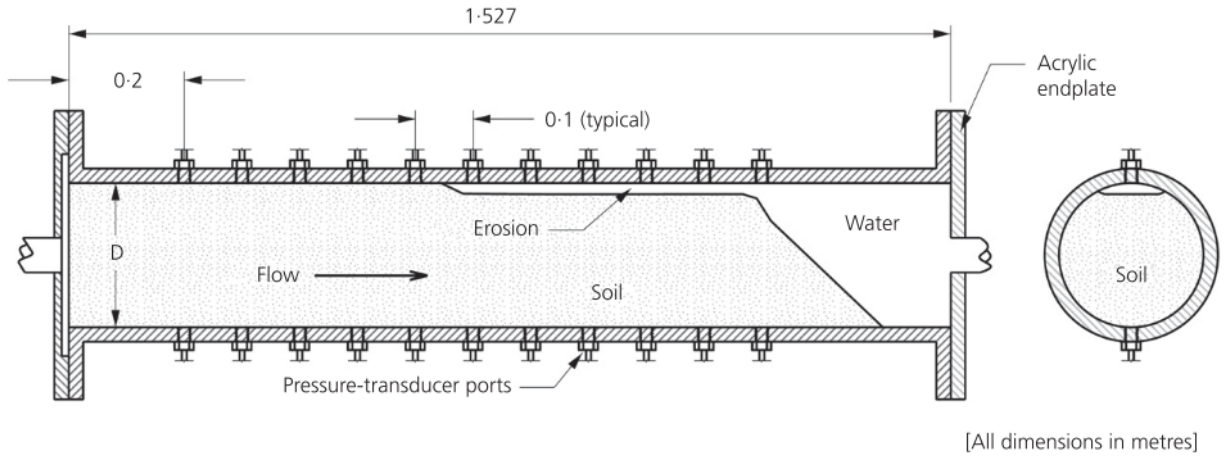

Figure 2.17. Cylindrical BEP laboratory test for measuring hydraulic gradients near the pipe tip (Robbins et al. 2018).

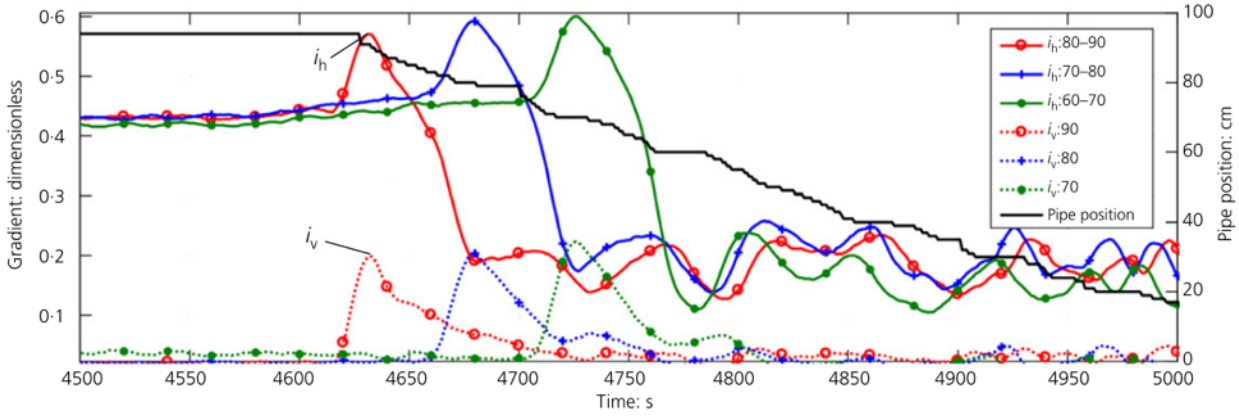

Figure 2.18. Recorded horizontal and vertical hydraulic gradients at the pipe tip from cylindrical piping tests (Robbins et al., 2018).

Vandenboer et al. 2019 performed normal, steady state groundwater modelling of a BEP experiment to infer values of the hydraulic gradients near the pipe tip. The pipe geometry was simplified and the pipe permeability was calibrated to the measured heads in experiments. The hydraulic gradient near the pipe tip was then extracted from the model. Rosenbrand and van Beek (2021) took a similar approach. They calculated an average hydraulic gradient of 0.6 over a distance of 10 cm in front of the pipe tip.

Xiao et al (2020) and Pol et al. (2021) ran experiments in rectangular flumes from which they were able to measure the gradients in front of the pipe. Sketches of their experimental configurations are illustrated in Figure 2.19. Xiao et al. ran a series of experiments; for one of their experiments the pipe progressed along the sensors as shown in Figure 2.19a. Pol et al. (2021) used guides on the lid of the sample container to ensure the pipe passed below the sensors. The measured values of the hydraulic gradient at the pipe tip from both studies are provided in Table 2.2.

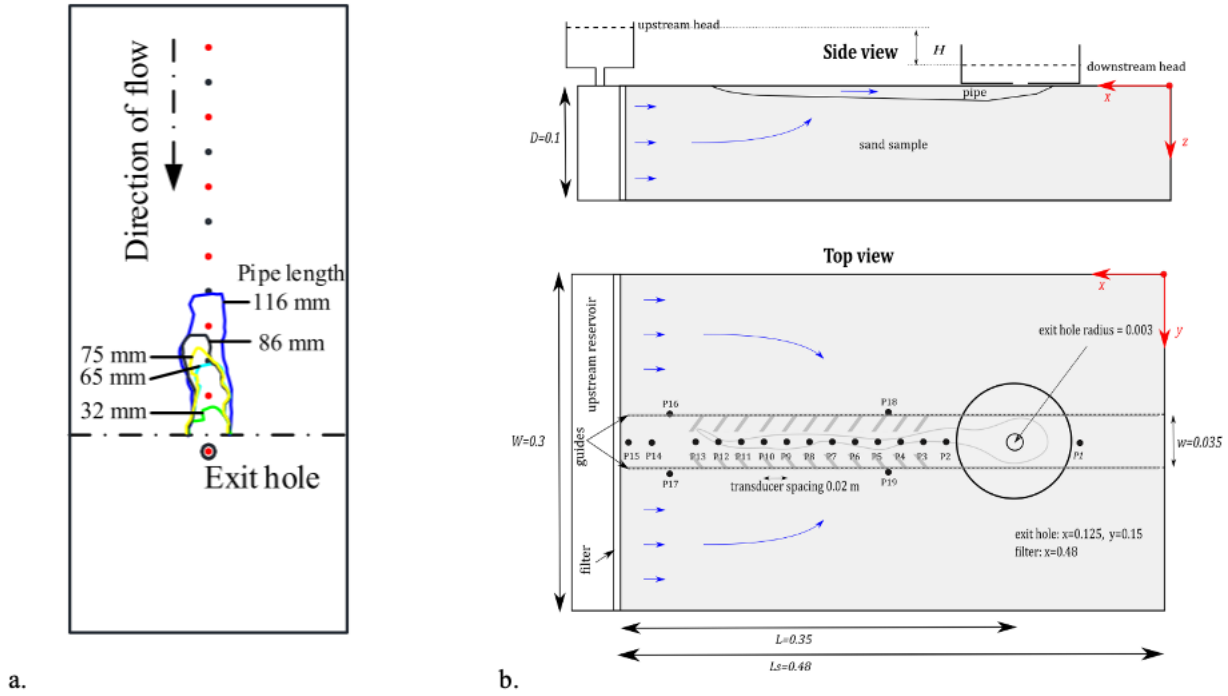

Figure 2.19. Sketches of the pipe progression in (a) plan view from Xiao et al (2020) experiment and (b) cross section and plan view from Pol et al. (2021) experiment.

In addition to obtaining measurements, Xiao et al. developed an analytical solution for the head distribution near the pipe tip using conformal mapping for the case of a uniform pipe and the case of a pipe with a local deep zone near the pipe tip (Figures 2-20 and 2-

21). The solution obtained is given by Equation 2.3 where $\omega = \phi + \mathrm{i}\psi$ is the complex potential in terms of complex coordinate $z = x + \mathrm{i}y$. The terms ϕ and ψ are the potential function and stream function of the seepage solution. By substituting a known point into Equation 2.3, the constant T was determined as shown in Equation 2.4 where k_h is the hydraulic conductivity of the soil and H_o is the differential head between a point and the pipe tip.

$$\omega = iT\sqrt{b_t \pm \sqrt{z^2 + b_t^2}} \tag{2.3}$$

$$T = \frac{k_h H_o}{Im(\sqrt{b_t \pm \sqrt{(x_0 + iy_0)^2 + b_t^2}})} \tag{2.4}$$

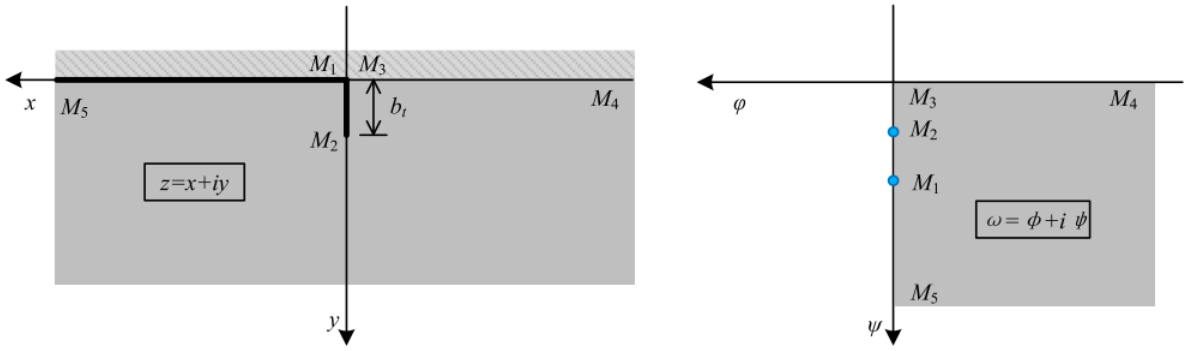

Figure 2.20. Problem geometry near the pipe tip for derivation of the analytical solution (Xiao et al. 2020).

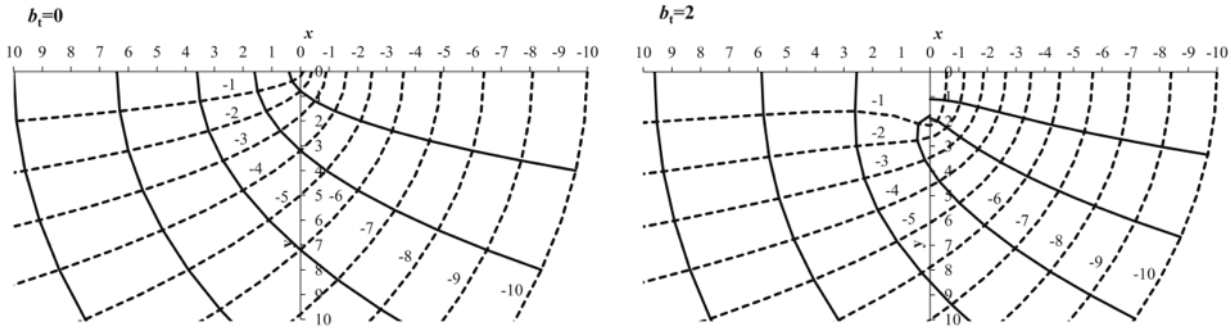

Figure 2.21. Flow net near the pipe tip derived from analytical solution (Xiao et al. 2020).

Fitting this analytical solution to the head measurements from the experiment yielded the complete description of the head profile in the vicinity of the pipe tip as illustrated in Figure 2.22. The solution deviated from the measurements with increasing distance away from the pipe tip. This could be due to the assumption of a constant head in the erosion pipe as a boundary condition for the analytical solution. Inspection of Figure 2.22 clearly illustrates that the head in the pipe is not a constant value. The hydraulic gradient in the pipe will be discussed in the following section.

While there have been limited measurements of the primary erosion mechanism, the values in Table 2.2 do clearly illustrate that the magnitude of the hydraulic gradients is quite high (0.3-1.8), and the distance over which the gradients increase is extremely small (mm to cm). This information is useful for designing approaches for measuring the primary erosion criterion. In Chapter 4, a detailed look at measuring the critical, horizontal gradients in front of the pipe tip is provide. The concept of a critical secant gradient function is proposed for use as the primary erosion criterion, and means of predicting it will be developed.

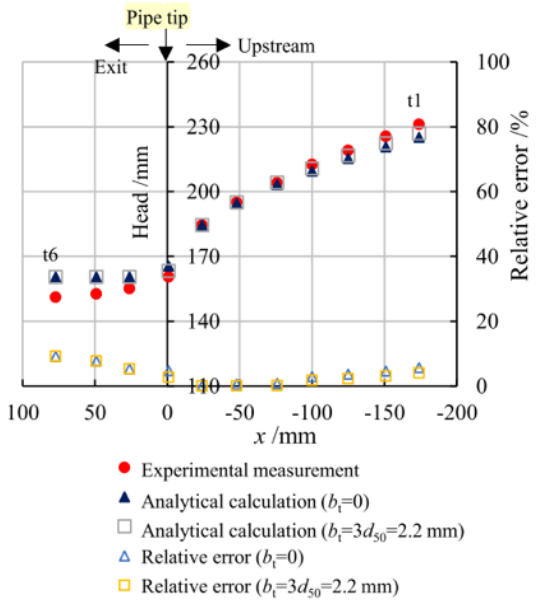

Figure 2.22. Comparison of head measurements near the pipe tip to analytical solution (Xiao et al. 2020).

2.2.5 Secondary Erosion

The enlargement of the pipe itself is due to the secondary erosion mechanism. The fluid flow through the pipe channel imparts a hydraulic shear stress (τ) on the walls of the channel due to the viscous drag of the flowing fluid (Figure 2.23). When $\tau > \tau_c$ where τ_c denotes a critical value of the shear stress for particle erosion and transport, the walls erode further and the pipe enlarges. Under steady flow conditions, the boundary shear stress on the wall of any pipe is given by

$$\tau = \frac{dh}{dx}\rho g \frac{A}{P} \tag{2.5}$$

where A denotes the cross-sectional area of the pipe and P is the perimeter. For rectangular or trapezoidal pipes of width w and depth a, $A = wa$ and $P = 2(w + a)$. For the case $w \gg a$, Equation 2.5 simplifies to

$$\tau = \frac{1}{2}\frac{dh}{dx}\rho g a \tag{2.6}$$

Van Beek (2015) demonstrated that Equation 2.6 results in less than 10% error when $w/a > 10$.

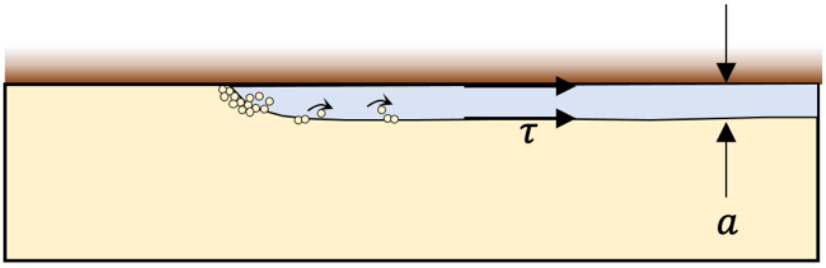

Figure 2.23. Illustration of hydraulic shear stress acting on pipe walls.

The value of τ_c for sands has been studied extensively over the last century as part of sediment transport studies for rivers. The Shields diagram (Shields 1936) is the best-known means of predicting critical shear stress of cohesionless soils. The Shields diagram is an empirically derived diagram that expresses the critical shear stress as

$$\frac{\tau_c}{\gamma_p' d} = \Psi_c = f\left(\frac{\rho u^* d}{\mu}\right) \tag{2.7}$$

where Ψ is known as the Shields parameter with Ψ_c being the critical Shields parameter at which particle motion begins, γ_p' is the buoyant density of the particle, $u^* = \sqrt{\tau/\rho}$ is the shear velocity, and μ is the water viscosity. The quantity $Re^* = \rho u^* d/\mu$ is known as the particle Reynolds number and quantifies the level of turbulence at the boundary. Van Beek et al. (2019) measured flow velocities, flow rates, and pressure gradients in BEP erosion pipes under equilibrium conditions for a sand with d_{50}=0.3 mm. From this information, the Shields parameter and

particle Reynolds number could be calculated and compared to the Shields diagram. The data obtained from these BEP experiments (denoted as "Tube test" in Figure 2.24) matches closely to the Shields diagram indicating that the Shields diagram provides a suitable means of predicting the critical shear stress for BEP pipes in cohesionless soils.

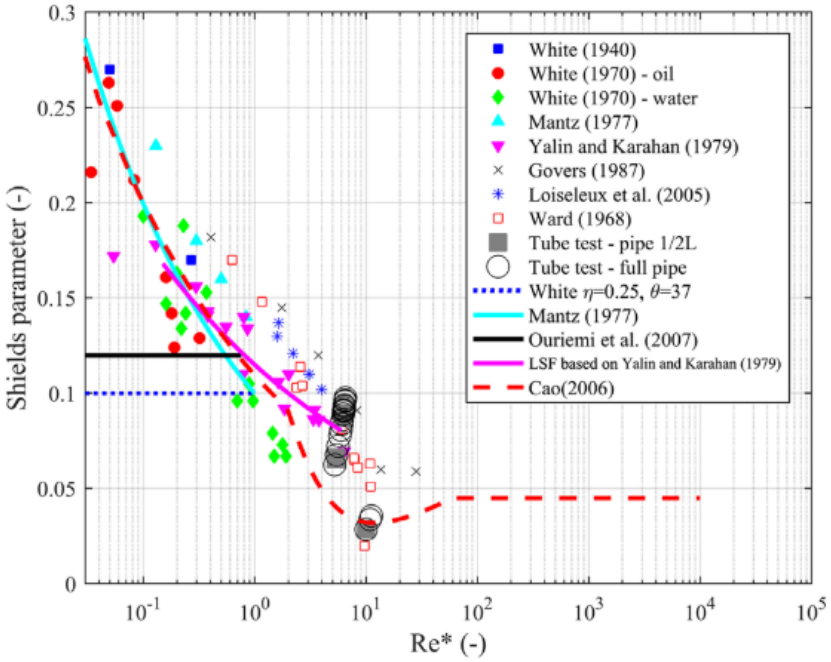

Figure 2.24. Shields parameter as a function of the particle Reynolds number showing experimental results for laminar flow (including cylindrical tests, or tube tests, illustrated in Figure 13), various fits, and theoretical relations (Van Beek et al, 2019).

As the use of the Shields diagram can be somewhat complicated due to the implicit nature of the relationship between grain size and critical shear stress, White (1940) proposed a simpler expression for the critical shear stress based on the rolling resistance of a single grain. White proposed the shear stress could be determined as

$$\tau = \eta \frac{\pi}{6} \gamma_p' d \cdot \tan\theta \tag{2.8}$$

where η is a parameter known as White's constant, d is the sand grain size, and θ is the bedding angle of the sand which represents the resistance to rolling of a single grain. Concepts from this simpler relationship were used in the first BEP model proposed by Sellmeijer (1988) as well as the following numerical implementations (Sellmeijer 2006, van Esch et al. 2013). Van Beek compiled the laminar flow data in Figure 2.24 and found that there is a logarithmic relationship between critical shear stress and particle diameter (Figure 2.25) rather than the linear relationship indicated by Equation 2.8. In order to permit the use of Equation 2.8 still (due to incorporation in Dutch policy and software), Van Beek back calculated the bedding angle using Equation 2.8 with $\eta = 0.3$. The relationship shown on the right side of Figure 2.25 was derived and is given by the equation

$$\theta = -8.125 \ln(d) - 38.77 \tag{2.9}$$

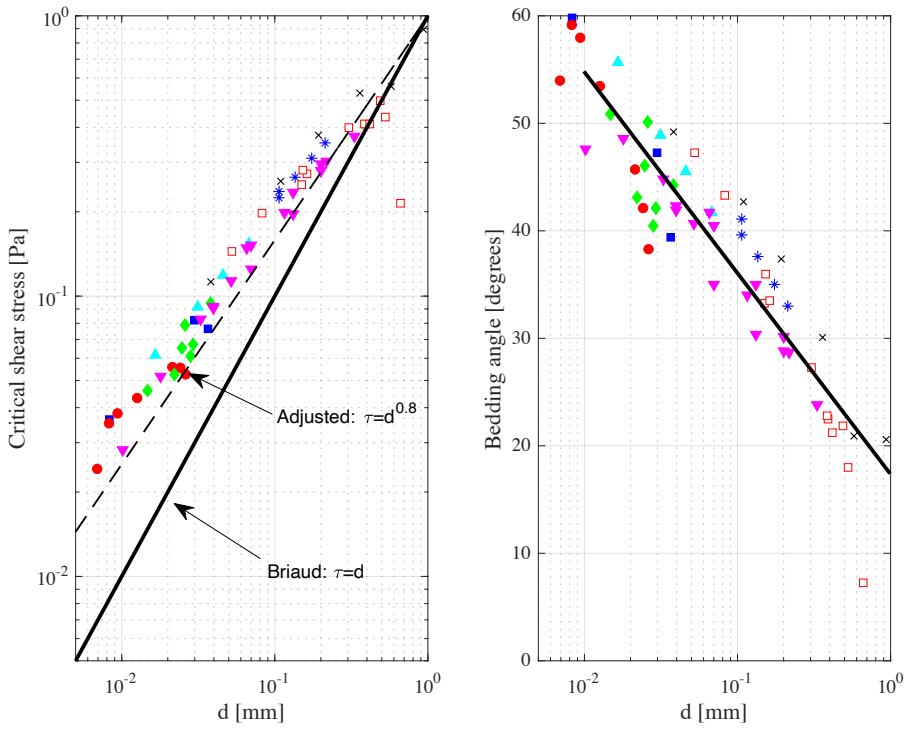

Figure 2.25. Relationship between particle diameter and critical shear stress for laminar flow conditions (left) and back calculated bedding angle as a function of particle diameter (right). (modified from Van Beek 2015)

When using Equation 2.9 in equation 2.8, the relationship in Figure 2.25a between particle diameter and critical shear stress is reproduced accurately. More recently, simpler relationships have been proposed. Briaud et al. (2017) proposed the following relationship based on a large compilation of data for cohesionless soils.

$$\tau_c = d_{50} \tag{2.10}$$

where τ_c is expressed in units of Pascals and d_{50} is expressed in units of mm. This relationship is also shown in Figure 2.25. As shown, the proposed relationship under predicts the critical shear stress. As part of this literature review, Equation 2.10 was adjusted to try and obtain a better fit resulting in Equation 2.11.

$$\tau_c = (d_{50})^{0.8} \tag{2.11}$$

Equation 2.11 yielded a much better fit over the range of particle diameters shown, where units for τ_c and d_{50} are the same as described for Equation 2.10.

While the Shields diagram is suitable for both laminar and turbulent flow conditions, the simpler relationships given by Equations 2.8 through 2.11 are valid only for laminar flow. Dye streamlines from the experiments in Robbins et al. (2018), which were the same experiments reported in Figure 2.24 and used in Van beek et al. 2019, indicate that laminar flow conditions indeed occur in the BEP pipe (Figure 2.26). However, close examination of where these "Tube test" points fall in Figure 2.24 indicate that the test conditions are approaching the range of turbulent flow conditions. For full scale conditions or cases of coarser sand, the flow rates will be higher and may become turbulent. As turbulent flow conditions yield lower critical shear stresses, it is important to consider the possibility of both laminar and turbulent flow in model formulation.

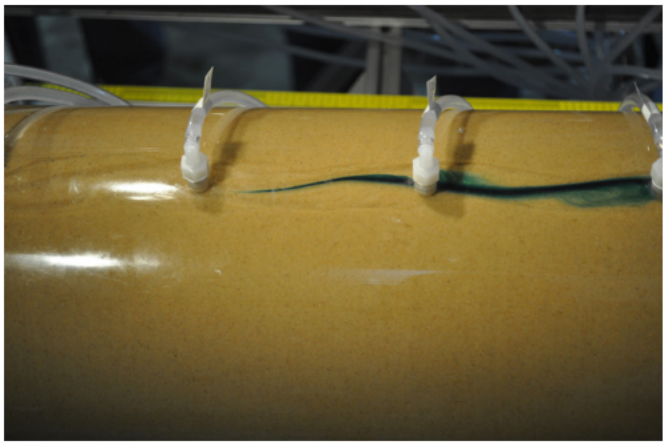

Figure 2.26. Laminar dye streamlines in BEP laboratory experiments on sand of d_{50}=0.3 mm (Robbins et al. 2018).

2.2.6 Pipe Growth

In addition to providing information regarding the primary and secondary erosion mechanisms, the experimental work conducted to date has also provided significant information regarding the progression of pipes once the critical condition for primary erosion has been exceeded. Allan (2018), Vandenboer (2019), Robbins et al. (2021), and Pol et al. (2021) all found a linear relationship between the applied head difference and the rate of pipe progression. That is, the degree of overloading beyond the critical value dictates the advancement rate of the pipe tip. This is illustrated clearly by the experiments of Allan (2018) in Figure 2.27.

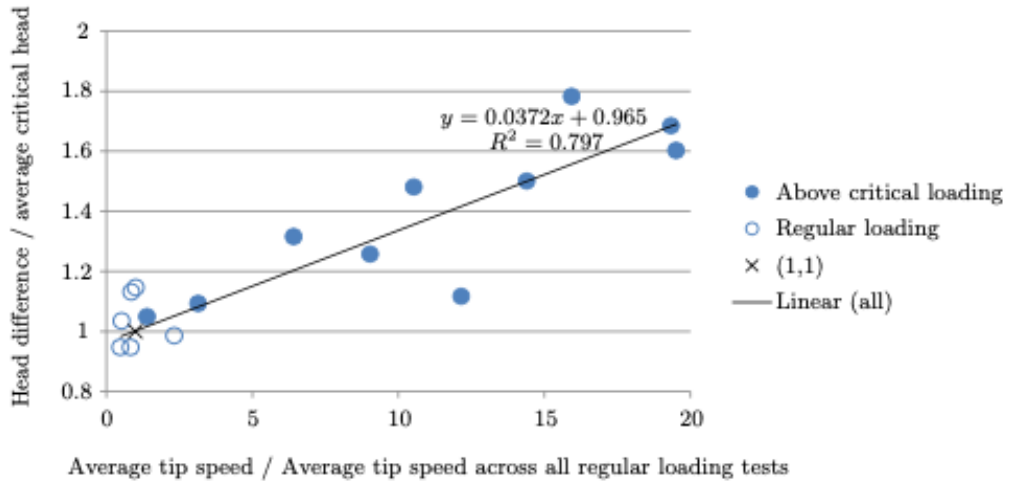

Figure 2.27. Experimental results indicating increase in pipe progression speed as applied differential head exceeds the critical head value (from Allan 2018). Axes are the dimensionless tip speed and dimensionless head difference due to normalization by experimental averages.

Exceeding the critical load for BEP failure not only changes the rate that a pipe progresses upstream, it also changes how the pipes enlarge. Vandenboer et al (2019) ran a series of repeat laboratory experiments in which the upstream head was set to various values in excess of the critical head from the onset of the experiment (sudden loading applied all at once). The erosion pattern that developed changed significantly with the degree of overloading (Figure 2.28). This behavior can be explained by the fact that the primary erosion criterion is simultaneously exceeded in multiple locations at once. As a result, the erosion grows in every direction simultaneously.

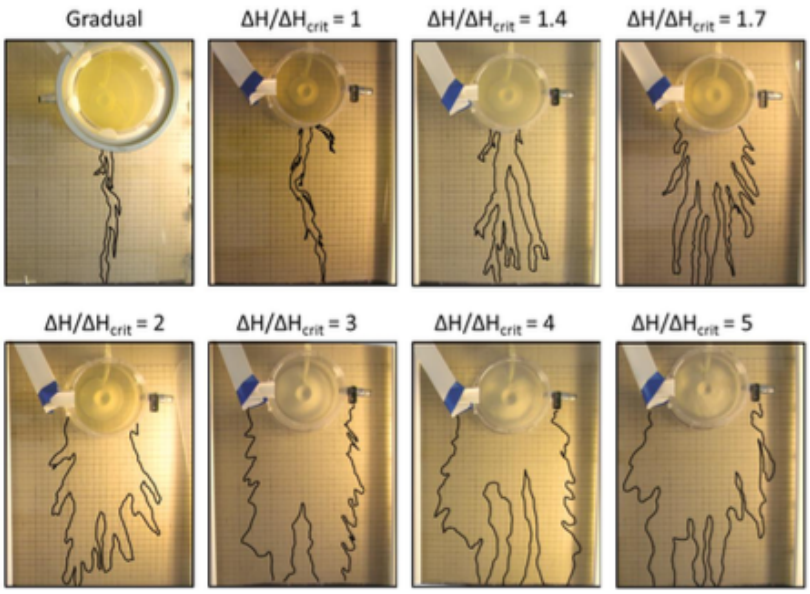

Figure 2.28. Erosion patterns observed in BEP laboratory experiments with an instantaneous applied differential head in excess of the critical value (Vandenboer 2019).

2.3 Current BEP Assessment Methods

There have been a number of analytical approaches proposed over the years for evaluating the progression of BEP. The earliest assessment approach was the creep ratios of Lane and Bligh mentioned earlier. In recent years, it has been recognized that these empirical approaches have limited value for assessing risks on modern structures due to the significant differences between embankment dams and levees and the masonry structures of the early 20th century. More recent studies have proposed simple calculation rules for assessing BEP (Hoffmans & Van Rijn, 2018; Ojha et al., 2001, 2003; Schmertmann, 2000; Sellmeijer, 1988, 2006; Sellmeijer et al., 2011). Only the methods proposed by Sellmeijer and Schmertmann have been widely accepted and applied in practice (ICOLD, 2015; USACE and USBR, 2012). For this reason, only these two approaches will be described in detail in the sections that follow to provide an understanding of the current state of engineering practice. Other methods that have been

proposed are similar to those described in that BEP is attempted to be predicted on the bases of the differential head, H, with adjustments for influential factors.

2.3.1 The Sellmeijer Approach

Sellmeijer (1988) developed an approach for predicting the critical head for piping based on the assumption that the secondary erosion on the bottom of the pipe drives the pipe progression. The problem geometry considered was an infinite half space as illustrated in Figure 2.29a, with a pipe progressing along boundary BCD. In Figure 2.29, the total head is denoted as ϕ ($\phi = H$). Along BD, $\partial\phi/\partial x$=p where p is a function derived from the concepts of fluid flow in the pipe (labeled slit in Figure 2.29) and secondary erosion. Boundary DA is a constant head boundary, and boundary CD is a no flow boundary.

To solve the groundwater flow problem, Sellmeijer made use of two techniques from complex variable theory: the Cauchy integral formula and the theory of conformal mapping. In complex variable theory, the solution is expressed as $\omega = f(z)$ where $\omega = \phi + \mathrm{i}\psi$ is the complex potential as a function of both the seepage potential (ϕ) and the stream function (ψ). Using the two approaches, the solution to the groundwater equation is given by

$$\omega = \frac{2}{\pi i}\sqrt{l-z}\int_0^l p(r)\frac{dr}{\sqrt{l-r}} - \frac{1}{\pi i}\int_0^l p(r)\sqrt{\frac{l-z}{l-r}}\frac{dr}{r-z} \tag{2.12}$$

and, alternatively,

$$\omega = \sum_{n=0}^{\infty} A_n \frac{l}{4}\left[\frac{\exp\left(-\left(n-\frac{1}{2}\right)\pi i\zeta\right.}{-\left(n-\frac{1}{2}\right)i} - \frac{\exp\left(-\left(n+\frac{3}{2}\right)\pi i\zeta\right.}{-\left(n+\frac{3}{2}\right)i}\right] \tag{2.13}$$

In Equation 2.12, $p(r)$ is an unknown function which represents the solution along the boundary DABC in terms of integration variable r. In equation 2.13, the boundary conditions are embedded in the unknown Fourier coefficients A_n, and

$$\zeta = \xi + i\eta \tag{2.14}$$

is the complex variable shown in Figure 2.29b after application of the mapping transformation

$$\zeta = \frac{2}{\pi}\arcsin\left(\sqrt{\frac{z}{l}}\right). \tag{2.15}$$

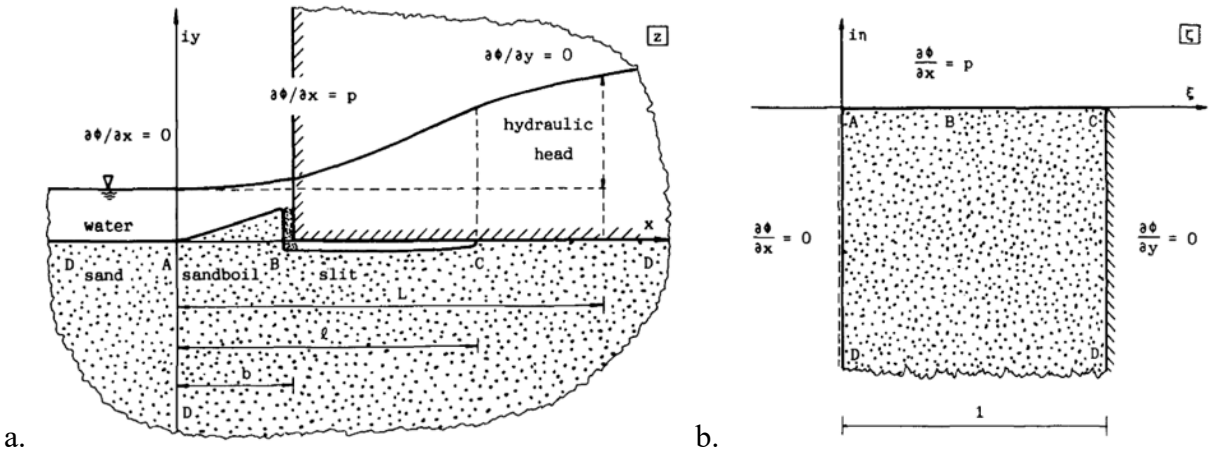

Figure 2.29. Illustration of problem (a) geometry and boundary conditions considered by Sellmeijer and (b) transformed plane after Schwarz-Christoffel transformation (Sellmeijer, 1988).

To solve these equations, Sellmeijer applied constraints along line DABCD. First, along line AB, Sellmeijer assumed that the sand in the sand boil was just at the limit state for sliding equilibrium given the sand boil geometry and effective friction angle in the sand. The resulting boundary condition for line AB is given by Equations 2.16 and 2.17.

$$\frac{\gamma_w}{\gamma_s'}q + \frac{p}{q}\cot(\theta) = 1 \tag{2.16}$$

$$B = \frac{\phi}{q} \tag{2.17}$$

In Equation 2.16, $q = dh/dx$, $p = dh/dy$, and θ is the bedding angle of the sand which represents resistance to rolling or sliding. In equation 2.17, B is the height of the sand boil. Along the pipe (BC), the pressure and flow are related by

$$Q = \frac{pa^3}{12\mu}. \tag{2.18}$$

The secondary erosion on the bottom of the pipe was evaluated by considering the rolling equilibrium of grains on the bottom of the pipe as shown in Figure 2.30. The bedding angle, θ, represents the angle of the resultant force acting on the particle at the onset of rolling instability. The upward seepage force F_s is a product of the vertical hydraulic gradient and a coefficient C. The viscous drag force acting on the particle F_d is a product of the applied boundary shear stress (Eq 2.6) and the effective particle area, given by White (1940) as d^2/η where η is known as White's coefficient, and the submerged particle weight is given by W. By summing moments about the rotation point, Sellmeijer derived Equation 2.19. Equations 2.18 and 2.19 define the boundary condition along boundary BC.

$$Cq + p\left(\frac{3}{\pi\eta}\frac{a}{d} + 1\right)\cot(\theta) = \frac{\gamma_p'}{\gamma_w}. \tag{2.19}$$

Sellmeijer assumed that the pipe would progress until Equation 2.19 was satisfied and particle equilibrium on the bottom of the pipe was achieved. Using Equations 2.12 and 2.13 along with equations 2.16 through 2.19 along with the constant head boundary conditions of $\phi = H$ at $x = L$ and $\phi = 0$ at $x \leq 0$, Sellmeijer developed a series of equations that could be used to describe the horizontal hydraulic gradient, vertical hydraulic gradient, pipe flow rate, and total head along

line ABCD as a function of the upstream head and pipe length. These functions were too complicated to solve analytically, so instead Sellmeijer developed a computer program to solve the system of equations numerically. With this computer program, the head required for reaching the particle limit state (Eq. 2.19) for each pipe length could be calculated as shown in Figure 2.31. The critical head, H_c, that would cause failure is the maximum value on each curve.

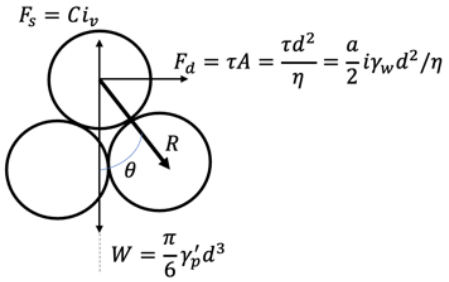

Figure 2.30. Forces acting on a grain on the bottom of a the pipe.

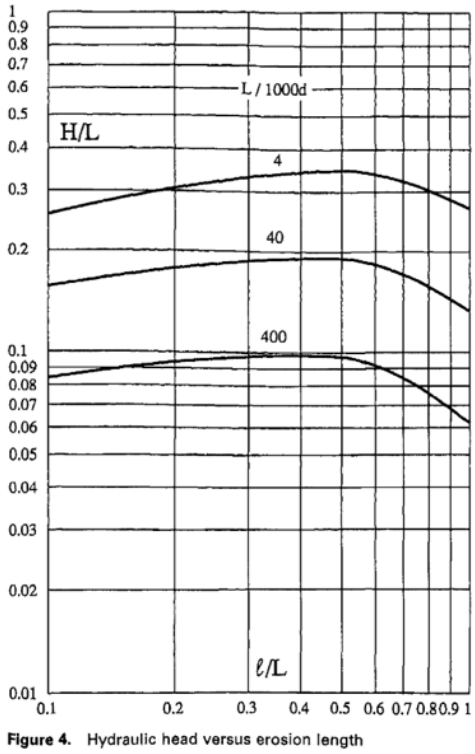

Figure 4. Hydraulic head versus erosion length

Figure 2.31.Numerically computed curves illustrating the upstream head (H) satisfying Equation 18 and 19 for various pipe lengths (Sellmeijer & Koenders, 1991).

In order to make the method widely accessible, a significant number of calculations were run for varying model scales and input parameters. A simplified calculation rule, known as Sellmeijer's rule, was derived from the results of these simulations by curve fitting. The resulting rule is given by

$$\frac{H_c}{L} = c\left(\frac{\gamma_p'}{\gamma_w}\right)\tan(\theta)\,(1-0.65c)^{0.42} \tag{2.20}$$

where

$$c = \frac{1}{4}\pi\eta\sqrt[3]{\frac{2d^3}{kL}}. \tag{2.21}$$

Sellmeijer later modified the approach to account for a sand layer of finite depth and clay cover layer on the land side of the dike and updated the calculation rule (Sellmeijer et al., 1989; Weijers & Sellmeijer, 1993). The resulting calculation rule became known as the original Sellmeijer rule and is shown in Table 2.3.

The Sellmeijer rule was subsequently modified by Sellmeijer (2006), Van Beek (2015), and Sellmeijer et al. (2011) as illustrated in Table 2.3. In 2006, Sellmeijer adjusted the model by eliminating the upward seepage forces acting on the particle from the force equilibrium used to determine the critical shear stress. As a result, the factor F_F was dropped from the model. Van Beek et al. (2013) noted that the Sellmeijer (2006) equation for F_G contained a singularity when applied outside the range of problem geometries used to derive the equation. Van Beek et al. (2013) therefore made a slight modification to the equation for F_G to eliminate the singularity while obtaining nearly identical values for F_G. The last modification was made by Sellmeijer et al. (2011) when it was realized that the calculation rule did not adequately account for the influence of soil relative density (D_r), soil uniformity coefficient (U), and particle angularity (KAS). To account for these factors, empirical correction factors were added to the

calculation rule. These correction factors were derived from a multivariate statistical analysis on a database of piping experiments available at the time. Because of the multivariate corrections, it is critical that the values of η and θ remain fixed to the values shown in Table 2.3 as these values were held constant during the statistical analysis.

Table 2.3. Sellmeijer calculation rule variations over time.

4-Factor Model *(Sellmeijer, 1989)*	**3-Factor Model** *(Sellmeijer, 2006)*	**3-Factor Model** (Van Beek et al., 2013)	**Adjusted Sellmeijer** *(Sellmeijer et al., 2011)*
Equations: $\frac{H_c}{L} = F_G F_R F_S F_F$ $F_G = \left(\frac{D}{L}\right)^{\frac{0.28}{\left(\frac{D}{L}\right)^{2.8}-1}}$ $F_R = \frac{\gamma'_p}{\gamma_w}\tan(\theta)$ $F_S = \eta\frac{d_{70}}{\sqrt[3]{kL}}$ $F_F = 0.68 - \ln(S)$	*Equations:* $\frac{H_c}{L} = F_G F_R F_S$ $F_G = 0.91\left(\frac{D}{L}\right)^{\frac{0.28}{\left(\frac{D}{L}\right)^{2.8}-1}+0.04}$ $F_R = \eta\frac{\gamma'_p}{\gamma_w}\tan(\theta)$ $F_S = \frac{d_{70}}{\sqrt[3]{kL}}$	*Equations:* Same as Sellmeijer 2006 with the following change to F_G: $F_G = 0.91\left(\frac{D}{L}\right)^{\frac{0.24}{\left(\frac{D}{L}\right)^{2.8}-1}}$	*Equations:* $\frac{H_c}{L} = F_G F_R F_S$ $F_G = 0.91\left(\frac{D}{L}\right)^{\frac{0.28}{\left(\frac{D}{L}\right)^{2.8}-1}+0.04}$ $F_R = \eta\frac{\gamma'_p}{\gamma_w}\tan(\theta)\left[\frac{D_r}{D_{r,\mu}}\right]^{0.35} * \left[\frac{U}{U_\mu}\right]^{0.13}\left[\frac{KAS}{KAS_\mu}\right]^{-0.02}$ $F_S = \frac{d_{70}}{\sqrt[3]{kL}}\left[\frac{d_{70}}{d_{70,\mu}}\right]^{0.6}$
Calibrated Values: $\eta = 0.25, \theta = 37°$	*Calibrated Values:* $\eta = 0.25, \theta = 37°$	*Calibrated Values:* $\eta = 0.25, \theta = 37°$	*Calibrated Values:* $\eta = 0.25, \theta = 37°$ *Multivariate Values:* parameter / minimum / maximum / mean RD / 34 % / 100 % / 72.5 % U / 1.3 / 2.6 / 1.81 KAS / 35 % / 70 % / 49.8 % d_{70} / 150 μm / 430 μm / 208 μm

The Sellmeijer rule became the standard means of evaluating BEP in the Netherlands. Later, the method gained attention internationally and also became a method used in many

countries for evaluating BEP (S. Bonelli, 2013; Fell, 2011; ICOLD, 2015a; USBR and USACE, 2010). More recently, the principles forming the basis of the Sellmeijer rules have been implemented in the finite element programs MSeep (Sellmeijer, 2006) and DgFlow (van Esch et al. 2013) for predicting pipe progression for more generalized problem geometries than permitted by the calculation rules. These numerical implementations will be discussed further in Section 2.4.

2.3.2 The Schmertmann Approach

Schmertmann (2000) compiled the results from 115 laboratory piping tests to develop a method for predicting BEP progression. Schmertmann clearly understood that BEP pipes were driven by the primary erosion criterion at the pipe tip, stating:

"*How easily a pipe can advance through a particular dam section depends on how easily the flow can concentrate to develop the 3D gradient conditions needed for piping. These gradients depend on such geometric and permeability factors as the total pipe length, the depth of the piping layer, and the relative permeability of underlying layers. Therefore, when predicting field behavior from a laboratory test with different geometry or boundary conditions and therefore different gradients, or a different sand, one needs to make corrections to account for the differences.*"

While Schmertmann understood the importance of the local, hydraulic gradients near the pipe tip that drive erosion, he also made the assumption that the erosion pipe would have a limited influence on the seepage flow patterns in the domain, stating:

"*Theoretically, the presence of a pipe has an influence, however small, on the seepage flow pattern in all other parts of the dam. Practically, a conservative interpretation of some flownet studies and UF flume tests in homogenous sand suggests a negligible effect when one considers*

a point more than 80 radii in any direction from a pipe channel with a half-circular X-section. Thus, when at a vertical or horizontal distance of more than 1m from a pipe channel with a 12.5mm radius, the remainder of the dam has essentially the same seepage flow pattern as if that pipe channel did not exist."

Based upon this premise, Schmertmann postulated that the gradients that develop at the erosion pipe tip are proportional to the ambient, pre-pipe values of the hydraulic gradient along the piping path. As such, he analyzed the hydraulic gradients (pre-pipe, intact sand sample) along the seepage length in each of the laboratory tests in an assembled database of experiments on the basis of constructed flownets (e.g., Figure 2.32). From these flownets, he determined the value of the pre-pipe, hydraulic gradient (i_x) at each location x along the seepage path for all tests. The minimum value along the seepage length was taken as the value from the experiment that controlled the pipe progression. This value was denoted as i_{pmt} as it was the value required to progress the pipe in the test.

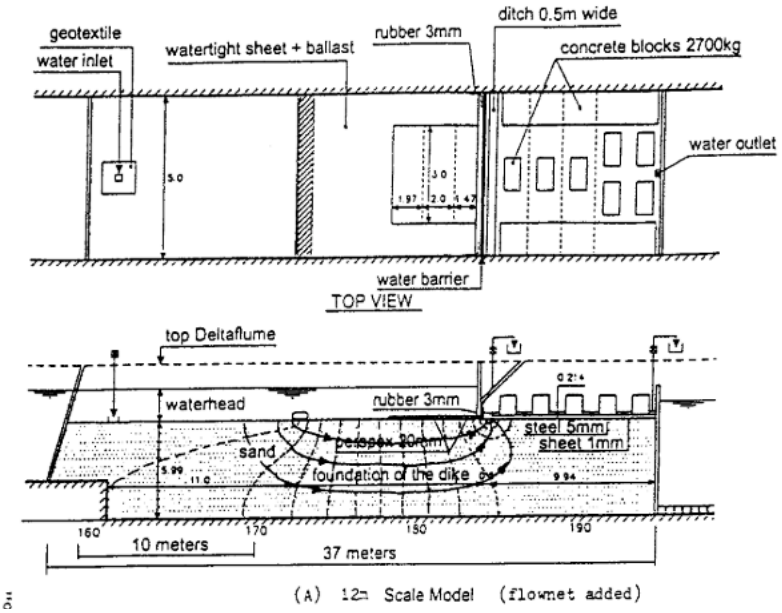

Figure 2.32. Flownet constructed to assess seepage patterns for test by Silvis (1991). (Schmertmann, 2000)

After calculating the values of i_{pmt} for all of the experiments, Schmertmann analyzed trends in the resulting values to begin formulating corrections that would account for influential factors that alter either (1) the degree of flow concentration towards the pipe or (2) the resistance of the soil to piping. As a result, he developed 11 correction factors that are used to adjust differing scenarios to a common reference frame and defined the factor of safety against piping as

$$F_p = \frac{\left(C_D C_L C_S C_k C_Z C_\gamma C_B\right)\left(C_G \bar{\imath}_{pm}\right)_t C_\alpha}{\left(C_G C_R \bar{\imath}\right)_f} \tag{2.22}$$

where the correction factors are defined as shown in Table 2.4. In the table, the subscripts 0 and 1 refer to any two scenarios being compared. The subscripts t and f refer to laboratory test and field scenarios, respectively.

Schmertmann applied these factors to correct 115 available laboratory tests to a common set of reference values. From the corrected values of i_{pmt}, Schmertmann developed the relationship illustrated in Figure 2.33 for predicting the laboratory test value of i_{pmt} based on the coefficient of uniformity of a soil. The finding that sands with high values of C_u are more resistant to piping was incredibly significant. Even today, the C_u of a sand is commonly used as the first means of screening out BEP issues for dams and levees on the basis of Schmertmann's work.

Schmertmann proposed two means of using Figure 2.33 and Equation 2.22 to assess the factor of safety with respect to BEP. The first approach compares the average hydraulic gradient at a dam to the corrected value from laboratory tests. In the author's experience participating, observing, and reviewing risk assessments over the last decade, this is the most common method used in practice in the U.S. as it is the simplest to implement. The second approach compares the point gradient along the piping path to the corrected values of the laboratory tests as

illustrated in Figure 2.34 to account for the site specific, pre-pipe flow patterns as well as any variation in correction factors that may occur along the pipe path.

Table 2.4. Correction factors for Schmertmann (2000) method.

Symbol	Correction For	Equation
C_D	(D/L)	$C_D = \frac{W_0}{W_1}$ where $W = \left(\frac{D}{L}\right)^{\frac{0.2}{\left(\frac{D}{L}\right)^{2}-1}}$
C_L	Seepage length	$C_L = \left(\frac{L_t}{L_f}\right)^{0.2}$
C_S	Grain size	$C_s = \left(\frac{d_{10f}}{0.20mm}\right)^{0.2}$
C_k	Anisotropic permeability	$C_k = \left(\frac{1.5}{R_{kf}}\right)^{0.5}$
C_z	High-k underlayer	Figure 12, Schmertmann (2000)
C_γ	Soil Density	$C_\gamma = 1 + 0.4(D_{rf} - 0.60)$
C_B	Domain width	$C_B = 1$, identified factor but did not use
C_G	Gradient in flownet	$C_G = \left(\frac{i_{pm}}{\bar{i}_{pm}}\right)_t$ or $C_G = \left(\frac{i_x}{\bar{i}}\right)$
C_R	Gradient due to radial flow	$C_R = (R_1 + R_0)/2R$
C_α	Pipe slope	Figure 13, Schmertmann (2000)

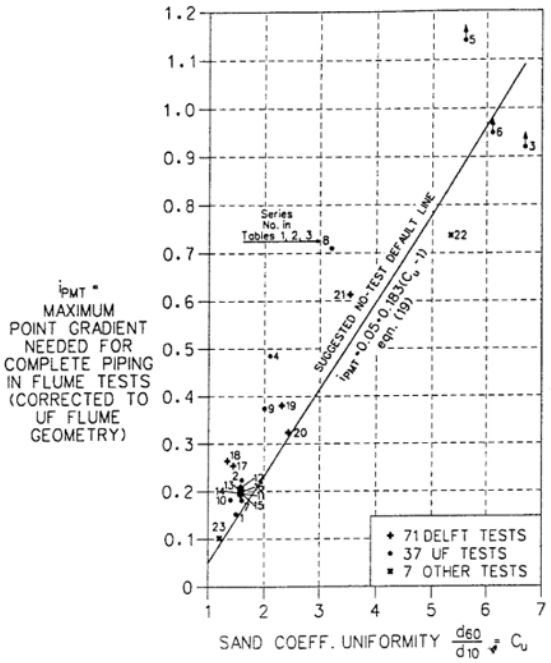

Figure 2.33. Predictive relationship for i_{pmt} from soil coefficient of uniformity (Schmertmann, 2000).

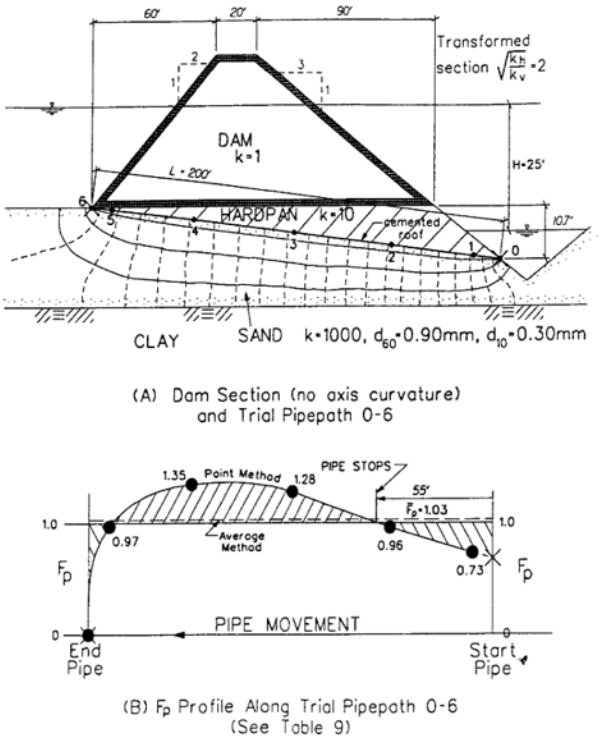

Figure 2.34. Illustration of Schmertmann Approach using pre-pipe hydraulic gradients along the piping path (Schmertmann, 2000).

It should also be recognized that the plotted points of i_{pmt} in Figure 2.33 represent average values for a study series. In reality, the variability in this trend is much more significant than shown. Robbins and Sharp (2016) recognized this issue and recompiled the database of tests used by Schmertmann. Rather than plotting the study averages, the individual test points were plotted in order to visualize the uncertainty in the results graphically (Figure 2.35). Additionally, a linear quantile regression was performed to provide estimates of the uncertainty in i_{pmt} in addition to the mean trend provided by Schmertmann (2000). At present, the practice in the United States typically uses Figure 2.35 when employing Schmertmann's method to assess BEP in a probabilistic manner. A few years later, Allan (2018) extended this original data set and assessed the resulting distribution of data analytically. Allan found that the variability in the critical point gradients could be adequately described by a lognormal distribution. She proposed empirically fit equations that can be used to estimate the distribution in place of Figure 2.35.

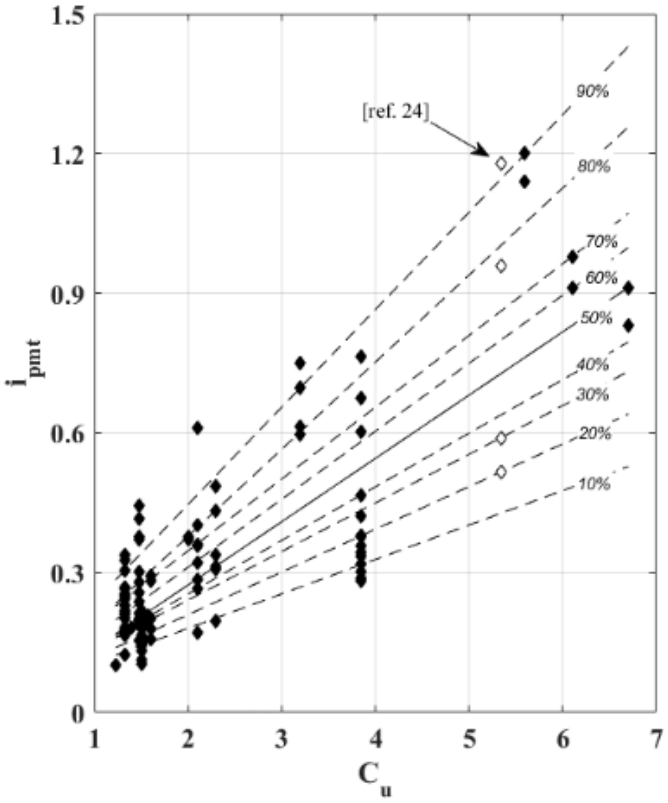

Figure 2.35. Critical point gradients from individual laboratory tests used by Schmertmann (2000) and corresponding best fit quantile regression lines for 10th to 90th quantiles (Robbins & Sharp, 2016).

2.3.3 Limitations of Current Approaches

The most significant limitation of both the Sellmeijer and Schmertmann approaches is caused by the assumptions made regarding the relationship between the average hydraulic gradient across the structure and the local, hydraulic conditions near the pipe. In the Sellmeijer model, a two-dimensional groundwater solution was used. As such, the model is only applicable to situations where the two-dimensional groundwater solution adequately explains the relationship between the upstream head and conditions near the erosion pipe. Likewise, Schmertmann's approach neglects the influence of the erosion pipe on the hydraulics near the pipe. As such, the method assumes that the relationship between the ambient gradient and the local gradients at the pipe tip is the same for all problems (or accounted for by the correction factors). Unfortunately,

this is not the case. The impacts of these limitations will be demonstrated through a few examples in the following paragraphs.

The clearest illustration of the issues with the Sellmeijer method was provided by Van Beek (2015). Both the original Sellmeijer rule and the adjusted Sellmeijer rule were developed through calibrations to series of experiments. These experiments consisted of primarily 2D situations (area, ditch, and sloped type exits) that closely paralleled the assumptions in the underlying analytical solutions for the groundwater flow. After these rules were developed, significantly more experiments became available that made use of hole type exits which result in highly three-dimensional groundwater flow patterns. A comparison of the predictions from the original and adjusted Sellmeijer rules to these hole type experiments is provided in Figure 2.36. It is readily seen that the Sellmeijer rules predict a critical upstream head that is twice the measured critical head for these three dimensional situations. This is a significant error that is highly unconservative for three dimensional situations. As many field scenarios are three dimensional, this is a major limitation of the method.

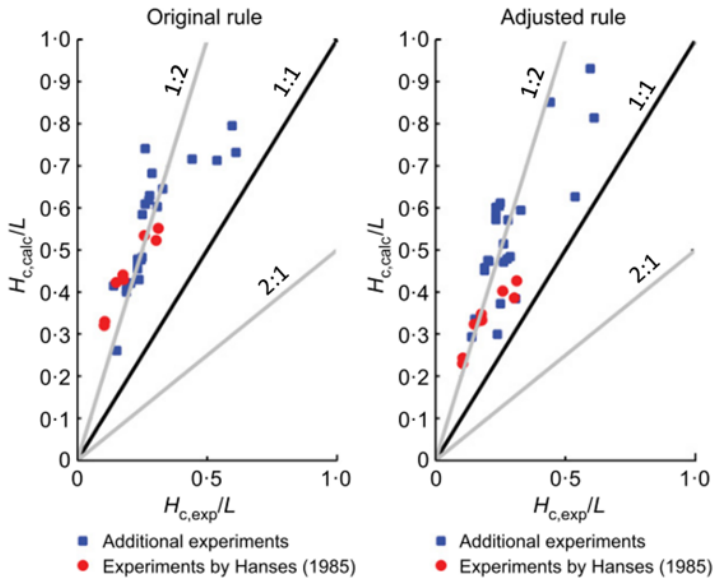

Figure 2.36. Error in Sellmeijer predictions for experiments with hole type exits (modified from van Beek, 2015).

While the Schmertmann approach is limited by the same factor, this issue has not been clearly illustrated by any studies to date. To demonstrate the issue, the Schmertmann method will be applied to two laboratory experiments conducted by Allan (2018) that are identical with the exception of the exit conditions. The laboratory tests were conducted in a flume with dimensions nearly identical to the flume used at the University of Florida by Schmertmann (2000) and Pietrus (1981). A cross-sectional schematic and photograph of the experimental flume is illustrated in Figure 2.37. In addition to the sloped seepage exit shown in Figure 2.37a, Allan also used downstream boundaries consisting of a horizontal area exit, slot (or ditch) type exit, and a hole type exit. Experiments using the slot type exit (Test 37) and hole type exit (Test 34) will be examined below. The exit geometries are illustrated in Figure 2.38 for these experiments.

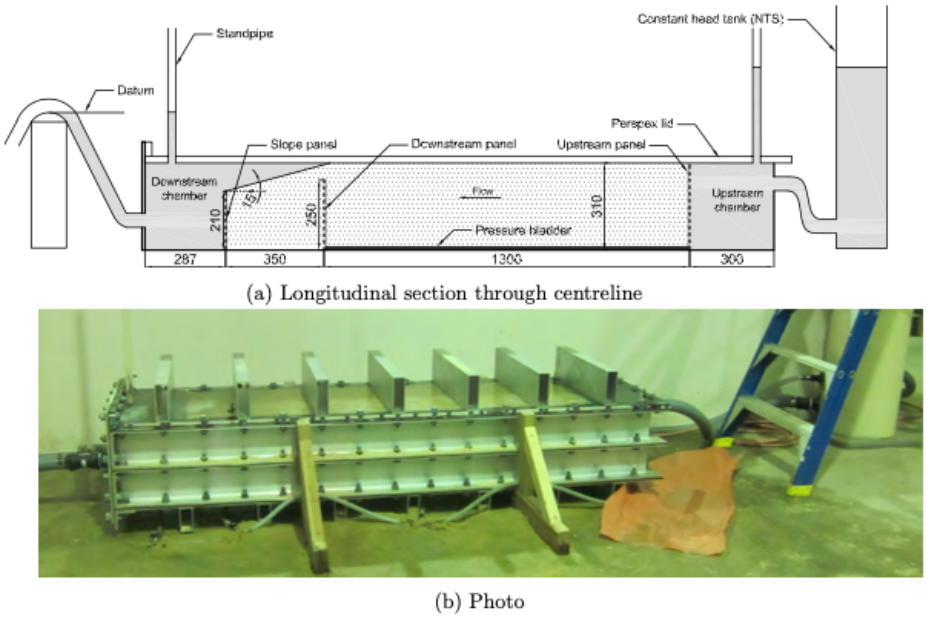

(a) Longitudinal section through centreline

(b) Photo

Figure 2.37. Schematic and photograph of the laboratory flume used by Allan (2018).

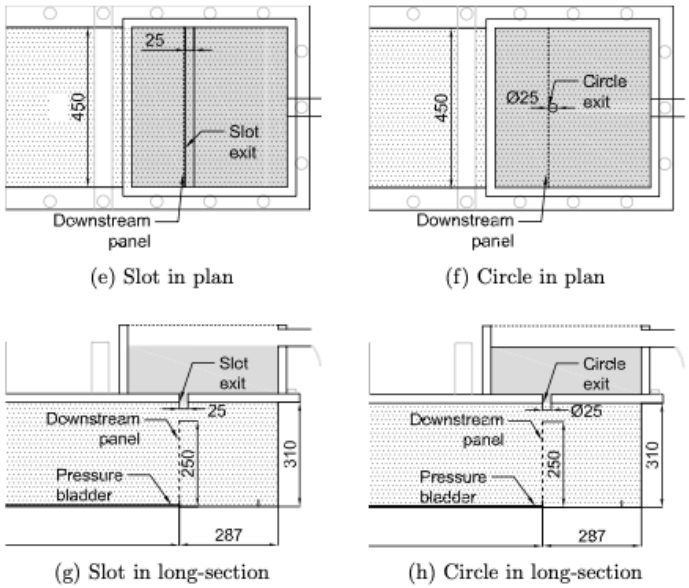

(e) Slot in plan

(f) Circle in plan

(g) Slot in long-section

(h) Circle in long-section

Figure 2.38. Slot (ditch) type exit condition and hole type exit condition used by Allan (2018) for Test 37 and Test 34 , respectively.

Allan (2018) describes in detail the sample preparation and testing procedures. For both of these experiments, the upstream boundary condition was increased until the pipe started progressing. Once the pipe began to progress, the upstream head was decreased, thereby causing

the erosion pipe to stop at various points throughout the sample. The head would then be increased again until the pipe started progression. This procedure was repeated with the pipe at various degrees of penetration through the sample to ensure the critical head for pipe progression was measured. The resulting critical value of the differential head (H_c) applied to each sample is provided in Table 2.5 along with key dimensions and soil properties.

Table 2.5. Experiment details and results from Allan (2018).

Test No.	**Exit**	L_s **(m)**	**Sand**	d_{50} **(mm)**	C_u	k_h **(m/s)**	D_r	H_c **(m)**
Test 34	Hole	1.3	Sydney Sand	0.30	1.3	3.7×10^{-4}	0.40*	0.203
Test 37	Slot	1.3	Sydney Sand	0.30	1.3	3.7×10^{-4}	0.40*	0.237

**Estimated on the basis of other tests with similar sample preparation technique*

The Schmertmann approach can be applied to these experiments using the average gradient approach and the point gradient approach. When applying the average gradient approach, C_g is ignored and the average gradient is used to predict the factor of safety. Since these two experiments are identical in all regards except for the exit condition, the correction factors (Table 2.4) would have identical values for both experiments with the exception of C_g, which accounts for the relationship between the average gradient and the point gradient along the pipe path. The average gradient approach would thus predict that the two experiments have the exact same critical head. Given how close the critical heads are to each other (18%), one could argue that the error easily falls within the uncertainty in the measurements (Figure 2.35). However, if the approach works, the point-by-point method should be more accurate and yield values closer to reality. This theory is tested by applying the point-by-point method recommended by Schmertmann (2000).

In order to apply the Schmertmann method to these two experiments using the point-by-point approach, a three-dimensional, steady state groundwater model of both experiments was constructed using the finite element method (Figure 2.39). The upstream boundary was set to a constant head equivalent to the critical head in the experiment, and the downstream boundary (ditch or hole) was set to a constant head of $h = 0.0$ m. All other model boundaries were no flow boundaries.

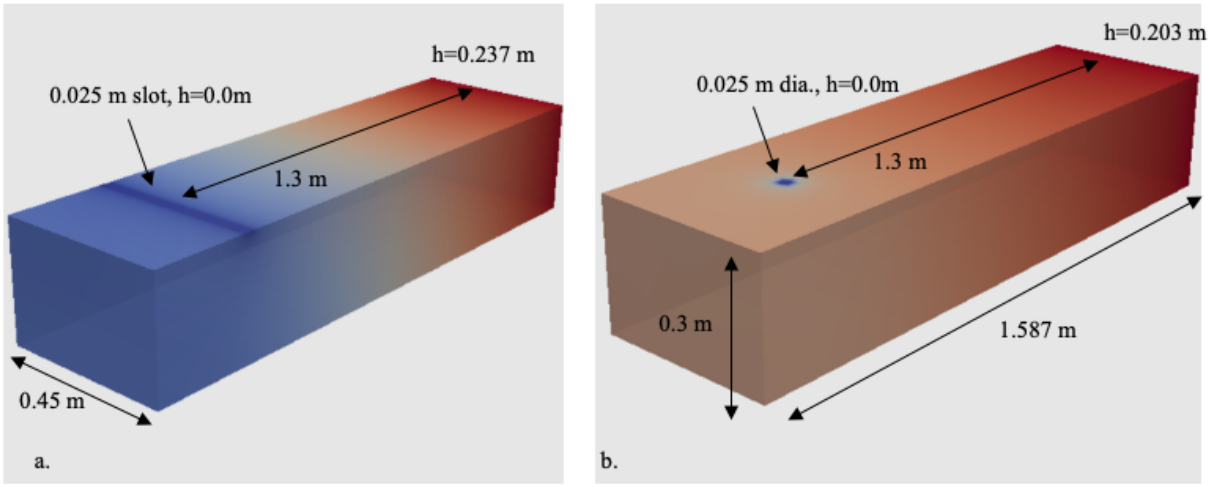

Figure 2.39. Steady-state, finite element solution for (a) Test 37 and (b) Test 34 from Allan (2018) with head differential of 1.0 m.

The value of both the head and the hydraulic gradient magnitude, i_x, was extracted along the centerline of the model at the top of the sample for each test. The results are shown in Figure 2.40. The minimum value of i_x along the pipe path controls the pipe progression. The minimum value of i_x was 0.058 for Test 34 and was 0.151 for Test 37. These values of i_x were used to calculate the C_g correction factor for both experiments as shown in Table 2.6. Values for the correction factors C_s and C_γ were also calculated and are presented in

Table 2.6. All correction factors except for those in Table 2.6 had values of 1.0 or were not applicable. This is solely due to the fact that Allan modelled her experiments after the Pietrus (1981) experiments that Schmertmann used as reference tests when making corrections, so the value of i_{pmt} has already been corrected to the reference values of Allan's experiments.

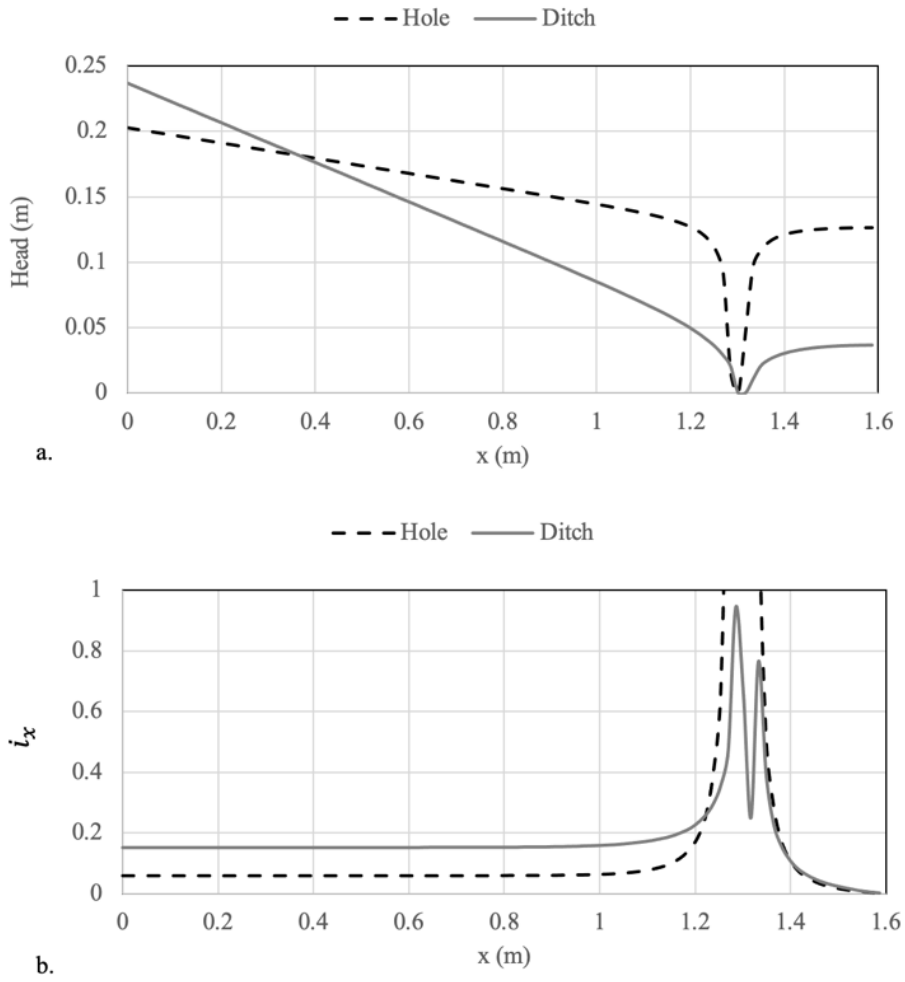

Figure 2.40. Modelled (a) head distribution and (b) hydraulic gradient (i_x) at each x location along centerline of the top of the domain.

Table 2.6. Schmertmann's correction factors applicable to Test 34 and Test 37.

C_s	C_γ	C_g – Test 34, Hole	C_g – Test 37, Ditch
1.08	0.92	$C_G = \left(\frac{i_x}{\bar{\imath}}\right)$ $\bar{\imath} = \frac{H}{L} = \frac{0.203}{1.3} = 0.156, \quad i_x = 0.058$ C_G =(0.058/0.156)=0.37	$C_G = \left(\frac{i_x}{\bar{\imath}}\right)$ $\bar{\imath} = \frac{H}{L} = \frac{0.237}{1.3} = 0.182, \quad i_x = 0.151$ C_G =(0.151/0.182)=0.82

The critical head predicted by Schmertmann's approach can then be calculated for each test by rearranging Equation 2.22 to yield

$$\frac{H_c}{L_s} = \bar{\imath} = \frac{C_s C_\gamma i_{pmt}}{C_g} \tag{2.23}$$

The calculated values of H_c were 0.366 m for Test 34 and 0.164 m for Test 37. These calculated values are compared to the experimental values in Figure 2.41. Clearly, the critical head is overpredicted by a factor of two using Schmertmann's method just as it was for the Sellmeijer model for the case of a hole type exit, whereas the predicted critical head is much closer for the 2D ditch scenario of Test 37. An explanation for the overprediction can be provided through examination of the modelled head profiles for the two experiments (Figure 2.40a). For the case of the hole type exit, the head loss is concentrated near the exit with a relatively limited amount of head loss occurring over the sample length when compared to the ditch scenario. As the pipe progresses backwards, the zone of concentrated head loss moves with the pipe tip through the sample, with the majority of head loss still occurring near the pipe head. As this geometry focuses the flow towards the pipe tip, it causes the lower value of H_c observed in the experiment. To the contrary, the 2D scenario of the ditch permits a more uniform flow distribution across the sample. As a result, it is more difficult to achieve high local gradients at the pipe tip resulting in the higher values of H_c observed in the experiments. This

illustrates the significant influence the geometry can have on the gradients that develop near the pipe tip, and indicates that the pre-pipe, ambient hydraulic gradient is not a suitable measure for evaluating the progression of BEP.

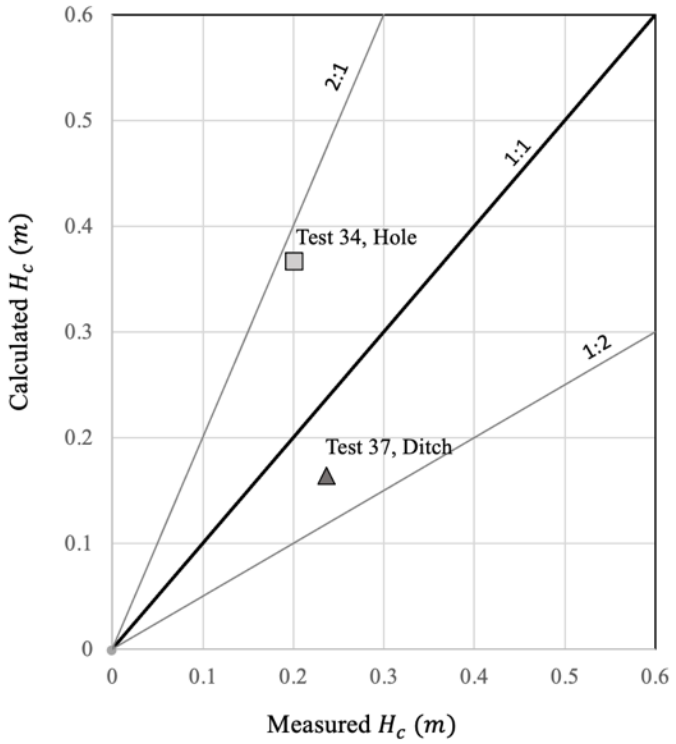

Figure 2.41. Comparison of critical head (H_c) calculated by Schmertmann method to measured values for Test 34 with a hole boundary condition and Test 37 with a ditch boundary condition.

The primary limitations of both the Sellmeijer method and the Schmertmann method are due to the indirect assessment of the conditions near the pipe tip causing progression. There are too many factors influencing the relationship between the applied boundary conditions and the hydraulics near the pipe tip to adequately account for all possibilities using simple rules and correction factors. This is especially true when considering field conditions where additional complexities are encountered due to variable ground conditions and problem geometries. To

overcome these limitations, it is necessary to develop validated, numerical modeling approaches that simulate BEP progression based on the local hydraulic conditions near the pipe tip. Progress to date in this area will be reviewed in the following section.

2.4 Numerical Modeling

Many studies have been conducted on numerical modeling of internal erosion. Unfortunately, the literature on modeling of internal erosion is perhaps the area with the greatest ambiguity regarding the type of erosion being considered. This confusion regarding erosion mechanisms is one of the primary reasons that validated predictive models have yet to be obtained for BEP. For this reason, all studies related to numerical modeling of internal erosion were reviewed as opposed to those focused specifically on BEP to ensure no significant developments were accidentally missed simply because of terminology. Of the literature reviewed, there were 219 references identified that conducted some form of numerical modeling of internal erosion. This review considered numerical modeling broadly, with studies varying from empirical predictions based on machine learning algorithms trained on lab data (Kaunda, 2015), to applications of commercial software to IE problems (e.g., Garcia Martinez et al., 2019), to custom developed codes solving coupled fluid particle interactions at the pore scale (Xiong et al., 2021).

Of these, there were 102 studies on internal instability (II), 76 studies on BEP, 13 studies on concentrated leak erosion (CLE), 25 studies on other topics, and only a few studies on contact erosion (CE) and global backward erosion (GBE/S) (Figure 2.42). The studies categorized as "Other" consisted of general studies on internal erosion, studies with ambiguous erosion

mechanisms, numerical studies of filter performance, and miscellaneous related studies, e.g., erosion of wellbore walls in oil and gas production (Detournay et al., 2006).

The temporal distribution of the 219 studies over the last 70 years is illustrated in Figure 2.43. With the exception of a few early studies from 1980 to 2000, the majority of work investigating numerical modeling of internal erosion has occurred in the last twenty years. Over this time, there has been an exponential increase in the number of studies on numerical modeling of internal erosion. Despite this surge in research, there are still no validated, widely accepted modeling approaches for predicting the progression of internal erosion in engineering practice. This statement is true for all types of internal erosion, including backward erosion piping.

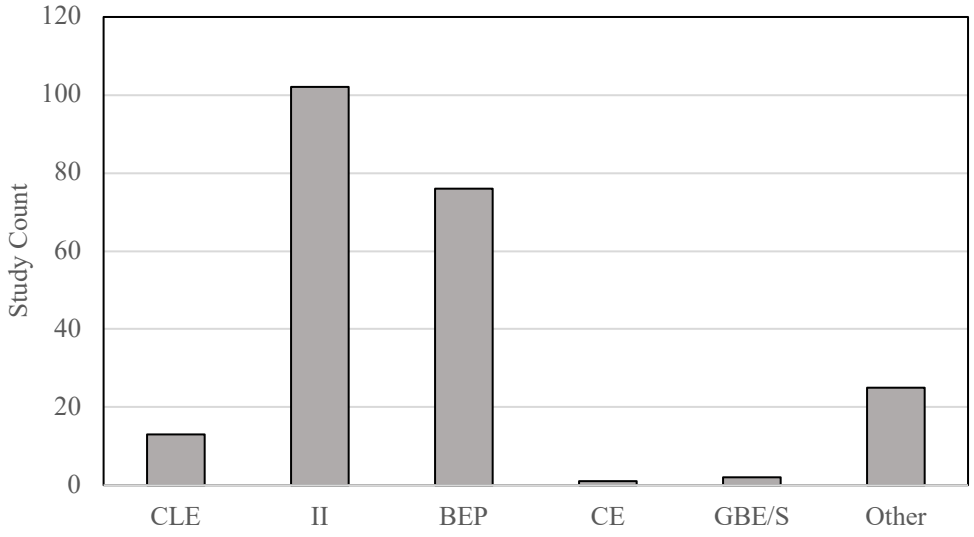

Figure 2.42. Numerical modeling studies by type of internal erosion.

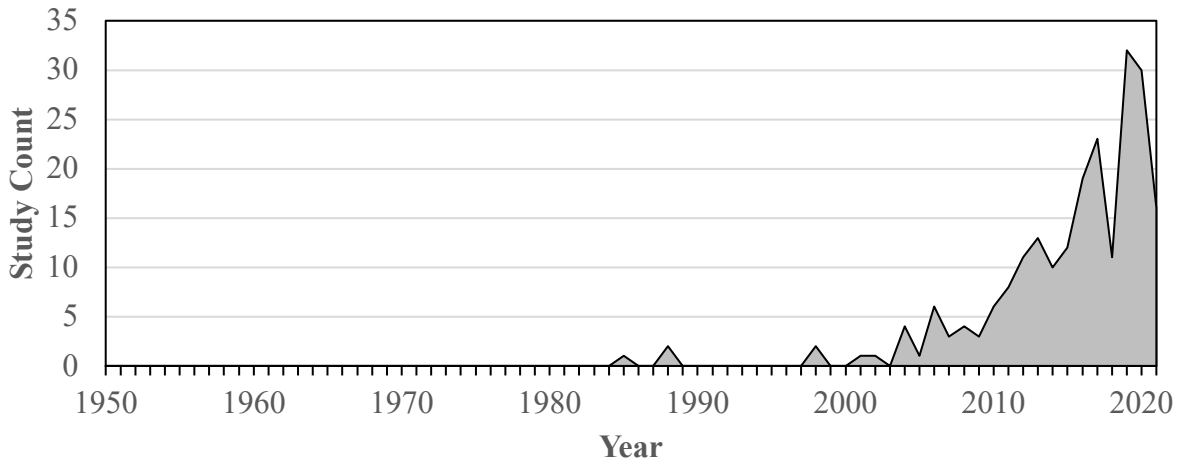

Figure 2.43. Temporal distribution of studies on numerical modeling of all types of internal erosion.

With regards to BEP specifically, the primary impediments to reaching a validated predictive model have been (1) ambiguity regarding the mechanisms of BEP, II, and CLE and (2) an unclear definition of the criterion used for pipe progression. The first of these issues has greatly impacted the choices made when selecting constitutive relations for representing the erosion process in numerical models. Because of this, consistent approaches for modeling BEP have not regularly been used which has made direct comparisons of studies and method validation difficult. Even when studies have used similar approaches, the second issue regarding the lack of clarity in the progression criterion has also made model validation difficult. There has been no consistency regarding the distance over which progression is assessed or the physical quantities used for assessing progression. Further, no approaches have been developed for independently measuring constitutive model parameters for BEP progression in the lab. As a result, model validation to date has consisted of little more than calibration of models to specific experiments to demonstrate the ability of a model to reproduce certain behaviors.

Given these issues, it is important to have an understanding of modeling of BEP, II, and CLE. In the sections that follow, a description of the most generalized case of modeling all three types of internal erosion is provided so that the subtle differences in physics, boundary conditions, and governing equations are understood. A system of categorizing models based on the degree to which the erosion process is represented is then introduced, as models of similar complexity tend to have similar capabilities, strengths, and weaknesses. Finally, a selection of BEP specific studies is reviewed to highlight the state of knowledge to date and corresponding limitations.

2.4.1 Governing Physics

While similar at first glance, the erosion processes of BEP, II, and CLE are quite different. Each process is dominated by differing physics, and the behavior of the erosion is different as a result. A generalized problem description for each type of erosion along with corresponding governing equations is provided below.

2.4.1.1 Backward Erosion Piping

Consider the general illustration of BEP as shown in Figure 2.44 for an arbitrary domain in three dimensions. The problem consists of a soil domain, Ω_s, and erosion pipe domain, Ω_p, with boundaries Γ_s and Γ_p, respectively. The erosion pipe domain is an open space through which viscous, incompressible flow passes. The soil domain is a porous media through which groundwater flow passes. The two domains share the boundary $\Gamma_{s,p} = \Gamma_s \cap \Gamma_p$, and $\boldsymbol{x}$ denotes the vector {x,y,z} to any point in the domain. The coordinate system is aligned with the gravitational acceleration such that $\boldsymbol{g} = \{0,0,g\}$.

For the general case of transient, partially saturated flow, the groundwater flow in the soil domain (Ω_s) is described by the Richard's equation given by (e.g., van Esch, 2013)

$$\frac{\partial}{\partial x}\left(k_x \frac{\partial h}{\partial x}\right) + \frac{\partial}{\partial y}\left(k_y \frac{\partial h}{\partial y}\right) + \frac{\partial}{\partial z}\left(k_z \frac{\partial h}{\partial z}\right) = \frac{\partial \theta}{\partial h}\frac{\partial h}{\partial t} \tag{2.24}$$

where $h = z + p/\rho g$ denotes the total head in terms of the elevation head (z) and the pressure head ($p/\rho g$), k_x, k_y, k_z denotes the hydraulic conductivity in the coordinate directions, $\theta = V_w/V$ denotes the volumetric water content in terms of volume of water (V_w) and total volume (V), and t indicates the time.

The viscous, incompressible fluid flow in the erosion pipe (Ω_p) is described by the incompressible Navier-Stokes equations given by (e.g., Smith and Griffiths, 2004; Sellmeijer, 1988)

$$\frac{\partial u}{\partial t} + u\frac{\partial u}{\partial x} + v\frac{\partial u}{\partial y} + w\frac{\partial u}{\partial z} + \frac{1}{\rho}\frac{\partial p}{\partial x} - \frac{\mu}{\rho}\left(\frac{\partial^2 u}{\partial x^2} + \frac{\partial^2 u}{\partial y^2} + \frac{\partial^2 u}{\partial z^2}\right) = 0 \tag{2.25}$$

$$\frac{\partial v}{\partial t} + u\frac{\partial v}{\partial x} + v\frac{\partial v}{\partial y} + w\frac{\partial v}{\partial z} + \frac{1}{\rho}\frac{\partial p}{\partial y} - \frac{\mu}{\rho}\left(\frac{\partial^2 v}{\partial x^2} + \frac{\partial^2 v}{\partial y^2} + \frac{\partial^2 v}{\partial z^2}\right) = 0 \tag{2.26}$$

$$\frac{\partial w}{\partial t} + u\frac{\partial w}{\partial x} + v\frac{\partial w}{\partial y} + w\frac{\partial w}{\partial z} + \frac{1}{\rho}\frac{\partial p}{\partial w} + \rho g - \frac{\mu}{\rho}\left(\frac{\partial^2 w}{\partial x^2} + \frac{\partial^2 w}{\partial y^2} + \frac{\partial^2 w}{\partial z^2}\right) = 0 \tag{2.27}$$

where $\boldsymbol{V} = \{u, v, w\}$ is the flow velocity vector and μ is the dynamic fluid viscosity. Equation 2.24 and Equations 2.25 through 2.27 are coupled via continuity of the pressure, p, and velocity, $\boldsymbol{V}$, along $\Gamma_{s,p}$.

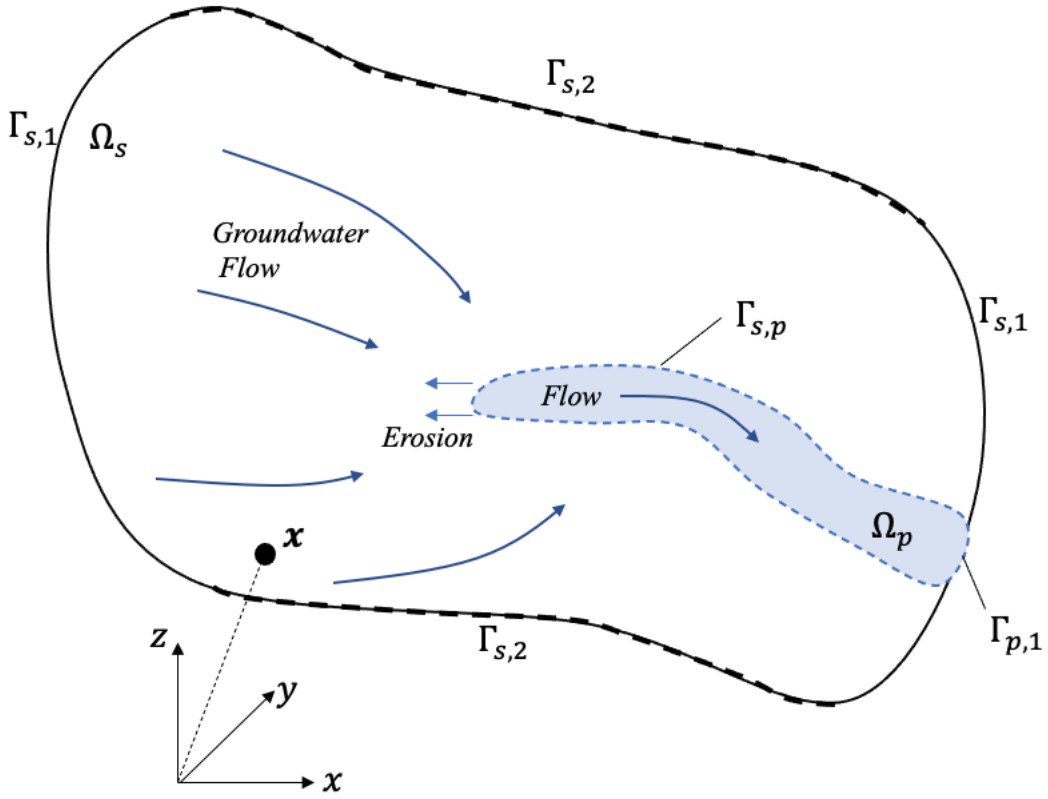

Figure 2.44. Illustration of BEP initial boundary value problem in three dimensions.

Initially, the pipe domain is an infinitesimal domain at the point of erosion initiation. The initial conditions for the problem are given by

$$h(\boldsymbol{x}, t_o) = h(\boldsymbol{x}) \; \forall \; \boldsymbol{x} \in \Omega \tag{2.28}$$

where $h(\cdot)$ is an arbitrary function describing the initial head distribution. The boundary conditions are given by

$$h(\boldsymbol{x}, t) = f(\boldsymbol{x}, t) \; \forall \; \boldsymbol{x} \in \Gamma_{s,1} \tag{2.29}$$

$$\nabla h(\boldsymbol{x}, t) \cdot \boldsymbol{n} = \frac{\partial h(\boldsymbol{x}, t)}{\partial n} = g(\boldsymbol{x}, t) \; \forall \; \boldsymbol{x} \in \Gamma_{s,2} \tag{2.30}$$

$$h(\boldsymbol{x}, t) = k(\boldsymbol{x}, t) \; \forall \; \boldsymbol{x} \in \Gamma_{p,1} \tag{2.31}$$

where $\Gamma_{s,1}$ and $\Gamma_{s,2}$ are a closed set of Γ_s, $\boldsymbol{n}$ is the unit vector normal to Γ_s, and $\Gamma_{p,1}$is the downstream outlet boundary of the erosion pipe. The functions $f, g,$ and k are again arbitrary functions that describe the indicated values over both space and time along the boundaries.

As noted previously, the erosion is primarily driven by the erosion at the pipe tip, and the pipe dimensions are driven by the wall shear stress exerted by the flow through the pipe. These two conditions can be described generically by the equations

$$\boldsymbol{V_p} = PE(p, \boldsymbol{V}, \boldsymbol{S}) \tag{2.32}$$

$$\boldsymbol{V_w} = SE(\tau, \boldsymbol{S}) \tag{2.33}$$

where $\boldsymbol{V_p}$ and $\boldsymbol{V_w}$ denote the velocity of the pipe tip and the pipe wall boundary $\Gamma_{s,p}$, respectively, as a function of the fluid pressure p, fluid velocity $\boldsymbol{V}$, hydraulic boundary shear stress τ, and influential soil properties provided as vector $\boldsymbol{S}$. The functions PE and SE are the primary erosion and secondary erosion functions. Alternatively, these functions could express the mass erosion rate at the pipe tip and pipe wall respectively instead of the velocity. Regardless of form, in order to be completely correct, the mass of the eroded material must be considered as a sink/source term in the coupling of the domains along $\Gamma_{s,p}$, and the total mass of the fluid sediment mixture must be considered in the pipe flow equations. Additionally, the concentration of the sediment mixture in the pipe can also be used to inform the deposition and transport rates in the erosion pipe (Wewer et al., 2021).

This general description of the BEP process describes all modeling studies of BEP. The differences between studies are determined by choices made with regards to simplifications of the physics, simplifications of the problem geometry, or choices of the functions PE and SE. These choices will be discussed in later sections when reviewing previous studies on BEP.

2.4.1.2 Internal Instability

Unlike BEP, internal instability consists solely of flow through porous media as illustrated in Figure 2.45. This is because the erosion process consists of fine soil grains being washed out of the coarse soil grains such that a soil matrix remains in place. The erosion of the fine particles results in a fraction of the soil being fluidized in the pore fluid as illustrated by the phase diagram in Figure 2.45. As such, the total pore space consists of an air volume (V_a), water volume (V_w), and fluidized soil volume (V_f). The total volume of the liquid phase is given by $V_l = V_f + V_w$. As a result of this fluidization, the porosity of the soil increases thereby creating a zone of higher permeability. Because of this, the erosion of the soil is simply tracked through the soil porosity, given by $n = V_l/V$ for saturated soils.

The problem domain consists of a single soil domain, Ω_s, with boundary Γ_s as illustrated in Figure 2.45. The flow in the domain is governed by a modified version of Richard's equation given by (e.g., Fujisawa et al. 2010a)

$$\frac{\partial}{\partial x}\left(k_x \frac{\partial h}{\partial x}\right) + \frac{\partial}{\partial y}\left(k_y \frac{\partial h}{\partial y}\right) + \frac{\partial}{\partial z}\left(k_z \frac{\partial h}{\partial z}\right) = \frac{\partial \theta}{\partial t} + \frac{\partial n}{\partial t} \tag{2.34}$$

where

$$\frac{\partial n}{\partial t} = f\left(\nabla h, C_p, \mathbf{S}\right) \tag{2.35}$$

is an erosion and deposition function that determines the change in the volume of the soil matrix based on the hydraulic gradient, the concentration of fluidized particles in the pore fluid, $C_p = V_f/V_l$, and select soil properties indicated by the vector **S.** The change in C_p over time is determined from the continuity equation of the eroded particles given by

$$\frac{\partial C_p \theta}{\partial t} + \frac{\partial}{\partial x}\left(C_p u\right) + \frac{\partial}{\partial y}\left(C_p v\right) + \frac{\partial}{\partial z}\left(C_p w\right) = \frac{\partial n}{\partial t} \tag{2.36}$$

After determining the sediment concentration and new porosity for a given time, the hydraulic conductivity of the soil is updated as

$$\{k_x, k_y, k_z\} = g(n) \tag{2.37}$$

where g is some function, such as the Kozeny-Carman equation, that relates the soil hydraulic conductivity to the porosity. In this manner, the increase in hydraulic conductivity due to erosion is represented in the model. For coupled hydromechanical models, other model parameters can also be updated on the basis of the soil porosity and phase relations.

While BEP and II models may appear similar at first glance, it is important to recognize the significant differences. First, II is not required to progress sequentially along an erosion path as BEP does. This is due to the fact that the eroded sediments can pass through the soil matrix. As a result, erosion can occur anywhere where hydraulic conditions are sufficient to cause erosion. Second, because the eroded zone is still porous media, the change in hydraulic conductivity is less dramatic than in the case of an open BEP pipe resulting in less severe concentration of flow. This is one of the primary areas of confusion between BEP and II in that many studies attempting to model BEP have used a porosity based erosion model similar to II as a means of representing the erosion process.

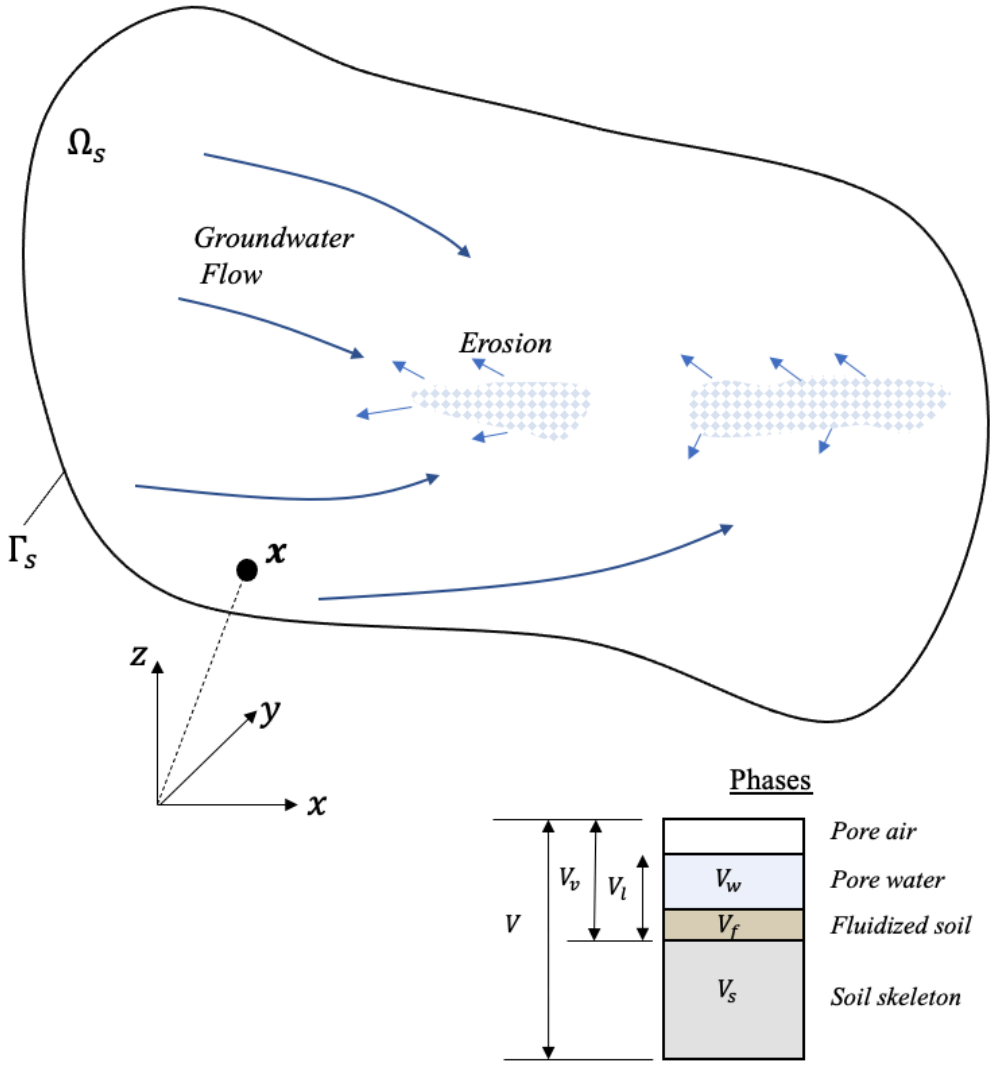

Figure 2.45. Illustration of multi-phase, internal instability initial boundary value problem.

2.4.1.3 CLE

Now consider the case of a concentrated leak as illustrated in Figure 2.46. The problem consists of a pipe domain, Ω_p, passing through a soil domain, Ω_s. In the case of CLE, the pipe is an open space that is once again governed by the Navier-Stokes equations (Equations 2.25 to 2.27). Because the pipe passes completely through the domain, the flow in the pipe is primarily driven by the pipe boundary conditions $\Gamma_{p,1}$ and $\Gamma_{p,2}$. In fact, concentrated leaks usually form in

soils that are somewhat cohesive and able to sustain a crack (Savage et al., 2019). As a result, the soil permeability is typically quite low and can usually be neglected altogether. In this case, the problem domain simplifies down to be the solution to the Navier-Stokes equations across only the pipe domain Ω_p with initial conditions given by

$$\boldsymbol{V}(\boldsymbol{x}, t_o) = f(x), \qquad p(x, t_o) = g(x) \tag{2.38}$$

where f and g are functions defining the initial velocity and fluid pressure distributions, respectively, and boundary conditions given by

$$p = k(t) \; \forall \; \boldsymbol{x} \in \Gamma_{\mathrm{p,1}} \tag{2.39}$$

$$p = 0 \; \forall \; \boldsymbol{x} \in \Gamma_{\mathrm{p,2}} \tag{2.40}$$

and

$$\frac{\partial \boldsymbol{V}}{\partial n} \approx 0 \;\; \forall \; \boldsymbol{x} \in \Gamma_{\mathrm{s,p}} \tag{2.41}$$

The velocity, or erosion rate, of the pipe boundaries is given by

$$\boldsymbol{V_w} = E(\tau, \boldsymbol{S}) \tag{2.42}$$

where τ again denotes the hydraulic shear stress applied to the boundary and **S** is a vector of relevant soil properties. While CLE can be modelled using the Navier-Stokes equations, it is usually assessed through simplifications that make use of 1D, analytical, pipe hydraulic equations. While confusion with BEP is not nearly as big of an issue as in the case of II, there are a few studies evaluating CLE that could be mistaken for BEP due to the use of the phrase "piping" in describing their work.

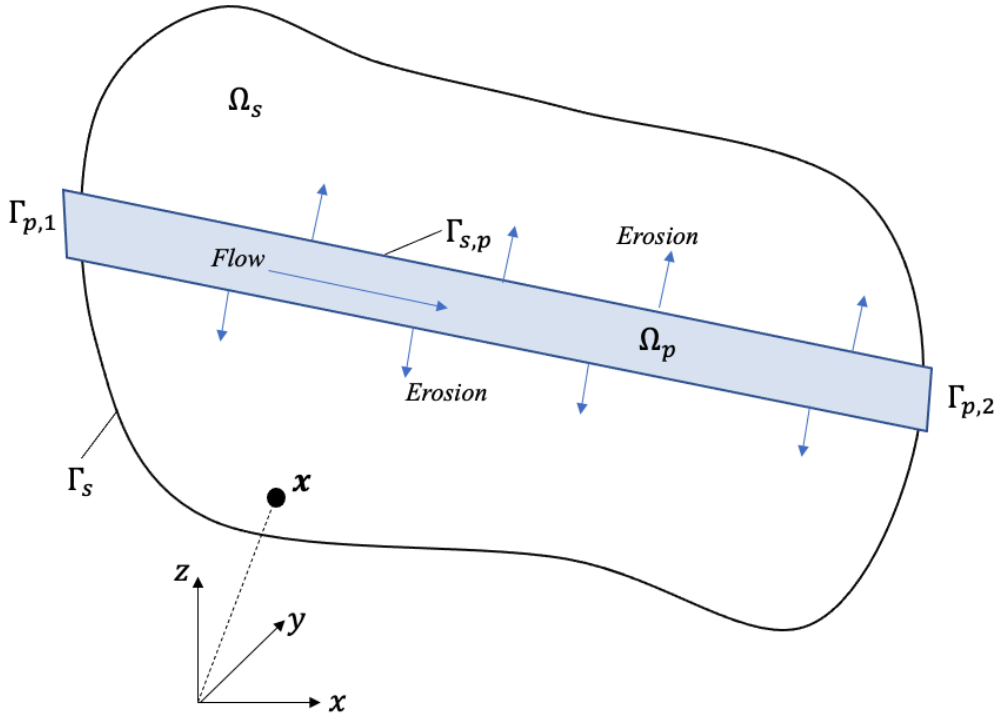

Figure 2.46. Illustration of general concentrated leak initial boundary value problem.

2.4.2 Developments in Modeling of BEP

The studies on numerical modeling were reviewed to identify all studies that were intended to model backward erosion piping. Only those studies that developed a new model, demonstrated a technique for the first time, or lead to significant findings regarding modeling were selected for review in this study. Therefore, studies that applied existing models to particular problems or performed repeat analysis were excluded. In addition, a few studies that used terminology that may be confused as numerical modeling of BEP were included to highlight the reasons why they are not actually BEP studies. This resulted in identification of 46 studies on numerical modeling of BEP for further review (Table 2.8).

Studies were grouped into categories based on the approach taken to model the erosion process. Wang et al. (2014) suggested that internal erosion models can be broadly grouped into

three categories: (1) models that consider only the influence of the erosion on the groundwater flow by introducing high permeability zones to represent the erosion, (2) multi-phase models that track eroded material through the model domain, and (3) coupled discrete element (DEM) and computational fluid dynamic (CFD) models that simulate the erosion process at the particle scale. This categorization system has been expanded slightly for classification of BEP related studies. As shown in Table 2.7, Category 0 models were added and Category 1 was split into Category 1 and 2. Category 0 models are those that conduct routine seepage analysis to evaluate only initiation potential of BEP. As Category 0 models do not model erosion in any way, they will not be discussed further. Category 1 models are those that model the influence of a high permeability zone on the overall groundwater flow pattern, but do not attempt to simulate erosion progression. Category 2 models are those that follow the same approach as Category 1, but include erosion laws for the automated analysis of erosion progression. Category 1 and 2 models can be further subdivided based on how the conductivity of the eroded zone is determined. Subcategory (a) denotes those studies that arbitrarily increased the conductivity, whereas subcategory (b) denotes those studies that based the increase in conductivity on the assumed physics governing flow in the eroded area (porous or pipe flow). The model developed in Chapter 3 of this thesis is a Category 2b model.

Category 3 models refer to multiphase flow models that explicitly track the transport of the eroded fraction through the domain. This category of models can be subdivided into (a) those that model only erosion and do not consider the impact of phases on the physics, and (b) those that have phase dependent physics where the concentration of eroded soils influences erosion rates, deposition rates, material properties, and flow behavior. Because internal instability is

usually modeled using multiphase models, the studies in this category are the ones with the greatest confusion and overlap between II and BEP physics.

Category 4 models refers to coupled computational fluid dynamics (CFD) and discrete element method (DEM) simulations that attempt to model the erosion process at the particle scale. Because of the heavy computational requirements for models in this category, most of these studies have not modelled the full erosion problem domain for field scale applications, but have instead attempted to evaluate specific micromechanical aspects of the erosion process.

Table 2.7. Model categories for classification of BEP modeling literature

Category 0	Routine seepage analysis to evaluate initiation potential. No erosion pipe.
Category 1	Routine seepage analysis with highly conductive zone for pipe *1a*. Arbitrary conductivity *1b*. Physics based conductivity
Category 2	Same as Category 1, but with erosion laws for automated pipe progression *2a.* Arbitrary conductivity *2b*. Physics based conductivity
Category 3	Multiphase flow *3a.* Erosion only *3b.* Phase dependent physics (flow, material properties, deposition, and/or erosion)
Category 4	Coupled DEM/CFD

In addition to model category, the studies were classified based on the following items:

1. Dimensions – indicates whether the study was two-dimensional (2D) or three dimensional (3D)
2. Type of IE – indicates what erosion mechanism the study is most applicable to based on the assumptions made
3. Method – indicates what numerical modeling approach was used (FEM= finite element method, FVM=finite volume method, DEM=discrete element method,

EFG =element free galerkin method, LBM = lattice boltzman method, FDM=finite difference method, RBF =radial basis function method, and ML= machine learning method).

4. Ground water flow – indicates whether the model used transient or steady state groundwater flow models
5. Transient erosion – indicates whether the model involved a time dependent erosion process for progression
6. Erosion pipe characteristics – indicates what assumptions were made regarding the following aspects of representing the erosion pipe:
    a. Type – specifies whether the pipe was assumed to be porous media, an open conduit, or hybrid situation that automatically transitions based on pore scale Navier-Stokes solutions (only applies to DEM models)
    b. Flow regime – specifies whether the flow in the pipe was treated as laminar or turbulent flow.
    c. Pipe Flow – Specifies whether the pipe flow was treated as steady state or transient pipe flow.
    d. Assumed Pipe Shape – Specifies the assumed cross-sectional shape of the erosion pipe
    e. Primary erosion – indicates if an erosion criterion was specified specifically for the advancement of the pipe tip
    f. Secondary erosion – indicates if a secondary erosion criterion was specified to account for the enlargement of the erosion pipe

g. Auto-progressing – indicates whether the model was formulated in a manner that automatically simulated the progression of the erosion pipe.

Major developments related specifically to the modelling of BEP are summarized in the following sections by model category.

Table 2.8. Summary of relevant numerical studies.

									Erosion Pipe Characteristics						
Author	**Year**	**2D/3D**	**Software**	**Type of IE**	**Method**	**Model Category**	**Ground water flow**	**Transient Erosion**	**Type**	**Flow Regime**	**Pipe Flow**	**Assumed Pipe Shape**	**Primary Erosion**	**Secondary Erosion**	**Auto-progressing**
Wong	1981	3D	Seep3D	BEP	FEM	1a	Steady	-	Porous	-	-	-	-	-	No
Jianhua	1998	2D	Seep/W	BEP/II	FEM	1a	Steady	-	Porous	-	-	-	No	No	No
Stavropoulou et al 1998	1998	2D	Unknown	II	FEM	3b	Transient	Yes	Porous	-	-	-	-	-	Yes
Hagerty and Curini	2004	2D	Seep/W	BEP/II	FEM	1a	Steady	-	Porous	-	-	-	-	-	No
Cividini and Gioda	2004	2D	Unknown	II	FEM	3b	Transient	Yes	Porous	-	-	-	-	-	Yes
Sellmeijer	2006	2D	MSEEP	BEP	FEM	2b	Steady	No	Conduit	Laminar	Steady	Parallel Plate	No	Yes	Yes
Ding et al	2007	3D	Unknown	BEP	FEM	2a	Steady	No	Porous	Laminar	Steady	-	Yes	No	Yes
El Shamy et al	2008	3D	PFC3D	DEM	DEM	4	Transient	-	NS	-	-	-	-	-	Yes
Fujisawa et al.	2010	2D	Custom	II	FEM/FVM	3b	Transient	Yes	Porous	-	-	-	-	-	Yes
Zhou et al.	2012	2D	Unknown	BEP	EFG	2a	Steady	No	Conduit Flow	Unknown	Steady	Rectangular	Yes	No	Yes
Zhang et al.	2012	2D	COMSOL	II	FEM	3a	Transient	Yes	Porous	-	-	-	-	-	Yes
Wang and Ni	2013	3D	PFC3D	BEP	DEM	4	Transient	Yes	NS	-	-	-	-	-	Yes
Lomine et al.	2013	2D	Custom	CLE	DEM/LBM	4	Transient	Yes	NS	-	-	-	-	-	Yes
Vandenboer et al.	2013	3D	Abaqus	BEP	FEM	1a	Steady	-	Porous	Laminar	Steady	Triangle	No	No	No
Kanning and Calle	2013	2D	Custom	BEP	FDM	1a	Steady	-	Porous	Laminar	Steady		No	No	Yes
Bersan et al.	2013	2D/3D	COMSOL	BEP	FEM	1b	Steady	-	Conduit Flow	Laminar	Steady	Parallel Plate	No	No	No
Van Esch et al.	2013	2D	DGFlow	BEP	FEM	2b	Transient	No	Conduit	Laminar	Steady	Parallel Plate	No	Yes	Yes
Polanco-Boulware and Rice	2014			BEP	FEM	0	Steady	-	-	-	-	-	-	-	-
Vandenboer et al.	2014	3D	Abaqus	BEP	FEM	1a	Steady	-	Porous	Laminar	Steady	-	No	No	No
Kramer	2014	2D	MSEEP	BEP	FEM+ML	2b	Steady	Yes	Conduit Flow	Laminar	Steady	Parallel Plate	No	Yes	Yes
Wang et al.	2014	2D	Unknown	BEP	EFG	2b	Steady	Yes	Conduit Flow	Unknown	Steady	Circle	No	No	Yes
Polanco-Boulware and Rice	2016	3D	Soil Vision?	BEP	FEM	0	Steady	-	-	-	-	-	-	-	-
Robbins, Griffiths, and Fenton	2016	2D	Custom	BEP	FEM	0	Steady	-	-	-	-	-	-	-	-

Table 2.8. (continued)

									Erosion Pipe Characteristics						
Author	**Year**	**2D/3D**	**Software**	**Type of IE**	**Method**	**Model Category**	**Ground water flow**	**Transient Erosion**	**Type**	**Flow Regime**	**Pipe Flow**	**Assumed Pipe Shape**	**Primary Erosion**	**Secondary Erosion**	**Auto-progressing**
Aguilar-Lopez et al	2016	2D	COMSOL	BEP	FEM	1b	Steady	-	Conduit Flow	Laminar	Steady	Various	No	Yes	No
Robbins	2016	3D	FLAC3D	BEP	FEM	2a	Steady	No	Porous	Laminar	Steady	Pore	Yes	No	Yes
Fujisawa et al.	2016	2D	Custom	BEP	FVM	2b	Transient	Yes	NS	Laminar	Transient	Arbitrary	Yes	No	Yes
Tran et al.	2017	2D	Custom	BEP	DEM	4	Transient	Yes	NS	Laminar	Transient	Arbitrary	Yes	Yes	Yes
Navin and Shewbridge	2017	2D	Seep/W	BEP	FEM	1a	Steady	-	Porous	Laminar	Steady	Pore	No	No	No
Garcia et al.	2017	3D	Plaxis	BEP	FEM	1a	Steady	-	-	-	-	-	No	No	No
Liang et al.	2017	2D	Unknown	II	FEM	3b	Transient	Yes	Porous	Laminar	Transient	Pore	Yes	Yes	Yes
Rotunno et al.	2017	2D	FEAP	BEP/II	FEM	3b	Transient	Yes	Conduit Flow	Turbulent	Steady	Circle	Yes	Yes	Yes
Tao	2018	3D	CFDEM	BEP/II	DEM	4	Transient	Yes	NS	Laminar/Turbulent	Transient	Pore	-	-	Yes
Robbins and Griffiths	2018	2D	S&G FEM*	BEP	FEM	2b	Steady	No	Conduit Flow	Laminar	Steady	Parallel Plate	Yes	Yes	Yes
Robbins and Griffiths	2018	3D	S&G FEM*	BEP	FEM	2b	Steady	No	Conduit Flow	Laminar	Steady	Parallel Plate	Yes	Yes	Yes
Froiio et al.	2019	2D	Custom	BEP	DEM	4	Transient	Yes	NS	Laminar	Transient	Arbitrary	Yes	Yes	Yes
Vandenboer	2019	2D/3D	Abaqus	BEP	FEM	1a	Steady	-	Porous	Laminar	Steady	-	No	No	No
Saliba et al.	2019	2D	Plaxis	II	FEM	1a	Steady	-	Porous	Laminar	Steady	Pore	Yes	No	No
Garcia et al.	2019	3D	Plaxis	BEP	FEM	1a	Steady	-	-	-	-	-	No	No	No
Khoury et al.	2019	2D	Custom	CLE	RBF/FDM	1b	Transient	-	NS	Laminar	Steady	Arbitrary	No	No	No
Fascetti and Oskay	2019	3D	Custom	BEP/II	FDM	2a	Transient	No	Porous	Laminar	Steady	Pore	Yes	No	Yes
Rotunno et al.	2019	3D	FEAP	BEP/II	FEM	3b	Transient	Yes	Conduit Flow	Turbulent	Steady	Circle	Yes	Yes	Yes
Barendsen	2020	3D	iMod	BEP	FDM	1a	Steady	-	Porous	Laminar	Steady	Pore	No	No	No
Rahimi and Shafieezadeh	2020	3D	FLAC3D	II	FDM	2a	Steady	Yes	Porous	Laminar	Steady	Pore	Yes	Yes	Yes
Callari and Froiio	2020	3D	FEAP	BEP/II	FEM	3b	Transient	Yes	Conduit Flow	Turbulent	Steady	Circle	Yes	Yes	Yes
Rahimi et al.	2021	3D	FLAC3D	II	FDM	2b	Unknown	Yes	Porous	Laminar	Unknown	Pore	Yes	No	Yes
Wewer et al.	2021	2D	COMSOL	BEP	FEM	2b	Transient	Yes	Conduit Flow	Laminar	Steady	Parallel Plate	No	Yes	Yes

**S&G FEM: Refers to Smith and Griffiths (2004) finite element software*

2.4.2.1 Category 1 Studies

Category 1 models of BEP refer to studies that attempt to represent the erosion process by manually defining zones of higher permeability to represent the erosion pipe in a standard seepage analysis. This modelling approach does not actually model the erosion process, but instead only examines the impact of an eroded zone on the groundwater solution. Taking this approach requires manual definition of the extent and hydraulic conductivity of the eroded zone for each step of erosion progression being analysed. As such, Category 1 modelling of BEP can be conducted with any groundwater modelling software. However, progression of erosion cannot be automatically assessed.

As the simplest approach, the earliest studies on modelling BEP followed this approach. Wong (1981) was the first to use a finite element model to simulate BEP as part of a parametric study conducted to evaluate correction factors for Schmertmann's quantitative piping theory which was eventually published in Schmertmann (2000). Wong (1981) created finite element models of a pipe penetrating various distances through a domain. The pipe was modelled as a zone of constant hydraulic conductivity, but the conductivity value used was not presented. The model results were used to define concentration factors that defined the secant gradient in front of the pipe tip. The variation in the concentration factors with distance from the pipe tip was evaluated, and the factors were used to define corrections to the average hydraulic gradient. Unfortunately, this work did not receive significant attention internationally, and the concept of a distance dependent secant gradient does not appear to have been applied in another study. This will be revisited as part of this study.

Yin (1998) and Hagerty & Curini (2004) both used the commercial software Seep/W to simulate pipe progression through a homogenous dam as illustrated in Figure 2.47. Yin varied

the hydraulic conductivity of the pipe from 2 to 10^6 times the conductivity of the surrounding soil, whereas Hagerty & Curini assumed the pipe was 20,000 times more conductive than the surrounding soil. Yin assessed the influence of a piping zone on the pore pressures and flow rates coming out of the dam. Hagerty & Curini also considered the influence of the piping zone on the stability of the downstream slope of the dam, finding an increase in stability as the pipe progresses due to the lowered phreatic surface. Neither study commented on how to use the information to assess the likelihood of pipe progression, but rather focused on the changes one would see in pressure and flow if a hypothetical erosion zone did indeed pass through a dam. Similar studies were conducted by Navin & Shewbridge (2017) and Saliba et al., (2019).

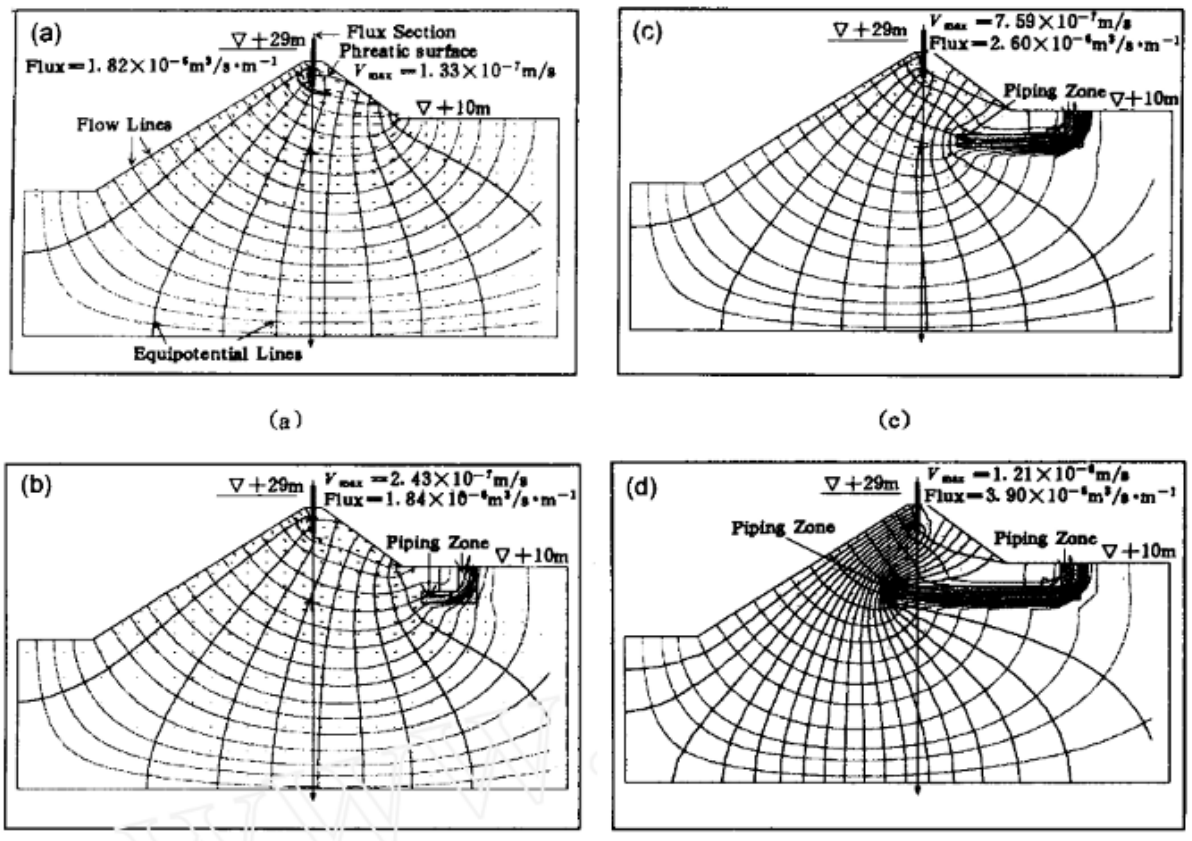

Figure 2.47. Example of manually defining erosion pipe zone in Category 1 model to assess impact of erosion on groundwater flow (Yin, 1998).

There have also been a few studies conducted in Category 1 that have yielded very useful information regarding the appropriateness of modeling assumptions. Most significant of these are studies that have validated approximations of the Navier-Stokes equations. Many authors have modeled the pipe flow as one-dimensional, laminar, pressure driven flow (Hoffmans, 2014; Sellmeijer, 1988, 2006; Van Esch et al., 2013). As noted by Bersan et al. (2013), this assumption is correct so long as the velocity component perpendicular to the pipe wall is negligible and the no-slip condition on the pipe boundaries is satisfied. This flow condition, commonly referred to as Hagen-Pouseuille flow, is described by the equation (e.g., Bersan et al. 2013)

$$\frac{Q}{A} = \frac{2D_h^2}{\beta\mu}\rho g \frac{\partial h}{\partial x} \tag{2.43}$$

where Q is the total flow rate in the pipe, $D_h = 4A/P$ is the hydraulic diameter for a pipe with cross-sectional area A and perimeter P, β is a friction factor dependent on the shape of the pipe section, and x is the coordinate direction along the centerline of the pipe. By comparing Equation 2.43 to Darcy's law for laminar flow through porous media, it is readily seen that the pipe flow can simply be approximated by Darcy's law with an equivalent hydraulic conductivity given by

$$k_{eq} = \frac{2D_h^2}{\beta\mu}\rho g \tag{2.44}$$

Making this approximation has significant advantages over using the Navier-Stokes equations as it reduces the problem to a single degree of freedom in terms of h rather than solving for the four degrees of freedom $\{p, u, v, w\}$ in the Navier-Stokes equations. To evaluate this approximation, Bersan et al. (2013) conducted a test problem as illustrated in Figure 2.48 with a rectangular pipe passing half way through a domain. The pipe was meshed precisely in

three dimensions, but was also approximated as a plane to assess the accuracy of a fracture-flow model that solves Equation 2.43 along the boundary. The problem was then solved as a steady state problem using the following 3 approaches:

1. Coupled Darcy-Navier Stokes: the Darcy flow was assessed using the Darcy-Brinkman equations in order to fully couple all 4 degrees of freedom at the soil-pipe interface so that the full Navier-Stokes equations could be solved in the pipe domain.
2. k_{eq} Approach: the problem was solved using only Darcy's equation with the pipe element conductivity set using Equation 2.44 based on the actual dimensions of the pipe as modeled.
3. Darcy – Fracture Flow: the problem was solved using the planar elements shown in Figure 2.48 to solve Equation 2.43 as a fracture flow problem along the boundary.

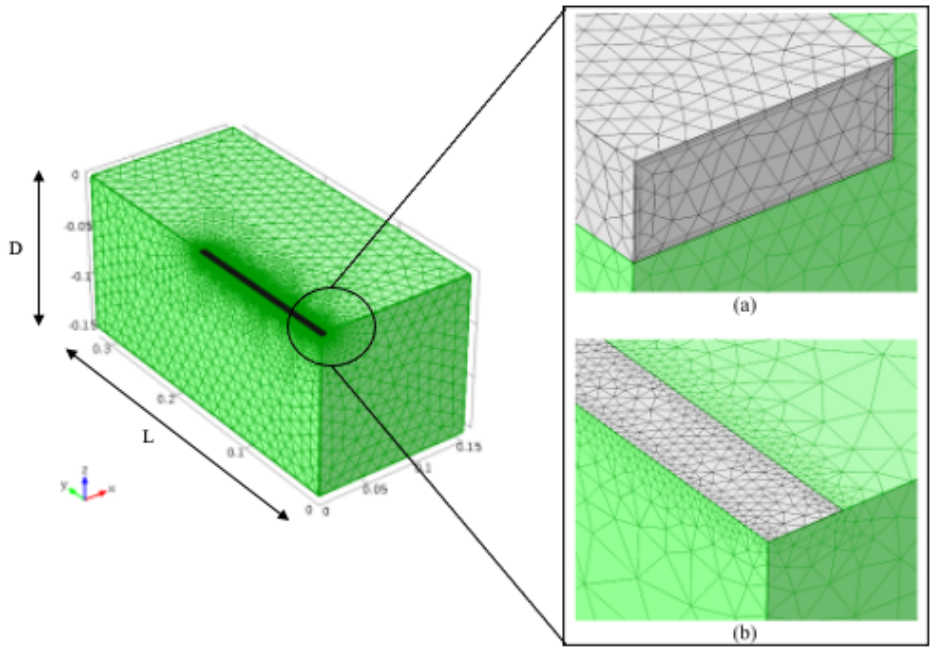

Figure 2.48. Illustration of volumetric pipe domain and equivalent planar domain (modified from Bersan et al. 2013).

The error in the approximations was evaluated on the basis of the total flow passing through the downstream end of the erosion pipe. Analyses were run with varying dimensions D and L as shown in Figure 2.48 to assess the error as a function of the problem geometry. The resulting error is shown in Table 2.9. The error of 0.1-1.5% for the k_{eq} approach is negligible, whereas higher errors were obtained for the planar, fracture flow approximation. The higher errors for the fracture flow may be due solely to the relatively large depth of the erosion pipe they modeled. Aguilar-Lopez et al. (2016) also used the k_{eq} approach and examined the influence of pipe cross sectional shape on the results. The assumed cross-sectional shape of the pipe had a significant difference on the calculations, indicating varying assumptions for this parameter may have a large impact on validation and comparison of studies.

Table 2.9. Calculated errors in Navier-Stokes pipe flow approximations. (Bersan et al, 2013)

Approximation Approach	**Error in Pipe Flow Rate**
k_{eq} approach	0.1-1.5%
Planar, fracture flow	2.8-11.2%

Lastly, Category 1 models have also been used to assess the 3D effects of groundwater flow on both the initiation and progression of piping in the laboratory and field. Vandenboer (2013,2014, 2019) compared exit velocities from 2D and 3D models to determine the model width required to prevent boundary effects. It was found that the model width must be 3 times the length of the erosion pipe for early stages of pipe progression, and 1-2 times the length of the erosion pipe for critical stages in order to prevent the boundary from influencing the flow patterns causing erosion. This corroborates with the finding of Bersan et al. (2013) that

negligible changes in flow rate are observed in pipe outflow once the model width is 1-2 times the pipe length. Barendsen (2020) considered the influence of 3D calculations on pipe outflow at the field scale and concluded that 2D and 3D calculations are significantly different, and caution should be used when using 2D calculations. Finally, Garcia et al. (2017, 2019) used a Category 1 model to assess the potential for a sand boil to reactivate at various differential heads in the field.

2.4.2.2 Category 2 Studies

Category 2 models are the simplest models that offer automatic analyses of erosion progression. As such, the majority of models developed for BEP progression have been Category 2 models. Sellmeijer (2006) developed the first model in this category by developing the software MSeep. This software was a finite element program that provided a numerical implementation of the Sellmeijer model (Sellmiejer, 1988; Sellmeijer et al. 1989, 1991) used to develop the Sellmeijer rules mentioned in earlier sections. The model was a two-dimensional, steady state, finite element model that simulated pipe progression on the basis of the secondary erosion in the pipe. The pipe path was manually defined along a line as illustrated in Figure 2.49. The pipe flow was assumed to be Hagen-Pouisille flow between parallel plates, which was implemented numerically as an internal boundary condition that iteratively adjusted the nodal head until the assumed relationship between the discharge and head was enforced along the pipe. The erosion advancement was evaluated based on the secondary erosion on the bottom of the pipe. The pipe only progressed further if τ exceeded τ_c along the bottom of the erosion pipe.

Later, Van Esch et al. (van Esch, 2013) improved the numerical implementation of the Sellmeijer rule by developing a new finite element program called DgFlow. The DgFlow software improved the numerical implementation of the Sellmeijer model by (1) modeling the

pipe as 1D rod elements assembled into the global conductivity matrix, (2) extending the groundwater calculations to transient conditions, and (3) providing the option for 3D calculations.

The models implemented in MSeep and DgFlow were the first studies to intentionally model the erosion pipe as laminar conduit flow according to the Hagen-Pousille equation. These studies were also the first software packages created solely for the purpose of predicting BEP progression. To this day, these software packages represent the only software tools the author is aware of that have been used in engineering practice to assess BEP. Because of the numerical solution to the groundwater flow, these programs provided the advantage of being able to account for flow through arbitrary soil domains with varying geometry and layering (Figure 2.49). That said, because MSeep and DgFlow are based on the principals of the 2D Sellmeijer model, the software tools have the same shortcomings as the simple Sellmeijer calculation rule. Recent research has demonstrated that even the 3D implementation in DgFlow cannot predict BEP progression more accurately than the simple 2D calculation rule (Van Beek et al. 2022). This is likely because the pipe progression is predicted based on the secondary erosion in the pipe rather than the primary erosion at the pipe tip further emphasizing the need for a primary erosion criterion.

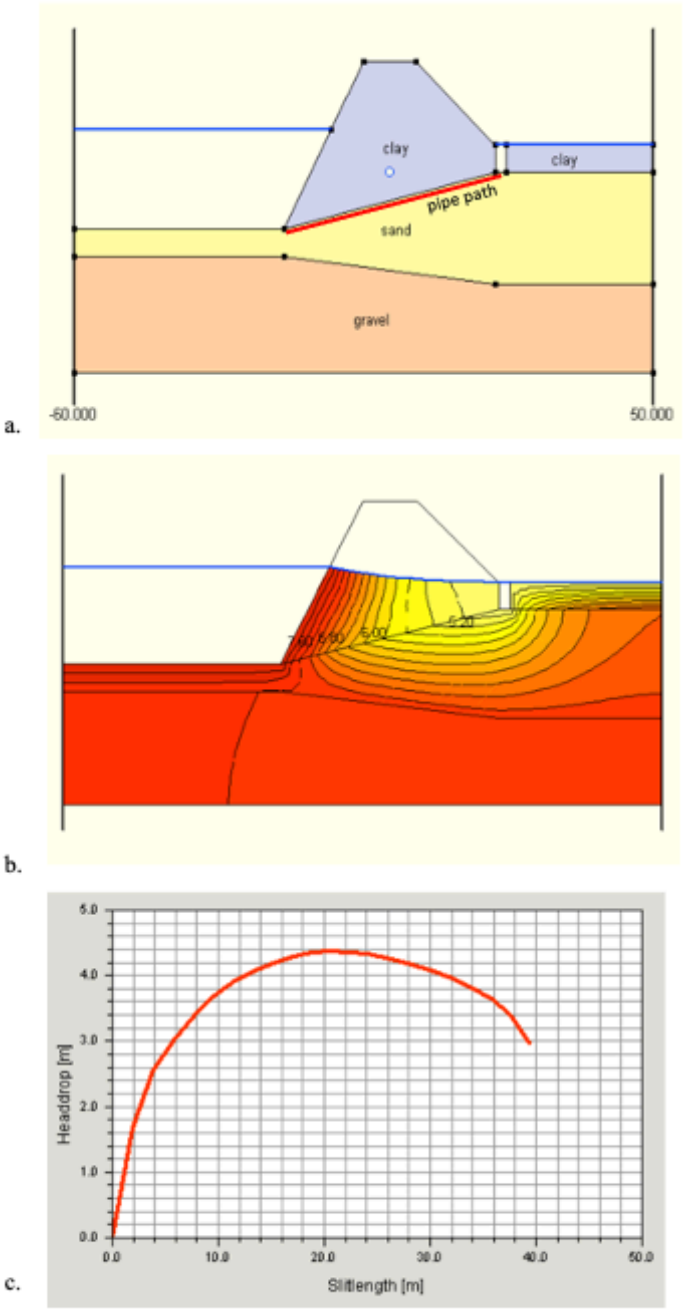

Figure 2.49. Illustration of finite element implementation of Sellmeijer's model (Sellmeijer, 2006) showing (a) problem geometry with pipe path added for emphasis, (b) head distribution with pipe partially progressed, and (c) results showing the equilibrium head for pipe progression at each pipe (slit) length.

Various authors have also developed Category 2 models that have assessed pipe progression based on the primary erosion at the pipe tip (Ding et al., 2007; Fascetti & Oskay, 2019; Rahimi & Shafieezadeh, 2020; Rahimi et al., 2021; Robbins, 2016; Robbins & Griffiths, 2018b; Robbins et al., 2021; Zhou et al., 2012). However, the majority of these studies have modeled the pipe as being flow through porous media or have used arbitrary increases in hydraulic conductivity to represent the eroded zone. For example, Ding et al. (2007) performed iterative, steady state, groundwater flow calculations with an advancing pipe where the pipe was represented by zones with hydraulic conductivity

$$k_{eq} = C_k k_h \tag{2.45}$$

where C_k is a constant valued permeability amplification factor. The progression of the pipe was assessed using a primary erosion criterion given by

$$i > i_{cr} \tag{2.46}$$

where $i = |\nabla h|$ is the magnitude of the hydraulic gradient. If i exceeded the critical value (i_{cr}) in an element adjacent to the pipe, the hydraulic conductivity was increased according to Equation 2.45 resulting in pipe progression as illustrated in Figure 2.50a. Ding et al. (2007) used C_k values varying from 100 to 1,000 as well as various values of i_{cr}. Neither sensitivity to element size nor the influence of distance on i_{cr} values was considered.

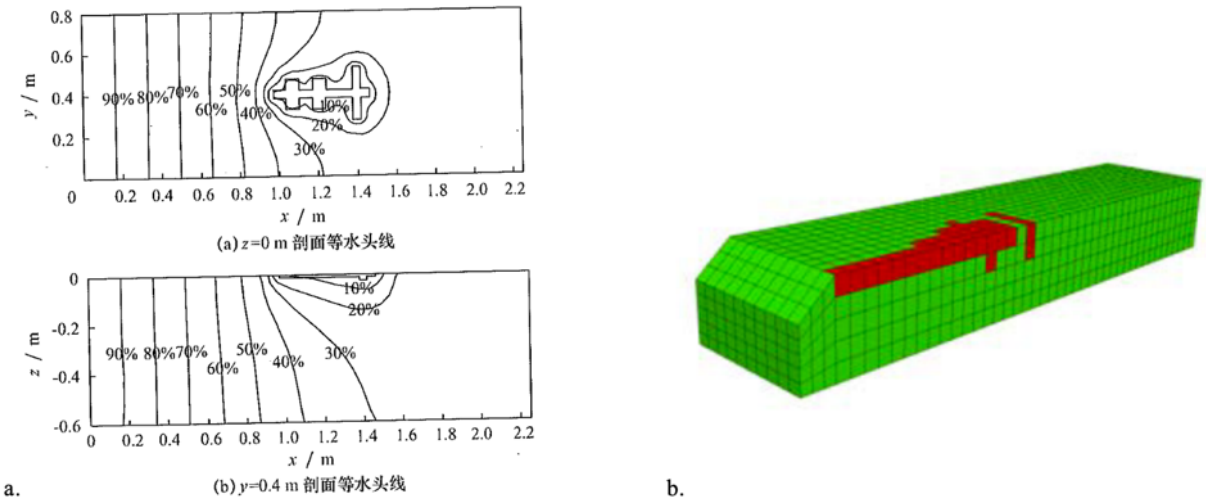

Figure 2.50. Simulations of pipe progression using i_{cr} as primary erosion criterion and constant permeability amplification factor (a – Ding et al. 2007, b- Robbins 2016).

Robbins (2016) implemented the same approach as Ding et al. (2007) (Figure 2.50b) using the finite difference program FLAC3D (Itasca, 2019). Models of two laboratory experiments with various grid sizes were calibrated to the critical boundary conditions measured in the laboratory by varying i_{cr}. As illustrated in Figure 2.51, the value of i_{cr} required to match the experimental data varied with grid size demonstrating that i_{cr} is a function of the distance over which it is assessed.

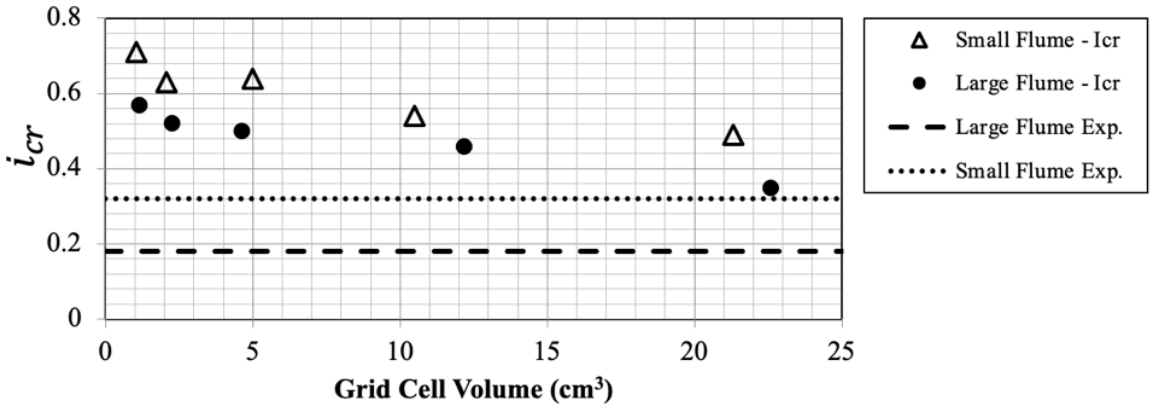

Figure 2.51. Illustration of the variation in i_{cr} required to replicate experimentally measured critical head for various grid cell sizes (Robbins, 2016).

Fascetti and Oskay (2019), Rahimi and Shafieezadeh (2020), and Rahimi et al. (2021) all followed a similar approach of assessing progression using Equation 2.46 with a constant value of i_{cr}. Fascetti and Oskay used a lattice based approach for solving the groundwater flow and employed a constant value of C_k in Equation 2.45, whereas Rahimi and Shafieezadeh (2020) and Rahimi et al. (2021) treated the pipe development as an internal instability process whereby k_{eq} was increased according to a computed increase in porosity. The porosity was increased on the basis of the hydraulic gradient in the pipe. Again, none of these studies considered the relationship between i_{cr} and the distance over which it is assessed, or appropriately modelled the pipe flow.

Kanning and Calle (2013) also modelled pipe progression using Equation 2.45 to represent the erosion pipe with C_k=10 as part of a study focused on deriving representative soil properties for applying the Sellmeijer rule to variable soil conditions. Because the resistance to piping in the Sellmeijer rule is primarily controlled by grain size, they simulated pipe progression through two-dimensional random fields of grain size in an attempt to identify the weakest path through the random field (path of smallest grain size). As such, the pipe was advanced into the zones adjacent to the pipe with the smallest grain size irrespective of the hydraulic conditions near the pipe. In this manner, representative grain sizes across the domain were determined for use in the Sellmeijer rule. It should be emphasized that this study was not suggesting the model be used as a tool for directly evaluating pipe progression.

The studies mentioned thus far that have used a primary erosion criterion at the pipe tip have all represented the pipe as a porous zone. There have also been a few studies that have properly represented the pipe using pipe flow equations. Zhou et al. (2012) and Wang et al. (2014) both developed steady state models for simulating erosion progression in two dimensions

using one dimensional, rod elements to solve the Darcy-Weisbach equation (Equation 2.43) for steady state pipe flow. Zhou et al. assumed the pipe was a fixed, rectangular cross section of arbitrarily chosen size, whereas Wang et al. assumed the pipe was a circular cross section of arbitrarily chosen diameter. Zhou et al. used the flow rate in the pipe as the criterion for progression of the pipe tip. To the contrary, Wang et al. (2014) assessed the pipe progression based on the seepage velocity upstream of the pipe tip, which was calculated based upon the hydraulic gradient. Recognizing the importance of obtaining an accurate solution near the pipe tip, Wang et al. used an element free Galerkin approach to enrich the FEM solution near the pipe tip with additional nodes as shown in Figure 2.52. They also assumed the mechanism advancing the pipe tip was an internal instability mechanism where the soil porosity at the pipe tip varied as

$$\frac{dn}{dt} = \frac{1}{\rho} K_3 (u - u_c) \tag{2.47}$$

In Equation 2.47, K_3 is a constant, ρ is the fluid density, $u = ki/n$ is the seepage velocity, and u_c is the critical seepage velocity above which erosion occurs. Because the groundwater and pipe flow calculations were steady, Equation 2.47 was evaluated in a piecewise, steady-state manner to evaluate the pipe progression in time. Once the porosity at the pipe tip decreased below a critical value (n_c), the soil was assumed to fail and the remainder of the soil fraction was removed. The overall pipe advancement rate was based on the accumulated mass removal at the pipe tip. While this approach may be useful for assessing BEP progression in internally unstable soils prone to suffusion, BEP in uniform sands (the soil types of greatest concern) do not gradually evolve at the pipe tip. As such, it is unknown how well the Wang et al. (2014) approach will apply to general BEP problems. Additionally, no consideration was given to the importance of element size or computation distance on evaluation of pipe progression.

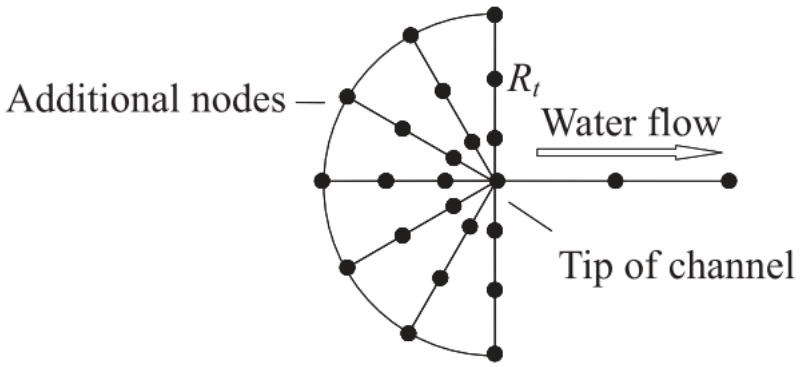

Figure 2.52. Nodes used for element free Galerkin enrichment near the pipe tip (Wang et al. 2014).

Finally, a few studies using Category 2 models have also attempted to simulate transient pipe progression. Fujisawa et al. (2016) solved both the groundwater flow and the pipe flow using the Darcy-Brinkman equation. The Darcy-Brinkman equation includes a phase variable that allows the equation to represent both the Laplace equation for groundwater flow and the Navier-Stokes equations for the pipe flow. The progression rate of the pipe boundary was assumed to be proportional to the seepage velocity allowing the progression to be assessed through time (Figure 2.53). Wewer et al. (2021) also simulated transient pipe progression, but on the basis of the sediment transport rates in the erosion pipe. This is an interesting concept as the pipe progression at the pipe tip may indeed be limited by the transport capacity of the erosion pipe when well beyond the equilibrium state. Recent laboratory studies also indicate this may be the case (Pol et al. 2022). Neither Fujisawa et al. (2016) or Wewer et al. (2021) were rigorously validated against experimental results or case studies.

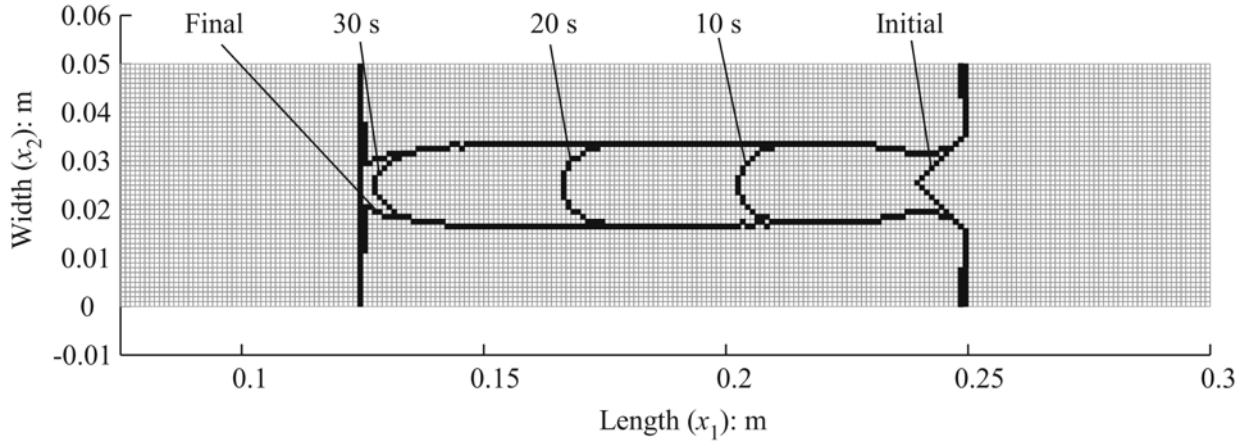

Figure 2.53. Simulation of pipe progression as a boundary tracking problem using Darcy-Brinkman equation for flow (Fujisawa, 2016).

2.4.2.3 Category 3 Studies

As mentioned previously, this category of models has been primarily used for modelling internal instability problems because the erosion is easily tracked in a multiphase approach (e.g., Cividini et al. , 2009; Cividini & Gioda, 2004; Fujisawa et al., 2010a; Zhang et al., 2012). However, there are a few studies that should be noted from this category as it pertains to BEP. These studies will be discussed chronologically, ending with the most significant BEP study in this category of Rotunno et al. (2019).

Cividini and Gioda (2004) developed one of the earliest multiphase erosion models in an attempt to model suffusion. This approach was replicated by Liang and Chen (2011) for the purposes of modeling "piping". While this study used a formulation more appropriate for internal instability, it is mentioned here as the paper describes the application of the model for situations that may be interpreted as BEP. Liang and Chen (2011) modelled the evolution of an erosion pipe over time as illustrated in Figure 2.54. Because the model was intended for suffusion, the variation in the permeability coefficient and eroded particles is gradual and

smooth. This does not realistically represent the BEP process and illustrates one of the fundamental issues with regards to using these types of models for simulating BEP. Instead, for a BEP erosion zone, the erosion pipe should represent an instantaneous increases in hydraulic conductivity due to the open voids that form.

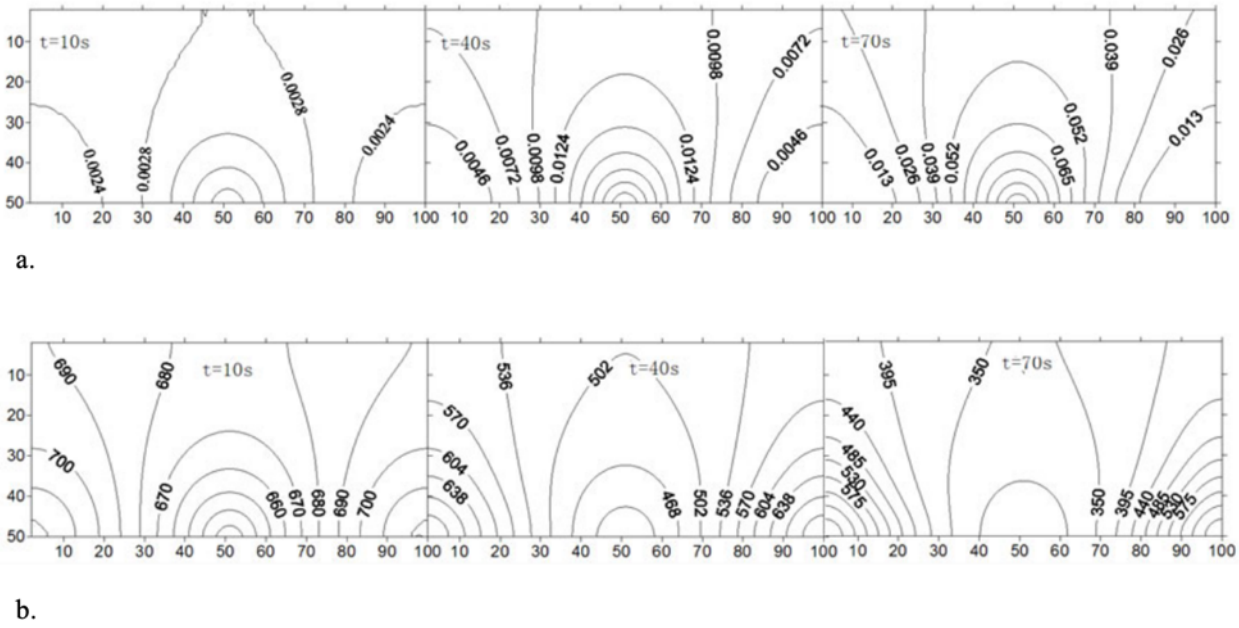

Figure 2.54. Illustration of erosion evolution (Liang et al., 2011) showing variation in (a) the permeability coefficient and (b) the remaining movable particles over time.

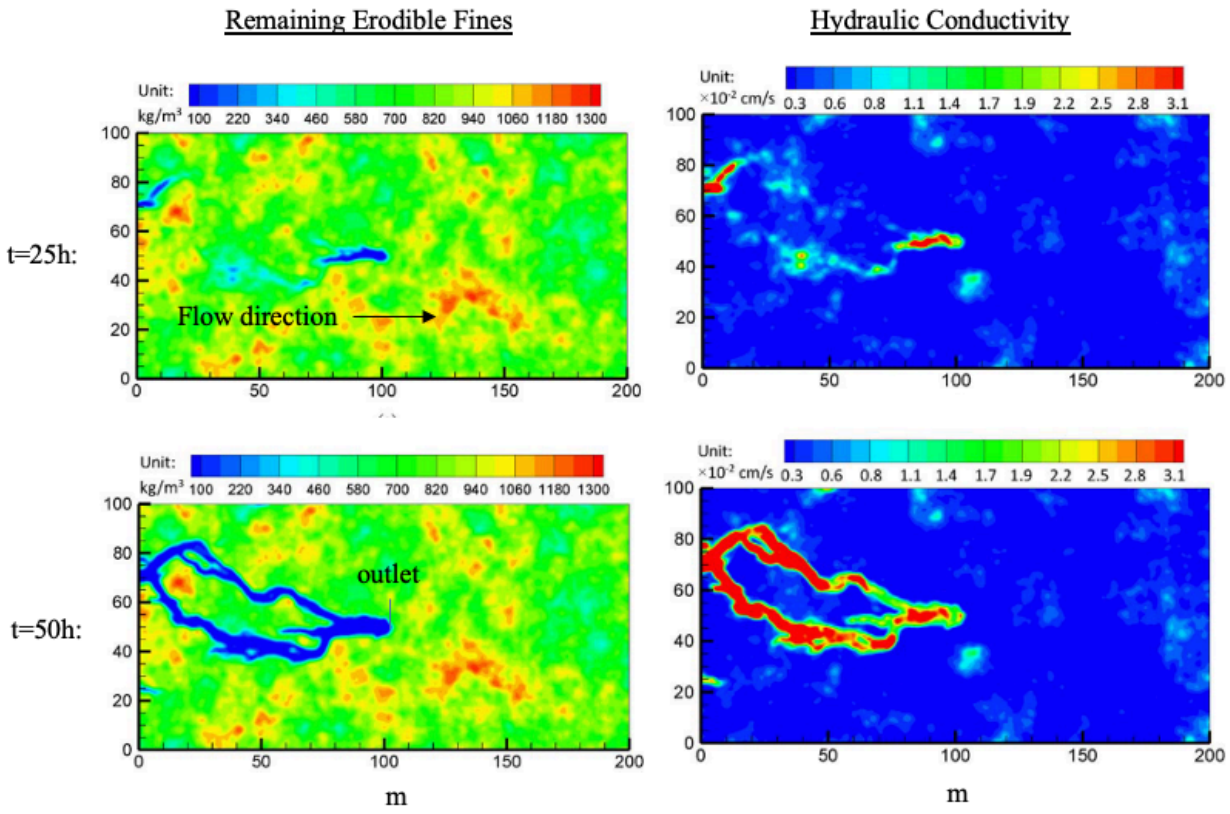

Figure 2.55. BEP simulation results illustrating the removal of fines (left) and resulting hydraulic conductivity (right) at simulation time t=25 hours (top) and t=50 hours (bottom) (Liang et al. 2017).

Liang et al. (2017) developed a model for simulating backward erosion piping in random fields using a model formulation identical to that previously described for internal instability in Section 2.4.1. Both the erosion and deposition of particles was linearly proportional to the seepage velocity. The results obtained for an example problem of erosion in a random field are illustrated in Figure 2.55. While these results look quite realistic, one of the fundamental issues with this approach is illustrated in the results. That is, the results at t=25 hours demonstrate how erosion may occur in multiple places simultaneously. This is not how BEP progresses. Instead, BEP pipes progress sequentially from the outlet towards the upstream direction.

The issues noted with the previous models were overcome by the multiphase model developed by Rotunno et al. (2019). Rotunno et al. (2019) developed a finite element model as illustrated in Figure 2.56. In this model, the erosion at the pipe tip was modeled as a suffusion process with a changing element porosity given by

$$\frac{dn}{dt} = c_n(\tau_n - \tau_{nc}) \tag{2.48}$$

where c_n is an erosion coefficient, τ_n is a representative hydraulic shear stress exerted on the soil pores immediately upstream of the pipe tip, and τ_{nc} is the critical value at which erosion begins. The value of τ_n was calculated as

$$\tau_n = \frac{\gamma_w D_r}{4}|\nabla h| \quad \text{with} \quad D_r = 4\sqrt{\frac{2k_h\mu}{n}} \tag{2.49}$$

where D_r is a representative pore diameter calculated from the hydraulic conductivity, viscosity, and porosity at the pipe tip. In this manner, the soil at the pipe tip is gradually eroded and transferred to the erosion pipe. Once a critical porosity is reached, the pipe tip propagates further and all remaining soil mass is transferred to the pipe.

The erosion pipe was modeled as one dimensional, steady flow using the Darcy-Weisbach equation for a circular pipe. Secondary erosion was incorporated by varying the radius of the erosion pipe based on the wall shear stress as

$$\frac{dr}{dt} = \frac{c_t}{\rho_s}(\tau - \tau_c) \tag{2.50}$$

where c_t is the tangential erosion coefficient, ρ_s denotes the sediment density, τ is the hydraulic boundary shear stress applied on the wall of the pipe, and τ_c is the critical shear stress at which erosion initiates. As the pipe enlarges, the eroded sediment is transferred to the pipe through a source term.

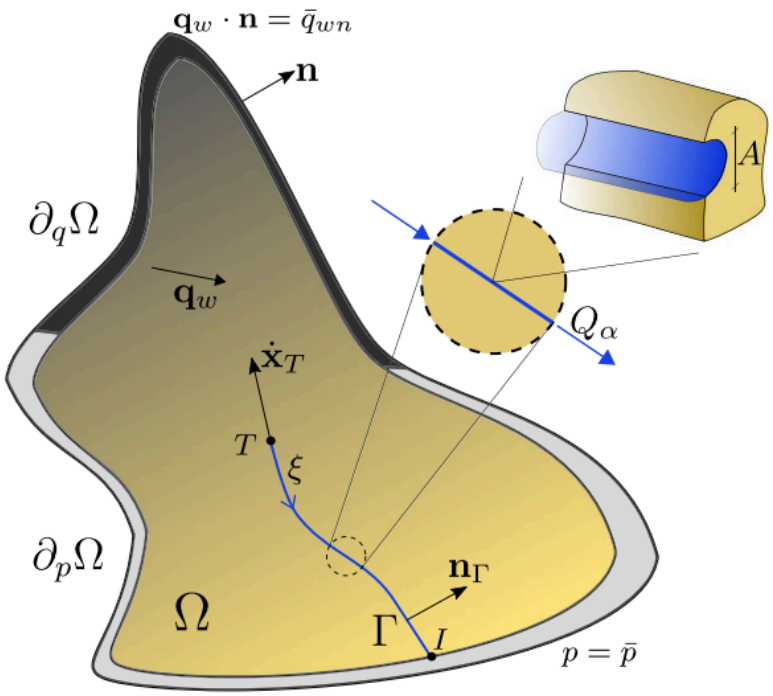

Figure 2.56. Illustration of finite element model developed by Rotunno et al. (2019).

Rotunno et al. (2019) calibrated their model to the full scale, IJkdijk field experiment (Knoeff et al., 2010) and 3 large scale laboratory experiments that were used to calibrate the Sellmeijer rule (Silvis, 1991). The results for the IJkdijk experiment are shown in Figure 2.57. Upon close inspection of the head profiles, it is observed that the head profile does not decrease at the pipe tip as one might expect (Figure 2.57b). This may be due to the tangential erosion assumptions of the erosion pipe. Nevertheless, the model was able to closely predict the measured outflow for the experiment. Similar results were obtained for the other three experiments, with the model able to closely predict the actual pipe progression and flow rate. However, the same issue was evident in the head profiles for the three other experiments as well.

While the Rotunno et al. (2019) model is a multiphase model, the information regarding the soil phases appears to only be used to adjust the hydraulic conductivity in front of the erosion pipe. The sediment transport and deposition along the erosion pipe was not

considered. Given the limited use of the phase information, it is unclear what benefit the multiphase model provides over the use of a Category 2 model. Nevertheless, the study by Rotunno et al. remains one of the most capable erosion models developed to date, primarily due to the incorporation of separate primary and secondary erosion criteria and the use of pipe flow equations to represent the erosion pipe.

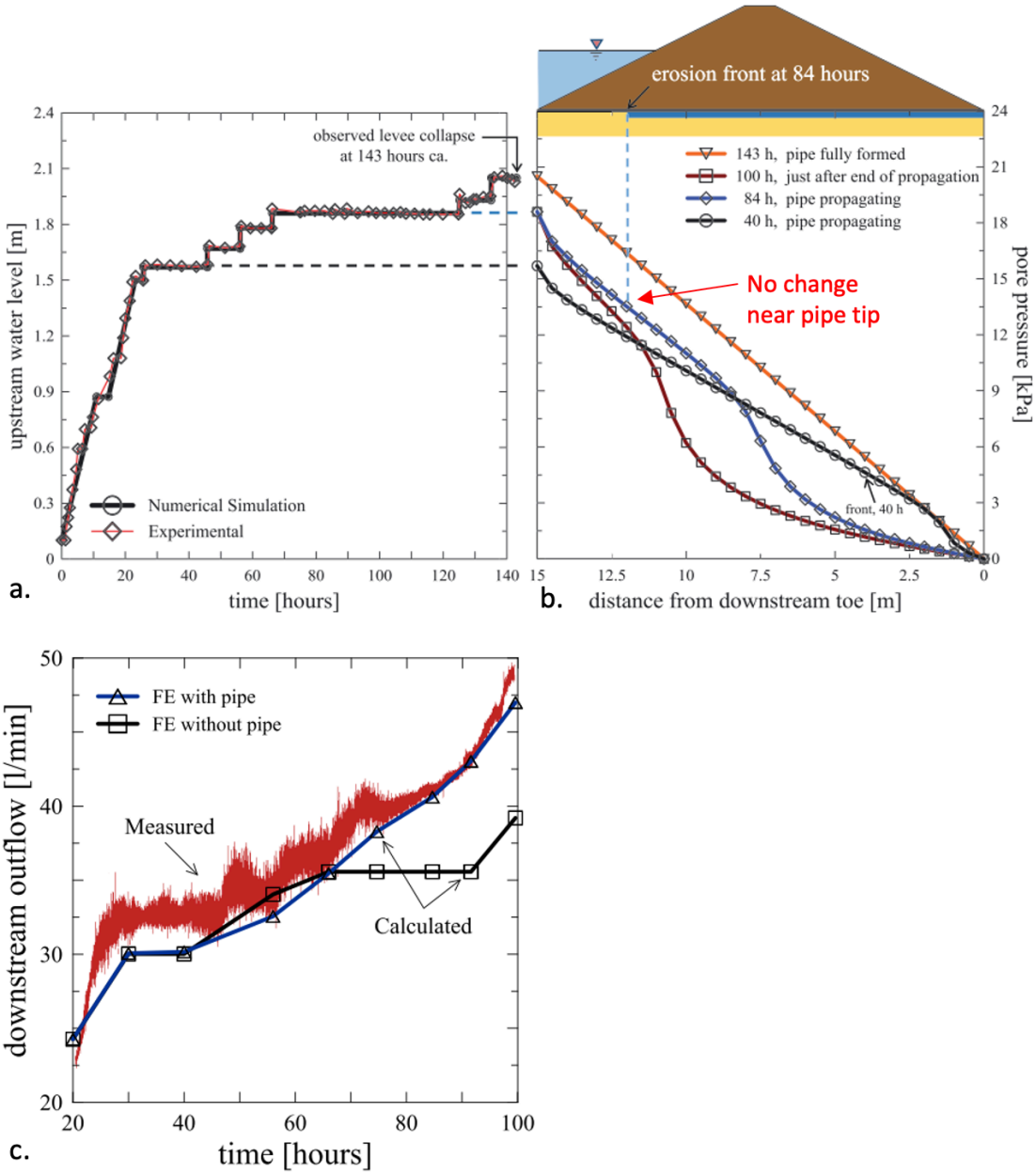

Figure 2.57. Illustration of the (a) upstream boundary, (b) modelled head profiles, and (c) modelled outflow for the IJkdijk field experiment (Rotunno et al. 2019).

2.4.2.4 Category 4 Studies

Category 4 models consist of coupled CFD-DEM models that attempt to resolve the erosion process at the particle scale. The discrete element method is used to model the particle interactions and stress distributions, while computational fluid dynamics is used to model the fluid flow. The fluid flow is most often modelled using a volume averaged approach that accounts for the interaction of the fluid and particles through empirical drag models (Knight et al., 2020), but can also be modelled at the pore scale using approaches such as the Lattice Boltzman Method that allow the fluid domain to quickly adjust to particle positions (Froiio et al., 2019).

As the most computationally intensive approach, it is very difficult to model full problem domains at any scale. Nevertheless, attempts to model BEP using this approach have been made by upscaling particle diameters in order to reduce the number of particles required in the model domain. El Shamy et al. (2008) attempted to model a field scale problem of BEP in this manner (Figure 2.58a). However, the upscaled particles were too large to allow an actual pipe to form, and the foundation simply fluidized at the downstream toe of the structure. Wang and Ni (2013) modelled a lab test that appeared to be a hybrid of BEP and II using upscaled particle diameters (Figure 2.58b). However, even at the lab scale the upscaled particle size hindered the process of pipe progression.

While the process is too computationally intensive to simulate full problem domains in a useful manner, valuable information regarding the erosion process has been obtained by using DEM models for simulating erosion over small subdomains (Figure 2.59). Lominé et al. (2013) simulated a concentrated leak through a cohesive soil sample using a coupled DEM-LBM model. While not BEP specific, this study is noteable as it is one of the earliest DEM-LBM studies on

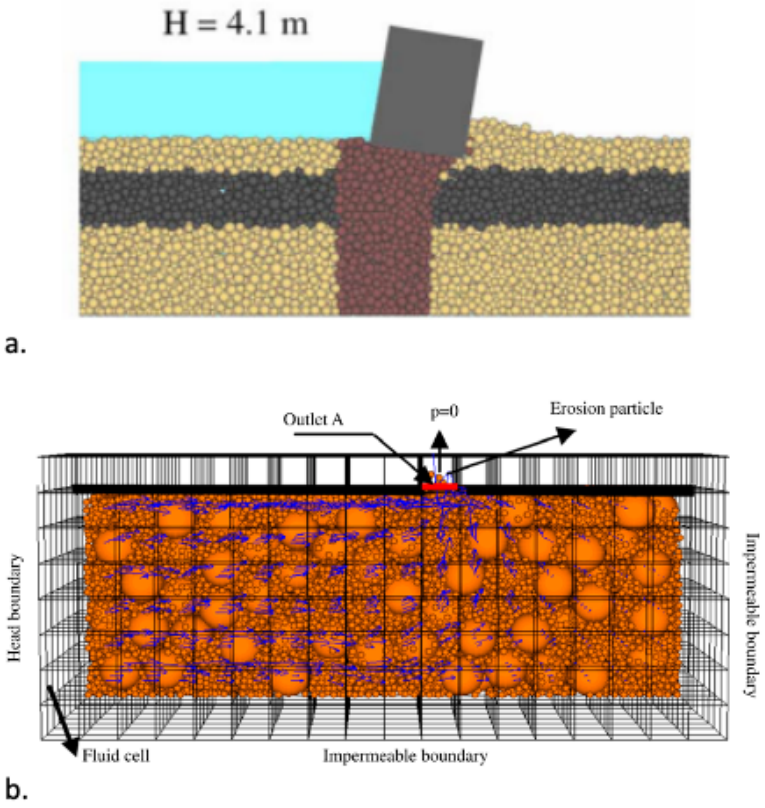

Figure 2.58. Examples of upscaled particle diamters for simulating BEP for (a) a field scale problem (El Shamy & Aydin, 2008) and (b) a laboratory scale problem (Wang & Ni, 2013).

soil erosion and is often mistaken for a study on BEP due to the terminology of "soil piping" that was used by the authors. The LBM approach developed also provided an efficient means of assessing pore scale fluid flow for BEP investigations.

Many other authors have also used DEM models to investigate erosion processes at the particle scale (Froiio et al., 2019; Tao, 2018; Tao & Tao, 2017; Tran et al., 2017). Others have simulated internal instability type erosion using DEM (e.g., Tao 2018), and a handful of studies have also assessed vertical fluidization of a soil column to test the CFD-DEM coupling (e.g., Tao and Tao 2017). Unfortunately, very few studies have actually simulated the BEP progression progress at the particle scale level. Only the studies by Froiio et al. (2019) and Tran et al. (2017) were identified as studies simulating BEP progression as illustrated in Figure 2.59b. As

illustrated by the force chains (red lines in Figure 2.59b) in front of the erosion pipe, these types of simulations can provide very useful information regarding the mechanics of pipe progression. Recently, multiscale models have been developed that attempt to use DEM simulations as illustrated in Figure 2.59b to inform constitutive model parameters in upscaled continuum models (Pirnia et al., 2020). This approach may offer significant utility in the future, but at present still suffers from the same issues as Category 2 and 3 models regarding the difficulty in measuring model parameters in the laboratory and validating the approach. Additionally, the computational time required to perform DEM-CFD simulations also limits the utility of this approach.

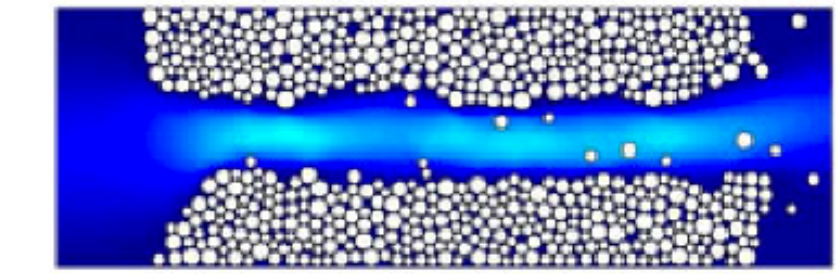

a.

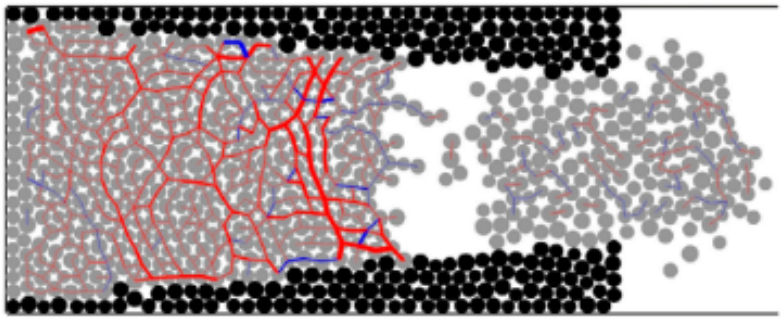

b.

Figure 2.59. DEM models used for fundamental investigations into (a) CLE erosion of cohesive soils (Lominé et al., 2013) and (b) BEP progression in sand (Tran et al., 2017).

2.4.3 Limitations of Prior Work

Although there has been a significant number of studies conducted on modeling of BEP, there are still no validated, widely accepted modelling approaches applicable to all scenarios encountered in engineering practice. The primary reasons for this are due to the following limitations of studies to date:

1. The primary erosion criterion for pipe progression has been poorly defined in studies to date. Some studies based progression at the pipe tip on the hydraulic gradient or velocity at the tip, whereas others have used the flow conditions in the erosion pipe. Further, while it has been demonstrated that the hydraulic gradient near the pipe tip is sensitive to mesh size (or calculation distance), no studies have developed means to account for this in the analysis.
2. Confusion regarding the physical process of BEP has resulted in very inconsistent model formulation. For example, confusion regarding the mechanisms of BEP and II has often resulted in porosity based II modeling concepts being used in models intended for BEP. As a result, some models have difficulty replicating the progressive downstream to upstream behavior of BEP or sharp concentration of flow near the pipe tip.
3. Rationale means for determining constitutive model parameters associated with primary and secondary erosion have not been rigorously described and validated. As such, studies have resorted to calibrating models to experiments in order to demonstrate model utility. This has greatly limited the usefulness of models to date as engineers have no means to reliably select model parameters. Overcoming this

limitation is an essential step towards achieving a validated, widely accepted predictive model for BEP.

To overcome these limitations, it is necessary to ensure future models are developed in a manner that is completely consistent with the physical processes of BEP observed in the laboratory. It is also essential that the criterion for primary erosion is formulated in a manner that is able to be measured in the laboratory and easily applied in numerical models. These principles will be considered as fundamental aspects of formulating a finite element model for simulation of BEP progression in the following Chapter.

CHAPTER 3

FINITE ELEMENT MODEL FORMULATION

Consider the scenario illustrated in Figure 3.1 of a BEP channel progressing backwards through a soil. The problem domain consists of a soil domain (Ω_s) and a pipe domain (Ω_p) as described in Chapter 2. For this study, a steady-state model is developed that searches for the maximum extent of pipe progression under imposed boundary conditions. A steady state model was pursued for the following reasons:

1. BEP laboratory tests are most often conducted in a steady state manner in which a set of boundary conditions is imposed until the erosion comes to equilibrium. A steady state model is therefore suitable for comparison to available laboratory data.
2. Steady state analysis of BEP is more conservative than transient analysis because the time required for pore pressure development, erosion, and sediment transport are neglected. Given the uncertainties associated with predicting BEP that exist today, it is prudent to start with steady state models in engineering practice to ensure assessments are conservatively biased.
3. Modeling transient behavior requires defining additional constitutive relations for defining the temporal evolution of erosion. Since the experiments available for comparison are conducted in a piecewise, steady state manner, the additional temporal aspects of the model are an unnecessary complication that will make it more difficult to rigorously assess the suitability of model assumptions under steady state conditions.

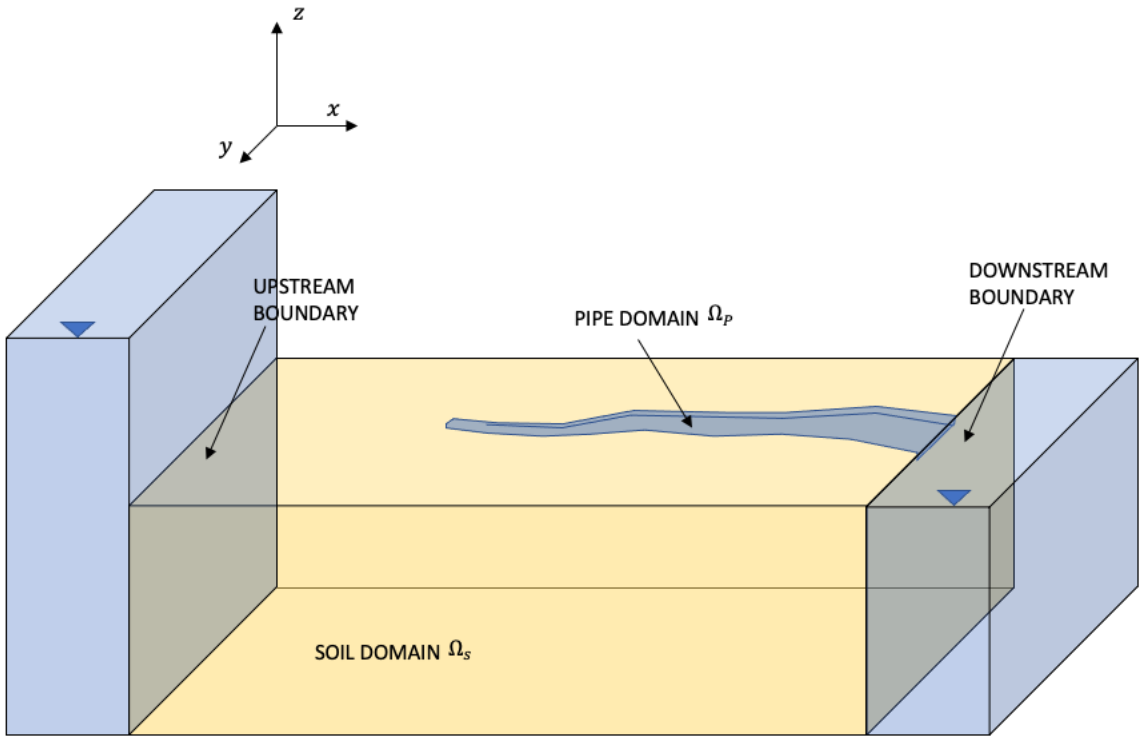

Figure 3.1. Illustration of a BEP pipe progressing through a soil domain.

In the sections that follow, the development of a finite element model for steady state analysis of BEP is described. The governing equations for steady state flow and erosion are first described, followed by a description of the finite element discretization. The algorithm for simulating BEP progression is then outlined before describing the model implementation in both two- and three-dimensions.

3.1 Governing equations

3.1.1 Groundwater flow

The groundwater flow in the soil domain was previously described for the general case by Richards' Equation (Equation 2.24). Under steady state conditions, $\partial h/\partial t = 0$, and Equation 2.24 becomes

$$\frac{\partial}{\partial x}\left(k_x \frac{\partial h}{\partial x}\right)+\frac{\partial}{\partial y}\left(k_y \frac{\partial h}{\partial y}\right)+\frac{\partial}{\partial z}\left(k_z \frac{\partial h}{\partial z}\right)=0 \quad (3.1)$$

where k_x, k_y, and k_z represent the hydraulic conductivities in the x, y, and z directions, respectively, and $h = z + p/\gamma_w$ denotes the total head (potential) in terms of the elevation head z and the pressure head given in terms of the pore pressure p and unit weight of water γ_w. For situations with isotropic hydraulic conductivity, Equation 3.1 becomes the Laplace equation.

3.1.2 Pipe Flow

The flow in the erosion pipe is assumed to be steady-state, one directional flow through a rectangular pipe as illustrated in Figure 3.2. The erosion pipes that form are typically very shallow in depth (order of 1-10 sand grains according to Van Beek, 2015 and Vandenboer, 2019) and have pipe widths that are on the order of 10-50 times the pipe depth (Van Beek, 2015, Robbins et al., 2018a, Vandenboer, 2019). As such, a rectangular pipe section was chosen as it closely approximates the shallow and wide cross sections of BEP pipes.

As noted in Chapter 2, the Navier Stokes equations provide the most accurate description of the flow in the erosion pipe. However, under the assumption of steady-state, one directional flow, the pipe flow can also be accurately described using the Darcy-Weisbach equation. Under these assumptions, it has been shown that both the Navier Stokes equation and Darcy-Weisbach equation can be simplified down to a form of Equation 3.1 such that the pipe flow can be described by an equivalent, or fictitious, hydraulic conductivity value applied to the pipe domain (Ω_p). This simplified, equivalent permeability approach has been used by many authors to model BEP (Sellmeijer, 1988; Bersan et al. 2013; Aguilar et al., 2016) and is a familiar concept in groundwater modeling as it once formed the theoretical basis for using viscous flow models to analyze groundwater flow (Harr, 1962). The derivation of the equivalent pipe hydraulic

conductivity from the Darcy-Weisbach equation is presented as a basis for introducing variations for both laminar and turbulent flow conditions.

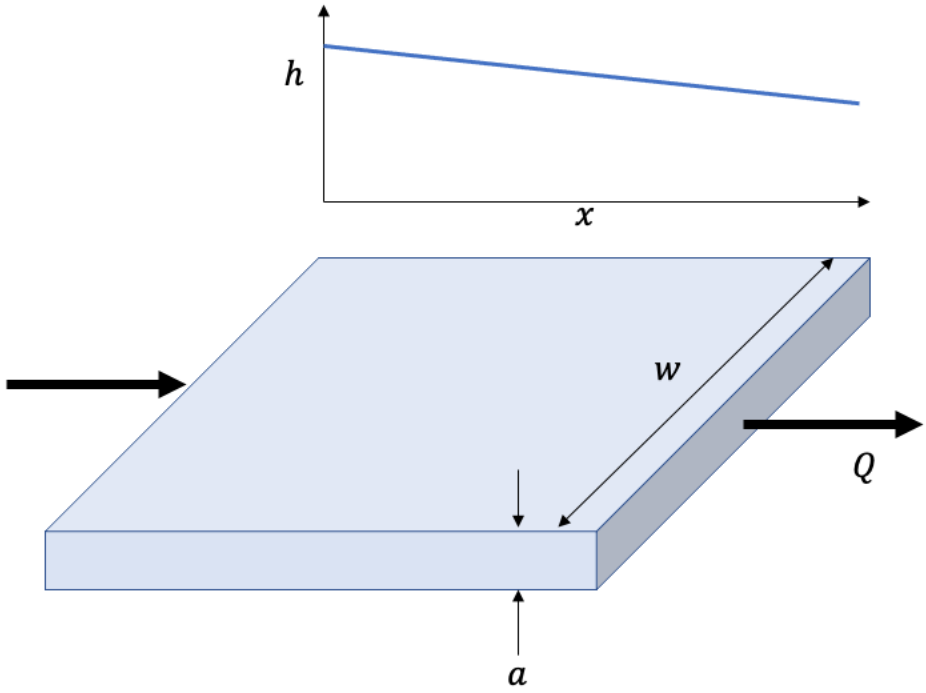

Figure 3.2. Illustration of one-dimensional flow through rectangular pipe.

For steady state, one dimensional pipe flow, the flow in the pipe is described by the Darcy-Weisbach equation, which can be expressed differentially as (e.g., Aguilar-López et al., 2016)

$$\frac{\partial h}{\partial x} = \frac{V^2}{2g}\frac{f}{D_h} \tag{3.2}$$

where dh/dx is the hydraulic gradient along the pipe, g is the gravitational acceleration, f is the Darcy-Weisbach friction factor, $D_h = 4A/P$ is the hydraulic diameter for a pipe with area A and perimeter P, and $V = Q/A$ is the average velocity. For rectangular pipe cross sections of width w and depth a, the hydraulic diameter is

$$D_h = \frac{4wa}{2(w+a)} \tag{3.3}$$

Considering the case of $w \gg a$, D_h can be approximated by D_h^* where

$$D_h^* = 2a \tag{3.4}$$

Substituting Equation 3.4 into Equation 3.2 yields the following governing equation for the pipe flow

$$\frac{dh}{dx} = \frac{f}{2a^2}\frac{V^2}{2g} \tag{3.5}$$

Under laminar flow conditions with the assumption that $w \gg a$, the friction factor is given by (e.g., Bersan et al. 2013, Van Beek (2015), Aguilar et al. 2016)

$$f = \frac{96}{Re} = \frac{96\mu}{\rho V D_h} \tag{3.6}$$

where $Re = \frac{\rho V D_h}{\mu}$ is the dimensionless pipe Reynolds number given as a function of the fluid density ρ, mean flow velocity V, hydraulic diameter D_h, and dynamic fluid viscosity μ. By substituting the laminar friction factor (Equation 3.6) into the pipe flow equation (Equation 3.5) and rearranging, the pipe flow equation takes the form of Darcy's equation

$$V = \frac{a^2 \rho g}{12\mu}\frac{dh}{dx} = k_{pl}\frac{dh}{dx} \tag{3.7}$$

where

$$k_{pL} = \frac{a^2 \rho g}{12\mu} \tag{3.8}$$

is the equivalent hydraulic conductivity for laminar pipe flow in a pipe of depth a. This relationship was also previously derived for BEP pipe flow through simplification of Navier Stokes equations by Sellmeijer (1988). For laminar flow conditions, the pipe flow can thus be described by Equation 3.1 with $k_x = k_y = k_z = k_{pL}$ over the domain Ω_p.

For turbulent flow conditions ($Re > 2500$), Equations 3.6 to 3.8 no longer hold true. In the case of turbulent flow, an analytical relation for f does not exist and the head loss must be expressed as a function of f. Equation 3.6 can still be rearranged to match the form of Darcy's law

$$V = 2a\sqrt{\frac{g}{f}\left(\frac{dh}{dx}\right)^{-1}}\left(\frac{dh}{dx}\right) = k_{pT}\left(\frac{dh}{dx}\right) \tag{3.9}$$

where

$$k_{pT} = 2a\sqrt{\frac{g}{f}\left(\frac{dh}{dx}\right)^{-1}} \tag{3.10}$$

is the equivalent hydraulic conductivity for turbulent flow in a pipe of depth a. The friction factor f must be determined using the empirically derived Moody diagram (Figure 3.3) or similar relations (Cengal and Cimbala, 2006). The Moody diagram describes the friction factor as a function of the pipe Reynolds number, Re, and the roughness of the pipe wall expressed in terms of the relative pipe roughness (ϵ/D_h) where ϵ is the average protusion height on the pipe wall. From Figure 3.3, it is easily seen that turbulent friction factors are higher than laminar friction factors due to the additional resistance caused by the variable flow. Additionally, the friction factor decreases with increasing turbulence until it becomes a constant value once flow has become fully turbulent.

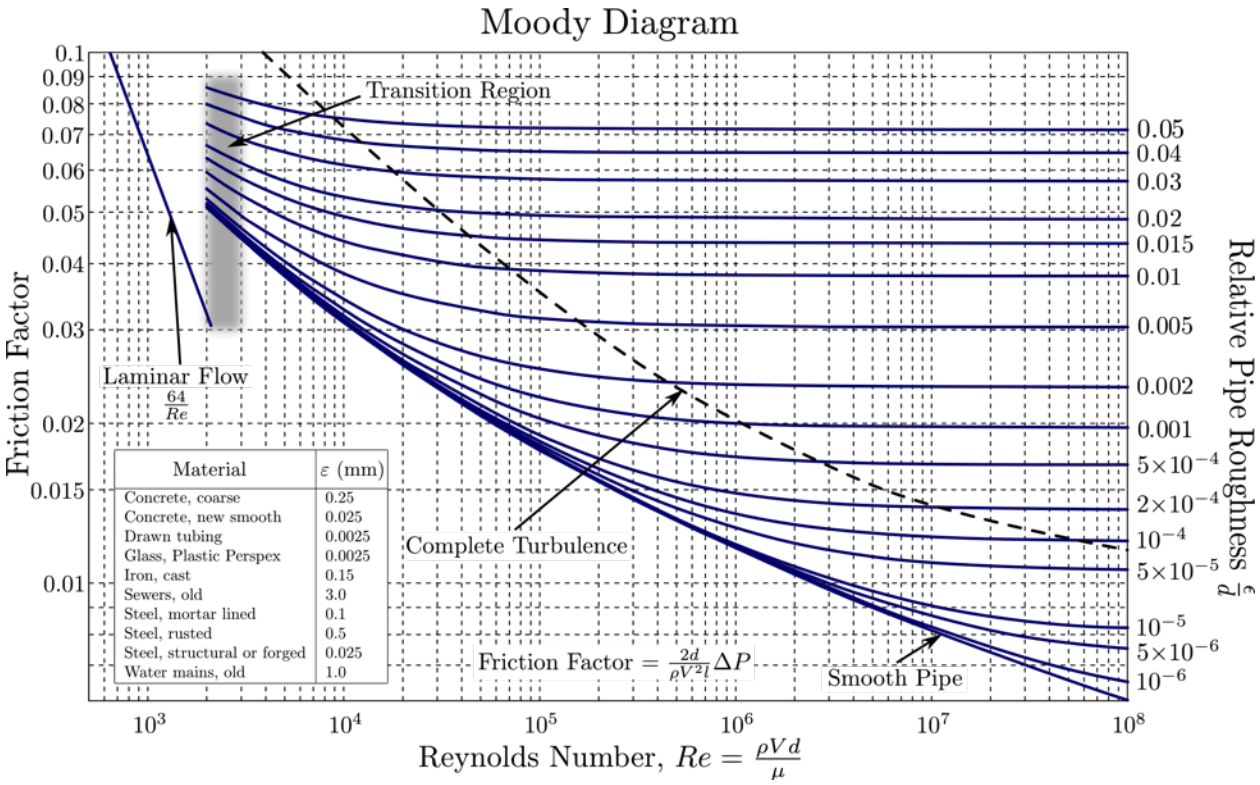

Figure 3.3. Moody diagram for determining Darcy-Weisbach friction factor. Original diagram by: S Beck and R Collins, University of Sheffield. CC BY-SA 4.0.

For this work, an explicit relationship proposed by Romeo et al. (2002) was used to describe f across the full range of Reynolds numbers as follows

$$\frac{1}{\sqrt{f}} = -2\log\left(\frac{\frac{\in}{D_h}}{3.7065} - \frac{5.0272}{Re}\log\left(\frac{\frac{\in}{D_h}}{3.827} - \frac{4.567}{Re}\log\left[\left(\frac{\frac{\in}{D_h}}{7.7918}\right)^{0.9924} + \left(\frac{5.3326}{208.815+Re}\right)^{0.9345}\right]\right)\right) \tag{3.11}$$

where ϵ denotes the pipe wall roughness. Additionally, a relationship proposed by Nikuradse (1950) for the fully turbulent friction factor was also used to have a simpler relationship for fully

turbulent flow in case of convergence issues with Equation 3.11. The Nikuradse friction factor for fully turbulent flow is given by

$$\frac{1}{\sqrt{f}} = 1.75 - 2\log_{10}\left(\frac{2\epsilon}{D_h}\right) \tag{3.12}$$

While Equation 3.12 is much simpler than Equation 3.11, it will underpredict the friction factor for laminar and transition Reynolds numbers.

For this study, it was assumed that $\epsilon = d_{50}/2$. As the Reynolds number Re, and in turn the friction factor f, depend on the velocity, V, k_{pT} cannot explicitly be solved for. Instead, the turbulent pipe flow is solved iteratively by solving Equation 3.1, but with $k_x = k_y = k_z = k_{pT}$ in the pipe domain, until convergence on f is obtained. In this manner, the turbulent pipe flow equations for a pipe with depth a are satisfied.

3.1.3 Primary Erosion

The progression of the erosion pipe is controlled by the local seepage forces near the pipe tip as suggested by numerous researchers (Hanses, 1985; Schmertmann, 2000; Van Beek, 2015). The seepage forces have been represented in numerical models using the hydraulic gradient (e.g., Ding et al., 2007; Fascetti & Oskay, 2019; Rahimi & Shafieezadeh, 2020; Robbins, 2016), seepage velocity (Fujisawa et al., 2016), and hydraulic shear stress at the pore level (Rotunno et al., 2019). There is presently no evidence that suggests one approach works better at predicting BEP progression than another. Additionally, in the numerical implementations of the various approaches, the seepage velocity and hydraulic shear stress in the pores are derived from the hydraulic gradient computed in the solution. Therefore, to keep it as fundamental as possible, this study uses the hydraulic gradient upstream of the pipe as the criterion for pipe progression.

Having decided to use the hydraulic gradient as the criterion for pipe progression, the question then becomes what hydraulic gradient should be used? The hydraulic gradient can be estimated at a point in the solution or computed as an average value over various distances. This is an issue that has been given very little attention to date in the literature, and, as will be demonstrated in later chapters of this thesis, may be a primary reason as to why it has been difficult to develop validated modelling approaches for BEP. The remainder of this section develops a new approach for quantifying the primary erosion criterion.

Consider the results of the discrete element simulation of a BEP pipe progressing through a domain that was illustrated in Figure 2.59b. The lines drawn across the particles are referred to as force chains and represent both the magnitude (line thickness) and orientation (line direction) of the contact forces between the particles. From the force chains in the figure, one can clearly see arches that form through the particles upstream of the pipe tip to transfer the seepage forces from the upstream particles to the remaining particle matrix. Ultimately, it is the failure of these force chains that drives pipe progression. Ideally, the seepage forces would be quantified across this force chain zone and compared to the forces required to fail the soil structure. The average seepage force per unit volume of soil can be calculated as (Terzaghi, 1943)

$$F_s = \rho g \nabla h = \rho g i \tag{3.13}$$

where $i = |\nabla h|$ is the notation for the magnitude of the hydraulic gradient as commonly used in geotechnical engineering. If the distance of the grain group size over which the arches form is known, the seepage forces over this zone can be calculated using Equation 3.13. Unfortunately, the dimensions of the zone near the pipe tip controlling pipe progression are not currently well established. Further, this distance is likely a function of the soil gradation and particle angularity.

Therefore, determining a consistent approach for calculating the size of the controlling zone is impractical, and a more generalized approach is developed.

Consider the head profile immediately upstream of an erosion pipe as illustrated in Figure 3.4. The head profile is expressed relative to the head at the pipe tip (h_{tip}) such that the value of the head profile is zero at the pipe tip and increasing with distance upstream from the pipe tip. As the average hydraulic gradient is proportional to the seepage forces acting on the soil between two points, the head profile will be quantified in terms of average gradients over specified distances.

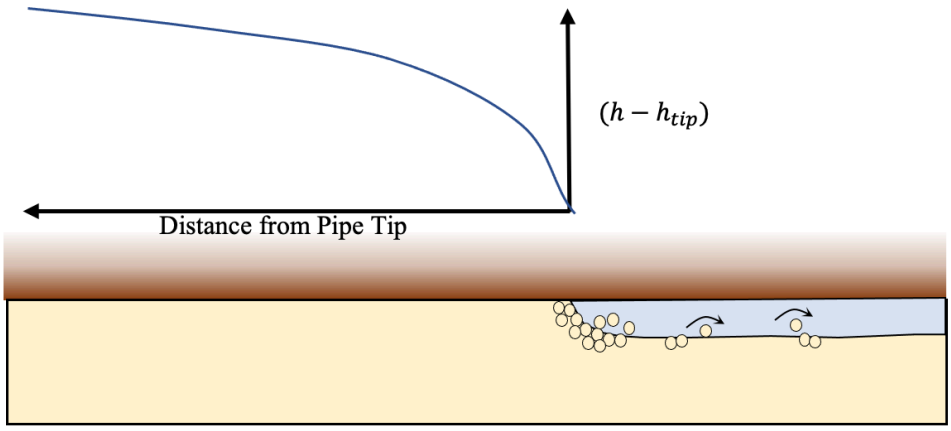

Figure 3.4. Head profile upstream of an erosion pipe.

The average hydraulic gradient between the pipe tip and any point along the profile is represented by a straight line as illustrated in Figure 3.5 for three select points. Because the line is a secant of the head profile, the hydraulic gradient will be called the secant hydraulic gradient, denoted as i_s. This distinction is important as it clearly communicates that the hydraulic gradient being considered is an average value over an associated distance. This terminology was originally proposed by Schmertmann (1981, unpublished notes) and Townsend et al. (1981) as

part of the development of Schmertmann's quantitative piping theory. If the head profile is the last stable head profile before pipe progression, it will be denoted as the critical head profile. The secant gradients associated with the critical head profile will be called the critical secant gradients, denoted by i_{cs}. The function

$$i_{cs} = f(x) \tag{3.14}$$

where x is the distance in front of the pipe tip is denoted as the critical, secant gradient function (CSGF). This function is illustrated in Figure 3.5. By quantifying i_{cs} at every point in front of the pipe, the CSGF captures a snapshot of the entire seepage field near the pipe tip. It is therefore not necessary to select a single hydraulic gradient or distance to use as a critical value as the full seepage field has been embodied in the function. All points on the CSGF are proportional to each other, and exceeding the value of i_{cs} at any one point indicates it has also been exceeded at all other locations. Because of this, the lack of knowledge regarding the controlling grain group size for progression becomes irrelevant. The secant gradient in front of the pipe can be checked at any location and compared to the CSGF to determine if the critical value has been exceeded.

The general form of the primary erosion criterion (Equation 2.32) described the velocity of the erosion pipe as a function of the pressure near the pipe tip. For steady state conditions, the pipe must be in equilibrium and the pipe velocity is zero. As the pipe will advance further if the CSGF is exceeded, the CSGF can be used as the criterion for pipe progression. The prediction of BEP progression thus becomes a matter of determining the CSGF $f(x)$.

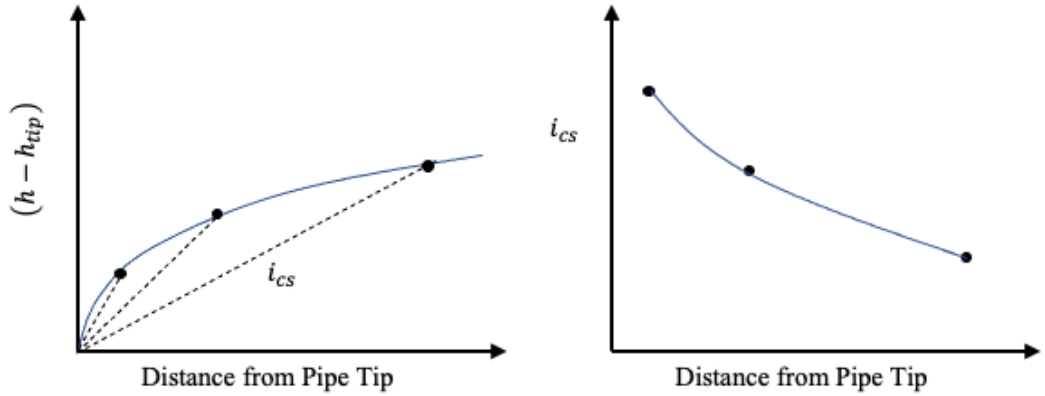

Figure 3.5. Illustration of secant gradient and corresponding critical, secant gradient function (CSGF) from head profile.

Without any knowledge of the functional form of $i_{cs}(x)$, the function can be determined empirically by simply measuring it in the laboratory with a dense array of pore pressure transducers. While this approach will be demonstrated in later chapters, it is highly desirable to have an analytical function for $i_{cs}(x)$ to minimize the measurements required for defining the CSGF. The functional form of $i_{cs}(x)$ can be determined by considering the conformal mapping solution of the seepage flow near the pipe tip developed by Xiao et al. (2020) and briefly discussed in Chapter 2. Consider once again the illustration of the domain near the pipe tip drawn on the z-plane as illustrated in Figure 3.6. This corresponds to the scenario described by Xiao et al. with $b_t = 0$.

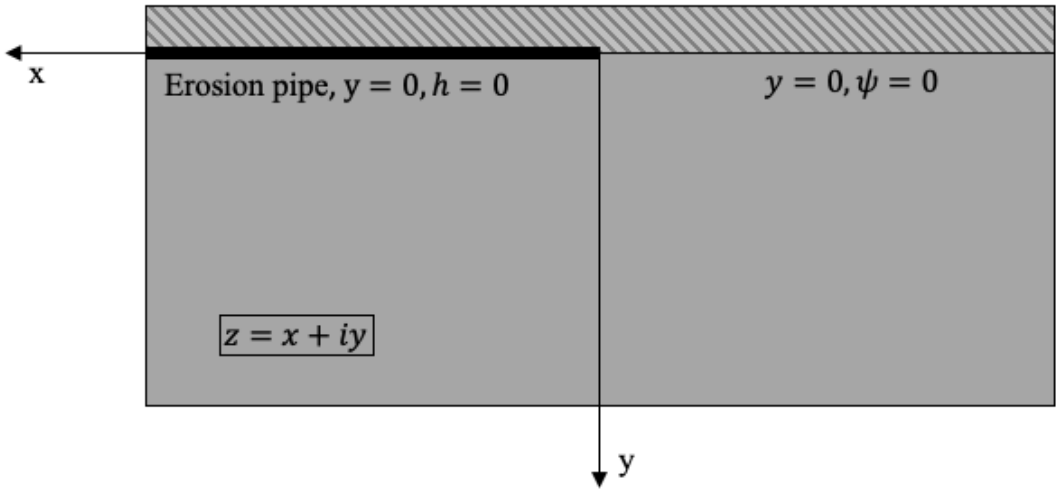

Figure 3.6. Domain near the pipe tip drawn in the z-plane for conformal mapping solution.

For this case, Equations 2.3 and 2.4 become

$$\omega = iT\sqrt{z} \tag{3.15}$$

$$T = \frac{k_h h_o}{Im(\sqrt{x_0 + iy_0})} \tag{3.16}$$

Rearranging Equation 3.15 yields

$$z = -\left(\frac{\omega}{T}\right)^2 \tag{3.17}$$

Substituting in the definitions of z and ω results in

$$x + iy = -\left(\frac{\phi + i\psi}{T}\right)^2 \tag{3.18}$$

Expanding Equation 3.18 leads to the expression

$$-x - iy = \left(\frac{1}{T}\right)^2 (\phi^2 + 2\phi\psi i - \psi^2) \tag{3.19}$$

As the CSGF $i_{cs} = f(x)$ only needs to estimate the value of i_{cs} in front of the erosion pipe, it is not necessary to carry the full solution forward. Instead, we can restrict Equation 3.19 to be only along the line in front of the erosion pipe at $y = 0$ and $x < 0$. With reference to Figure 3.6, it is

recognized that the pipe domain is modelled as a constant head of $h = 0$ at $y = 0$ for $x > 0$. Additionally, for $x < 0$, $\psi = 0$ at $y = 0$. Substitution of these values into Equation 3.19 yields the following expression

$$\phi = T\sqrt{-x} \tag{3.20}$$

where $\phi = k_h h$ is the seepage potential, k_h denotes the hydraulic conductivity, and h denotes the hydraulic head. The value of T is a constant (Equation 3.16) that is based on the hydraulic head, h_o, at a point (x_0, y_o) in front of the erosion pipe. Recognizing that $y_o = 0$ along the line $y = 0$ and $x < 0$, Equation 3.16 becomes,

$$T = \frac{k_h h_o}{\sqrt{|x_o|}} \tag{3.21}$$

Substitution of 3.21 into Equation 3.20 yields the following expression for the seepage potential in front of the erosion pipe

$$\phi = \frac{k_h h_o}{\sqrt{x_o}}\sqrt{x} \tag{3.22}$$

where x and x_o are now defined as the positive distance in front of the erosion pipe. The head profile in front of the erosion pipe is obtained by dividing by k_h yielding

$$h(x) = \frac{h_o}{\sqrt{x_o}}\sqrt{x} \tag{3.23}$$

From 3.23, the CSGF is defined as

$$i_{cs}(x) = \frac{h(x) - h(0)}{x} = \frac{\frac{h_o}{\sqrt{x_o}}\sqrt{x} - 0}{x} = \frac{h_o}{\sqrt{x_o}\sqrt{x}} \tag{3.24}$$

Finally, recognizing that $h_o/\sqrt{x_o}$ is a constant, the CSGF can be defined as

$$i_{cs}(x) = f(x) = Cx^{-0.5} \tag{3.25}$$

where

$$C = \frac{h_o}{\sqrt{x_o}} \tag{3.26}$$

Thus, the CSGF is defined in terms of a known head at a single point in front of the erosion pipe. It should also be noted that the analytical solution used to derive Equations 3.25 and 3.26 is based on a two-dimensional analysis. While it is possible that the shape of the function will not adequately describe the true three-dimensional CSGF, Xiao et al. (2020) found that the analytical solution adequately captured the head profile in front of a pipe progressing through a rectangular, three-dimensional soil sample. As Equation 3.25 is derived directly from the head profile, this implies that Equation 3.25 and 3.26 would provide a suitable fit to their experiments as well. This will be checked further through comparisons with new laboratory measurements in subsequent sections.

The CSGF is therefore defined in terms of a known head at a single point in front of the erosion pipe. Using Equation 3.25 as the critical secant gradient function, BEP will progress further if

$$i_s(x) > i_{cs}(x) \tag{3.27}$$

If the condition expressed by Equation 3.27 is not met, the pipe will not progress further and an equilibrium state is achieved under the given boundary conditions. Equation 3.27 is thus the primary erosion criterion that will be used to search for equilibrium conditions for the steady state model of BEP progression.

3.1.4 Secondary Erosion

The erosion along the pipe walls, termed secondary erosion, controls both the deepening and widening of the erosion pipe. As reviewed in Chapter 2, the erosion pipes tend to have a fairly constant width to depth ratio along the pipe profile. As such, the pipe width can be determined from the pipe depth, and only the depth of the erosion pipe must be determined as part of the FE solution.

The depth of the erosion pipe that forms is controlled by the hydraulic shear stress on the bottom of the erosion pipe. For flow in rectangular channels with $w \gg a$, the hydraulic shear stress on the top and bottom of the pipe is given by

$$\tau = \frac{a\gamma_w}{2}\nabla h \tag{3.28}$$

where ∇h is the gradient of h. The erosion pipe will deepen until the condition

$$\tau < \tau_c \tag{3.29}$$

is met. Therefore, the erosion pipe is initiated to a depth of $a = g_m d_{50}$ where g_m is a user-defined grain size multiplier that specifies the initial pipe height in terms of d_{50}. The pipe is iteratively deepened until Equation 3.29 is satisfied and the equilibrium depth of the erosion pipe is found.

Once the depth of the pipe has been determined, the width of the erosion pipe can also be determined as

$$w = Ra \tag{3.30}$$

where $R = w/a$ is a user defined pipe width-to-depth ratio. A constant value of this ratio is assigned for the entire pipe domain.

As the secondary erosion is controlled by the value of τ_c, it is important to accurately select values of τ_c. As noted in Chapter 2, the Shields diagram is perhaps the most

common means of determining τ_c for cohesionless soils. This diagram has been further developed with additional data by many authors (Yalin & Karahan, 1979), and both implicit and explicit relationships have been fit to the Shields diagram yielding predictive equations for determining critical shear stress (Brownlie et al. , 1981; Cao et al., 2006; Mantz, 1977; Romeo et al., 2002). Unfortunately, these equations are in terms of Ψ_c and Re^*, which often causes significant confusion for geotechnical engineers. Various explicit relations were also described in Chapter 2, summarized for convenience in Table 3.1. The performance of these equations was evaluated by comparing the predicted values of critical shear stress to measured values of critical shear stress obtained from the literature for particles in laminar flow (Figure 3.7). This data set was compiled as part of van Beek (2015) and expanded in van Beek et al. (2019).

Table 3.1. Explicit equations for critical shear stress.

Shear Stress Equation	**Eq. No.**	**Reference**
$\tau_c = \eta \frac{\pi}{6} \gamma_p' d \cdot \tan\theta$ where $\eta = 0.25$ and $\theta = 37°$	2.8	White (1940), Sellmeijer (1988,2011), van Beek (2015)
Eq. 2-8 with $\theta = -8.125 \ln(d) - 38.77$ where d is in meters.	2.9	Van Beek (2015)
$\tau_c(Pa) = d_{50}(mm)$	2.10	Briaud (2017)
$\tau_c(Pa) = d_{50}(mm)^{0.8}$	2.11	Current Study

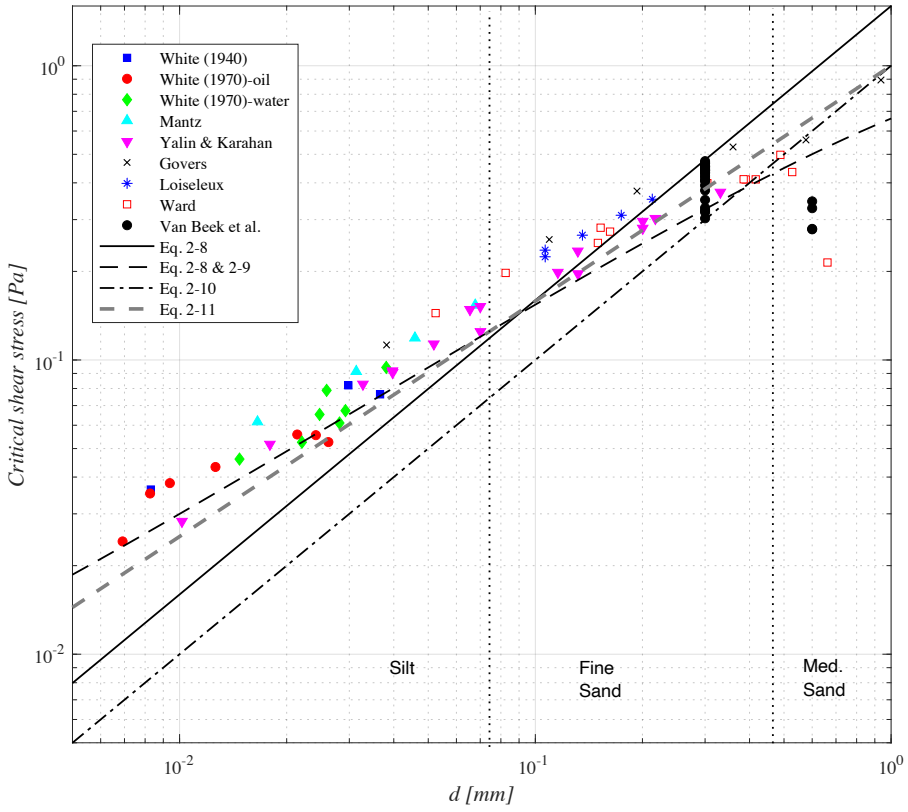

Figure 3.7. Comparison of critical shear stress equations to measurements of critical shear stress in laminar flow.

From inspection of Figure 3.7, it is observed that Equation 2.8 as used by Sellmeijer (1988, 2006, 2011) matches the experimental data well for fine sands with particle diameters of 0.1 mm to 0.3 mm, which corresponds to the particle size range Sellmeijer studied. Above this particle range, Equation 2.8 overpredicts the critical shear stress. For particle diameters smaller than 0.1mm, Equation 2.8 underpredicts the critical shear stress.

With the exception of a few data points, Equation 2.9 used in conjunction with Equation 2.8 provides a very reasonable lower bound for the critical shear stress across the full range of particle diameters included in the data set. Of all of the methods examined, this method

appears to be the most accurate. Equation 2.10 on the other hand underpredicts the critical shear stress for all particle diameters less than 0.2 mm. As fine sand is often the material of most concern with regards to BEP, Equation 2.10 will provide a conservative estimate of the critical shear stress. For medium sands, Equation 2.10 may be slightly unconservative as it appears it may overpredict the critical shear stress.

As the simplicity of Equation 2.10 is highly desirable, the author attempted to adjust Equation 2.10 to better fit the data across the full range of particle diameters. The adjusted predictive equation is given as Equation 2.11 and was developed for this study. This adjusted equation is also compared to the experimental data in Figure 3.7. As shown, Equation 2.11 provides a lower bound of the experimental measurements up to a particle diameter of 0.2 mm. For particle diameters of 0.2 mm to 0.5 mm , Equation 2.11 appears to provide the best estimate of the critical shear stress. Beyond a diameter of 0.5 mm, Equation 2.11 has the same issue as Equation 2.10 regarding possible over prediction of the critical shear stress.

While all of the predictive equations are fairly close to the experimental data, it is recommended that either Equation 2.9 or Equation 2.11 be used to predict the critical shear stress of a sand when a simple relationship is desired with only grain size as an independent variable. Either of these equations appear to accurately describe the critical shear stress for fine sand in laminar flow conditions.

3.2 Finite element approximation

Using the Galerkin weighted residual method, the finite element discretization of Equation 3.1 is (e.g. Smith and Griffiths 2004)

$$[K_e]\{H\} = \{Q\} \tag{3.31}$$

where $[K_e]$ is the hydraulic conductivity matrix, $\{H\}$ is the piezometric head at the element nodes, and $\{Q\}$ represent the net inflow or outflow at the nodes. The hydraulic head, h, is approximated across the domain as

$$h \cong \hat{h} = \{N\}\{H\} \tag{3.32}$$

where $\{N\}$ denotes the element shape functions. The global hydraulic conductivity matrix across the entire domain Ω is given by

$$[K_e] = \int_{\Omega_s} [T]^T [k_s][T] d\Omega_s + \int_{\Omega_p} [T]^T \left[k_p\right][T] d\Omega_p \tag{3.33}$$

where Ω_s is the soil domain, Ω_p is the pipe domain, and the matrices $[k_s]$, $[k_p]$, and $[T]$ are defined by Equations 3.34 through 3.36.

$$[k_s] = k_{ij} \tag{3.34}$$

$$\left[k_p\right] = \delta_{ij} k_p \tag{3.35}$$

$$[T] = \nabla \mathrm{N_i} \tag{3.36}$$

In these equations, $i = 1, \ldots, n$ and $j = 1, \ldots, n$ where n denotes the number of dimensions, k_{ij} is the hydraulic conductivity tensor of the soil, δ_{ij} is the Kronecker delta function, k_p is the equivalent hydraulic conductivity of the pipe, and N_i are the element shape functions used in the approximate solution. The solution of Equation 3.31 yields the value of the hydraulic head at the FEM nodes. The hydraulic gradient can then be calculated from the approximate solution as

$$\nabla h \cong \nabla \hat{h} = \nabla N_i H_i \tag{3.37}$$

The finite element solution obtained from Equations 3.31 through 3.37 describes the coupled ground water flow and pipe flow solution for an erosion pipe of known extent and depth. However, the extent and depth of the erosion pipe is not known *a priori* and must be determined through an iterative solution procedure. The algorithm for this iterative procedure

will be described in the sections that follow after first discussing choices for discretizing the problem domain in both two- and three-dimensional domains.

3.3 Domain discretization

The problem of a BEP pipe progressing in Figure 3.1 can be assessed using various approaches for discretizing the erosion pipe in both two-and three dimensional domains as illustrated in Figure 3.8. While the problem is highly three-dimensional in nature, the majority of studies reviewed in Chapter 2 were formulated in two dimensions. Unfortunately, a rigorous comparison of two- and three-dimensional solutions for BEP models has not been performed, and the degree of error in two-dimensional solutions is uncertain. For this reason, approaches for discretizing the problem in both two-and three dimensional domains are developed. This section assumes laminar pipe flow (Equation 3.8) for convenience, but applies equally to turbulent pipe flow (Equation 3.10).

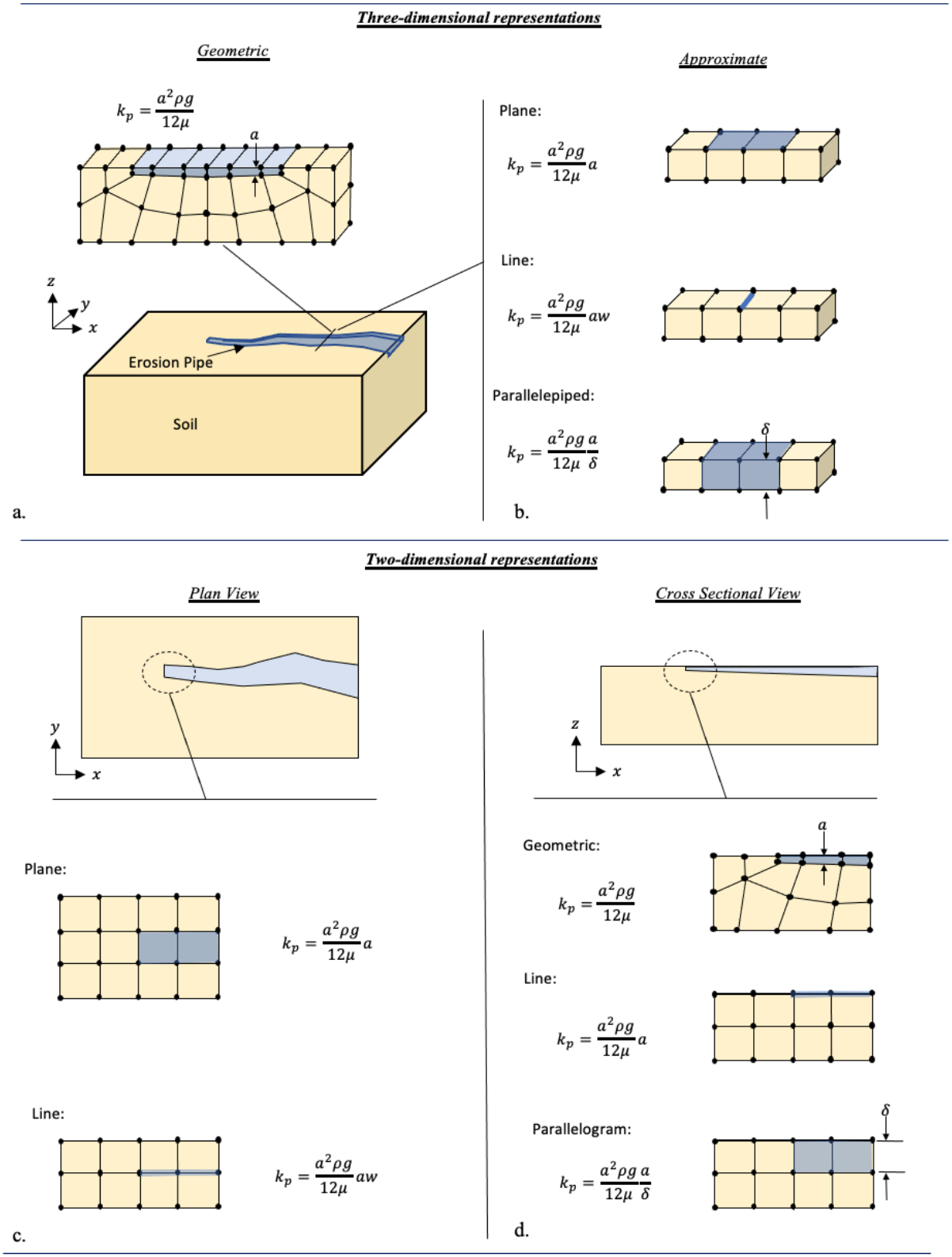

Figure 3.8. Illustration of finite element discretizations of the BEP process in three-dimensional (a-b) and two-dimensional (c-d) domains.

3.3.1 Three-dimensional models

Three dimensional approaches to discretizing the BEP problem can be separated into geometric representations (Figure 3.8a) and approximate representations (Figure 3.8b). Geometric approximations are those in which a geometrically accurate pipe domain is discretized using volumetric elements as illustrated in Figure 3.8a. When using this approach, the value of k_p computed using Equation 3.8 and 3.10 can be applied directly to the pipe elements as the full pipe geometry is accurately represented by the pipe domain in the model. Section 2.4 reviewed the work of Bersan et al. (2013) that demonstrated this approach matches the full Navier-Stokes solution in the BEP pipe with an error of only 1%. This approach has been rarely used, however, because of the difficulty in accurately meshing the BEP pipe. Using this approach requires remeshing the problem to account for changes in the pipe geometry due to secondary erosion of the pipe walls. Additionally, given the small dimensions of erosion pipes (mm in depth), this approach also requires the use of very small elements to accurately represent the erosion pipe. As such, the number of elements required for simulating BEP progression through an entire domain quickly becomes computationally prohibitive, especially at the field scale where pipe paths may be hundreds of meters in length.

To resolve these issues with representing the BEP pipe geometrically, approximate approaches are usually used. The BEP pipe domain can be approximated in three dimensions using planar elements, one dimensional line elements, and parallelepiped, volumetric elements as illustrated in Figure 3.8b. The majority of three dimensional studies reviewed in Chapter 2 used line elements to approximate the erosion pipe. No prior studies have used the plane approximation or parallelepiped approximation of the erosion pipe, although the fracture flow interface model employed by Bersan et al. (2013) is equivalent to the planar pipe elements. For

each approximate approach, the pipe geometry is not precisely represented by the elements used to discretize the pipe domain. As such, adjustments to the equivalent pipe hydraulic conductivity must be made to account for the difference in flow area between the approximate geometry and true pipe geometry. In this manner, the total flow rate through the pipe can accurately be represented in the BEP model when using approximate pipe geometries. These adjustments are elaborated upon in the following paragraphs.

For the planar approximation of the pipe domain in three-dimensions, the width of the pipe is closely approximated by the domain of the pipe elements, but the pipe depth cannot be accounted for geometrically due to the two-dimensional elements being used. The flow rate computed for the two-dimensional pipe elements is a specific discharge per unit length in the z direction given by

$$\{q_e\} = [k_e]\{H_e\} \tag{3.38}$$

where $\{q_e\}$ is the specific discharge at the element nodes, $[k_e]$ is the element conductivity matrix for the pipe elements, and $\{H_e\}$ is the value of the total head at the element nodes. To convert 3.38 to total discharge, $\{Q_e\}$, for assembly into Equation 3.31, the flow rate must be scaled by the actual dimension of the erosion pipe in the z-direction. This equates to multiplying Equation 3.38 by the pipe depth a, yielding

$$\{Q_e\} = \left[k_p\right]\{H_e\}a_e \tag{3.39}$$

Because a_e is a constant value within the element subdomain, it can be distributed into the integration of $\left[k_p\right]$ yielding a scaled value of k_p for planar pipe elements of

$$k_p = k_p a = \frac{a^2 \rho g}{12\mu} a \tag{3.40}$$

This can also be thought of in terms of scaling the hydraulic conductivity by the ratio of the flow area. The true flow area of the rectangular pipe cross section is $A = wa$, whereas the flow area approximated by planar elements is $\hat{A} = w \cdot 1$ as the planar elements represent a specific discharge per unit length in the z-direction. The adjusted pipe hydraulic conductivity is determined by multiplying k_p by the ratio of the flow areas to ensure the pipe elements are approximating the actual cross sectional area of the erosion pipe.

$$k_p = k_p \frac{A}{\hat{A}} = k_p a = \frac{a^2 \rho g}{12\mu} a \tag{3.41}$$

Similarly, for parallelepiped elements, $\hat{A} = w\delta$, where δ is the length of the parallelepiped element in the *z*-direction. As such, the hydraulic conductivity of the parallelepiped, pipe elements is approximated as

$$k_p = k_p \frac{A}{\hat{A}} = k_p \frac{a}{\delta} = \frac{a^2 \rho g}{12\mu} \frac{a}{\delta} \tag{3.42}$$

Equation 3-42 only applies to parallelepiped elements as it was assumed that the element had a constant height, δ, in the z-direction. Because of this, the use of elements that are not paralellpiped will result in additional errors in the approximation.

In the case of 1D linear elements, the element has no area associated with it, and the entire pipe cross sectional area must be accounted for in the pipe hydraulic conductivity as

$$k_p = \frac{a^2 \rho g}{12\mu} aw \tag{3.43}$$

Equations 3-41 through 3-43 are the approximate, pipe hydraulic conductivities for planar, parallelepiped, and 1D line elements in three-dimensional domains. While the error in the planar approximation has previously been shown to be negligible (Bersan et al. 2013), the errors in the

linear and parallelepiped approximations have not been assessed. This will be explored in later Chapters.

3.3.2 Two-dimensional models

Two-dimensional approximations of the piping problem can be made in a plan view perspective (Figure 3.8c) and also from a cross sectional perspective (Figure 3.8d). The plan view perspective assesses the pipe progression in the $x - y$ plane whereas the cross sectional perspective assesses the pipe progression in the $x - z$ plane. For both two-dimensional perspectives, correction factors can be applied to perform a pseudo three-dimensional analysis. The physical meaning of each perspective is discussed in the sections that follow before describing the formulation of the three-dimensional correction factors and various approximations for representing the erosion pipe.

3.3.2.1 Plan View Models

Consider the plan view analysis of pipe progression through the $x - y$ plane illustrated in Figure 3.8c. The analysis in two-dimensions is formulated per unit length in the z-direction (perpendicular to the analysis plane). As such, an analysis conducted in this manner computes flow quantities into the pipe that are equivalent to flow quantities associated with a 1-m thick soil layer. The analysis assumes that all flow in the soil is horizontal, all flow in the pipe is horizontal, and no flow occurs in the soil beneath the erosion pipe. Unfortunately, most BEP analyses are for scenarios with foundations much thicker than 1 m. As the pipe remains very shallow relative to the thickness of the sand layer, the flow concentrates strongly towards the pipe in the vertical direction with increasing concentration of flow as the foundation depth

increases. As a result, the pipe progresses more readily in layers of greater depth, which has been demonstrated both experimentally (de Wit 1984) and theoretically (Sellmeijer 1988, Sellmeijer 2006). The physical explanation for this lies in the fact that thicker soil layers can convey more water towards the pipe, which in turn leads to higher flow rates in the pipe, larger pipe dimensions, and lower head losses in the erosion pipe. While this cannot be fully accounted for in the two-dimensional model due to the highly three-dimensional flow field around the pipe, an approximation can be made to partially correct for the soil thickness in the *z*-direction.

The specific discharge through the soil domain in Figure 3.8c is given by Darcy's law as

$$q = k_s \nabla h \tag{3.44}$$

where k_s is the soil hydraulic conductivity and q is the discharge per unit length in the z-direction. The specific discharge can be converted to a total discharge by multiplying Equation 3.44 by the the thickness of the soil layer, D, in the z-direction. This yields

$$Q = D \cdot k_s \nabla h \tag{3.45}$$

Thus, it is readily seen that the thickness of the sand layer can be accounted for in the plan view analysis by scaling the soil hydraulic conductivity by a factor D. Applying D as a correction to the hydraulic conductivity yields a depth corrected hydraulic conductivity for all elements in the soil domain given by

$$k_{s,d} = D \cdot k_s \tag{3.46}$$

where the depth corrected value of hydraulic conductivity ($k_{s,d}$) is expressed in terms of the original soil hydraulic conductivity (k_s) and the aquifer depth (D). By scaling the hydraulic conductivity of all elements in the soil domain, the flow rates into the pipe are two-dimensional approximations of the three-dimensional flow.

Because the flow into the pipe is approximating the actual three-dimensional flow into the pipe, the pipe elements can be approximated using the three dimensional approximations previously described. In plan view, only the planar pipe approximation and the line element approximation are applicable. The values of k_p are given by Equation 3.41 for the planar elements and Equation 3.43 for the line elements. Using these approximations for the pipe, the two dimensional, plan view model approximates horizontal, two dimensional flow through a soil layer of thickness D into a three dimensional erosion pipe.

3.3.2.2 Cross Sectional View Models

Consider the cross-sectional view of the pipe progressing through the $x - z$ plane as illustrated in Figure 3.8d. Because the pipe progresses across the top of the sand layer, the pipe progression must be restricted to the top of the model in the plane. The analysis is now per unit length in the y direction. Without making any corrections for three-dimensional conditions, the analysis represents the progression of a pipe through a domain of infinite width in the y direction. Both the pipe domain and the soil domain are infinitely wide, and the discharge in both domains is the specific discharge per unit width.

For this scenario, the pipe can be represented geometrically, using 1D line elements, and also using parallelograms as illustrated in Figure 3.8d. For the geometric representation, the pipe is meshed using elements that actually represent the true depth of the erosion pipe similarly to the three-dimensional situation. Because the analysis is per unit width, no adjustment for the width is necessary and the value of k_p is the same as the three dimensional scenario (Equation 3.8). The value of k_p for line elements in profile view must be adjusted to be per unit width. As

such, k_p is determined by dividing Equation 3.43 for a three dimensional line element by the width of the erosion pipe

$$k_p = \frac{a^2 \rho g}{12\mu} aw \cdot \frac{1}{w} = \frac{a^2 \rho g}{12\mu} a \tag{3.47}$$

For the case of the parallelogram in two dimensions, k_p is the same as in the case of a parallelepiped in three dimensions (Equation 3.42). This is due to the fact that the pipe width in three dimensions is accounted for by the actual element geometry, and k_p is already expressed per unit area. Additionally, the parallelogram in 2D must still be adjusted by the element height to account for the error in approximating the flow area when using elements that are significantly larger than the actual pipe depth in the z-direction.

As noted previously, an analysis conducted in a cross sectional view is assessing the specific discharge in both the soil and pipe per unit width in the y direction. Similar to the plan view perspective, a pseudo three-dimensional analysis can be made by scaling the hydraulic conductivity of the soil and the erosion pipe to account for the effective width of both domains. The corrected hydraulic conductivities for the soil and pipe are

$$k_{s,w} = W k_s \tag{3.48}$$

and

$$k_{p,w} = w k_p \tag{3.49}$$

where W and w are the width of the soil domain and the pipe domain, respectively. However, the width of the erosion pipe is proportional to the depth of the erosion pipe. Therefore, Equation 3.49 is more appropriately defined in terms of the pipe depth as

$$k_{p,w} = aR k_p \tag{3.50}$$

where $R = w/a$ is again the pipe width-to-depth ratio. By using Equations 3.48 and 3.50 in place of the hydraulic conductivities for the soil and pipe, a pseudo-three dimensional analysis of

flow through a soil layer of width, W, into a pipe with constant width-to-depth ratio R is obtained.

3.4 Simulation algorithm

The previous sections of this Chapter have described the finite element formulation used to solve the coupled groundwater – pipe flow problem for various representations of a pipe of known position and depth. However, the depth of the pipe is not known *a priori* and must be determined as part of the solution. This is done through a series of iterations that check the pipe depth, pipe width, and pipe progression sequentially. Because the model is a steady state model, the simulation searches for the steady state equilibrium position of the pipe at each applied boundary condition. The simulation algorithm used to perform this search is described in this section.

A diagram of the simulation algorithm is illustrated in Figure 3.9, and an illustration of the major algorithm components being applied to a simple problem is provided in Figure 3.10. The erosion process is typically simulated by incrementally finding equilibrium states of the erosion pipe for gradually increasing boundary condition values. The boundary conditions are initially set to a nominal value with very little differential head. The erosion process is then simulated through the following steps:

1. Erosion is initiated by activating a pipe element at the desired initiation location. The depth of the pipe element is initialized to a value of $g_m d_{50}$ where g_m is a user defined value. The value $g_m = 1$ is used as a default value based on observations in the laboratory of initial pipe depths (Vandenboer, 2019).

2. The equivalent hydraulic conductivity of the pipe element is then calculated using the appropriate equation for k_p for the pipe representation chosen (Figure 3.8).
3. The FE problem is solved to obtain an initial hydraulic solution.
4. Using the updated hydraulic solution, the depth of the pipe element is checked to determine if $\tau < \tau_c$ by calculating τ according to Equation 3.28 and comparing to the defined value of τ_c for the sand. If the critical shear stress is exceeded, the pipe depth is increased by $d_{50}/2$ as illustrated for 1 element in Figure 3.10. The problem is then solved again with the new depth. These iterations continue until the pipe depth is determined in all pipe elements, thereby yielding the solution to the BEP problem that satisfies the conditions of sediment equilibrium in the erosion pipes.
5. After the pipe depth has been determined in all elements, the width of the erosion pipe is evaluated based on the prescribed width-to-depth ratio, R. Widening is only checked when conducting analysis in three dimensions or in two-dimensional plan view. The widening of the pipe is achieved by switching all neighboring elements to pipe elements if

$$Ra > 2t \tag{3.47}$$

where $R = w/a$ is the width to depth ratio, a is the depth of the erosion pipe, and t is the width of the pipe element. As the pipe will grow from 1 element in width to 3 elements in width once all neighbors are activated (Figure 3.10), a factor of 2 was selected as an average value for the widening threshold. Alternatively, the widening may be implemented in two steps whereby 1 neighbor is activated when $Ra > t$ and 2 neighbors are activated when Ra>2t. If any elements are activated through the widening algorithm, Step 4 must be repeated to check the pipe depth again.

6. Once the pipe depth and width has been obtained, the pipe progression is evaluated by Eq. 3.27 in all soil elements adjacent to the pipe elements. In this study, only horizontal progression of the erosion pipe is considered. As such, only the horizontal component of the hydraulic gradient is considered when evaluating $i_s(x)$ in the soil elements. If Eq. 3.27 is satisfied, the pipe will progress further. When using parallelepiped or parallelogram pipe elements, the pipe is advanced by switching the soil elements that satisfy Eq. 3.27 to pipe elements resulting in an updated pipe position. For planar and linear pipe elements, the pipe progression is advanced by activating new pipe elements attached to the soil elements that satisfied Eq. 3.27. Figure 3.10 illustrates a scenario where i_{cs} is exceeded in only 1 element. The identified element is then switched from a soil element to a pipe element with an initial pipe depth of $g_m d_{50}$.
7. The algorithm then returns back to step 2 with the updated pipe geometry. The iterations over the pipe depth and width are repeated to evaluate the solution for the new pipe position. This process is repeated until Eq. 3.27 is no longer met in any soil elements adjacent to the erosion pipe indicating the pipe has come to equilibrium under the applied boundary condition.
8. At this point, the upstream boundary condition is increased slightly in value, and the simulation process (steps 1-7) is repeated until the pipe progresses through the domain or reaches a target boundary condition value.

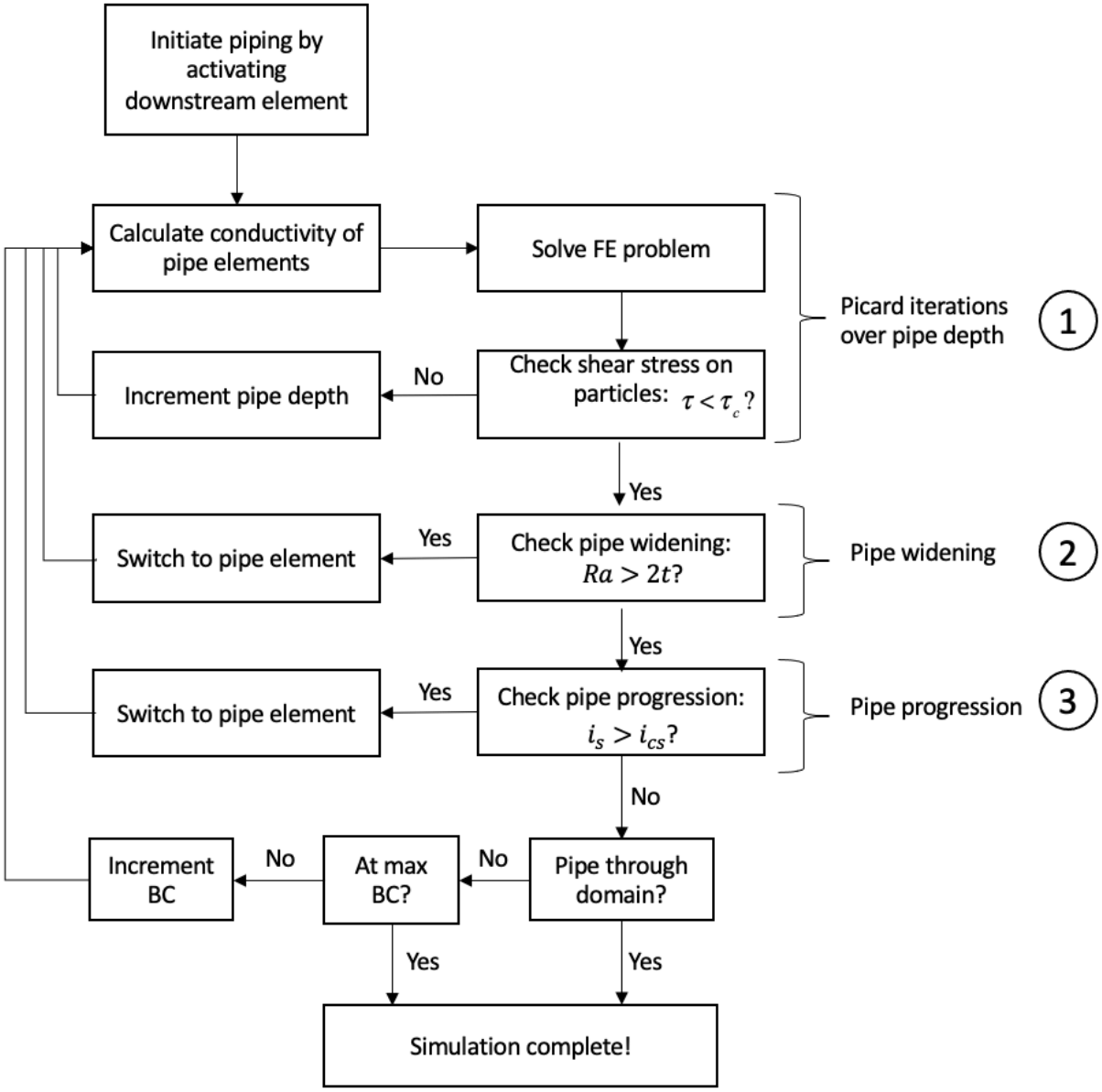

Figure 3.9. Simulation algorithm for pipe progression under steady-state conditions.

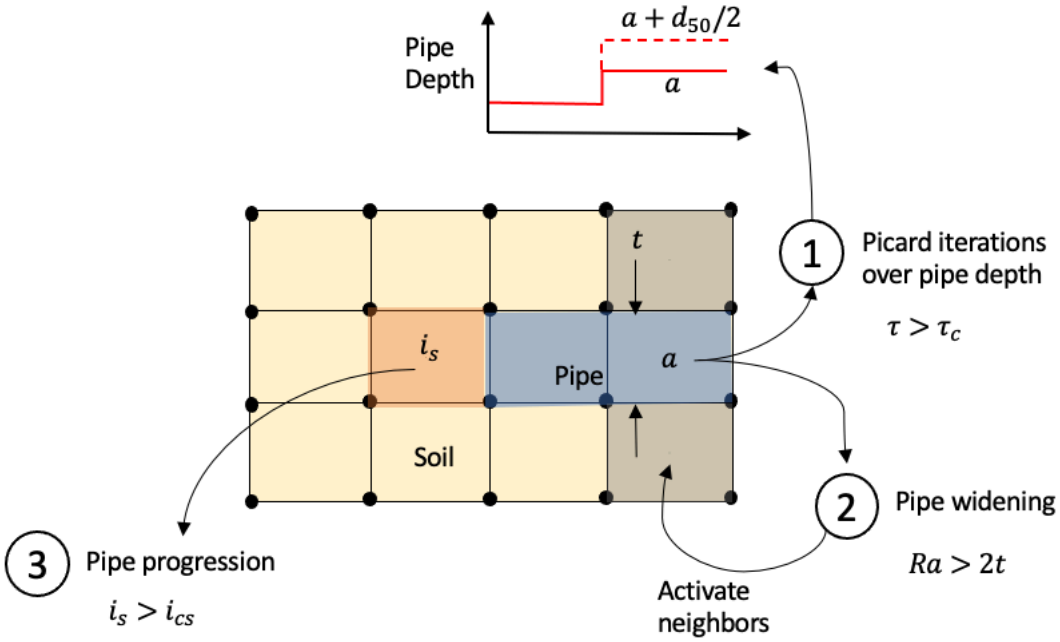

Figure 3.10. Illustration of algorithm steps applied to simple example.

3.5 Example Analysis

To demonstrate the simulation algorithm, consider the example problem of a large scale laboratory experiment as shown in Figure 3.11. The domain is 1.9 m in length, 0.9 m in width, and 0.4 m tall. The downstream boundary consists of a single exit hole fixed at a constant head of h=0.0 m. The upstream boundary is a constant head boundary that is gradually increased as pipe equilibrium is found. All other boundaries are no flow boundaries. Erosion is initiated at the edge of the downstream exit hole. The finite element mesh used hexahedral elements for both the soil domain and the pipe domain. The elements were 0.02 m in size.

The soil properties used for the simulation are provided in Table 3.2. The properties were chosen for demonstration purposes. The pipe width to depth ratio, R, was set to a value of 20 to demonstrate the pipe widening portion of the algorithm in addition to the pipe progression. The constant head, H, applied to the upstream boundary is plotted in Figure 3.12. As shown, the

head had to be gradually increased with the pipe finding equilibrium up until the critical head of H_{cr}=0.134 m was reached. At this point, equilibrium could not be obtained again and the pipe progressed through the rest of the domain without any further increases in head.

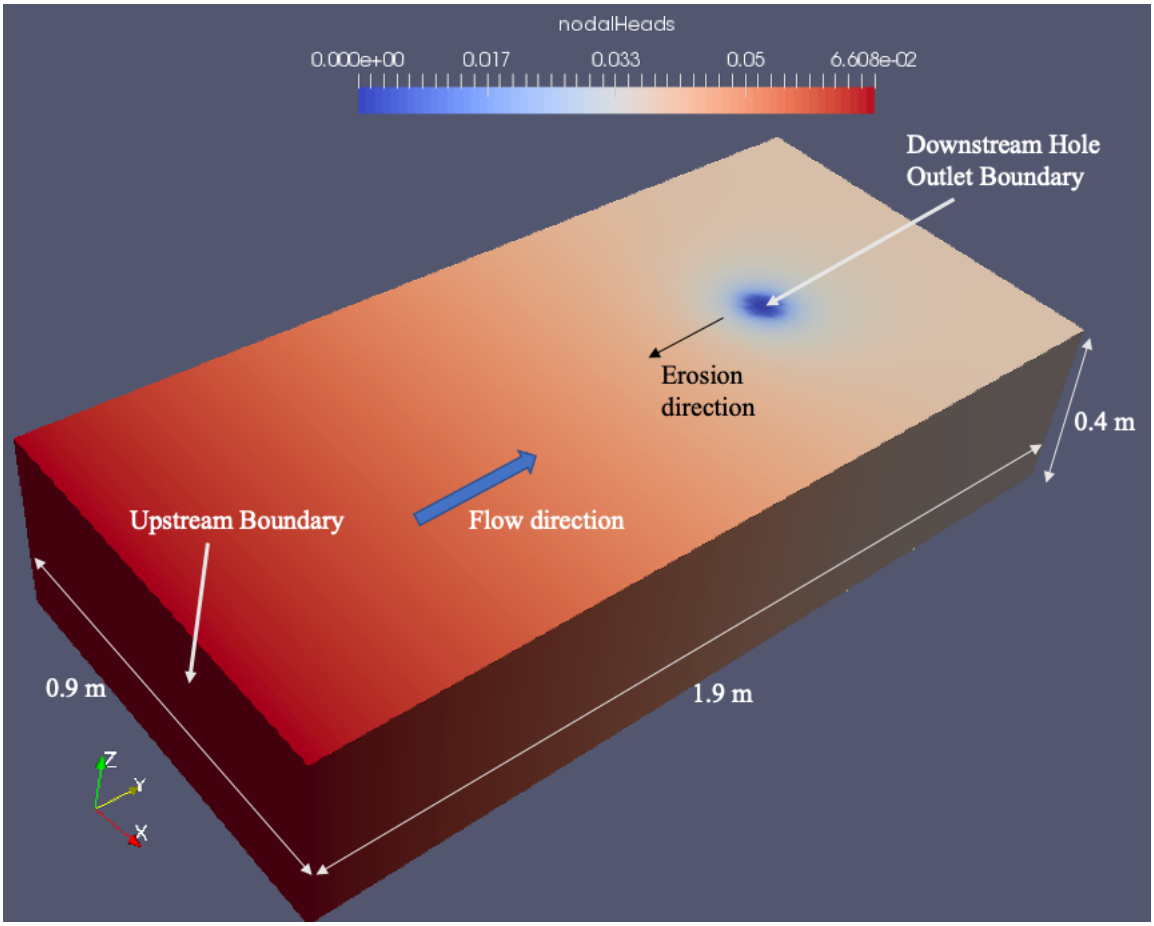

Figure 3.11. Example simulation of a large scale laboratory experiment.

Table 3.2. Properties used in BEP simulation.

Property	**Assigned Value**
d_{50} (mm)	0.154
k_h (cm/s)	0.008
τ_c (Pa)	0.25
i_{cs}	0.85
R	20

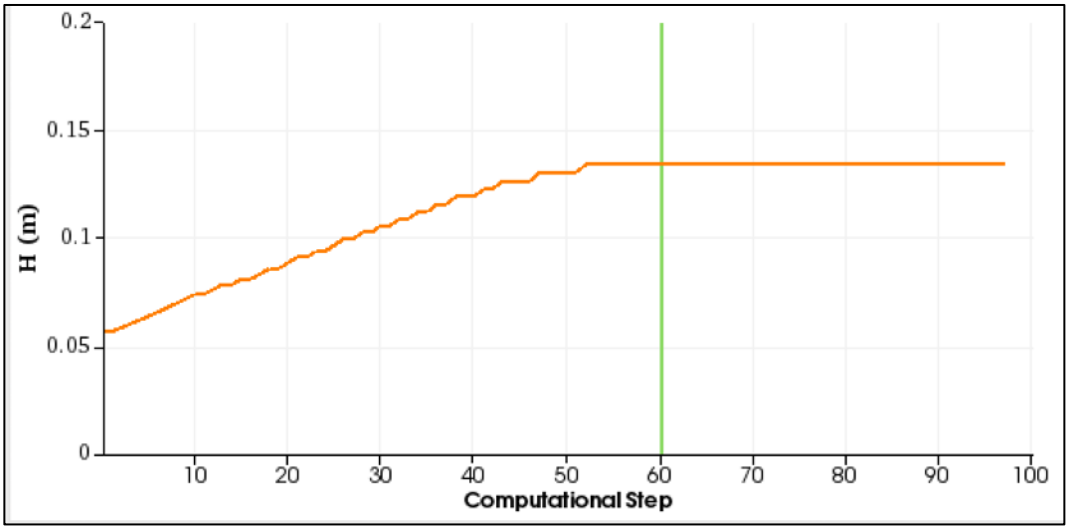

Figure 3.12. Increase in differential head up to $H_{cr} = 0.134$ m for example simulation. Green line indicates computational step corresponding to results in Figures 3.13 and 3.14.

Figure 3.13 shows the pipe geometry corresponding to computation step 60 in Figure 3.12 shortly after the critical head had been exceeded. The separate pipe progression and widening of the erosion pipe are readily visible from the geometry of the erosion pipe. Additionally, the influence of the erosion pipe on the groundwater flow is seen by the constant head contours surrounding the erosion pipe. The head profile and pipe depth profile along the centerline of the model domain are also provided in Figure 3.14. The pipe depth increases towards the downstream exit due to increases in flow along the pipe length, which in turn leads to the widening of the pipe illustrated in Figure 3.13. Additionally, the concentration in flow towards the pipe tip is readily seen from the nonlinear head profile at the upstream end of the pipe.

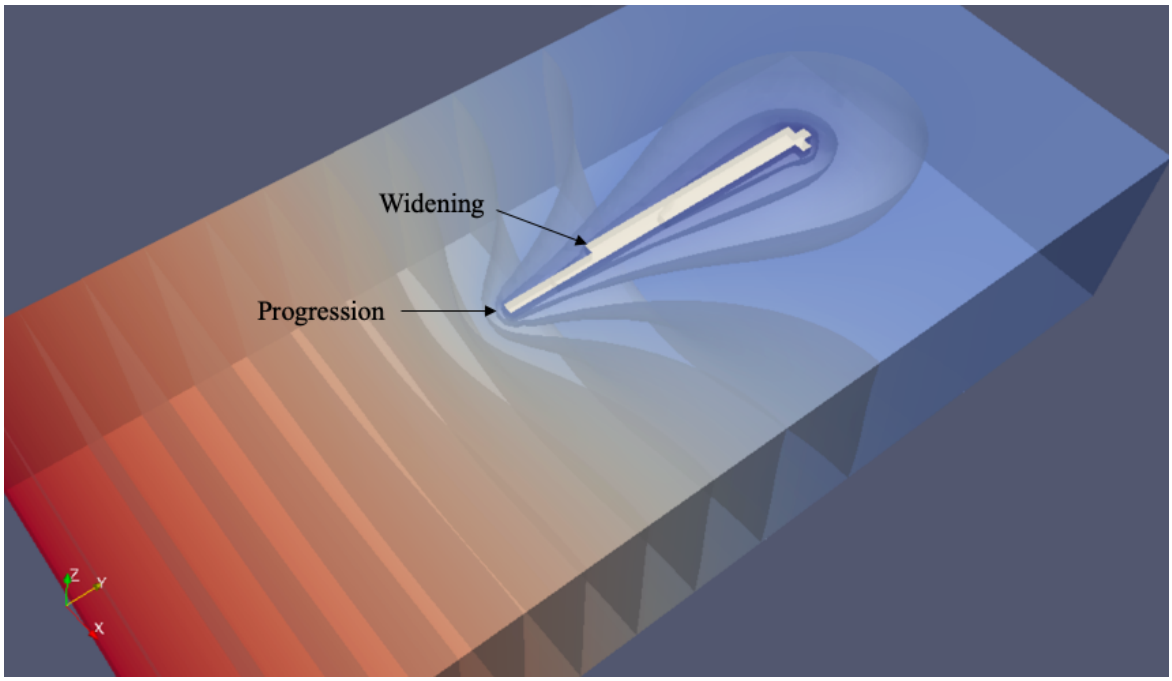

Figure 3.13. Simulated pipe progression through domain highlighting both progression and pipe widening. Contours are equal head contours of 0.01 m.

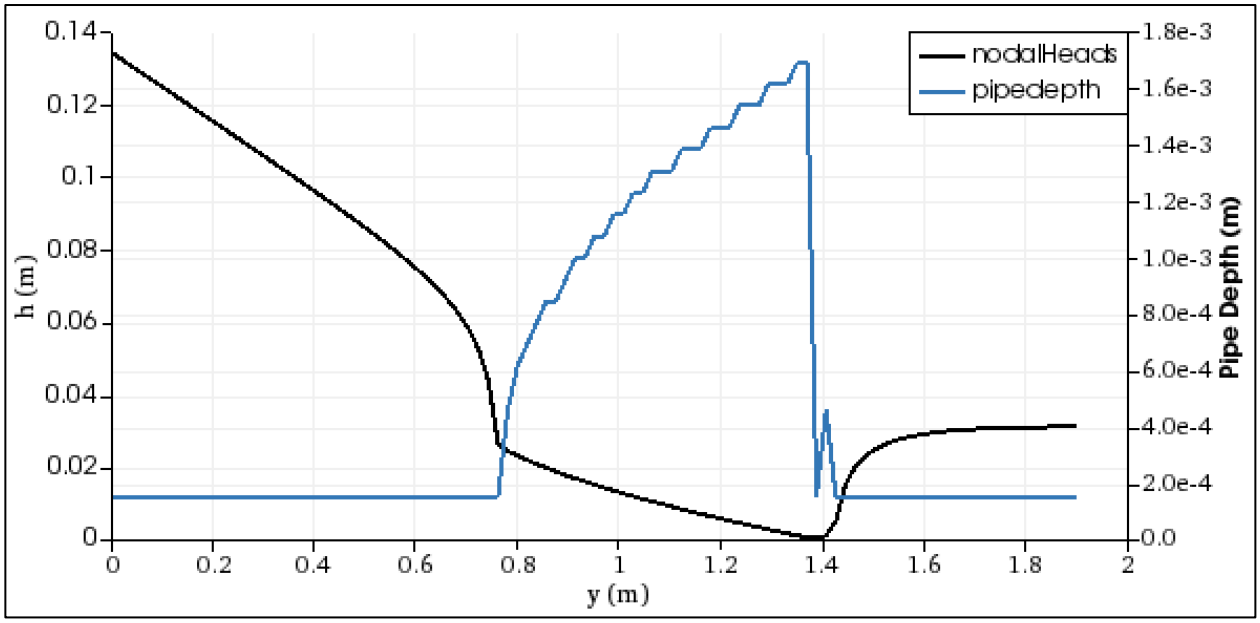

Figure 3.14. Profile of head (h) and pipe depth along centerline of pipe.

The example presented has demonstrated the finite element analysis of the progression of BEP, including both the mechanisms of primary erosion at the pipe tip and secondary erosion along the pipe. While the example has demonstrated that the steady-state approach is capable of simulating BEP progression, the input properties were arbitrarily selected for the sake of demonstration. In the following Chapter, approaches for measuring and predicting the value of i_{cs} for pipe progression are developed. In subsequent chapters, the use of the steady state finite element model in conjunction with the CSGF for predicting BEP progression will be validated through hindcasting of experimental results.

CHAPTER 4

MEASUREMENT AND PREDICTION OF THE CRITICAL SECANT GRADIENT FUNCTION

The previous chapter defined a finite element model for evaluating BEP progression. However, the model requires an estimated value of the critical secant gradient (i_{cs}) from the critical secant gradient function (CSGF) in order to assess the pipe progression. The CSGF has been defined analytically in Chapter 3 using the head in front of the erosion pipe at one point. It is therefore necessary to measure the head in front of an erosion pipe at the moment of progression for defining the CSGF. Additionally, it is of interest to evaluate how well the analytical solution describes the actual CSGF. For this reason, the cylindrical experimental device described in Robbins et al. (2018) was modified to have pore pressure transducers spaced at 2 cm intervals in order to measure the head profile in front of the erosion pipe. A series of 24 experiments on 7 different sands was conducted to measure the CSGF. In the following sections, the laboratory equipment, materials, test procedures, experimental program, and example measurements are described.

4.1 Laboratory Test Equipment

Robbins et al. (2018) developed a cylindrical, acrylic flume as illustrated in Figure 4.1 specifically for conducting BEP experiments. The device originally consisted of an acrylic cylinder with an internal diameter of D=0.152 m and a length of 1.527 m with 11 pore pressure ports along both the top and bottom of the cylinder. Because of the cylindrical shape, the BEP pipes that form pass directly under the sensors thereby permitting the measurement of the pressures immediately upstream of the erosion pipe. To obtain higher spatial resolution, the

original device was modified to have pore pressure measurements at 2 cm spacing over the central 50 cm of the sample as illustrated in Figure 4.1.

The pore pressure measurement ports are connected by vinyl tubing to Honeywell 26PC pressure transducers. The upstream endplate contains a porous filter and is bolted to the test cylinder. The end plate is sealed by an o-ring seal on the bolted flange. The downstream endplate is also sealed by an o-ring and bolted to the flange; however, a filter is not needed on the downstream end plate as the sand does not contact the downstream wall.

A full schematic of the test equipment is illustrated in Figure 4.2, and a photograph of the assembled apparatus and instrumentation is provided in Figure 4.3. A free overflow constant head tank is connected to the inlet wall of the cylinder. The outlet hose on the cylinder runs to a fixed, free overflow, tailwater that is vented to the atmosphere. The outflow is then directed to the outflow tank that is weighed by a loadcell to monitor the flow rate. Lastly, a stringpot was fixed to the frame that held the cylinder. The stringpot was attached to a pipe position indicator that was manually advanced along the cylinder as the pipe progressed to track the pipe position as illustrated in Figure 4.4. The erosion pipe was clearly visible as it progressed beneath the sensors (Figure 4.5), so it was easy to visibly track the pipe tip location and move the position indicator accordingly. The data from the loadcell, stringpot, and pressure transducers is recorded by a National Instruments 6255 USB data aquisition device at a frequency of 1 Hz. A more detailed description of the test equipment is provided in Robbins et al. (2018) with the exception of the stringpot. The use of the stringpot for monitoring the pipe position was a new addition for this testing.

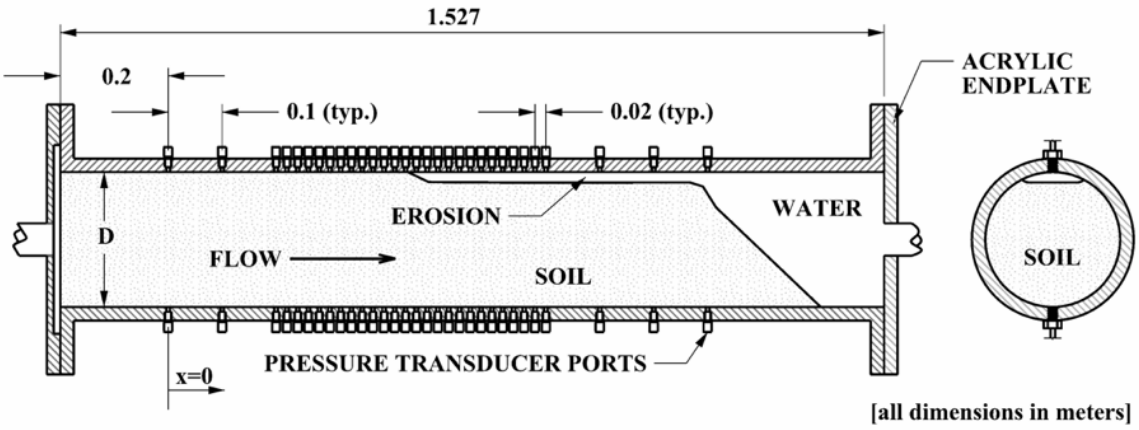

Figure 4.1. Schematic of the modified cylindrical flume for CSGF measurements.

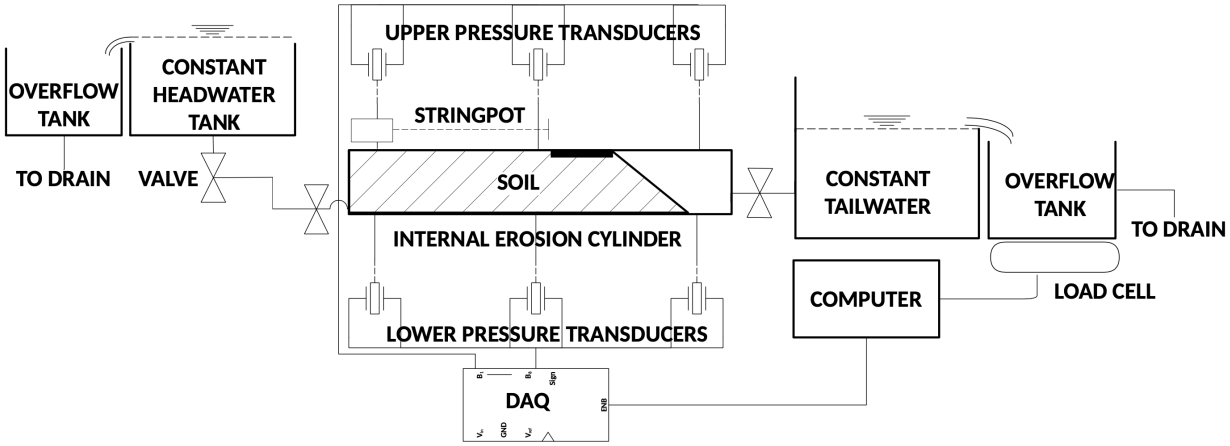

Figure 4.2. Schematic diagram of laboratory test configuration.

Figure 4.3.Photograph of complete experimental setup.

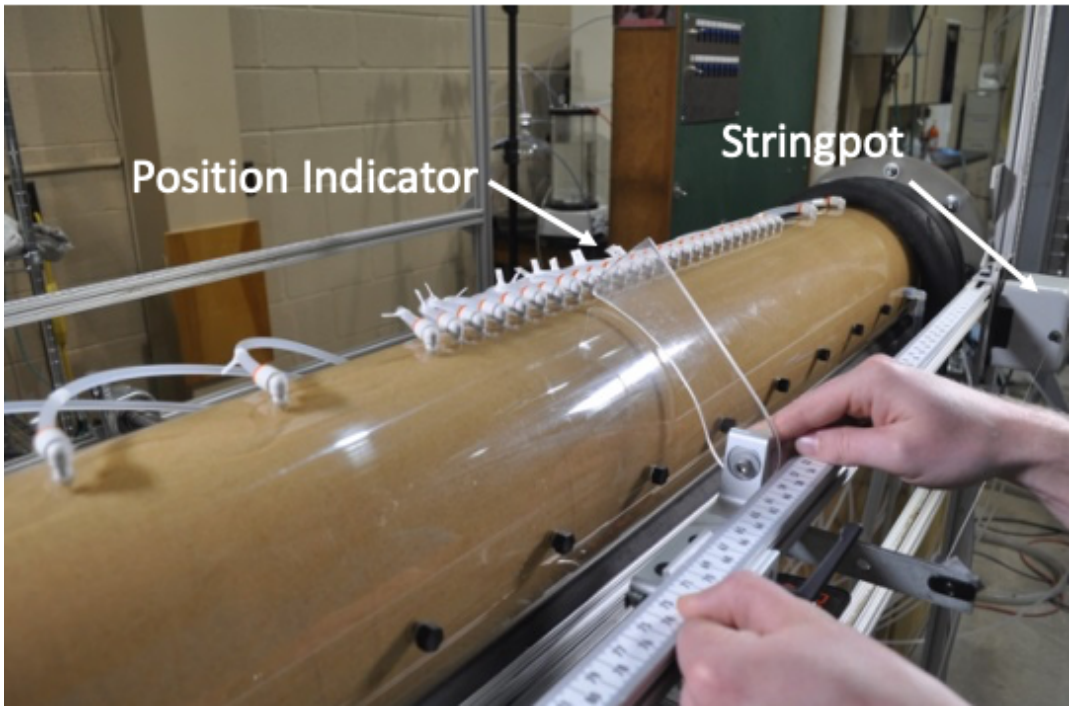

Figure 4.4. Photograph of pipe position indicator and stringpot.

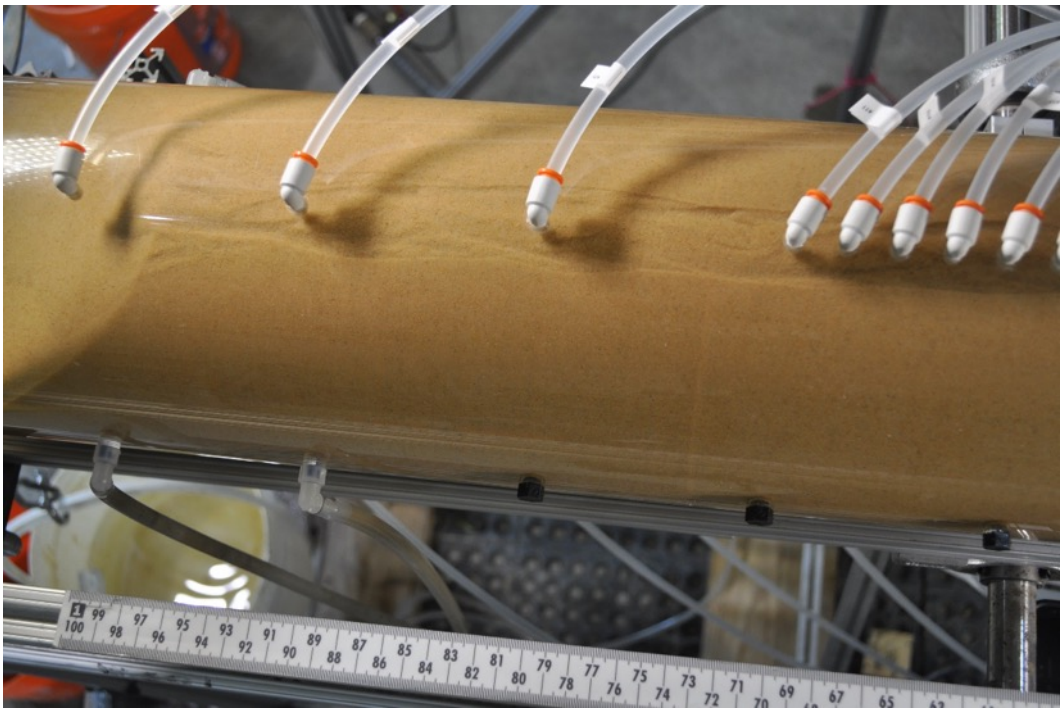

Figure 4.5. Photograph of erosion pipe passing beneath pressure measurement ports.

4.2 Materials

For this test program, eight relatively uniform sands were used with properties as shown in Table 4.1. The 40/70 sand was used previously by Robbins et al. (2018) and was tested again in the modified experimental apparatus to ensure consistency between test programs. The CSGF was not measured for the 16/30 sand, but the sand was used in experiments as described in the following section. The remaining six sands were procured from a concurrent research program in the Netherlands investigating the concept of using a coarse grained sand barrier in the foundation as a long term solution for preventing BEP failures (e.g., Akrami et al., 2021; Bezuijen et al., 2021; Rosenbrand & Van Beek, 2021; Rosenbrand et al., 2019; Rosenbrand et al., 2021; Rosenbrand et al., 2020; Van Beek et al., 2015). These sands were selected as the initial sands for measuring the CSGF because the same materials were being used in independent experiments of completely differing geometry and configuration. As a result, the measured CSGFs can be used to model the other experiments as part of validating the approach.

Table 4.1. Physical characteristics of tested sands.

Properties	40/70 Sand	16/30 Sand	Baskarp 15 (B15)	Baskarp 25 (B25)	GZB 1	GZB 2	GZB 3	Metselzand (MZ)
d_{10} (mm)	0.227	0.642	0.103	0.150	0.413	0.375	0.738	0.187
d_{30} (mm)	0.268	0.755	0.129	0.191	0.940	0.766	0.820	0.278
d_{50} (mm)	0.304	0.855	0.150	0.230	1.400	0.870	0.910	0.380
d_{60} (mm)	0.322	0.906	0.161	0.246	1.510	0.927	0.961	0.440
C_c	0.98	0.980	1.00	1.00	1.40	1.70	0.90	0.90
C_u	1.42	1.41	1.60	1.60	3.70	2.50	1.30	2.40
e_{min}	0.560	0.516	0.553	0.543	0.414	0.437	0.546	0.466
e_{max}	0.800	0.742	0.924	0.848	0.669	0.684	0.808	0.681
Specific gravity	2.65	2.65	2.65	2.65	2.65	2.65	2.65	2.65

4.3 Laboratory Testing Program

The laboratory testing program consisted of 24 experiments as outlined in Table 4.2. The majority of experiments consisted of tests on uniform samples of one sand type as indicated by the configuration column in Table 4.2. Because this test program was being conducted in part to support research efforts on using coarse sand barriers to prevent piping, four experiments were run with a barrier configuration (4-14C, 4-27C, 4-28C, 4-30C). For the barrier experiments, the sand tested consisted of an approximately 0.40 m layer of sand surrounded by different sands both upstream and downstream of the sand barrier. For these tests, the CSGF was measured for the barrier sand which consisted of the test sand as noted in Table 4.2, with the upstream and downstream sands as also indicated in Table 4.2. The sample length (L) refers to the length of the soil layer for which the CSGF is measured along the top of the sample. The slope angle refers to the slope of the downstream sample face.

Table 4.2. Cylindrical flume testing series details.

Test No.	Sand	e	Configuration	US Sand, DS Sand	L (m)	Slope Angle
4-3C	S4070	0.365	Uniform	-	1.297	33.5
4-4C	S4070	0.372	Uniform	-	1.268	33.5
4-5C	S4070	0.408	Uniform	-	1.288	32.9
4-6C	S4070	0.407	Uniform	-	1.287	32.0
4-7C	GZB3	0.369	Uniform	-	1.252	32.4
4-9C	B15	0.383	Uniform	-	1.299	32.3
4-10C	B25	0.363	Uniform	-	1.149	34.2
4-11C	B25	0.393	Uniform	-	1.166	31.9
4-12C	GZB2	0.342	Uniform	-	1.203	33.5
4-14C	GZB1	0.345	Barrier	B15, 16/30	0.425	34.7
4-15C	GZB2	0.337	Uniform	-	1.178	36.2
4-16C	S4070	0.398	Uniform	-	1.145	33.1
4-17C	S4070	0.377	Uniform	-	1.147	33.6
4-18C	S4070	0.377	Uniform	-	1.156	32.5
4-19C	GZB2	0.372	Uniform	-	1.156	34.0
4-21C	GZB2	0.333	Uniform	-	1.1549	33.1
4-22C	B25	0.377	Uniform	-	1.127	32.4
4-23C	MZ	0.359	Uniform	-	1.083	31.8
4-24C	MZ	0.349	Uniform	-	1.136	35.7
4-25C	GZB3	0.408	Uniform	-	1.12	34.1
4-26C	MZ	0.343	Uniform	-	1.19	33.8
4-27C	GZB2	0.333	Barrier	B25, B25	0.419	31.0
4-28C	GZB1	0.327	Barrier	B25, 16/30	0.392	31.7
4-30C	GZB2	0.361	Barrier	B25, 16/30	0.411	32.7

4.4 Test Procedure

A completely new sample was prepared for each test by emptying and refilling the flume. The procedures for preparing the sample were as follows:

1. The empty flume was rotated to the vertical position with the downstream end of the cylinder oriented upwards as shown in Figure 4.6, and the downstream hose and valve were disconnected for sample preparation.

2. The flume was filled completely with de-aired water. All vinyl tubing connected to submerged pressure ports were flushed to remove air from the system. The inlet hose was also flushed to remove air bubbles that may have existed.
3. Oven dried sand was then pluviated into the de-aired water using a funnel. As the sand was pluviated, the sample container was tapped with a rubber mallet to produce dense samples. For loose samples, the sand is only tapped slightly to ensure an integral contact with the cylinder walls. As the sand was being pluviated, excess water was drained from drainage ports at the top of the vertically oriented cylinder.
4. Upon completion of sand pluviation, the sample height is measured in multiple locations around the cylinder to get an average sample height for density calculations. The density of the sample is computed based upon the final mass of sand and the computed volume of the sample using the vertical sample height. For barrier tests, only the density of the barrier sand for which the CSGF is measured is reported.
5. The downstream outlet hose and valve were then connected to the cylinder, and all cylinder and outflow hoses were filled completely with water.
6. The sample was then rotated gently to a horizontal position as shown in Figures 4.1 and 4.3. The sand near the end of the sample gradually slid to the natural angle of repose as the sample was rotated.
7. Measurements of the sample length were taken with the cylinder set in the horizontal position for testing. The exit slope angle was calculated based upon the measured length along both the top and bottom of the cylinder.

8. With the upstream valve still closed, the downstream valve was opened. The outflow hose was filled with water until it spilled over the tailwater overflow. All pressure transducers were zeroed to this water level as the reference datum.
9. The pipe position indicator (connected to the stringpot) was moved to the $x = 0$ position at the furthest upstream pressure transducer (as indicated in Figure 4.1). The stringpot was then zeroed to this location before moving to the x-coordinate at the top of the exit slope to record the advancement of the pipe throughout the test.

Figure 4.6. Photograph of cylindrical flume oriented vertically for sample preparation.

Once the sample was prepared and fixed in the horizontal position, it was ready for testing. The test procedure varied slightly from that reported in Robbins et al. (2018) in that the pipe was

intentionally stopped during each test by lowering the upstream head. This was done to ensure the critical conditions for pipe progression were measured as the experiments were initiation controlled for uniform samples. For samples with a barrier configuration, the pipe naturally stopped at the barrier sand and there was no need to manually stop pipe progression. The test procedure (with reference to Figure 4.7) was as follows

1. The upstream head was raised to a height of 1 cm above the tailwater to ensure a positive pressure prior to opening the valve. The upstream inlet valve on the cylinder was then fully opened.
2. The upstream head tank was then gradually raised until the hydraulic gradient across the sample registered at some value less than 0.05 (Figure 4.7, t=300 seconds). A starting gradient of 0.05 was selected for the tests as it was small enough not to cause particle movement while also allowing sufficient flow to test the instrumentation.
3. The upstream head tank was then raised in increments. Larger increments were used in initial stages of testing. After each increase in head, the test was allowed to sit for a period of at least 2 minutes. If any particle movement was observed, the upstream head was left unchanged until no particle movement was observed for two minutes.
4. Once erosion initiated, the time, flow rate, and average hydraulic gradient at initiation were recorded. As the pipe progressed, the pipe position indicator was moved along with the pipe to register the pipe position with the data acquisition system in real time. Once the pipe reached the dense array of pressure measurements, the upstream head was lowered to stop the pipe as close to a measurement port as possible. This ensured pressures were able to be measured at approximately 2 cm intervals upstream of the pipe tip. The x location that the pipe stopped at was determined visually and recorded as x_{eq}.

As noted previously, manually stopping the pipe was not necessary for barrier configurations as the pipe naturally stopped when it reached the coarser sand.

5. The differential head was held constant with the pipe stopped to ensure no particles were moving (Figure 4.7, t=2300-2500 seconds). The upstream head tank was then gradually raised again (t=2500 seconds), stopping when substantial particle movement in the pipe occurred. The head was incrementally increased each time particle movement ceased (t=2500-3000 seconds). In this manner, the pipe gradually washed out sediment that had dropped in the pipe when the valve closed thereby re-establishing the natural pipe geometry.
6. Eventually, the pipe would begin progressing again (t=3080 seconds). The pressure measurements upstream of the pipe tip as close to the moment of erosion initiation as possible were used to calculate the values of the CSGF at each pressure transducer location.

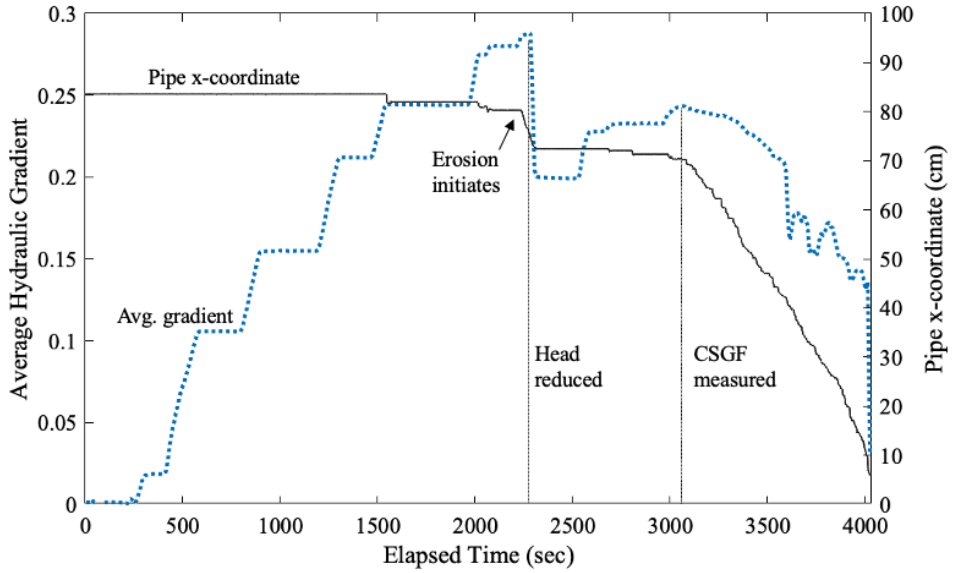

Figure 4.7. Test procedure as illustrated by measured average hydraulic gradient and pipe position for test 4-18C.

4.5 Results

The results of the experimental test series are presented in Table 4.3. The hydraulic conductivity was determined for each sand based on the measured flow rate and hydraulic gradient in the sand sample before erosion occurred. The value of x_{eq}, the position the pipe tip was stopped for measuring the CSGF, is also noted in Table 4.3 for each test. The pressure measurement at the pipe tip was used in conjunction with the pressure measurements in front of the pipe to calculate the CSGF value at each measurement location as illustrated in Figure 4.8. Equation 3.25 was then evaluated for each test using the head measured at x=2, 4, 6, and 10 cm in front of the erosion pipe for calculating the value of C needed to define the CSGF using Equation 3.26. The measured CSGF values are compared graphically to the analytical fits for all 24 experiments in Figure 4.9. For many of the tests, the uncertainty in the CSGF measurement was negligible as indicated by the nearly identical CSGF curves obtained for all measurement points (e.g., Test 4-4C). For other tests (e.g., Test 4-7C), the uncertainty in the measured CSGF was larger as indicated by the variation in the analytical CSGF curves based on the measurement point used to fit Equations 3.25 and 3.26. The values of i_{cs} calculated for each pressure measurement point are also provided in Table 4-3. It should be noted that the x positions of 2, 4, 6, 8, and 10 cm associated with each i_{cs} measurement are approximate for Test 19C and Test 21C due to the pipe tip not precisely aligning with a pressure transducer in these tests. The pipe tip stopped 0.70 cm away from a transducer for Test 19C and 0.18 cm away from a transducer for Test 21C. While the positions in Table 4.3 are approximate as a result, the measurements are plotted at the measured locations in Figure 4.9.

Visual examination of the comparison between the measured CSGF values and the analytical CSGF defined by Equations 3.25 and 3.26 (Figure 4.9) indicate that the analytical equation for the CSGF closely matches the measured data for 16 of the 24 experiments. For the

experiments that do not match as closely, the analytical CSGF fit to the measurement at x=10 cm provides an upper bound of the measured data (black curve in Figure 4.9). It is possible that the deviation of the measured CSGF values from the analytical equation may be due to experimental issues with the laboratory test. Therefore, to assess this possibility, a more quantitative analysis of the goodness of fit is performed. The goodness of fit of Equation 3.25 to the data was evaluated by calculating the mean squared error (MSE) for each experiment, given by

$$MSE = \frac{1}{5}\sum_{i=1}^{5}\left(i_{cs,ppt,i} - i_{cs}(x_i)\right)^2 \tag{4.1}$$

where $i_{cs,ppt}$ is the measured value of i_{cs} at each pressure transducer location, and $i_{cs}(x_i)$ is the predicted value of i_{cs} at each transducer location x_i for transducers 1 to 5 in front of the pipe tip based on the C value obtained using the head measured at $x = 10$ cm. The calculated values are also provided in Table 4.3. The MSE was found to increase with increasing grain size and soil density (Figure 4.10). However, the fit was excellent for all of the smaller grain sizes tested. Two possible explanations for this trend will be offered. First, it is well known that the hydraulic conductivity of the acrylic-sand interface is higher than the sand. It is possible that this influence is more pronounced in the coarser soils, which would become increasingly significant as the density of the sample increases and the hydraulic conductivity decreases. The effect of this issue would be that the boundary essentially drains the sample leading to less flow concentration and lower CSGF values as observed in the test results. A second possible explanation is the fact that erosion pipes are proportional to grain size. As the grain size increases, the width of the erosion pipe increases. At some point, the erosion pipe will completely span the top of the cylinder as illustrated in the cross section of the tube in Figure 4.1. This may lead to a one dimensional progression situation where the sand in front of the pipe is fluidizing all at once and moving

towards the pipe as it is no longer restrained by the sand on the sides of the pipe tip. The increased porosity over a larger zone in front of the pipe would lead to higher permeability and lower gradients in the fluidized zone near the pipe tip. While this may also provide an explanation for the lower CSGF values near the pipe tip with increasing grain size, it does not explain the influence of the density.

The influence of both possible explanations of error would be an erroneously low value of i_{cs} near the pipe tip. Because of this, the CSGF values determined using the measurement at x =10 cm were taken as the best estimate of the CSGF for all of the tests. These best estimate CSGF curves are shown as the black CSGF lines in Figure 4.9. Additionally, the best estimate C values from these curves are provided in Table 4.3 along with the associated MSE and calculated i_{cs}(1cm) values.

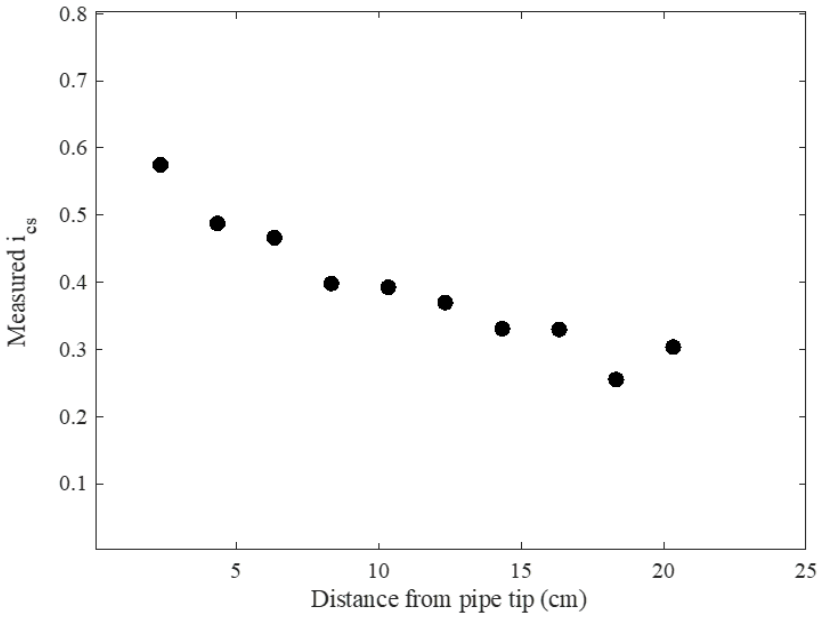

Figure 4.8. Measured CSGF for Test 4-18C.

Table 4.3. Cylindrical flume test results and analytical fit to head measured at x=10 cm.

			Measured CSGF at approximate x locations (cm)					Analytical Solution fit at $x = 10cm$ (Eq. 3-26)		
Test No.	k_h (cm/s)	x_{eq} (cm)	2	4	6	8	10	C	MSE	$i_{cs}(1\ cm)$
4-3C	0.088	71.6	0.71	0.52	0.45	0.39	0.35	0.112	0.002	1.12
4-4C	0.102	68.0	0.65	0.45	0.37	0.33	0.29	0.092	0.000	0.92
4-5C	0.144	69.6	0.51	0.39	0.32	0.27	0.24	0.076	0.000	0.76
4-6C	0.130	75.2	0.54	0.42	0.32	0.29	0.26	0.082	0.000	0.82
4-7C	0.996	66.1	0.57	0.51	0.42	0.4	0.38	0.120	0.018	1.20
4-9C	0.014	73.6	0.63	0.46	0.37	0.31	0.29	0.093	0.000	0.93
4-10C	0.031	68.2	0.75	0.48	0.42	0.35	0.32	0.102	0.000	1.02
4-11C	0.040	52.1	0.57	0.38	0.31	0.26	0.26	0.083	0.001	0.83
4-12C	0.370	52.2	1.44	0.99	0.78	0.71	0.67	0.210	0.003	2.10
4-14C	0.089	59.3	1.28	1.18	1.05	0.92	0.87	0.275	0.098	2.75
4-15C	0.372	56.0	1.07	0.95	0.88	0.77	0.74	0.235	0.082	2.35
4-16C	0.072	56.4	0.66	0.51	0.44	0.38	0.37	0.117	0.007	1.17
4-17C	0.050	52.3	1.02	0.72	0.55	0.55	0.47	0.147	0.001	1.47
4-18C	0.059	71.3	0.83	0.54	0.5	0.42	0.41	0.129	0.004	1.29
4-19C	0.421	38.7	0.83	0.56	0.47	0.41	0.38	0.125	0.001	1.25
4-21C	0.229	48.2	1.54	1.32	1.12	1.09	0.98	0.311	0.076	3.11
4-22C	0.024	63.4	0.76	0.52	0.5	0.43	0.41	0.130	0.009	1.30
4-23C	0.094	48.0	1.23	0.9	0.7	0.62	0.58	0.185	0.002	1.85
4-24C	0.066	46.0	1.37	0.81	0.86	0.71	0.61	0.193	0.006	1.93
4-25C	0.913	52.6	0.66	0.53	0.46	0.38	0.4	0.127	0.016	1.27
4-26C	0.052	60.8	0.77	0.66	0.54	0.48	0.47	0.150	0.020	1.50
4-27C	0.086	56.7	2.35	1.75	1.48	1.36	1.23	0.389	0.043	3.89
4-28C	0.066	61.3	2.4	2.15	1.8	1.6	1.48	0.469	0.179	4.69
4-30C	0.095	52.2	1.31	0.94	0.84	0.78	0.65	0.205	0.006	2.05

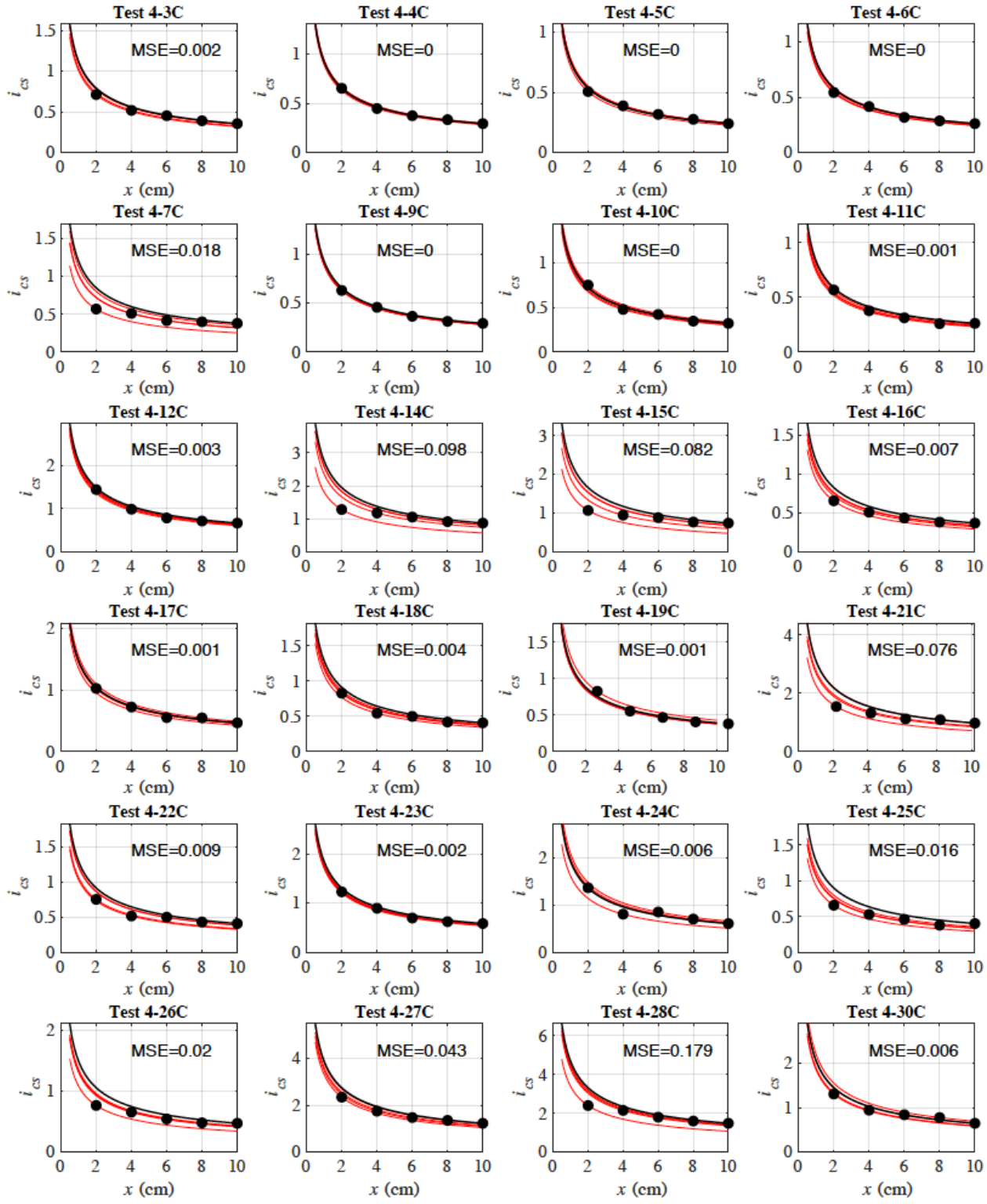

Figure 4.9. Comparison of measured CSGF to analytical fit for all 24 tests (black curve for x=10cm)

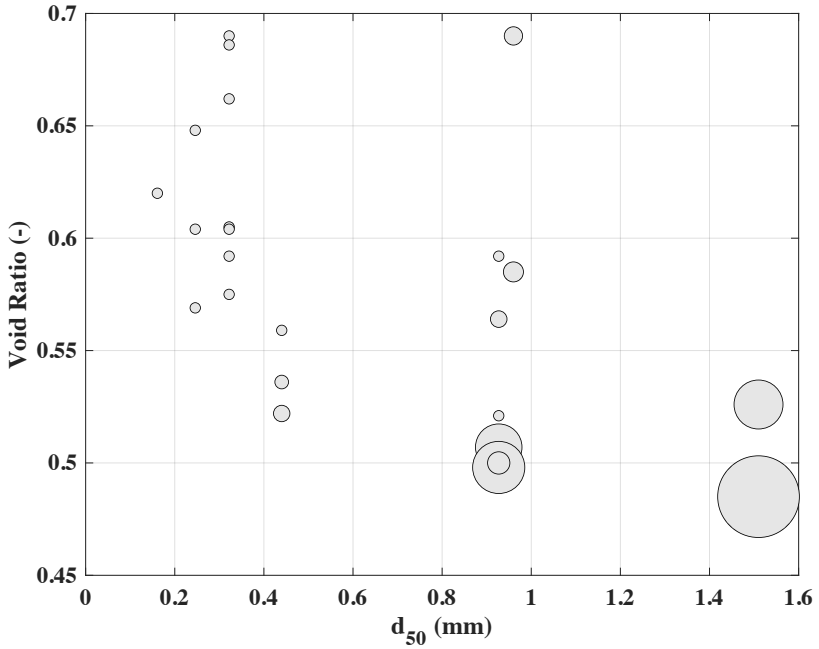

Figure 4.10. Mean squared error (as indicated by circle diameter) of analytical fit as a function of grain size and void ratio.

4.6 Prediction of i_{cs}

While the previous sections have demonstrated how the CSGF can be measured in the laboratory, it is also highly desirable to be able to predict the CSGF indirectly from soil properties. If this can be done accurately, it negates the need for the expensive laboratory tests discussed in the previous sections. The CSGF was defined by Equation 3.25, which is given below for convenience. Because the CSGF is defined by the single scalar value C, only an approach for predicting the value of C is needed to predict the CSGf.

$$i_{cs}(x) = Cx^{-0.5}$$

To develop a preliminary approach for predicting the CSGF, a statistical analysis of the C values in Table 4.3 was performed. Prior knowledge regarding trends in BEP studies informed the analysis. Schmertmann (2000), Sellmeijer et al. (2011), van Beek (2015), and Allan (2018) have demonstrated that soils become more resistant to piping with increasing grain size,

uniformity coefficient, and soil density. Based on this knowledge, trends between the calculated C values and these three soil properties were evaluated (Figure 4.11). The value of C appears to decrease nonlinearly with increasing void ratio, but increases linearly with increasing coefficient of uniformity and median grain diameter. Based on these trends, a predictive relationship of the form shown as Equation 4.2 is proposed where $d_{50,\mu}$, $C_{u,\mu}$, and e_μ represent the mean values of d_{50}, C_u, and e for the data set. For the data in this study, the values of $d_{50,\mu}$, $C_{u,\mu}$, and e_μ were 0.581, 2.02, and 0.581 respectively.

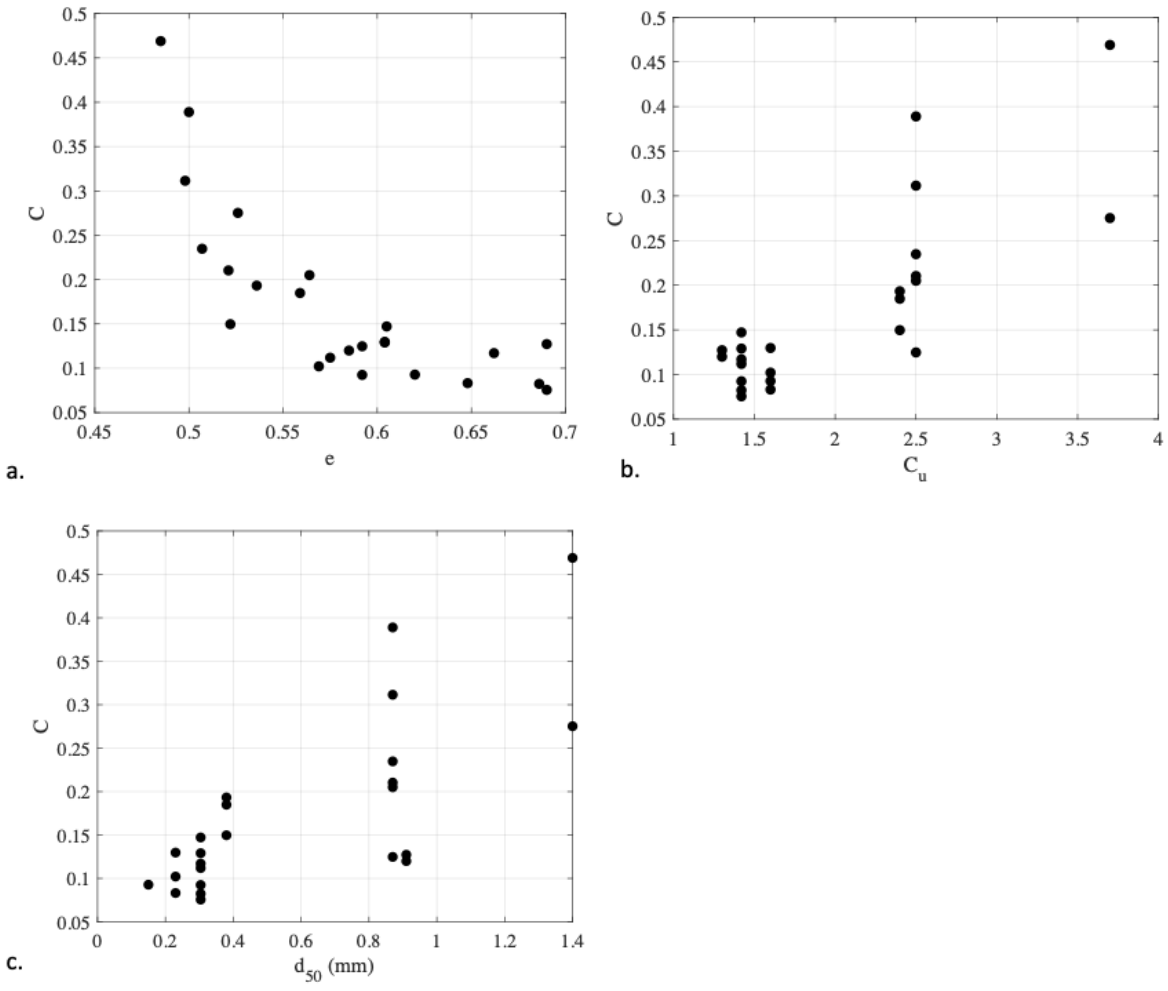

Figure 4.11. Relationships between soil properties and C values in Equation 3.25.

The proposed relationship was fit to the data yielding Equations 4.2 through 4.5 for the regression coefficients where $t_{\left(1-\frac{\alpha}{2},20\right)}$ is the value of the $100(1-\frac{\alpha}{2})$ percentile of the student's t-distribution for 20 degrees of freedom. The best estimate of the coefficients is obtained by setting the value of $t_{\left(1-\frac{\alpha}{2},20\right)}$ to zero, whereas the upper and lower confidence intervals can be obtained at a desired significance level by evaluating the t-distribution values. The prediction model for C fit the measured C-values in Table 4.3 quite well, yielding an R^2 value of 0.90. The p-values for the coefficients β_1, β_2, β_3, and β_4 were 0.28, 0.000002, 0.33, and 0.002 suggesting that C_u is the most influential parameter. This is consistent with the previous findings of Schmertmann (2000) and Allan (2018). However, for uniform soils, the other variables are still very relevant. For this reason, all explanatory variables were left in the predictive model. The predicted C values obtained from the model are plotted against the measured values in Table 4.3 in Figure 4.12. As illustrated by this figure, the model provides a suitable explanation of the variation in C-values for the sands tested. To compare the model to the test results in more detail, the predicted CSGF function obtained for each experiment using Equation 4.2 was compared to the measured values (Figure 4.13). For the majority of the experiments, the measured CSGF values fell within the predicted 95% confidence intervals. This indicates that Equation 4.2 is able to reliably predict the experimentally measured CSGF values for the experiments conducted in this study. Additional measurements are needed to further evaluate the proposed predictive model.

$$C = \beta_1\left(\frac{d_{50}}{d_{50,\mu}}\right) + \beta_2\left(\frac{C_u}{C_{u,\mu}}\right) + \beta_3\left(\frac{e}{e_\mu}\right)^{\beta_4} \tag{4.2}$$

$$\beta_1 = 0.019 \pm 0.017\, t_{\left(1-\frac{\alpha}{2},20\right)} \tag{4.3}$$

$$\beta_2 = 0.115 \pm 0.021\, t_{\left(1-\frac{\alpha}{2},20\right)} \tag{4.4}$$

$$\beta_3 = 0.006 \pm 0.007\, t_{\left(1-\frac{\alpha}{2},20\right)} \tag{4.5}$$

$$\beta_4 = -19.8 \pm 5.647\, t_{\left(1-\frac{\alpha}{2},20\right)} \tag{4.6}$$

In addition to Equation 4.2, trends were assessed specifically for 40/70 sand as it was the sand with the largest number of test results. A very strong correlation was found between the measured C-values and the hydraulic conductivity for this sand (Figure 4.14). This relationship should not be used for other sands as the influence of grain size and coefficient of uniformity are not accounted for. However, the knowledge that there is a strong linear correlation between k_h and the measured C-value is a significant observation for future research into the CSGF.

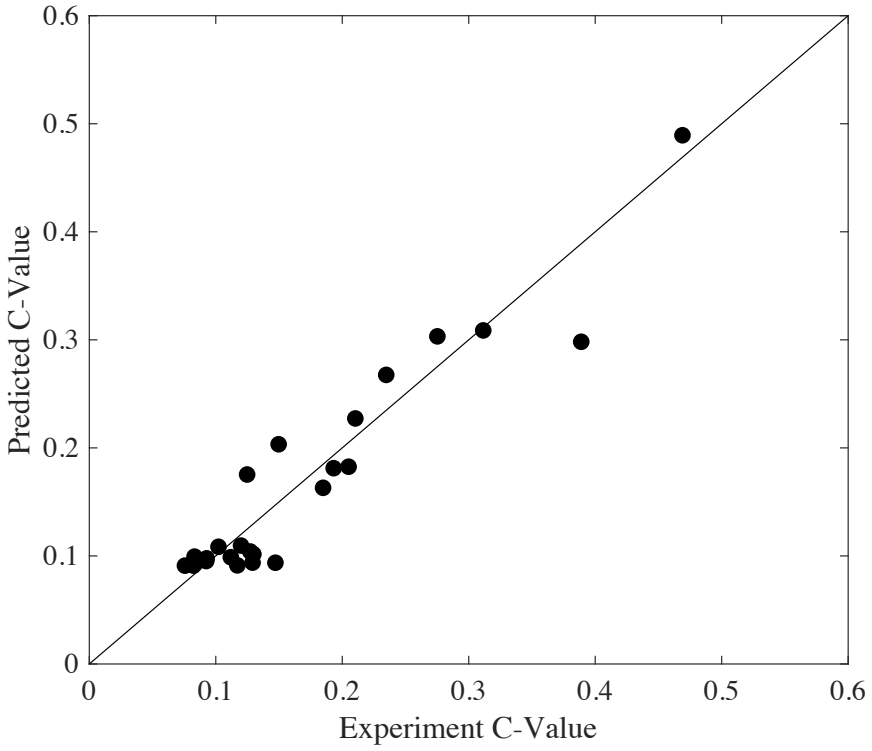

Figure 4.12. Comparison of predicted and measured C-values.

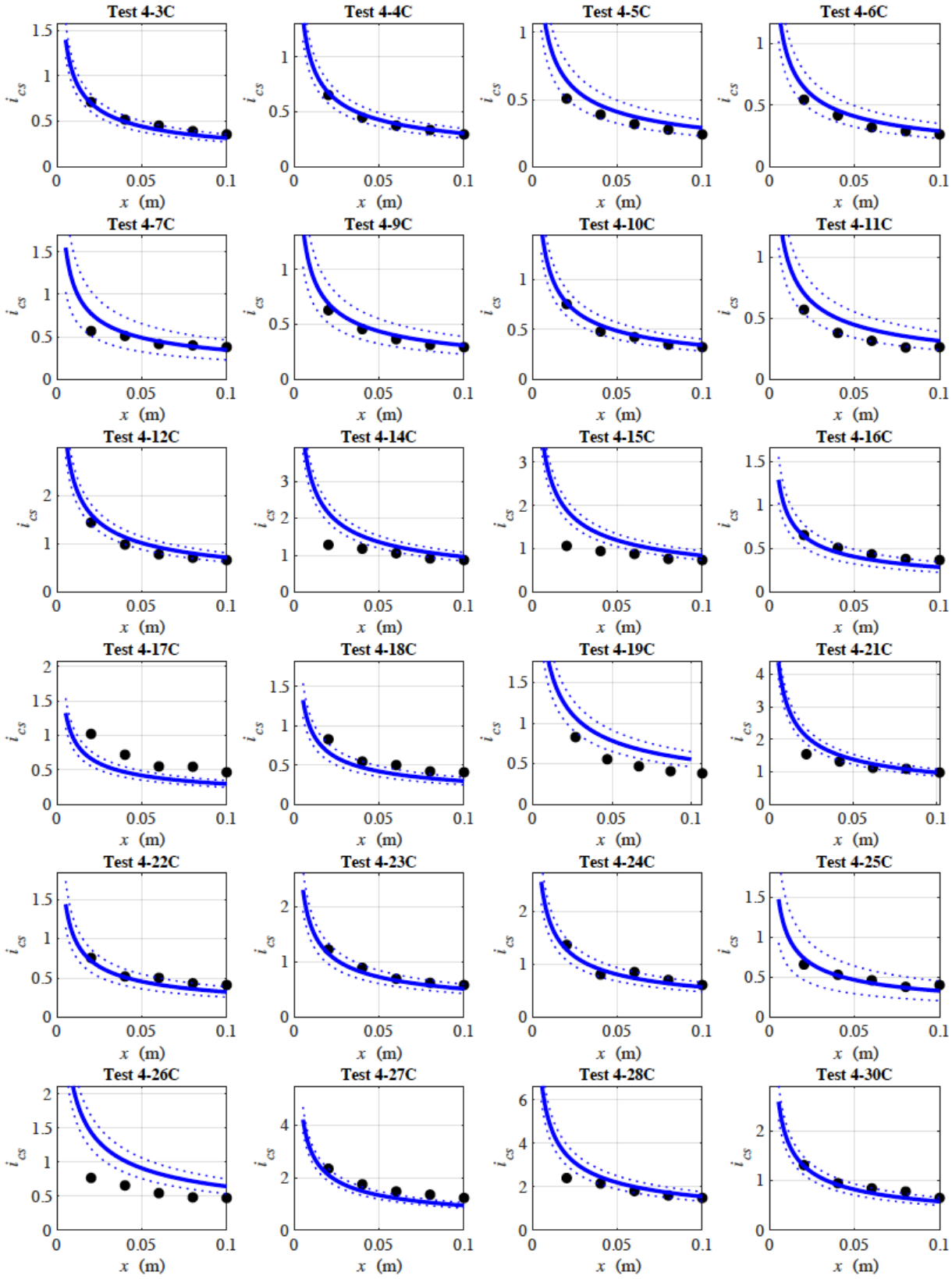

Figure 4.13. Comparison of precited CSGF to measured results with 95% confidence intervals..

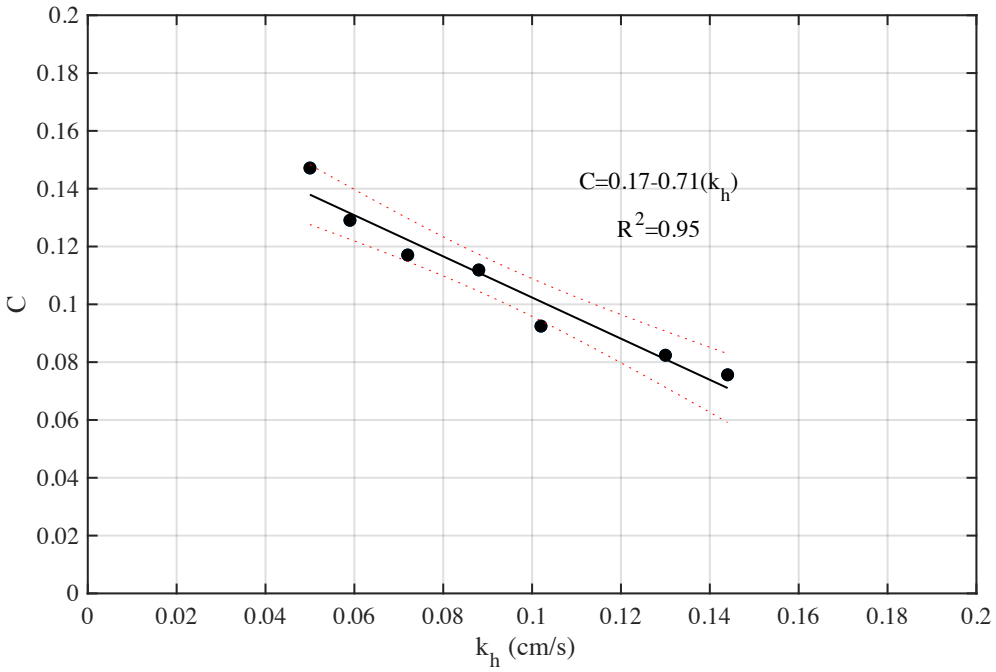

Figure 4.14. Relationship between C-value and hydraulic conductivity for 40/70 sand.

CHAPTER 5

MODEL VALIDATION: SIMULATION OF LABORATORY EXPERIMENTS

Based partially on a paper published in *Geomechanics for Energy and the Environment**

B.A. Robbins[1], V.M. van Beek[2], J.C. Pol[3], and D.V. Griffiths[1]

One of the primary limitations of previous studies on modeling of BEP is the lack of incremental validation of the modeling approaches. As noted in Chapter 2, previous studies on numerical modeling of BEP have calibrated models to reproduce various behaviors observed in erosion tests. Rotunno et al. (2019) conducted the most robust validation of a BEP numerical model that has been performed by validating their model against 4 separate large scale tests. However, the model was validated on the basis of the critical differential head, the overall flow rate, and the observed pipe position. The hydraulic solution in the pipe was not validated, and the calibrated values of the model parameters were not checked against physical measurements. Validation of other numerical modeling studies has been even more limited. This has greatly restricted the adoption of BEP numerical models as it has made it difficult to establish confidence in the results. The limited comparisons to physical measurements has also made it impossible to relate model parameters to quantities that can be independently determined.

To overcome this limitation, this chapter takes an incremental approach to validating the BEP model through detailed comparisons with various experiments from the literature. The first experiment examined is used to validate the coupled hydraulic solution of the groundwater flow and pipe flow, including validation of the approaches taken for determining the pipe dimensions.

[1] Colorado School of Mines, Civil and Environmental Engineering
[2] Deltares
[3] Delft University of Technology, Civil Engineering and Geoscienses
*See Appendix C for permission and citation

The first example also provides one data point for validating the CSGF's that were measured in Chapter 4. The second experiment examined is used to independently validate both the concept of measuring the CSGF and the pipe progression algorithm. This is achieved by modelling a completely independent laboratory experiment on the sands for which the CSGF was measured in Chapter 4. Finally, a series of larger scale experiments from Allan (2018) is simulated to validate the numerical model and CSGF at larger scales.

5.1 Experiment Simulation 1 – Validation of Hydraulic Solution and CSGF

A series of piping experiments were conducted in the Netherlands in rectangular samples with a restricted pipe path and dense array of pressure measurements. Because of the sample geometry and high sensor density, these tests provide a perfect data set for validation of BEP models. One test with test number B25-245 was particularly well suited for comparison purposes because (1) the pipe passed directly beneath the sensors and (2) the critical head was gradually approached such that the pipe stopped in equilibrium and the erosion channel cleared of sediment. This scenario matches the assumptions of the BEP model previously described and provides an excellent opportunity to validate the numerical model and evaluate errors that exist in the solutions. A brief overview of this experiment is provided in the sections that follow. For further experiment details, refer to Pol et al. (2022). The following sections are excerpts from Robbins et al. (2022). The experimental work reported was conducted by Joost Pol; and all numerical work was conducted by the author.

5.1.1 Experiment Description

The experiment consists of a rectangular soil sample that is 0.48 m in length, 0.30 m in width, and 0.10 m in depth as illustrated in Figure 5.1. The sample has a constant head upstream boundary condition on the entire upstream wall of the box. The downstream outlet consists of a

single hole through the acrylic top with a diameter of 6 mm. The differential head between the upstream and downstream water levels is incrementally increased to cause erosion to occur. For each head applied, the pipe is allowed to come to equilibrium at a given pipe length before the head is increased further. Once the critical differential head is reached, the pipe progresses the remainder of the way through the sample without stopping and the test is terminated.

As shown in Figure 5.1, pore pressure measurements were made at 2cm intervals along the pipe path to measure the head profile along the centerline of the sample. Pore pressures were measured by differential pressure transducers (Sensortechnics RPOP001D6A) through the ports P1-P19 at a sampling frequency of 10 Hz. A photograph of the piping test is provided in Figure 5.2. The test reported here was conducted on Baskarp B25 sand, which was also one of the sands for which the CSGF was measured in Chapter 4. The characteristics of the sand are given in Table 4.1.

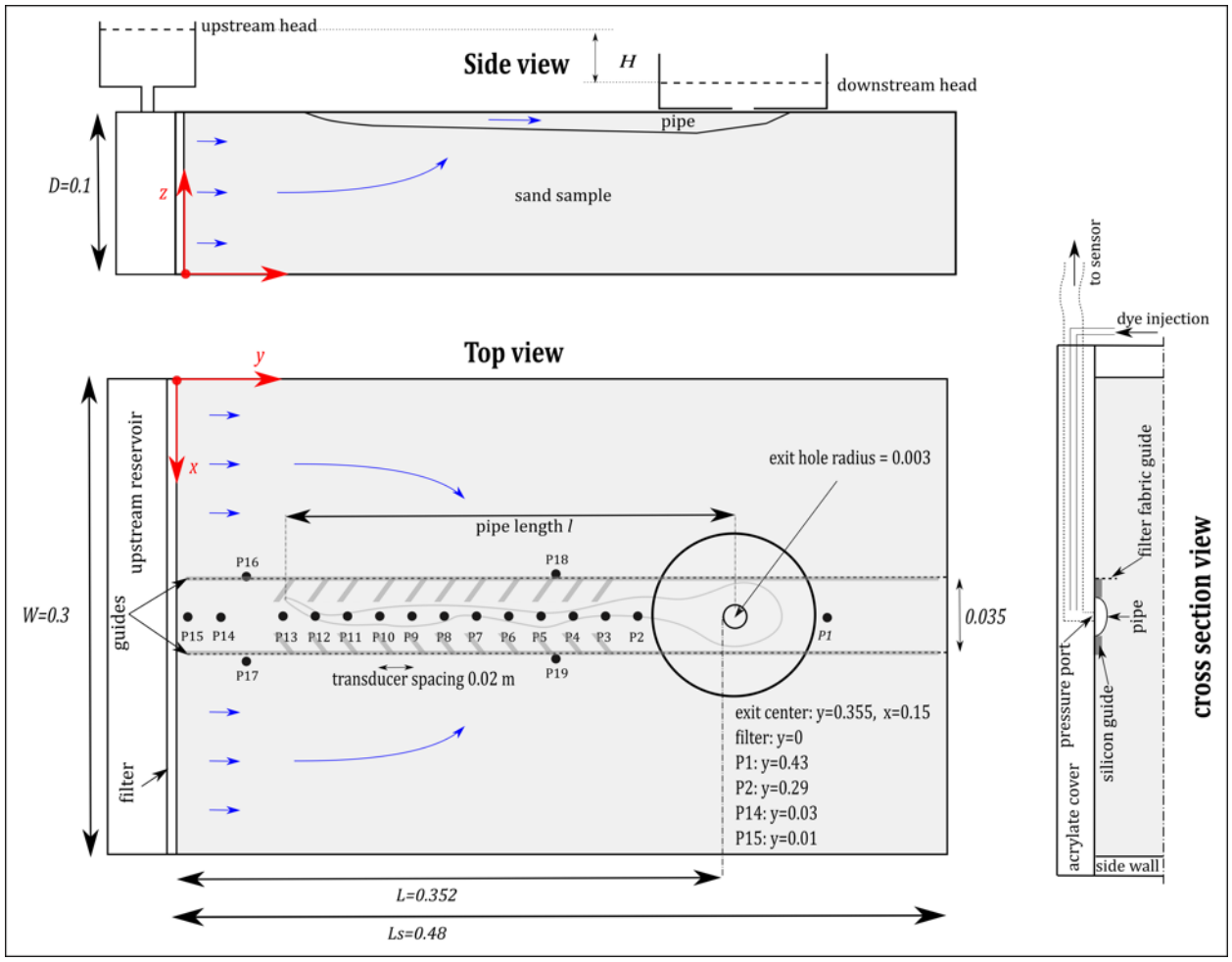

Figure 5.1. Experimental setup (Pol et al., 2022).

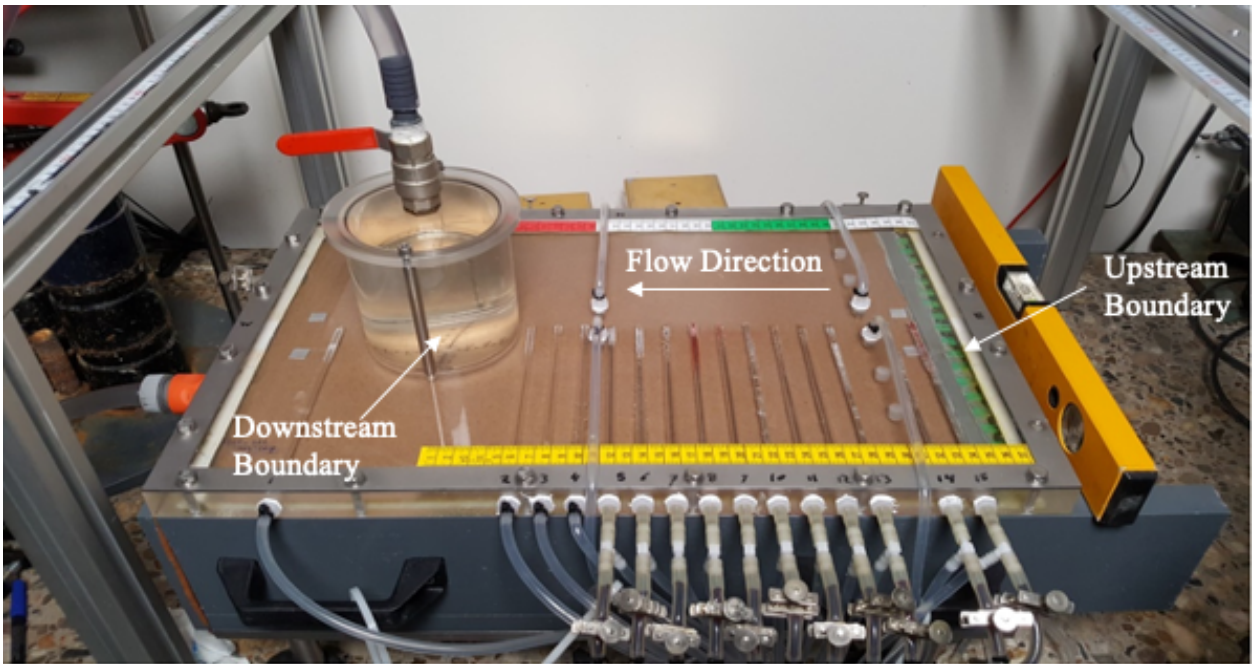

Figure 5.2. Photograph of the experiment.

The sample was prepared with the box in the vertical position with the upstream end of the box resting on a table. Dried sand was rained into de-aired water in the box and compacted by tapping the box with a hammer. Then the box is closed and placed in the horizontal position, and the head at both sides of the sample is leveled. The differential head was then gradually increased in intervals by lowering the downstream water level. The differential head was held constant at each interval until the pipe came to equilibrium and no further erosion was visible. Throughout the test, the pipe location was recorded with a camera, and the pressures were recorded.

5.1.2 Experimental Results

The erosion process observed can be broken down into three phases: fluidization at the exit, regressive erosion, and progressive erosion. These three phases are shown relative to the differential head applied to the sample and corresponding pipe position in Figure 5.3. As the

differential head was increased, the sand near the exit hole fluidized creating a small erosion cavity near the exit. This erosion cavity gradually enlarged until a distinct pipe began to form and progress in the upstream direction. The formation of a distinct pipe marked the beginning of BEP, which begins with the regressive erosion phase in this experiment. During the regressive phase, the pipe would erode upstream with each increase in head and come to equilibrium again. The pipe repeatedly comes to equilibrium because the flowrate increases with each increase in pipe length, and the increased flow rate leads to increased headloss through both the pipe and the exit hole. This incremental erosion process continued until the pipe reached the critical pipe length of 19.7 cm, corresponding to a pipe position of y=0.158 cm at a time of 4,920 seconds. At this point, the increase in the differential head triggered a transition to the progressive erosion phase in which the pipe progressed completely through the remainder of the sample without any further increase in the differential head. The progressive phase begins when the increases in headloss in the pipe and exit hole are no longer sufficient to keep the hydraulic gradient at the pipe tip below the critical value.

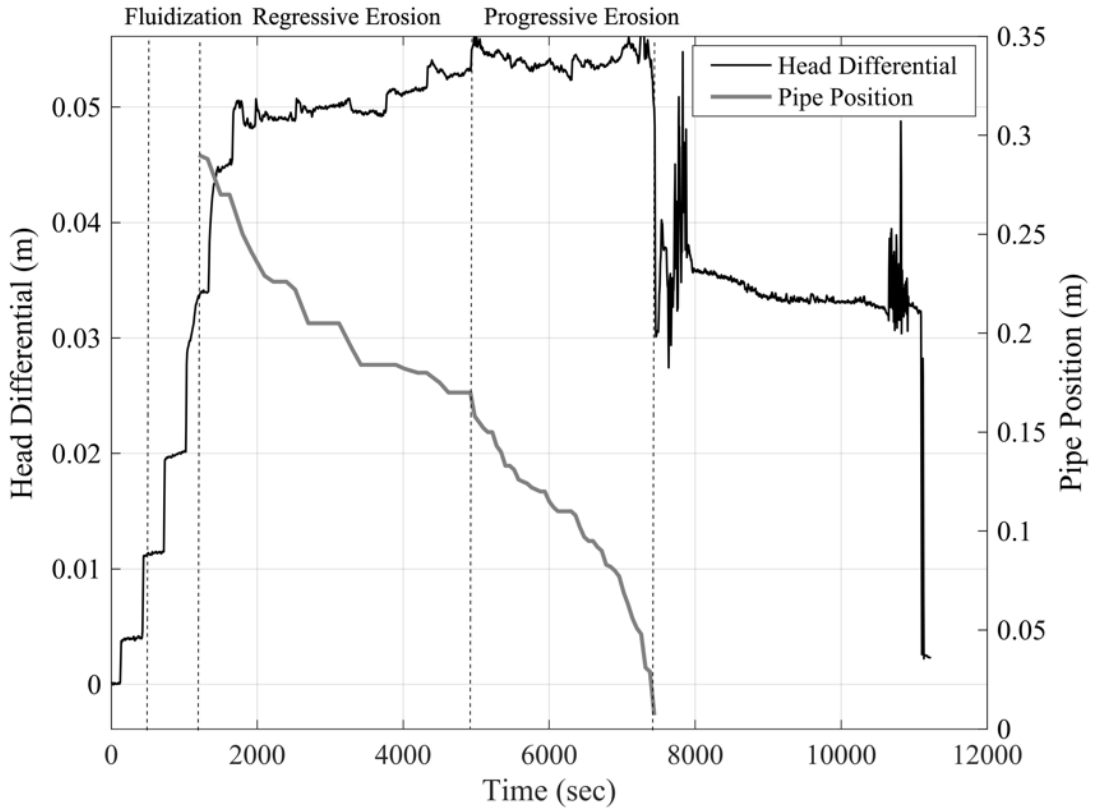

Figure 5.3. Differential head (based on a projection of the 4 upstream [12-15] and 3 downstream [2-4] pressure transducers) and pipe y-position (distance from downstream end of the sample) for test B25-245.

The results of test B25-245 are summarized in Table 5.1. The sand sample had a relative density (D_r) of 0.577. The average hydraulic conductivity was determined to be $k_h = 3 \times 10^{-4}$ m/s based on the measured flow rate and hydraulic gradient. This hydraulic gradient was calculated using a linear fit of the pressures measured by transducers P12 to P15 over the time period from 2,000 to 4,000 seconds. The hydraulic conductivity calculated in this manner was nearly constant for the entire time period as the pipe did not influence sensor P12 during this timeframe. As a result, the calculated value of the hydraulic conductivity was considered to be representative of the undisturbed sand in the entire sample.

Table 5.1. B25-245 Test Results.

Test Number	D_r [-]	e [-]	k [m/s]	*results*			
				H_c [cm]	l_c [cm]	$i_{c,tip}$ [-]	H_{eq} *at y=0.17 m* [cm]
B25-245	0.577	0.672	3×10^{-4}	5.4	19.7	0.43	*5.2*

This particular experiment was conducted to primarily study (1) the value of the critical head, H_c, or differential head that caused progressive erosion, and (2) to investigate the rate of erosion in the progressive phase (Pol et al. 2022). The value of H_c that caused progressive erosion and failure was 5.4 cm which occurred when the erosion pipe was at the critical pipe length of l_c=19.7 cm (corresponding to the pipe tip position of y=0.158m). However, as the focus of the present study is on evaluating FE models of the hydraulic solution with the pipe in equilibrium, the point of interest for this study is the equilibrium condition just prior to H_c being reached. At $t = 4{,}600$ seconds, the pipe was in equilibrium at the position of $y = 0.17$ m with an applied differential head of H_{eq}=0.052 m.

A photograph of the pipe at y=0.17 m is shown in Figure 5.4. The pipe was estimated to be approximately 9 mm in width near the pipe tip and 5-6 mm in width along the erosion pipe. These visual estimates of the erosion pipe width were found to be slightly smaller than the dimensions determined through laser measurements. Unfortunately, no laser measurements of the pipe cross section were obtained when the pipe was in equilibrium at this location. A cross section was measured, however, at the y=0.26 m transect when the pipe tip was located at y=0.22 m (Figure 5.5). From this cross section, we see that the pipe width is approximately 1 cm and the maximum pipe depth is approximately 1.5 mm. The pipe developed an additional 5 cm after this measurement was taken which causes increased flow rates through the pipe. As such, the dimensions of the actual erosion pipe when the tip is at y=0.17 m are likely slightly larger

than that shown in Figure 5.5. The visually obtained measurements of pipe width in Figure 5.4 are thought to be smaller than the laser width due to the fact that extremely shallow edges of the pipe may not be visible in the photograph. As such, the dimensions in Figure 5.5 are thought to be the most reliable assessment of the actual pipe dimensions. The equilibrium position of the pipe shown in Figure 5.4 will be modeled using the finite element model to evaluate how well the modeled solution compares to the head profile obtained from the pressure transducers.

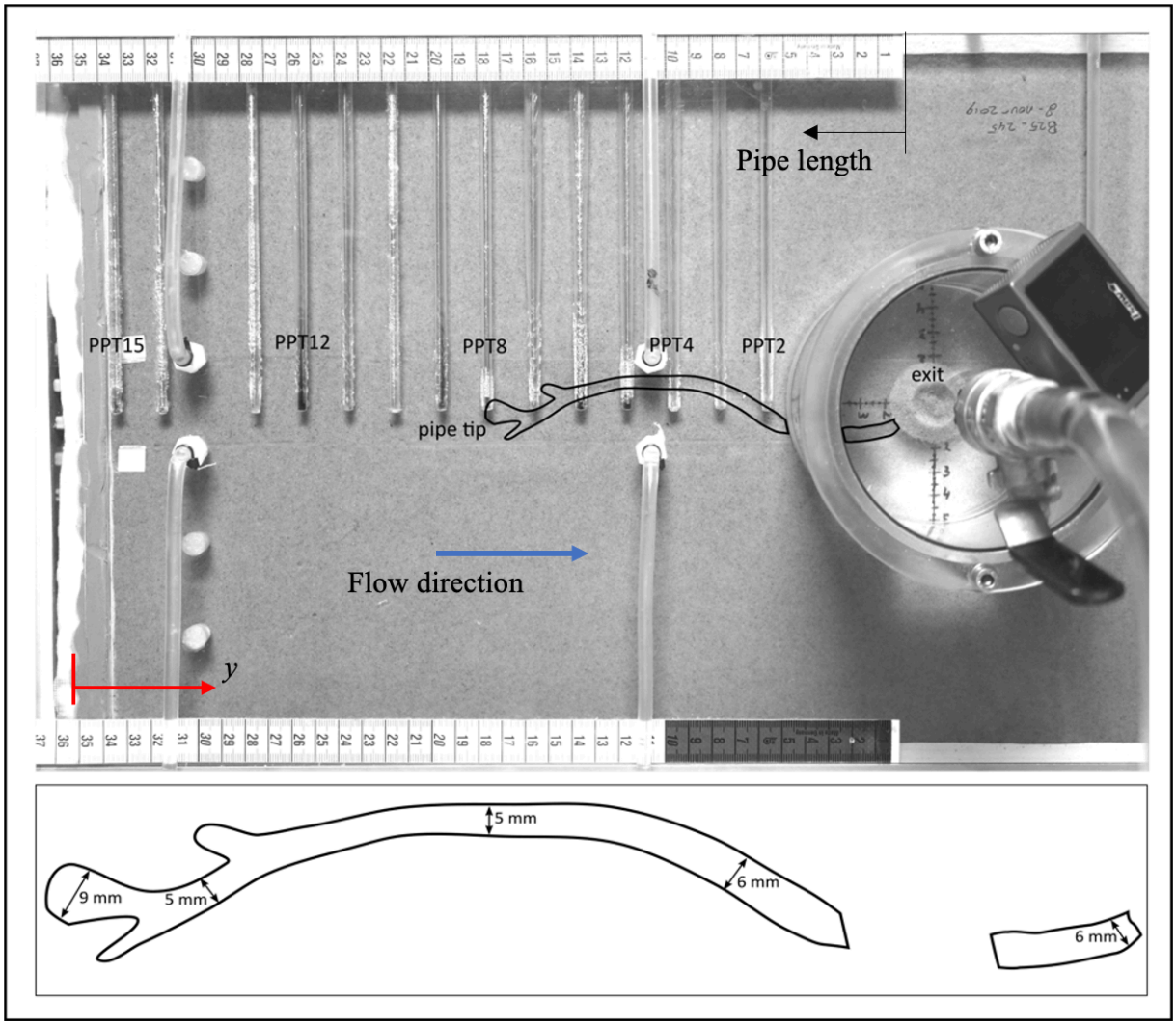

Figure 5.4. Photograph of the experiment with the erosion pipe outlined when in equilibrium at y=0.17m. Visual estimates of the pipe widths were made based upon the photograph scale and visual edge of the pipe in the photograph.

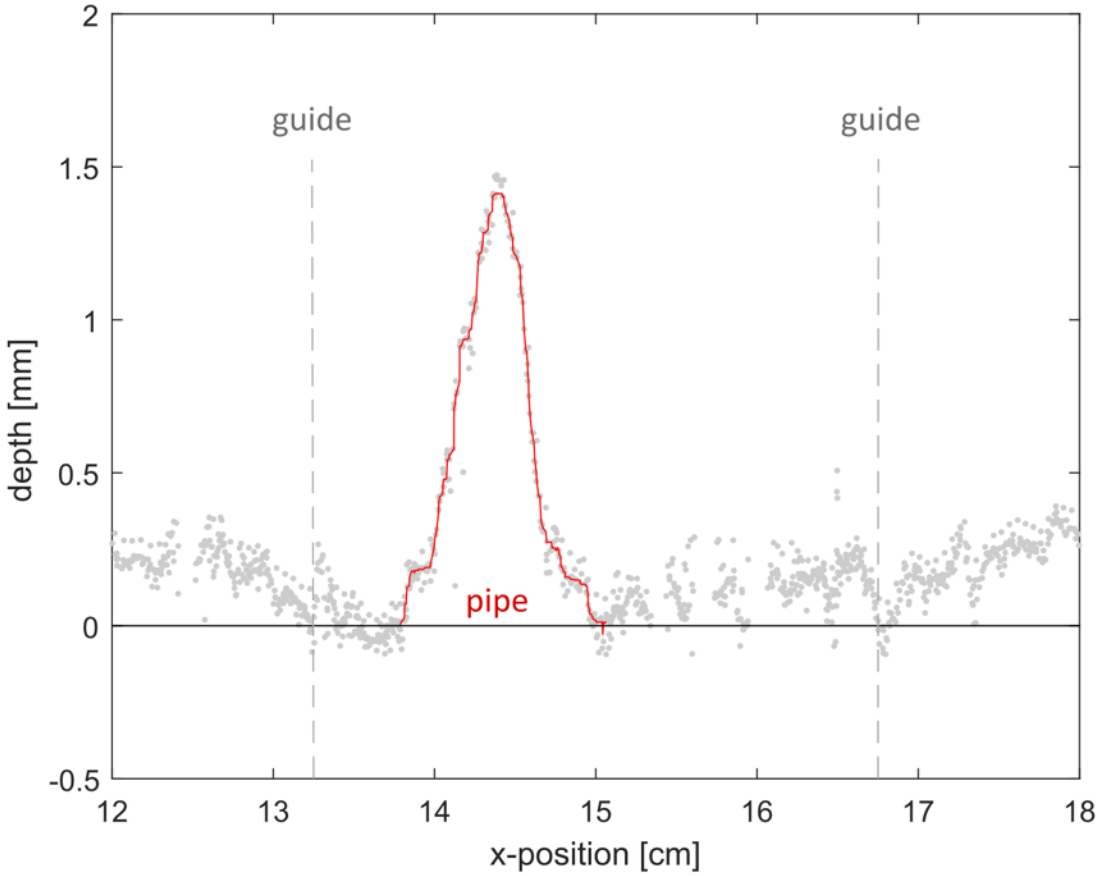

Figure 5.5. Laser cross-section of the pipe taken at y=26 cm when the pipe tip was at y=22 cm. Raw measurement indicated by grey dots and erosion pipe by red line.

5.1.3 Finite Element Analyses

Finite element models of test B25-245 were produced for the condition at t=4,600 seconds with the pipe in equilibrium at y=0.17 m. Models were developed for meshes of varying element sizes and pipe element types (line vs. hex). The following sections describe the various scenarios modeled and corresponding results.

Model Description

The experiment was modeled as a symmetric half space as illustrated in Figure 5.6. The half space was 0.1 m in height, 0.15 m in width, and 0.48 m in length. The downstream

outlet hole was modeled as a 0.02 x 0.02 m square. In the half space model, the outlet dimensions correspond to a 0.01 m wide by 0.02 m long area with constant head boundary conditions set to h=0.0 m. Representing the downstream exit area with a square that was larger than the actual 0.006 m diameter hole was found to be a suitable assumption and did not greatly impact the modelled heads. This is because (1) a void formed around the hole due to fluidization of the sand thereby creating an exit area larger than the hole alone and (2) the majority of the head loss was away from the exit hole due to the erosion pipe.

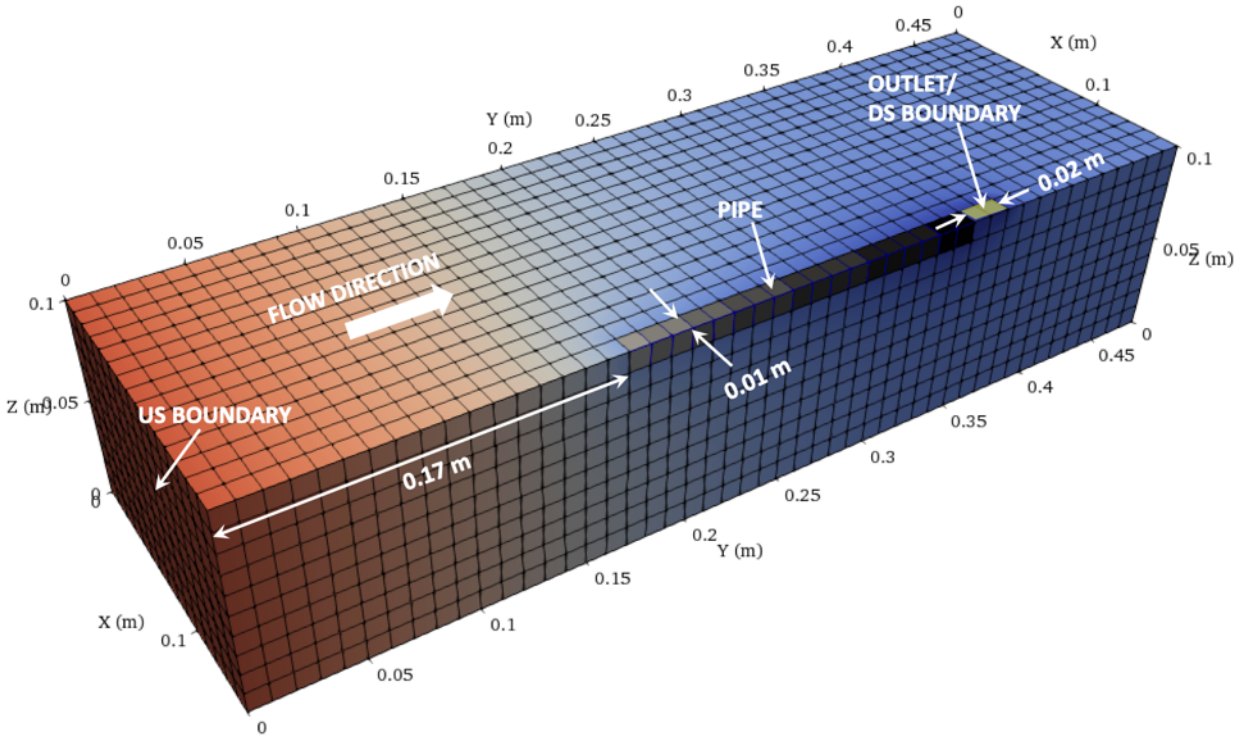

Figure 5.6. Illustration of the symmetric half-space finite element mesh for representing the experiment. Example shown used 1 cm elements and hexahedral pipe elements.

The erosion pipe was set to extend from the downstream exit area to a position 0.17 m from the upstream boundary. Models were run using the three-dimensional approximate approaches with the pipe represented by hexahedral pipe elements (as shown in Figure 5.6), quadrilateral planar elements, and 1D line elements to represent the pipe. When the pipe was

represented by hexahedral or quadrilateral elements, the width of the erosion pipe was determined by the total width of the elements used to represent the pipe. The pipe was fixed to a half space width of 0.01 m (0.02 m in total width) in all models using hexahedral and quadrilateral elements to achieve precisely the same geometry with varied element sizes. If the pipe width was not fixed, the geometric evolution of the pipe would be more refined with smaller element sizes. As a result, the simulation results would not be directly comparable, hence the reason why the pipe width was fixed to a common width for all simulations in this section. Element sizes of 0.01 m, 0.005 m, and 0.002 m were used such that the pipe was represented using 1 element, 2 elements, and 5 elements to ensure the half space pipe width of 0.01 m remained constant when using different element sizes. In addition, one additional analysis with 0.005 m elements was run using a pipe width of 0.005 m (one element) to assess the influence of the pipe geometry on the results.

Models using 1D line elements for the pipes were also developed using mesh sizes of 0.01, 0.005, and 0.002 m elements. When using line elements, the width of the pipe was set to be a ratio of the pipe depth. A width (w) to depth (a) ratio of w/a=20 was applied such that the cross-sectional area of the erosion pipe in the halfspace was given by

$$\frac{wa}{2} = a \cdot a \cdot \frac{w}{2a} = 10a^2 \tag{5.1}$$

The choice of w/a=20 was made in an attempt to represent a similar pipe width as the 1cm hexahedral representation for a pipe with an average depth of 1 mm (Figure 5.5). That is, for a depth of 1 mm, a w/a ratio of 20 yields a pipe width of 20 mm which corresponds to a width of 10 mm, or 1 cm, in the halfspace model. In addition to making this assumption for line elements, an analysis was also conducted using line elements with the pipe width for the line elements fixed to 1 cm (regardless of pipe depth) to precisely match the scenario modeled with the

hexahedral elements. Lastly, an analysis was also conducted with w/a=10 to match the geometry of the actual pipe cross section shown in Figure 5.5.

The soil properties used in the models are provided in Table 5.2. The critical shear stress of the sand was determined by Pol et al. (2022) to be 0.37 Pa. This is higher than the value of 0.31 Pa that one would obtain using Equation 2.11 to predict τ_c which is an artifact of Equation 2.11 being a conservative lower bound of the critical shear stress measurements (Figure 3.7). As the purpose of this section is to validate the numerical model, the measured value of 0.37 will be used to model the experiment as accurately as possible. The hydraulic conductivity and grain size were measured as described previously.

Table 5.2. Sand properties used in finite element models.

Test Number	τ_c [Pa]	k_h [m/s]	d_{50} [mm]
B25-245	0.37	3.00E-04	0.228

To model the equilibrium conditions in test B25-245, the boundary conditions were set to the equilibrium boundary conditions in the experiment (h=0.052 m upstream, h=0.00 m downstream) with the pipe elements activated over the full critical pipe length as shown in Figure 5.6. Iterations were conducted over the pipe depth in all pipe elements until the pipe depth was determined that satisfied the sediment equilibrium conditions. Once the pipe depth was determined, the coupled hydraulic solution was obtained which yielded the head distribution in the soil and the erosion pipe. The solutions obtained will be compared to the measured head values in the following section.

Results

The measured heads from the B25-245 experiment are compared to the modeled head distributions obtained from the finite element models in Figures 5.7, 5.8, and 5.9. Figure 5.7 compares the head profiles obtained from simulations with line elements representing the erosion pipe to the measured heads. Figure 5.8 compares the head profiles obtained from simulations using hexahedral and quadrilateral pipe elements. Finally, Figure 5.9 compares the line element simulations with fixed pipe widths of 1cm and 5mm to the equivalent hexahedral simulations to evaluate the influence of the pipe width assumptions on the results.

A few observations can be made immediately from the results. First, the results obtained using line elements (Figure 5.7) are nearly all identical, regardless of the mesh size. Further, the results obtained using line elements tend to concentrate flow too severely near the upstream pipe tip which results in significant local head loss near the pipe tip and higher head values along the profile than measured. To the contrary, the simulations run with hexahedral pipe elements match the measurements much more closely, with the 1cm and 5 mm hexahedral elements giving the closest match to the measured values. The head profile in the erosion pipe appears to be consistent for fixed pipe geometry assumptions when using quadrilateral or line elements to represent the pipe, but the results with hexahedral elements indicate the pipe hydraulics may be sensitive to mesh size for this formulation. Reasons for this will be explored in subsequent paragraphs.

With regards to the head profile in the erosion pipe, 3 of the measurements appear to match the slope of the hexahedral pipe element simulations conducted with 5mm and 1cm elements as well as the w/a=20 line element simulations (sensors at positions of 0.19, 0.21, and 0.23), while 3 of the measurements appear to match the slope of the line element simulation with w=1 cm

(sensors at positions of 0.25, 0.27, and 0.29). By examining Figure 5.4, it is seen that the pipe did not pass under the sensors at 0.25, 0.27, and 0.29 which may explain the slightly higher head values at these locations. The pipe is directly under the sensors at positions of 0.19, 0.21, and 0.23, however. As such, it appears that the pressure transducer measurements made in these positions are more representative of the actual head values in the erosion pipe.

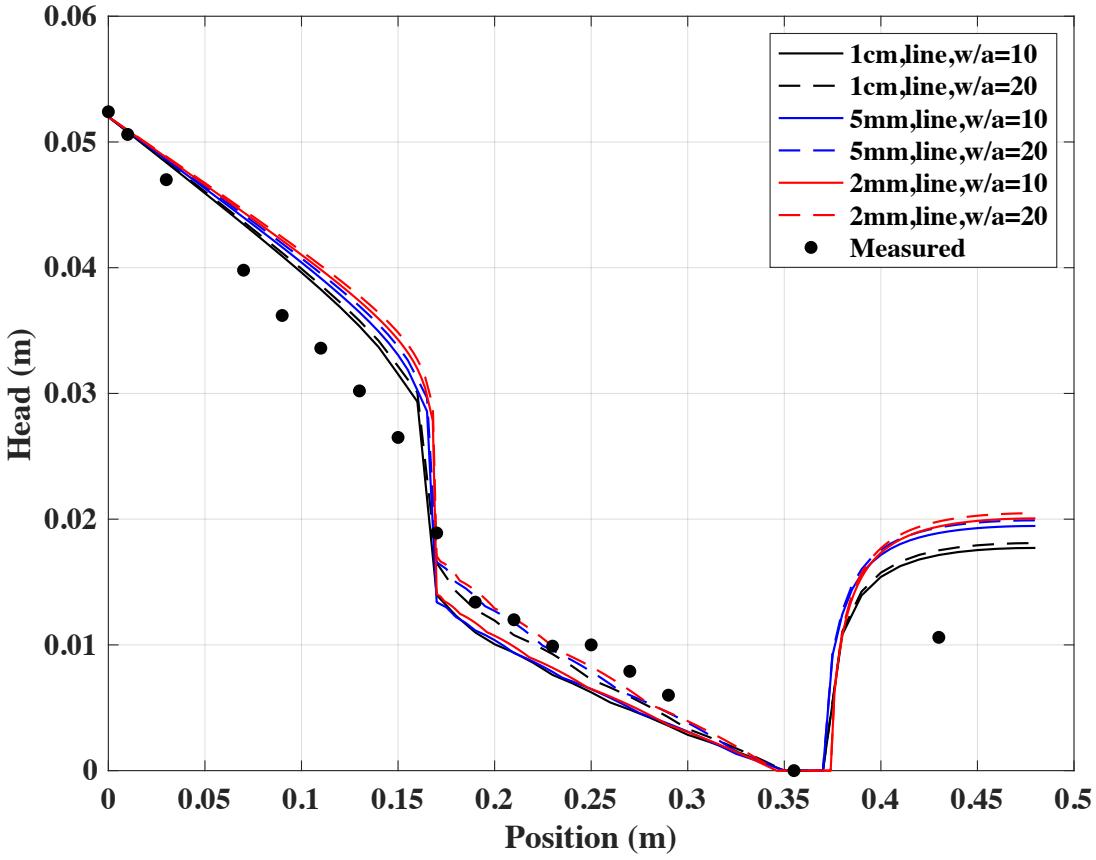

Figure 5.7. Comparison of measured and modeled head distributions for t=4,600 seconds with the pipe tip in equilibrium at y=0.17m for simulations using 1D line elements for the erosion pipe.

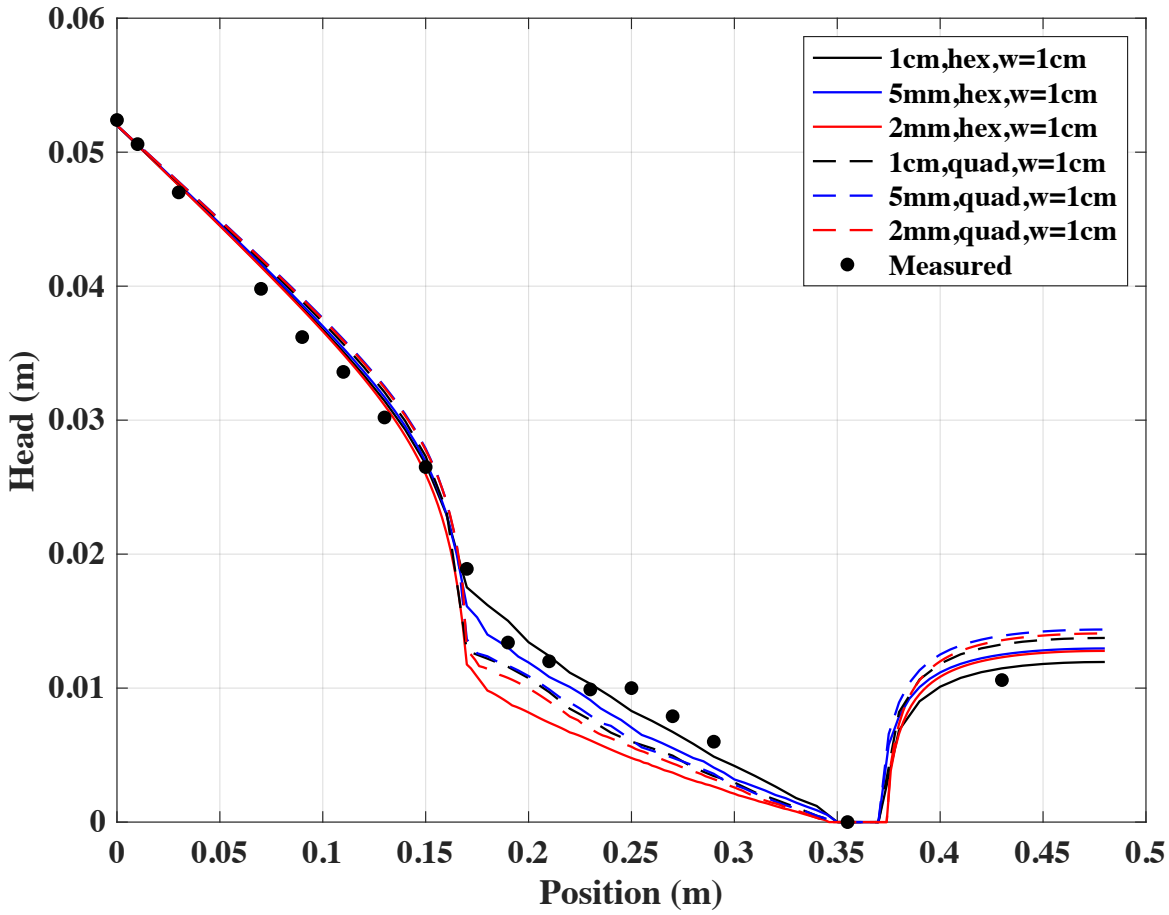

Figure 5.8. Comparison of measured and modeled head distributions for t=4,600 seconds with the pipe tip in equilibrium at y=0.17m for simulations using hexahedral and quadrilateral pipe elements.

The influence of the pipe width on the head profile in the erosion pipe is illustrated by the simulation results with varying pipe width assumptions (Figure 5.9). For both line elements and hex elements, a reduction in the pipe width causes the hydraulic gradient in the pipe to decrease. This is due to the fact that a wider pipe results in shallower pipe depths for the same flow rate, which leads to higher hydraulic gradients for a constant shear stress (Equation 3.28). Additionally, it is interesting to note that the line element with constant width $w = 1$ cm did not

match the simulations using a hexahedral pipe 1 cm in width. The line element with both $\frac{w}{a} =$ 20 and w= 5mm closely matched the measurements. As these dimensions are quite close to the actual pipe width (5mm in half space and w/a=20), this indicates that the line elements accurately represent the true pipe geometry and hydraulics. For hexahedral and quadrilateral elements, however, it appears that the pipe width must be represented as twice the actual pipe width to closely match the pipe hydraulics. The reason for this is not currently clear.

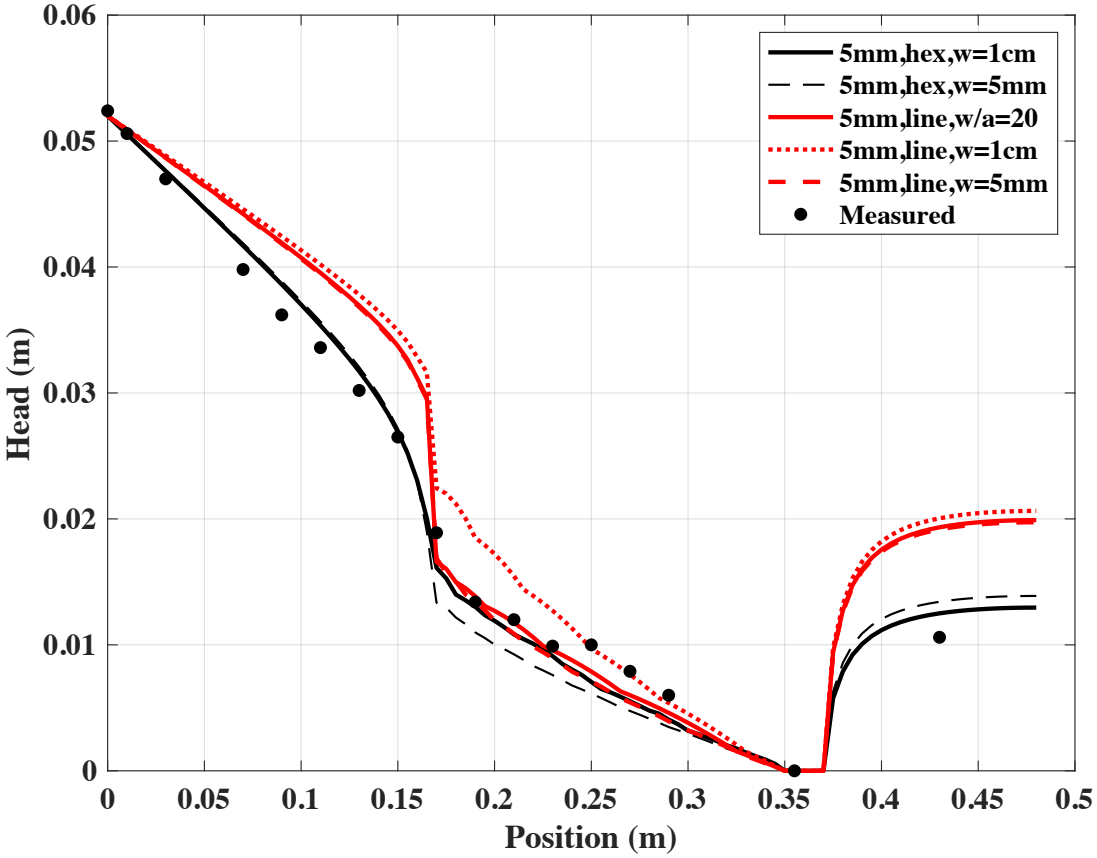

Figure 5.9. Comparison of measured and modeled head distributions for t=4,600 seconds with the pipe tip in equilibrium at y=0.17m for simulations using hexahedral and line pipe elements of varying pipe widths.

The head profile upstream of the pipe tip was reasonably approximated by all of the FE analysis using hexahedral and quadrilateral pipe elements. The head distribution and resulting hydraulic gradients and seepage velocities upstream of the pipe tip are of great interest as most numerical models evaluate pipe progression using these values (Bersan et al., 2013; Fascetti & Oskay, 2019; Liang et al., 2017; Rahimi & Shafieezadeh, 2020; Robbins & Griffiths, 2018; Robbins, 2016; Rotunno et al., 2019; Wang et al., 2014). As one can see from Figures 5.7 and 5.9, the head profiles obtained using line elements are erroneously high. This is more clearly illustrated by examining the secant gradient over various distances in front of the erosion pipe. As the hexahedral and quadrilateral solutions are nearly identical upstream of the pipe, only the hexahedral solutions are used for comparison to the line element solutions. Figure 5.10 shows the secant hydraulic gradient between each position along the profile and the pipe tip at the 0.17 m position. Near the pipe tip location, the hydraulic gradients determined using the line element solutions are significantly higher than their counterparts determined using the hexahedral solutions. By calculating the ratio of the line to hex gradient (Figure 5.11), we see that errors of 50-300% would be obtained when using line elements if the same value of i_{cs} for pipe progression was used in both the hexahedral pipe element and linear pipe element simulations. This is a substantial error that may limit the usefulness of 1D line elements for representing the erosion pipe. Potential explanations for the error in the linear pipe element solutions will be presented in Chapter 7.

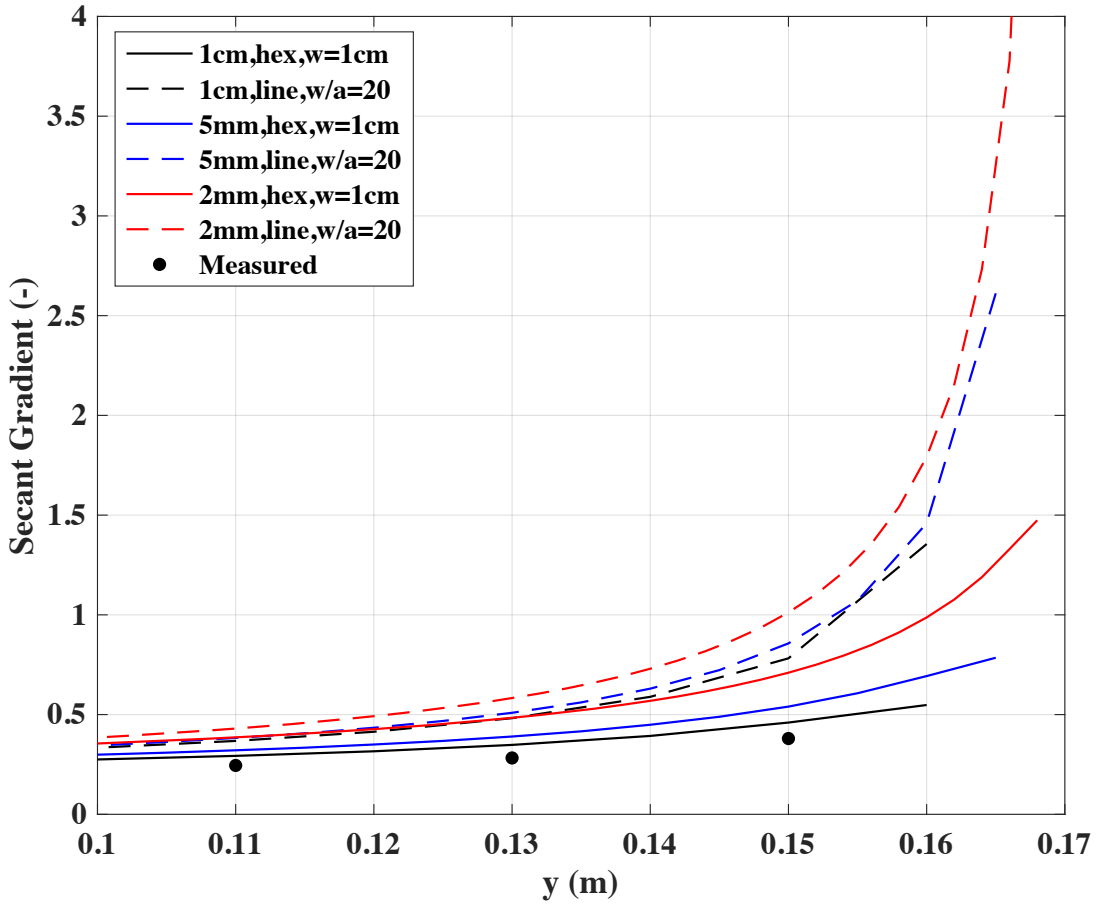

Figure 5.10. Average hydraulic gradient at various positions in front of the pipe tip for FE solutions. (pipe tip is at the 0.17 m position)

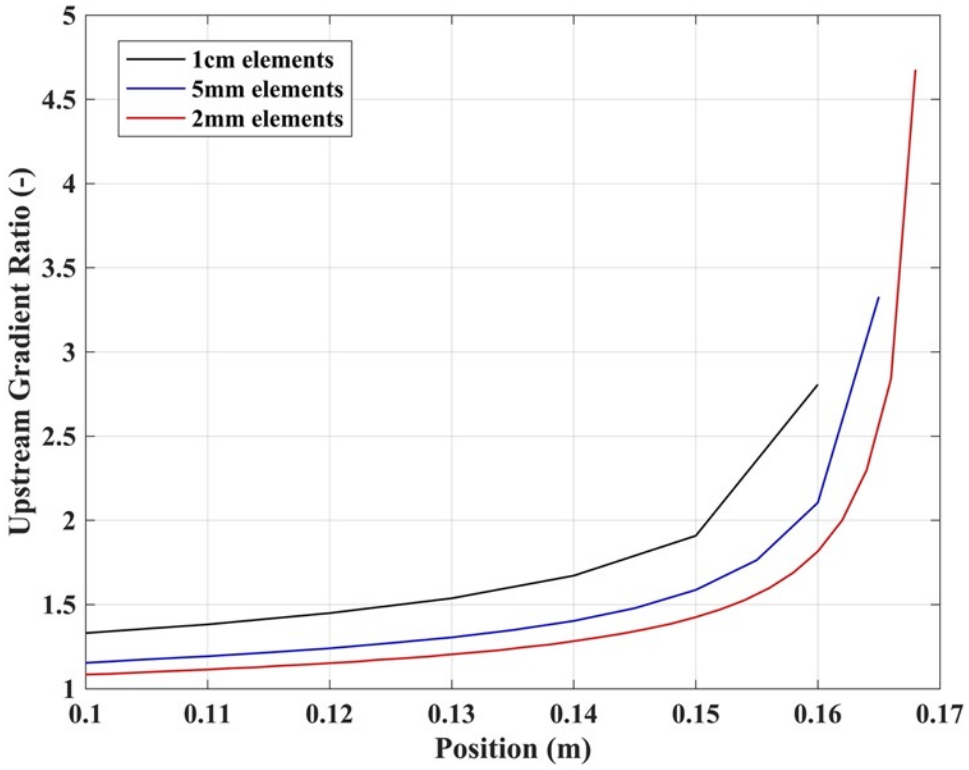

Figure 5.11. Ratio of the hydraulic gradient calculated with 1D line pipe elements to the hydraulic gradient determined using hexahedral pipe elements for mesh sizes of 0.01m.

In addition to evaluating the head profiles and hydraulic gradients, it is also of interest to evaluate the predicted dimensions (namely pipe depth) obtained from the numerical solutions. Figure 5.12 shows the calculated pipe depth profile along the centerline of the model (plane of symmetry in halfspace). The depth of the erosion pipe for the 1cm, hexahedral pipe element solution approaches 1 mm near the end of the pipe. This is similar in magnitude to the actual depth of the erosion channel of 1.5 mm shown in Figure 5.5. While the depth for the 1cm hexahedral solution monotonically increases towards the maximum depth, the hexahedral and quadrilateral solutions obtained with 5 mm and 2 mm elements vary along the pipe profile. This is due to the fact that the pipe does not maintain a constant pipe depth across the full pipe width

(i.e., each pipe element has its own pipe depth). Figure 5.13 shows the calculated depth of the erosion pipe in each pipe element for the 2mm, hexahedral solution. Because the pipe is multiple elements wide, a "main channel" develops that has higher pipe depths than the remainder of the pipe. This narrower, deeper channel that develops results in higher hydraulic conductivities in the deep pipe elements (Eq. 3.39) than if a more uniform, shallower channel were assumed. The higher pipe hydraulic conductivity explains why the 2mm hexahedral solution yielded a lower head profile in the erosion pipe (Figure 5.8). Further, the lower heads in the erosion pipe lead to the higher values of i_{cs} in front of the pipe (Figure 5.10), despite the head profiles in front of the tip being nearly identical. From these observations, we see that the variable pipe depth provides an explanation for the apparent increase in average gradient with decreasing mesh size for simulations with hexahedral pipe elements.

The analysis results thus far have demonstrated that the finite element approximation of BEP erosion provides a suitable approximation of the pipe hydraulics so long as hexahedral or quadrilateral pipe elements are used. This serves as a validation of the models coupled groundwater and pipe flow hydraulic solution. However, it is also necessary to validate the concept of the CSGF for three dimensional scenarios as assessed in the current experiment simulations. The head profile in Figure 5.8 was the last stable head profile before the pipe progressed to failure. As such, this head profile represents the critical head profile for pipe progression. Values of $i_{cs}(x)$ can be calculated from this head profile and compared to the measured CSGF obtained for B25 sand in Chapter 4 from the cylindrical experiments. As the measurements in Figure 5.8 are for more of a three dimensional scenario, this comparison provides an opportunity to validate both the use of the cylindrical measurements and the 2D analytical solution for the CSGF.

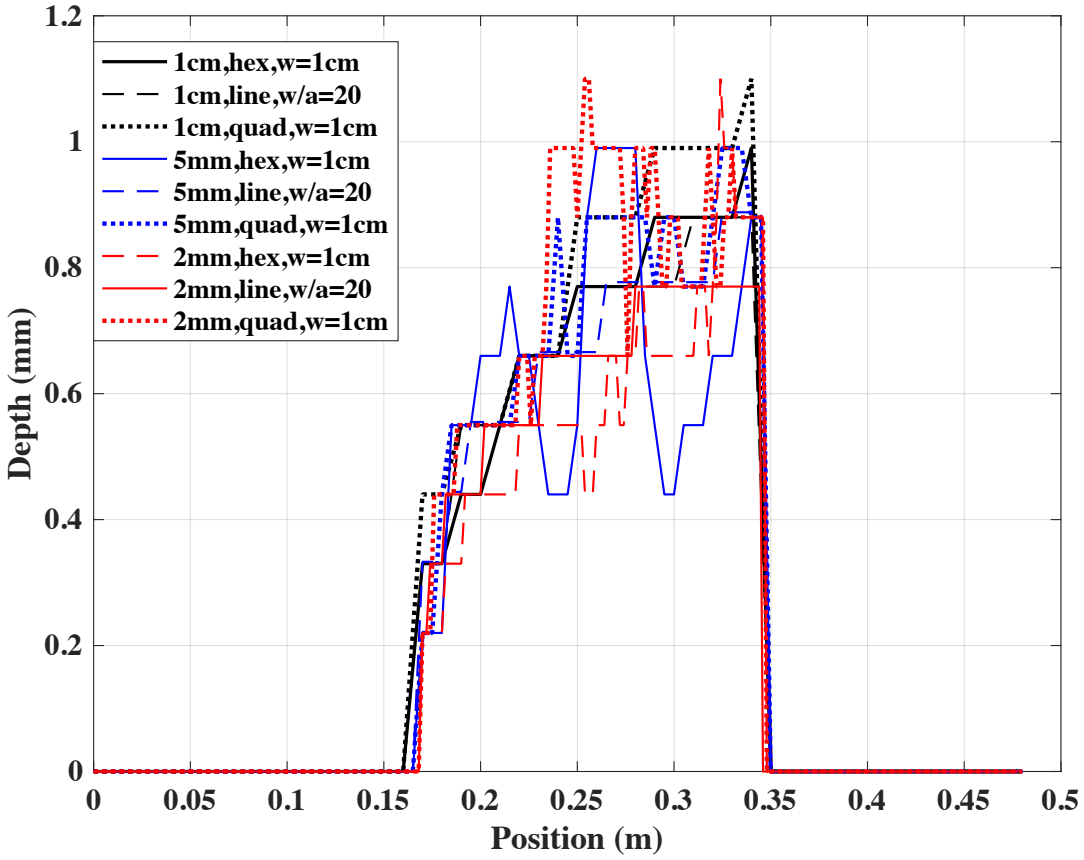

Figure 5.12. Predicted depths of the erosion pipe obtained from the FE numerical solutions.

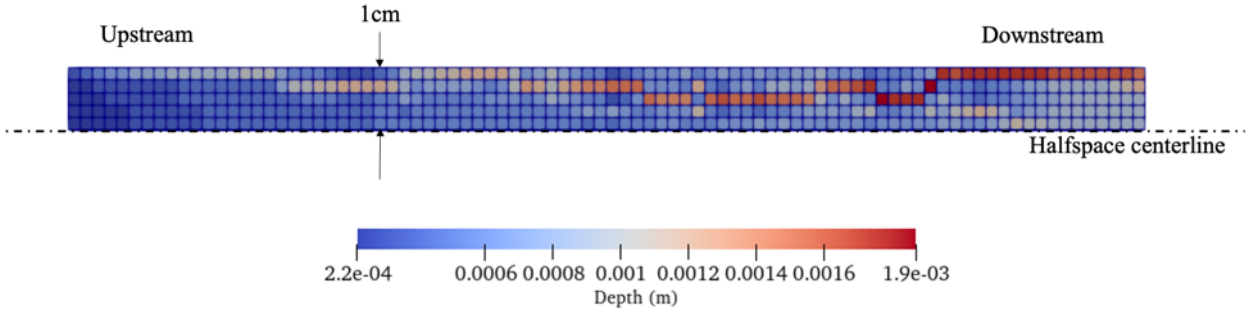

Figure 5.13. Modelled depth of the erosion pipe for the 2mm hexahedral pipe element model (only the pipe domain is shown).

The simulated head profiles obtained for the 1cm and 5mm hexahedral pipe element simulations were selected as being the most representative of the true head profile. These simulations are shown again in Figure 5.14 with the measured head values. Additionally, a straight line projection through the three measurements in the pipe that were deemed to be reliable was made to aide in estimating the head at the pipe tip. From this linear projection, the head at the pipe tip location of x= 0.17 m was estimated to be 0.014 m. The head at a location 1 cm away was estimated from the simulated head profiles to be $h = 0.023$ m. From these points, the value of i_{cs} over 1 cm is calculated as

$$i_{cs}(1cm) = \frac{0.023 - 0.014}{0.01} = 0.90 \tag{5.2}$$

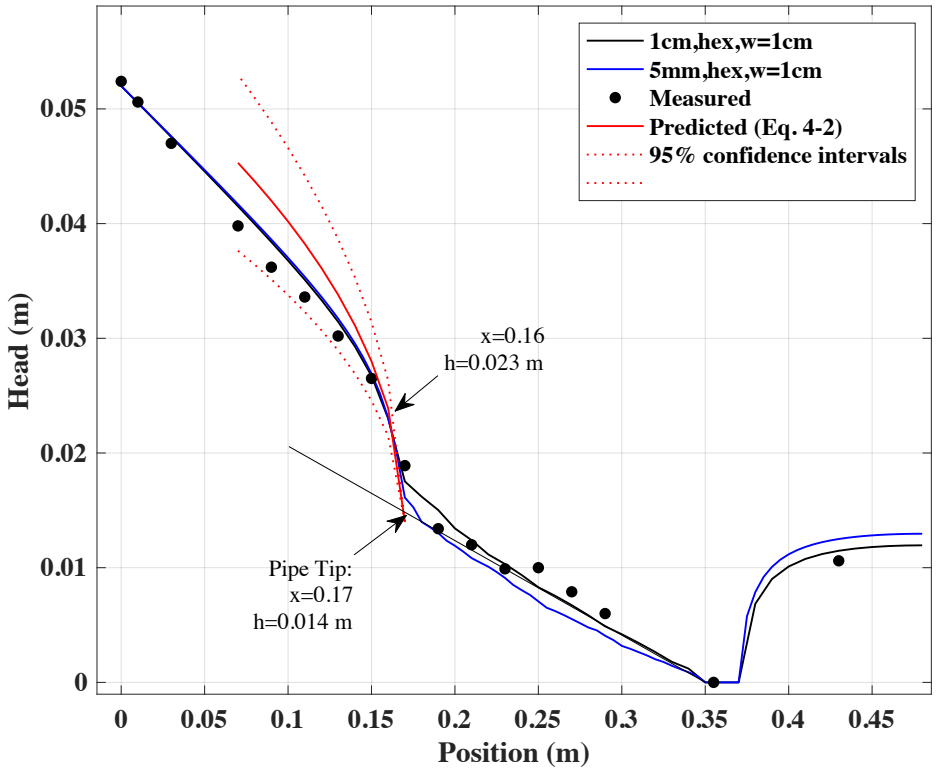

Figure 5.14. Calculation of i_{cs} over a distance of 1 cm from the best estimate of the B25-245 head profile.

This can be compared to the value of $\boldsymbol{i_{cs}}$(1 cm) for B25 sand determined from the cylindrical flume tests in conjunction with the 2D analytical solution (Table 4.3). Tests 4-10C, 4-11C, and 4-22C were conducted on B25 sand. The hydraulic conductivities of the sand in these 4 tests were 0.031 cm/sec, 0.040 cm/sec, and 0.024 cm/sec, respectively. The B25-245 experiment had a hydraulic conductivity of 0.030 cm/sec, which was nearly identical to the hydraulic conductivity of test 4-10C. The estimated value of $\boldsymbol{i_{cs}}$(1 cm) for test 4-10C was 1.02 as compared to the value of 0.90 computed by Equation 5.2 from the head profile in Figure 5.14. This is a difference of approximately 10%, indicating excellent agreement between the previously measured CSGF in Chapter 4 and the value determined from Figure 5.14. Additionally, it should be noted that the global differential head in experiment B25-245 had to be increased to 0.054 before the sample failed. Assuming the value of $\boldsymbol{i_{cs}}$ scales proportionally, the actual critical value for test B25-245 may be closer to 0.94 (within 5% of 1.02). This is remarkable agreement between the two independent cases which suggests the 2D analytical equation and cylindrical flume experiment may be adequate for measuring the CSGF in more three-dimensional scenarios.

Finally, it is also of interest to compare the head profile obtained using the predicted CSGF obtained from Equation 4.2 to that measured in experiment B25-245 as it provides an independent validation of Equation 4.2. The CSGF C value was predicted using Equation 4.2 for the grain size, void ratio, and uniformity coefficient of test B25-245 (Table 5.1). The head profile associated with the CSGF was then determined using Equation 3.23. The predicted critical head profile is shown in Figure 5.14 along with 95% confidence intervals. Both the measured head profile and FE profile fell within the 95% confidence intervals of the predicted head profile. Not only does this comparison further validate Equation 4.2 for predicting the

CSGF, it also demonstrates that the measured values obtained from the cylinder test may be applicable to the more generic, three-dimensional scenario of an arbitrary rectangular domain. This will be further validated in the next section through a completely predictive model where the measured CSGF is used directly to predict the progression of erosion and critical head in another independent, rectangularly shaped experiment.

5.2 Experiment Simulation 2 – Validation of CSGF and Progression Algorithm

The sands for which the CSGF was measured in Chapter 4 were also used in a series of laboratory experiment to test the concept of using a coarse layer of sand for preventing BEP progression (Rosenbrand et al., 2020). This concept differs from the concept of a filter in that it does not provide drainage. As such, the performance of the coarse sand layer is entirely dependent on the erosion resistance of the coarse sand. The experiment, finite element model, and simulation results are described in the following sections.

5.2.1 Description

The experiment, numbered S191, consisted of a rectangular sample that was 48 cm in length, 30 cm wide, and 10 cm tall as illustrated in Figure 5.15a. The sample consisted of 3 layers as illustrated in Figure 5.15b. An upstream layer of the finer MZ sand was first placed that extended 0.18 m from the upstream boundary. A 5 cm thick layer of the coarser GZB2 sand was then placed in the middle of the sample as illustrated in Figure 5.15b. The finer MZ sand was then placed for the remainder of the sample. The properties of both sands are provided in Table 4.1.

The sample was prepared by orienting the sample container vertically on a table with the upstream boundary wall resting on the table. The sands were then water pluviated into deaired

water. Once the first portion of the finer, MZ sand was placed, the sample was levelled and tamped. The coarser, GZB2 sand was then water pluviated on top of the MZ sand until a 5cm thick layer was obtained. Finally, the remainder of the sample was constructed by continuing to water pluviate the MZ sand until the sample container was filled. The box was then sealed, rotated to the horizontal position, and the downstream outlet hole was unplugged so that the cylindrical outlet reservoir could be attached as shown in Figure 5.15a. The density and hydraulic conductivity of the MZ and GZB2 sands as placed in the sample are provided in Table 5.3. Further details regarding the experiment are available in Rosenbrand et al. (2020) and Rosenbrand and van Beek (2017).

a.

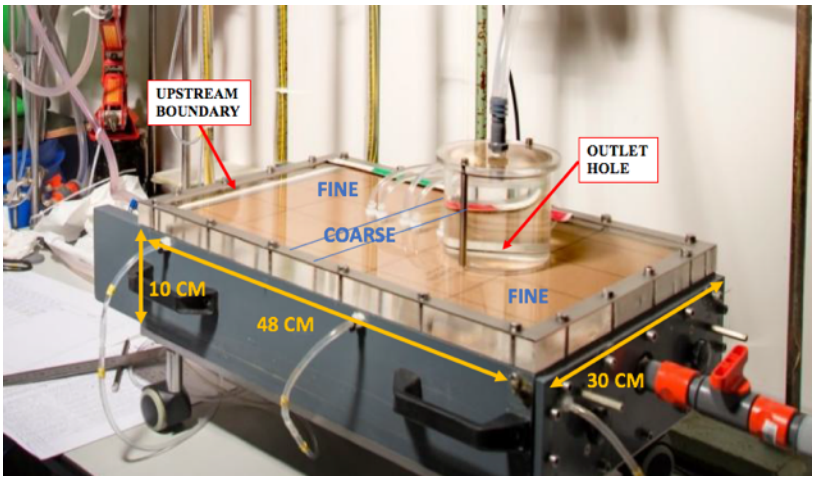

b.

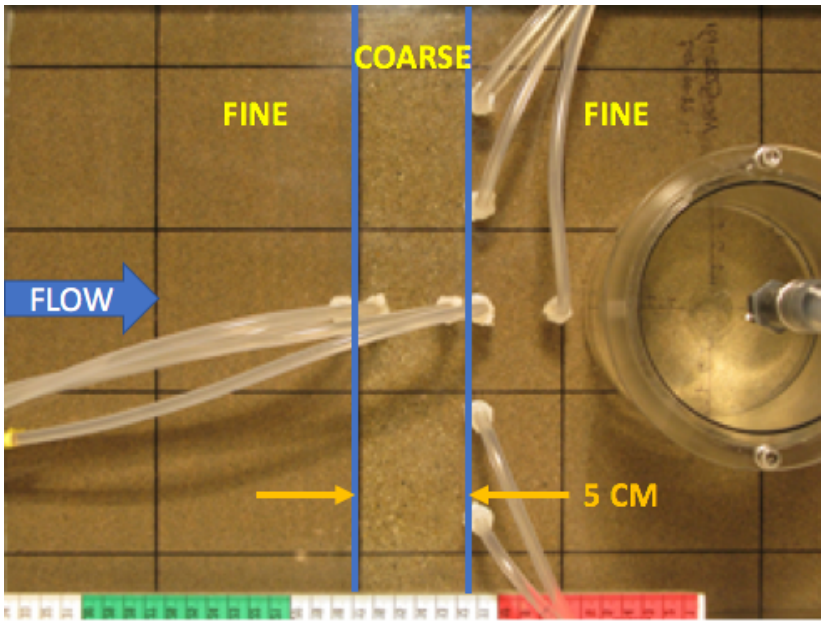

Figure 5.15. Photograph of (a) small-scale, coarse sand barrier experiment set-up and (b) top view of experiment.

Table 5.3. Sand properties in S191 experiment.

Sand Name	MZ	GZB2
Porosity	0.32	0.31
k (m/s)	2.5e-4	2.0e-3

A constant head boundary condition was applied to both the upstream boundary and the downstream outlet. All other boundaries were no flow boundaries during the BEP progression experiment. The differential head was gradually increased across the sample. With each increment, the pipe would progress a little further. Each time the differential head was increased, it was held constant until complete equilibrium was obtained. In this manner, a piece-wise, steady state progression of the BEP pipe through the sample was obtained. The head was increased until the pipe progressed completely through the sample at a critical head of 1.30 m. Further details regarding the pipe progression behavior will be discussed as part of reviewing the numerical model results.

5.2.2 Finite Element Model

The S191 experiment was modeled using a 3D finite element model with hexahedral pipe elements as described in Chapter 3. The finite element mesh consisted of 1 cm cubic elements as shown in Figure 5.16. The downstream outlet was simulated as a 2 cm x 2 cm square with a constant head of $h = 0.0$ m. While this was larger than the actual outlet diameter, the effects were deemed negligible because (1) an erosion cavity forms around the exit hole due to sand fluidization and (2) the majority of the head loss becomes transferred upstream as the erosion progresses such that very little head loss occurs in the vicinity of the exit hole. The coarse sand barrier is highlighted in Figure 5.16. The properties used in the simulation for both sands are provided in Table 5.4. The hydraulic conductivities were selected to match the measured values in Table 5.3. The value of τ_c was selected based on the values presented in van Beek et al. (2019). Equation 2.11 also gives similar values for τ_c. The value of i_{cs} used in the model was selected to match the element size. In this manner, the average hydraulic gradient over the element is compatible with the CSGF used to evaluate BEP progression. As the elements were 1

cm in length, the values of $i_{cs}(1\ cm)$ from Table 4.3 were used. The value of i_{cs} of 1.93 for the MZ sand was selected on the basis of test 4-24C. This test was used to represent the CSGF for the MZ sand as it had the highest value of i_{cs} as well as the lowest MSE error. Test 4-26C was actually the sample closest in density to the MZ sand in the S191 experiment. However, Test 4-26C had a poor fit to the analytical solution and lower values of i_{cs} than both of the other experiments (4-24C and 4-23C). This contradicts the observed trend in Figure 4.9 between void ratio and C (i_{cs}). Additionally, the values of i_{cs} obtained for test 4-24C and 4-23C were similar. Based on these observations, test 4-26C was determined to be in error, and the higher value of the remaining two tests was used to represent the MZ sand because the S191 sand was denser than the sand samples in all of the cylindrical experiments.

The value of i_{cs} for the GZB2 sand was based on experiment 4-21C. This test was selected to represent GZB2 as it was the uniform sample experiment that was closest in density to the GZB2 sand used in the S191 experiment.

Table 5.4. Properties used in numerical simulation of S191.

Sand	**k (m/s)**	**τ_c (Pa)**	**i_{cs} (1 cm)**	**d_{50} (mm)**
MZ	2.5e-4	0.45	1.93	0.378
GZB2	2.0e-3	0.82	3.1	0.873

5.2.3 Results

The final erosion pattern observed in the FE model is illustrated in Figure 5.16. Additionally, various extents of the erosion (indicated by letters A-F) are called out on Figure 5.16 and labelled on the plot of the differential head applied to the model in Figure 5.17. The erosion initiated at a relatively low head (A) and progressed to the coarse sand barrier (B). The

differential head then had to be increased substantially before the erosion spread completely along the downstream edge of the coarse sand barrier (C). The erosion then penetrated into the barrier and stopped two separate times (D and E) before failing the barrier (F) at a critical differential head of 1.28 m. The critical head predicted by the FE model was only 1.5% lower than the actual critical head. Further, the qualitative behaviors in the model of (1) the pipe spreading along the downstream edge of the barrier and (2) the pipe partially penetrating the barrier in multiple locations and stopping prior to failure were both observed in the actual experiment. It is remarkable that the model matched the experimental results both in behavior and in terms of the critical head with this degree of accuracy. This agreement suggests that the proposed approach of using the measured CSGF to predict BEP progression may have significant merits. Additional studies are needed to further validate the approach as a reliable means of predicting BEP progression.

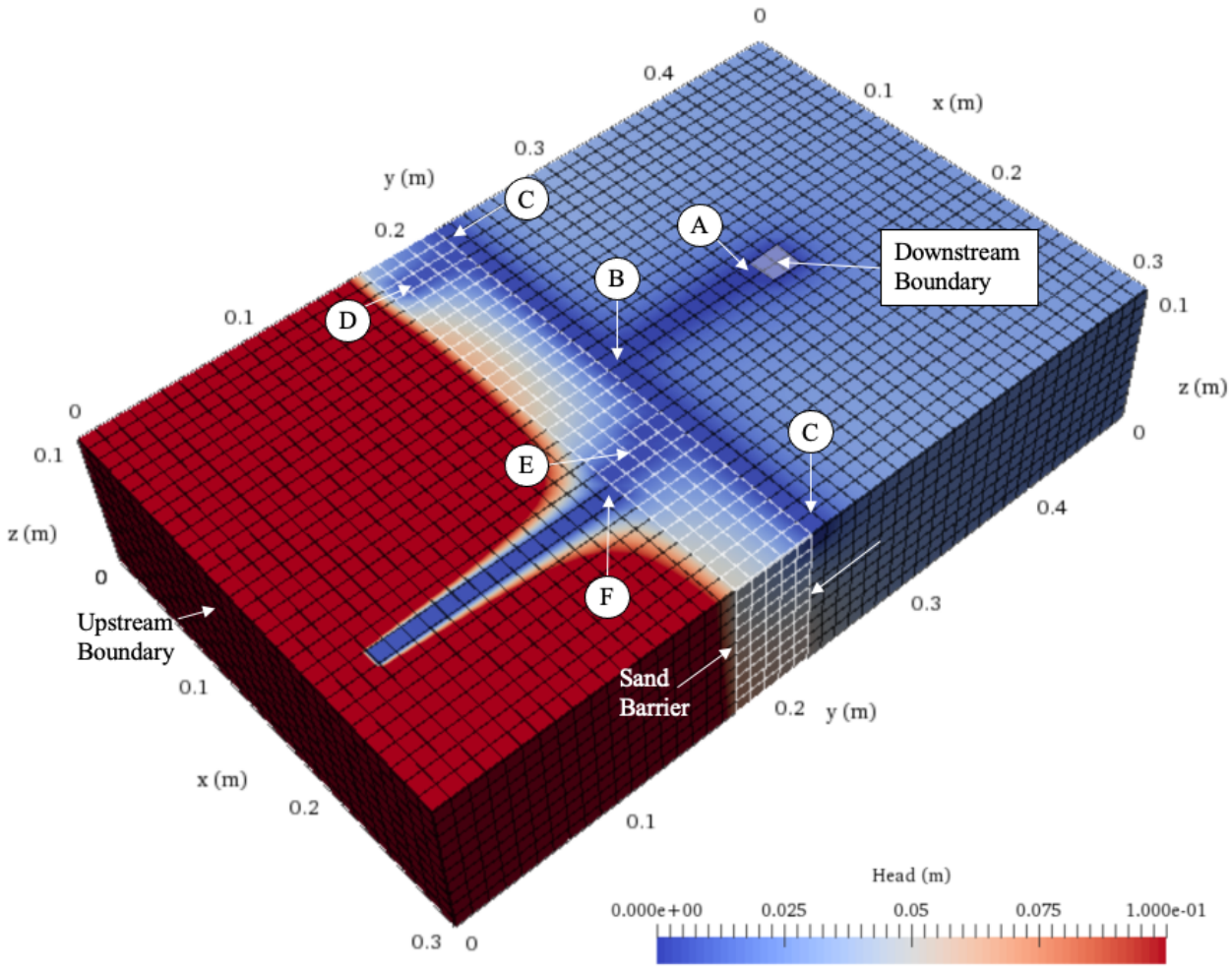

Figure 5.16. Simulated BEP pattern in FE model of KSP 191 experiment (letters correspond to heads in Figure 5.17).

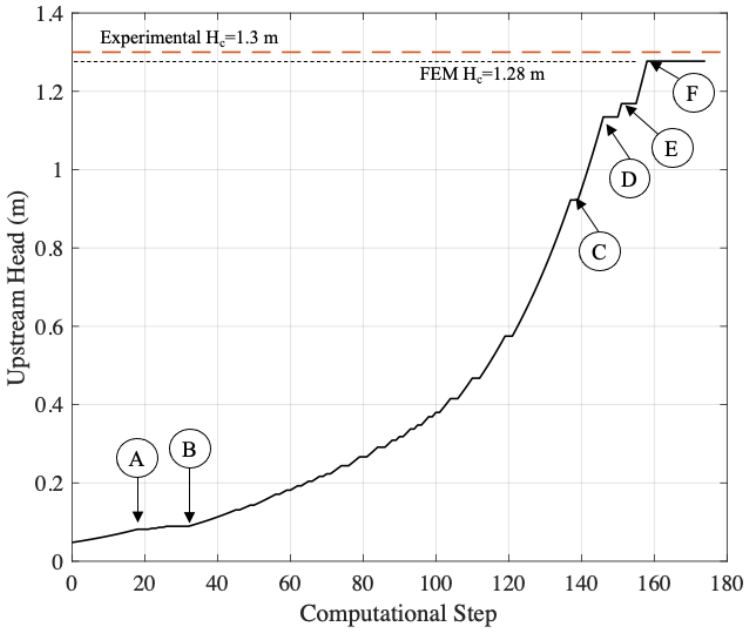

Figure 5.17. FE simulation results of KSP 191 experiment.

5.3 Experiment Simulations 3 to 5 – Validation at Larger Scales

The previous two examples have validated the finite element model assumptions (coupled ground water and pipe flow, progression algorithm, and both primary and secondary erosion) as well as the concept of using the CSGF as a primary erosion criterion. While the experimental and numerical model results compared favorably, both experiments were conducted at relatively small scales. BEP is known to exhibit significant scale effects (Van Beek 2015), therefore it is also necessary to validate the approach at a larger scale. Additionally, as noted in Chapter 2, the geometry of the downstream boundary condition also has a significant effect on the critical value of the differential head (H_c) depending on the degree of flow concentration at the exit. Because the two validation cases presented have had hole type exits with highly concentrated flow, additional validation cases with differing exit configurations are also needed. The experiments conducted by Allan (2018) provide an excellent series of larger scale experiments with various exit configurations that can be

hindcasted for further model validation. Three experiments were selected that were conducted on the same sand with area, ditch, and slope type boundary conditions. These experiments were selected as they were performed on a sand with nearly identical properties as the 40/70 sand for which the CSGF was measured in Chapter 4. The sections that follow describe the experiments, numerical models, and model results.

5.3.1 Description of Experiments

While the experiments by Allan (2018) were previously described in Sections 2.2.2 and 2.3.2 briefly, a more detailed description of the specific experiments used for model validation will be provided in this section. The experiments selected for model validation were Tests 23, 28, and 35 with slot, plane, and slope type boundary conditions, respectively. A drawing of the experimental set up and various boundary conditions is provided in Figure 5.18. The sample container consisted of an aluminum box with an acrylic top. The box was 2.24 m in length, 0.45 m in width, and 0.31 m in depth. For all tests, the seepage length along the piping path from upstream to downstream was 1.3 m. The bottom of the sample rested on a bladder that was inflated prior to testing to ensure integral contact between the sand and the acrylic top. Because of the bladder, pervious panels were included in the sample as shown in Figure 5.18 to prevent lateral movements in the sand when the bladder was inflated.

Test 23 had a slot exit that was formed by a slot through the plexiglass top as illustrated in Figure 5.18b. The slot had a width of 25 mm. Test 28 had a planar exit area as illustrated in Figure 5.18c. For test 23 and Test 28, the downstream boundary consisted of solely the slot and plane area, which were held at a constant head. Test 35 had a slope type exit as illustrated in Figure 5.18d. The downstream end of the slope was restrained with a pervious

panel as illustrated in Figure 5.18a and 5.18d. The exit slope had an angle of 15 degrees, and both the sloped boundary and boundary along the downstream pervious panel were constant head boundary conditions.

The sand used for the experiments was called Sydney sand and had a median grain diameter of 0.30 mm and a coefficient of uniformity of 1.3. The sand samples were prepared by tamping the sample in the box in lifts to achieve a desired density. The sample was then saturated with CO_2 prior to conducting a gradual sample saturation with de-aired water by introducing water to the sample through the inlet and outlet.

Once the sample was saturated, the test consisted of incrementally raising the upstream head. At each head increment, the head was held constant until there was no particle movement or pipe progression before raising the head again. The differential head at initiation (H_{init}) and the critical differential head at progression (H_c) were both recorded for each experiment. Additionally, the length of the erosion pipe at the critical head, l_c, was obtained from the experimental notes in Allan (2018). These values are approximate as the exact values were not recorded in Allan (2018). Table 5.5 provides a summary of sample properties, geometry, and experiment results for all three tests. For each test, the exit condition, seepage length (L_s), sand particle diameter (d_{50}), sand coefficient of uniformity (C_u), hydraulic conductivity (k), void ratio (e), differential head at initiation, critical pipe length, and critical head for pipe progression are all recorded. The critical pipe lengths were all very short (10 to 50 mm) indicating these experiments were nearly controlled by erosion initiation. However, as H_c was greater than H_{init} for each test, progression did control the critical condition, and the FE model should still be valid for assessing the critical head.

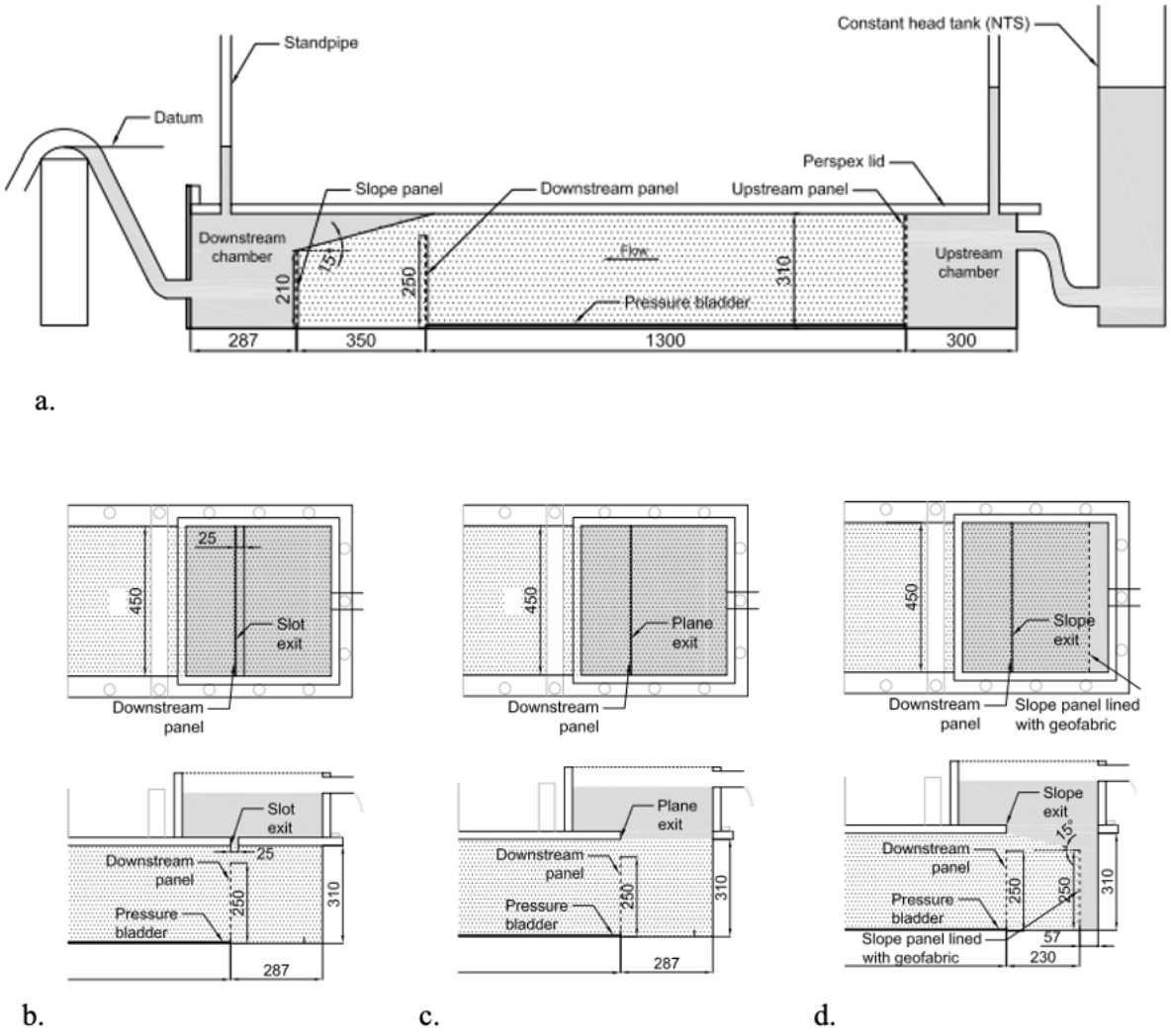

Figure 5.18. Schematic of large scale experiments with slope type exit (a,c), slot type exit (b), and plane type exit (c) (Allan, 2018).

Table 5.5. Experiment details and resulting critical head (Allan, 2018).

Exp. No.	Exit	L_s (m)	d_{50} (mm)	C_u	k (m/s)	e	H_{init} (m)	l_c (mm)	H_c (m)
23	Slot	1.3	0.30	1.3	3.1 x 10^{-4}	0.61	0.212	20-30	0.256
28	Plane	1.3	0.30	1.3	6.4 x 10^{-4}	0.55	0.268	10-20	0.293
35	Slope	1.3	0.30	1.3	4.3 x 10^{-4}	0.58	0.253	40-50	0.307

5.3.2 Finite Element Models

Finite element models were created for all three experiments as illustrated in Figure 5.19. The software Cubit was used to generate the meshes for all three tests with a target element size of 12.5 mm. By using cubit, the geometry of the sample was precisely meshed such that the boundaries of the slot, plane, and slope exactly matched the geometry of the experiments. The downstream boundaries were set to a constant head of $h = 0.0$ m as illustrated in Figure 5.19, and the upstream boundaries were set to an initial head of 0.01 m. BEP was initiated by switching 1 soil element in the middle of the domain to a pipe element as shown in Figure 5.19.

The hydraulic conductivity of the soil was set to the measured values from the experiments. As the grain size and coefficient of uniformity for the Sydney sand were identical to the 40/70 sand tested in Chapter 4, the trend for the i_{cs} C-value as a function of hydraulic conductivity (Figure 4.11) measured for the 40/70 sand was used to determine the C-value and corresponding value of i_{cs} over the element length of 12.5 mm. The resulting values of i_{cs} used in the numerical models are provided in Table 5.6. Additionally, the critical shear stress of the sand was determined based on the median grain size to be τ= 0.38 Pascals using Equation 2.11. The pipe width to depth ratio was set to a value of 20, and the pipe was initiated to a depth of twice the grain diameter.

Table 5.6. FE model inputs and results.

Exp. No.	Exit	k (m/s)	El. Size (mm)	i_{cs}	τ_c (Pa)	Calc. $l_{p,c}$ (mm)	Calc. H_c (m)
23	Slot	3.1 x 10^{-4}	12.5	1.32	0.38	38	0.230
28	Plane	6.4 x 10^{-4}	12.5	1.11	0.38	88	0.230
35	Slope	4.3 x 10^{-4}	12.5	1.25	0.38	63	0.340

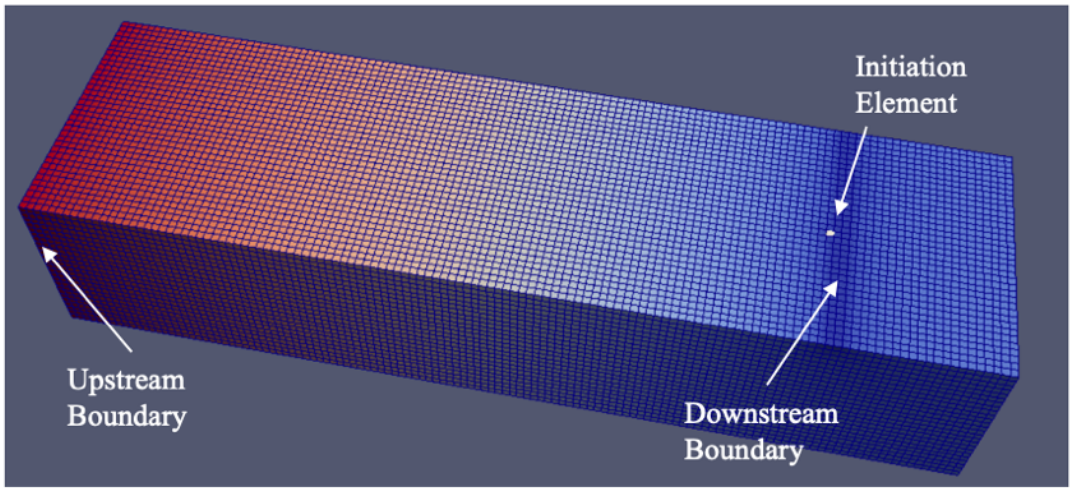

a.

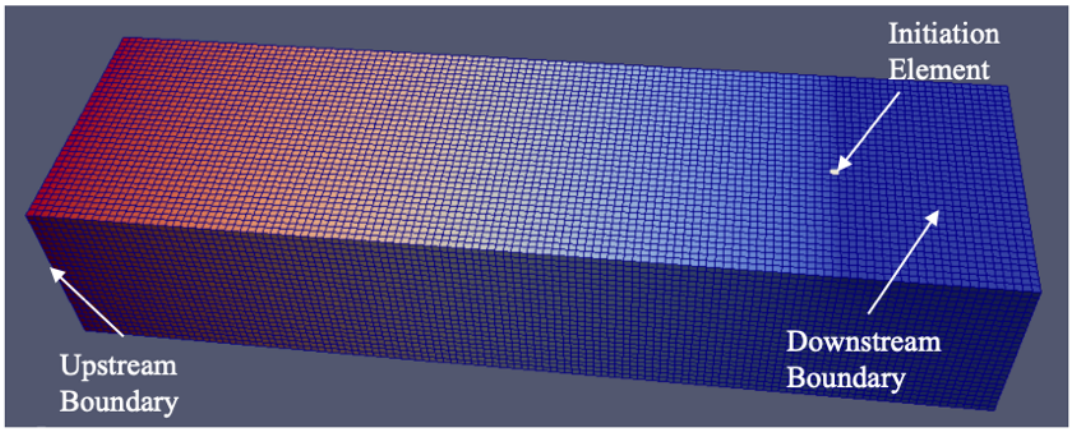

b.

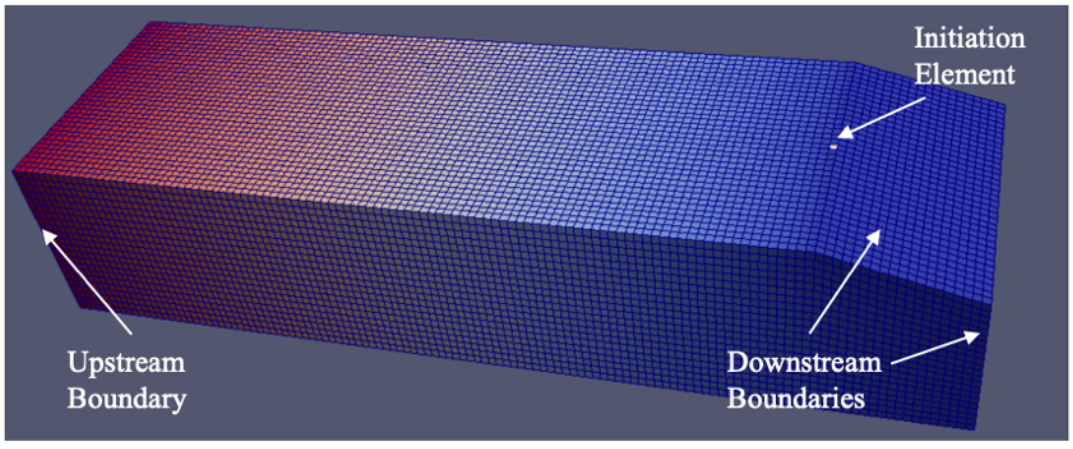

c.

Figure 5.19. Geometry, boundary conditions, and initial head distribution for (a) Test 23, (b) Test 28, and (c) Test 35.

5.3.3 Finite Element Results

The resulting erosion pipes are shown at the critical pipe length ($l_{p,c}$) and critical head (H_c) in Figure 5.20. The calculated values of $l_{p,c}$ and H_c are provided in Table 5.6, and a comparison of the numerical predictions of H_c to the experimentally measured values is provided in Figure 5.21. In general, the simulation results compare favorably to the experimental results, predicting the critical head with only 10% error for Tests 23 and 35, and 21% error for Test 28. Additionally, the finite element results also predicted that the pipes would reach the critical head at very short pipe lengths (approximately 40 to 90 mm).

Because of the short critical pipe lengths in these experiments, the predicted critical head and critical pipe length will be very sensitive to the actual pipe geometry. For longer pipe lengths, the head loss in the pipe becomes significant. As such, the exact geometry of the pipe becomes less important as the general trend of the head loss in the erosion pipe and the geometry at the pipe tip controls the computed values of i_s for elements upstream of the pipe tip. For these short critical pipe lengths very near to the downstream boundary, the hydraulic gradients near the pipe tip are heavily influenced by the actual pipe geometry and downstream boundary condition. This may be one reason why the errors in the critical heads are higher for these experiments than the small scale experiments presented in the previous two sections. However, the errors of 10-20% are still considered remarkable agreement given the fact that the predictions were made with direct estimation of model parameters from the Chapter 4 i_{cs} measurements. This suggests the approach adequately captures the physics of the BEP progression process and is valid across all problem scales. Further validation will not be provided in this research. Additional validation at field scale is needed and should be performed before implementing this approach in practice.

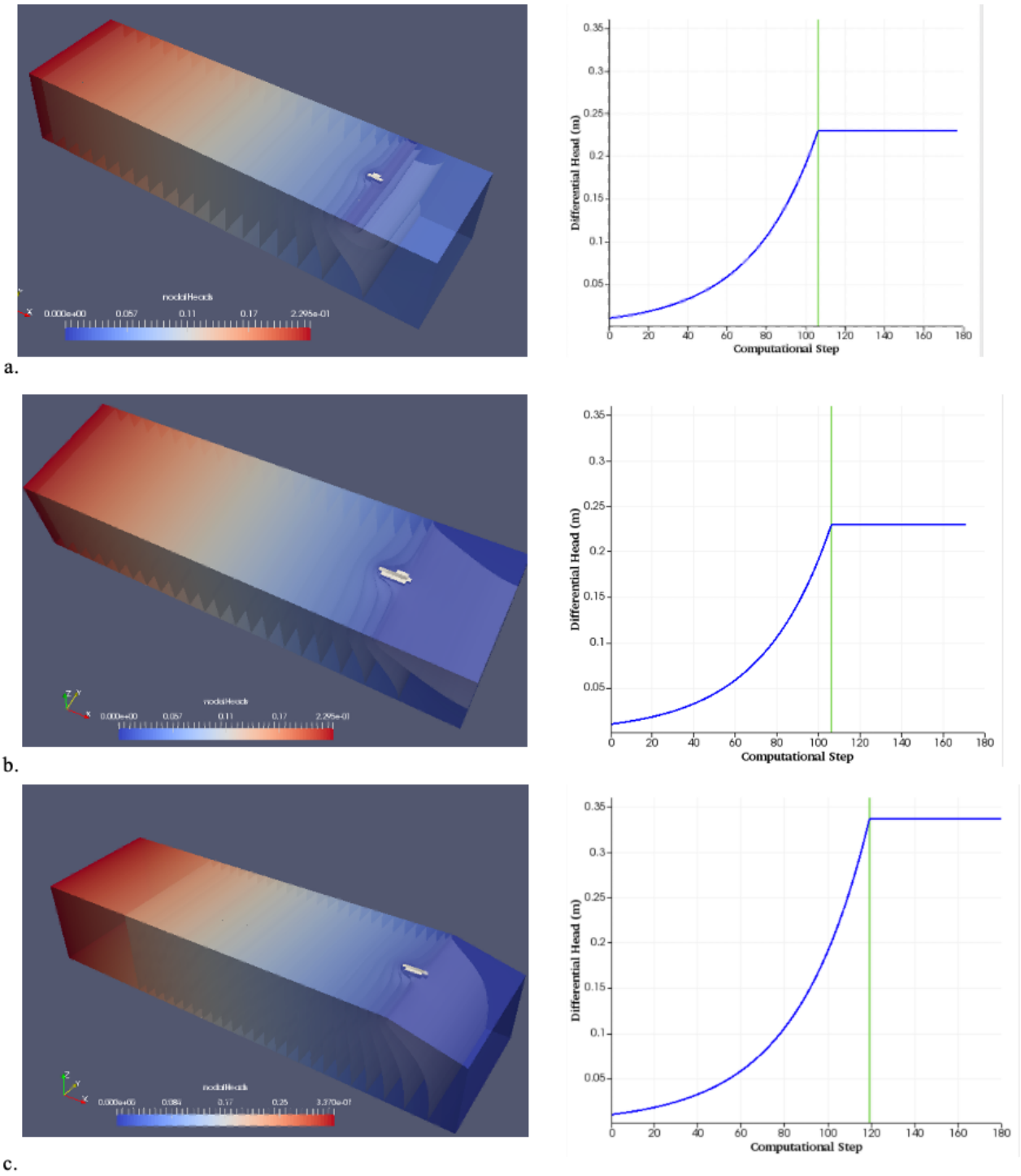

Figure 5.20. Finite element results of head distribution and pipe length at the critical head for (a) Test 23, (b) Test 28, and (c) Test 35.

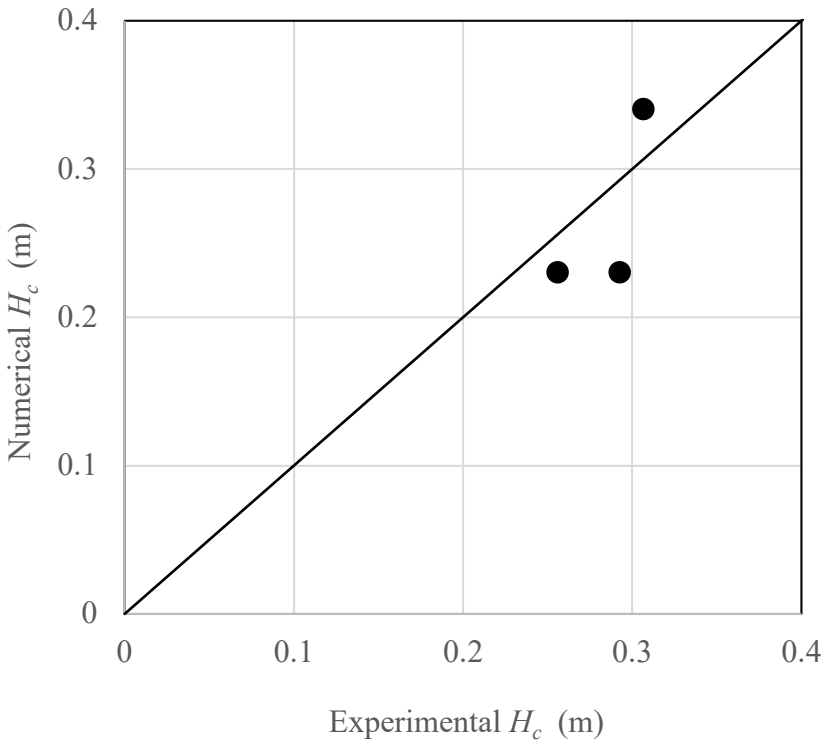

Figure 5.21. Comparison of numerical and experimental critical heads for large scale experiments.

CHAPTER 6

ERRORS IN FINITE ELEMENT MODELING OF PIPING

Based partially on a paper published in *Geomechanics for Energy and the Environment**

B.A. Robbins[1], V.M. van Beek[2], J.C. Pol[3], and D.V. Griffiths[1]

And partially on a paper published in *Numerical Methods in Geotechnical Engineering IX**

B.A. Robbins[1] and D.V. Griffiths[1]

In the previous chapter, the finite element model for steady-state simulation of BEP was validated through hindcasting of 5 laboratory experiments of varying scale, geometry, and soil types. The results demonstrated that the CSGF and steady-state approach for predicting BEP progression are capable of accurately predicting BEP progression when using hexahedral or quadrilateral elements to discretize the pipe domain. The use of one dimensional line elements for representing the pipe resulted in significant errors in the hydraulic solution in front of the pipe. This Chapter explores the cause of these errors in addition to examining potential errors that may exist in the solution when discretizing the pipe using the parallelepiped and parallelogram approximations with oversized elements.

6.1 Types of error

In general, errors in finite element solutions can be attributed to the following sources (Reddy, 2004):

1. *Finite arithmetic errors* due to the roundup and truncation on a computer.

[1] Colorado School of Mines, Civil and Environmental Engineering
[2] Deltares
[3] Delft University of Technology, Civil Engineering and Geoscienses
*See Appendix C for permission and citation

2. *Quadrature errors* due to the numerical evaluation of integrals
3. *Approximation error* due to the approximation of the solution using shape functions.
4. *Domain approximation error* due to the approximation of the problem domain by finite elements.

The first and second types of error, while present in all finite element solutions, is relatively small and cannot explain the 50-300% error in the solutions obtained using line elements in Chapter 5. The third type of error, approximation error, can be large in the vicinity of singularities where the solution is changing rapidly, especially when using linear shape functions. For elliptic PDE's with singularities (as is the case for the present study), this type of error can be reduced by either increasing the refinement of the mesh in locations where the solution is changing rapidly or by increasing the order of the shape functions used in the finite element solution. Both of these approaches at reducing the error were tested for the problem that was presented in Section 5.1. As illustrated in Figures 5.10 and 5.11, refining the mesh from 1 cm elements to 2 mm elements only increased the magnitude of the error in the solution obtained near the pipe tip. This suggests that the errors in the line element solutions are of the third type, domain approximation errors. While it seems intuitive that approximating the erosion pipe as a line would result in domain approximation errors, the magnitude of these errors was surprising as the erosion pipes are quite small (1cm wide x 1 mm deep), and line elements were previously thought to be a suitable approximation. To further confirm that the errors are indeed due to domain approximation, the gradient in front of the pipe tip for this same example was compared for cases of w=1 cm, w=5 mm, and line elements (Figure 6.1) using both linear, 8-node hexahedral and higher order, 20-node hexahedral elements to examine the influence of the pipe geometry and approximation order on the calculated upstream secant gradient. The results

demonstrate that there is a gradual increase in the secant gradient with decreasing pipe width, regardless of the polynomial order for the approximation functions, further indicating that the errors are caused by the domain approximation error due to the poor physical representation of the pipe by the line elements. An explanation for the error can be provided by considering the number of elements connected to the pipe. For the case of line elements, only one soil element is connected to the pipe tip such that all of the flow into the pipe is conveyed through one element resulting in high gradients. In the case of a single hexahedral element, the flow towards the pipe tip is spread across the four upstream elements connected to the hexahedral pipe element. As a result, the flow is spread out much more resulting in lower hydraulic gradients. These observations are best illustrated by the equipotential surfaces surrounding the pipe tip (Figures 6.2 and 6.3). As shown in Figure 6.2 for 1D line pipe elements, the equipotential planes are all grouped near the node at the upstream pipe tip. Switching to higher order elements only exacerbates the problem by causing the equipotential planes to group more tightly near the node. While the higher node elements more accurately represent the problem of flow towards a line, they yield slightly higher errors (Figure 6.1) immediately upstream of the tip. This further supports the idea that the errors in the line elements are domain approximation errors. To the contrary, the equipotential planes are much more dispersed and evenly distributed in the case of hexahedral pipe elements (Figure 6.3).

Without being addressed in some manner, the large domain approximation errors that result from using 1D pipe elements will lead to overly conservative solutions. As shown by the results obtained with 1 cm elements in Figure 5.11, the hydraulic gradients in front of the erosion pipe can be 50-300% higher than the equivalent solution obtained using hexahedral pipe elements. Attempting to use the same physical criterion for erosion (whether based on gradient

or velocity) in the two different discretizations will yield significantly differing differential heads at failure. This is unfortunate as 1D line elements are more convenient from a software development perspective and as a result have been more widely used (e.g., Van Esch et al 2013, Rotunno et. al 2019, Rahimi et al. 2019). While additional research is needed to evaluate the issue further, this study has demonstrated that the errors can be significant and must be considered when performing numerical analysis of BEP. Non-standard numerical techniques may need to be explored in the future to accurately predict BEP progression. In particular, multi-scale modelling that makes use of coupled CFD-DEM simulations to simulate the pipe tip at the micro-scale may inherently capture the relevant processes for pipe progression. Alternatively, more advanced FEM techniques such as regularized solutions or enriched elements (XFEM) may yield efficient approaches for accurately assessing BEP progression when using line elements. For now, it is recommended that hexahedral and quadrilateral elements be used to represent the erosion pipe to avoid the large domain approximation errors obtained with 1D line elements.

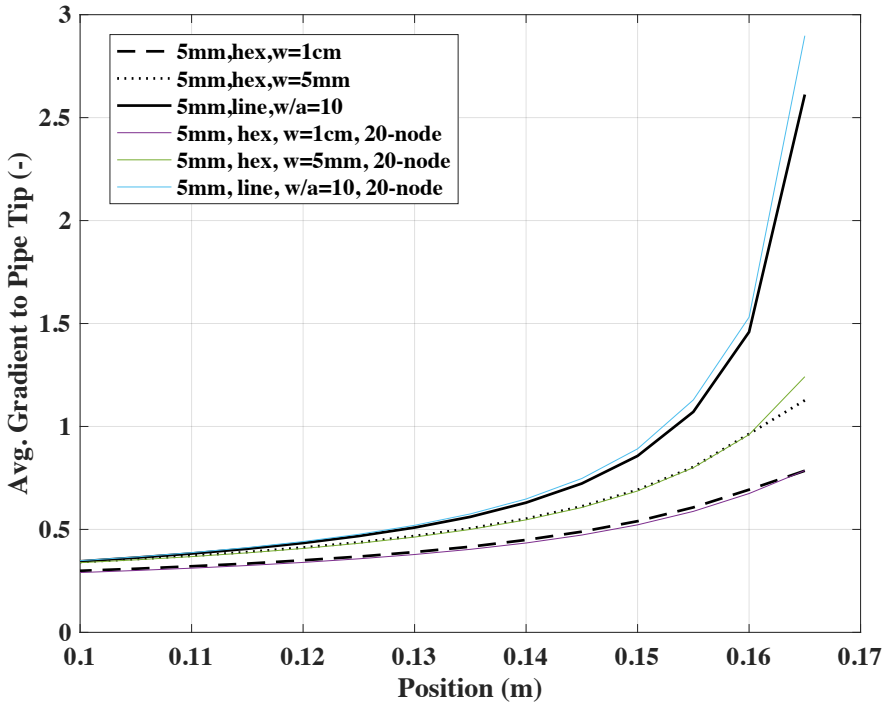

Figure 6.1. Calculated secant gradients in front of the pipe tip for different pipe widths using linear and higher order elements.

a.

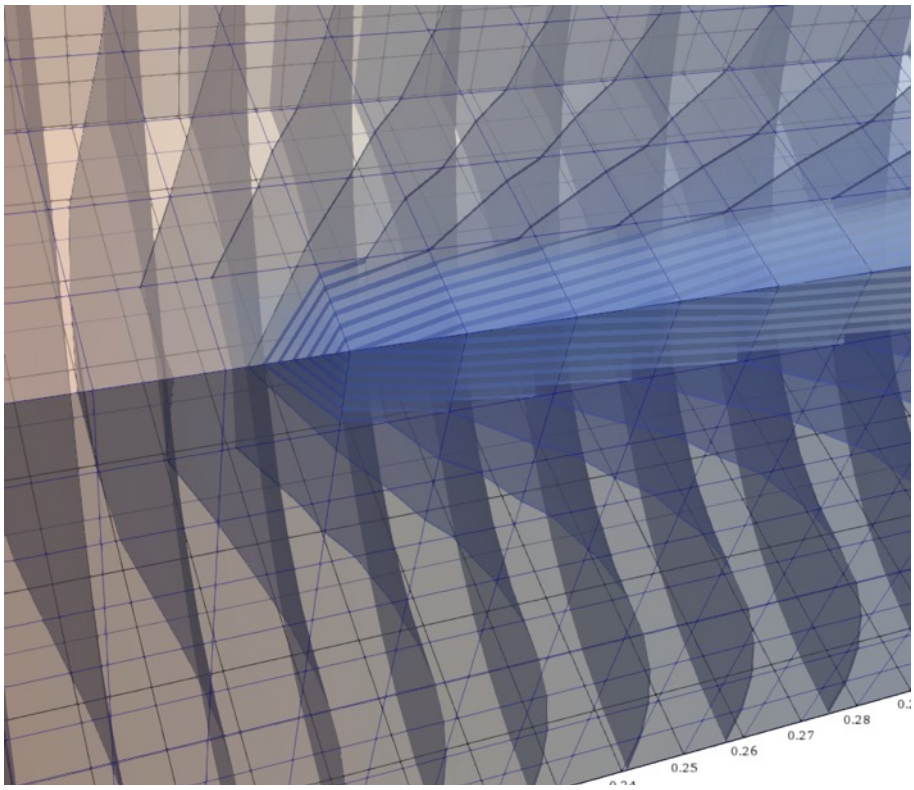

b.

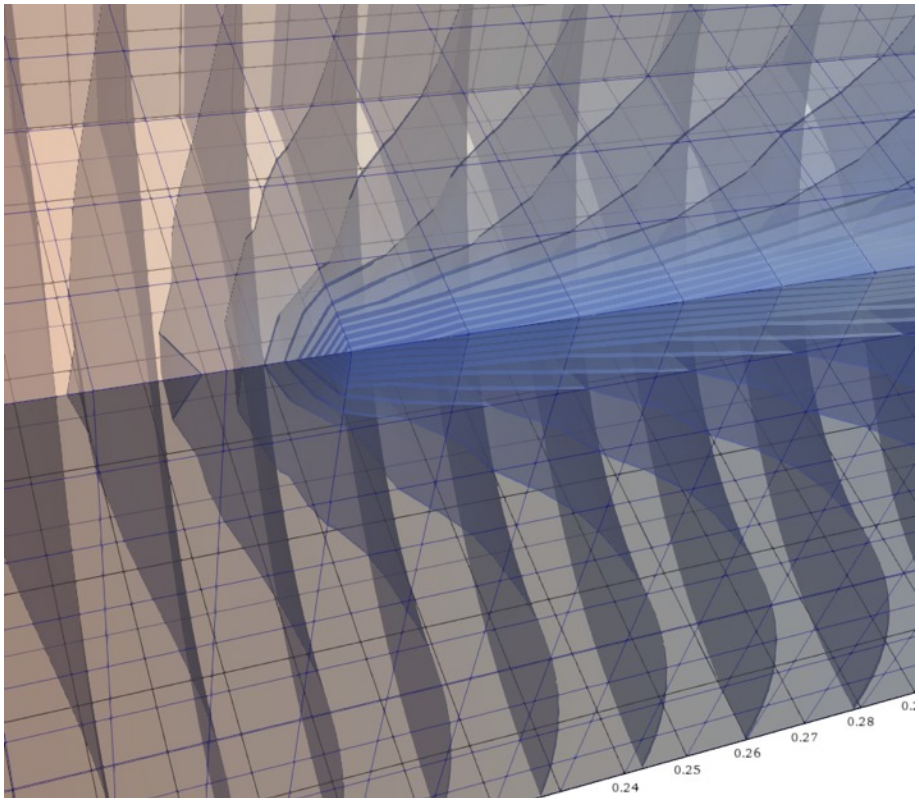

Figure 6.2. Equipotential planes upstream of the pipe tip for 1D line pipe elements with (a) 8-node hexahedral soil elements and (b) 20 node hexahedral soil elements.

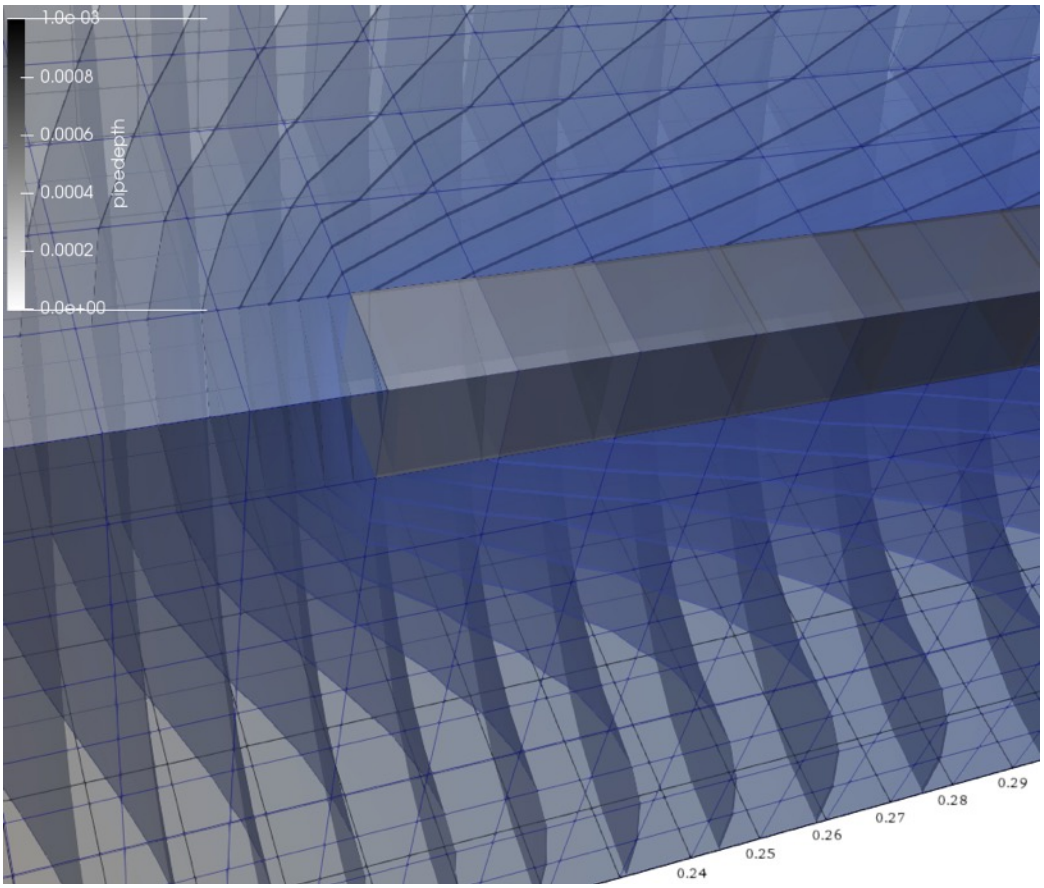

Figure 6.3. Equipotential planes near the pipe tip for 20-node hexahedral elements for both the pipe and the soil domain.

6.2 Domain approximation errors due to oversized pipe elements

While the use of 1D line elements leads to high domain approximation errors due to the pipe inflow area being too small, approximating the pipe with oversized parallelepiped and parallelogram elements can also lead to domain approximation errors because the pipe inflow area is too large. Consider the simple example of linear and quadrilateral pipe elements in Figure 6.4. As the quadrilateral element size increases, the use of quadrilateral, or parallelogram, pipe elements will distribute the pipe flow over an increasing area. This will have impacts on the groundwater flow near the pipe and the overall hydraulic solution. In addition, when assessed in three dimensions, changing the element size will also impact the pipe width. As illustrated in the previous section, the pipe width also has a large influence on the domain approximation errors.

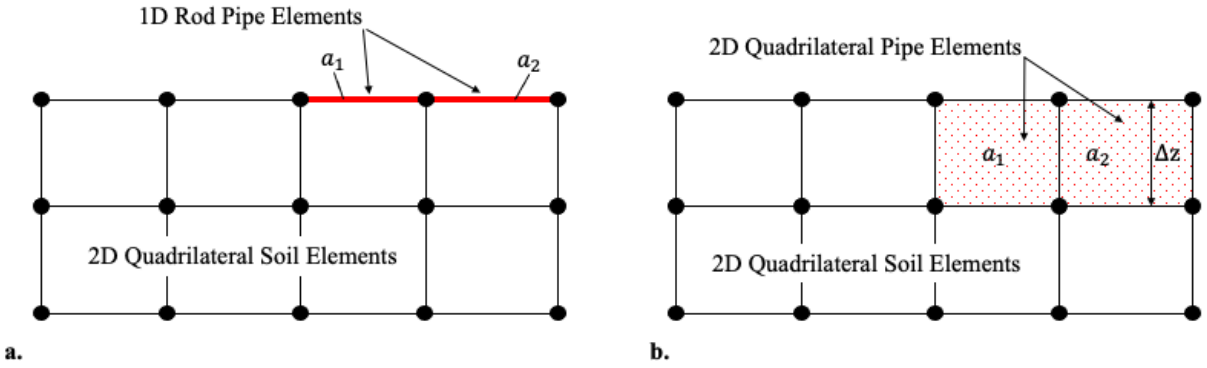

Figure 6.4. Illustration of (a) 1D line and (b) quadrilateral pipe elements.

To assess the approximation error caused by solely the parallelogram, or parallelepiped, pipe element approximation, a two-dimensional analysis is performed in the cross-sectional perspective. In this manner, the analysis is per unit length in the third dimension, and the width of the pipe becomes irrelevant. The analysis using line elements and quadrilateral

elements to represent the erosion pipe can then be compared to evaluate the domain approximation error due to solely the parallelogram approximation.

As significantly larger element sizes may need to be used to cause large approximation errors, a field scale problem was modelled in two-dimensions. The test problem of a simplified dam geometry presented in Van Esch et al. (2013) was used to evaluate the performance of the two discretization approaches. The geometry of the problem is presented in Figure 6.5 with a flownet illustrating the impact of the pipe. The pipe elements influence the flow net similarly to a "leaky boundary", causing the flow lines to exit the domain at an acute angle due to the unique pressure- discharge relationship imposed by the pipe hydraulics. The foundation consists of a homogenous soil layer with no-flow boundaries (Neumann conditions) at the left, bottom, and right boundaries. An impervious structure resting on the foundation is simulated through a no-flow boundary as well. The horizontal ground surface both upstream and downstream of the structure are constant head (Dirichlet) boundary conditions. Foundation soil properties are provided in Table 6.1.

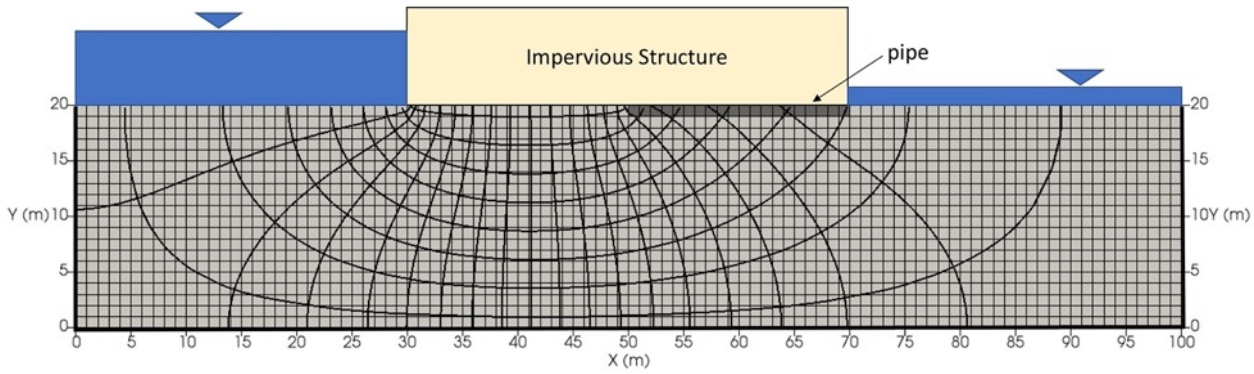

Figure 6.5. Two dimensional, simplified dam problem for example analyses (after Van Esch et al. 2013).

Table 6.1. Soil properties for example problem.

k_H (m/s)	d_{50} (m)	γ_w (N/m^3)	μ (Ns/m^2)	$\gamma_p{}'$ (N/m^3)	η (-)	θ (°)
1.16×10^{-3}	2.08×10^{-4}	1.0×10^{4}	1.0×10^{-3}	1.65×10^{4}	0.25	37

The analysis results presented in Van Esch et al. (2013) for a differential head of 1.85 m were replicated. The total head at the downstream ground surface was set to 0 m, and the total head at the upstream ground surface was set to a head of 1.85 m.. As the focus of this analysis was solely on the approximation in the hydraulic solution (as opposed to assessing pipe progression), the pipe elements were manually activated from x = 60.0 m to x = 70.0 m and no pipe progression was simulated.

Computations were performed using both 1D line and 2D quadrilateral pipe discretizations for element sizes of 0.25 m, 0.50 m, 1.0 m, and 2.0 m. For line element computations, 1D pipe elements were set to the same length as the quadrilateral element edges such that all 1D element nodes were connected to quadrilateral nodes.

The results obtained using both 1D linear pipe elements and 2D quadrilateral pipe elements for the various element sizes are provided in Figure 6.6 and Figure 6.7, respectively. For each simulation, the total head along the base of the dam and the depth of the eroded pipe is plotted in the vicinity of the pipe (*x*=60 to 70 m). Additionally, the line element approach results obtained with 0.25 m elements are repeated in Figure 6.7 for purposes of comparison with quadrilateral pipe element calculations. The simulation with the smallest elements was selected for comparison, as it was considered to be the most accurate solution.

The first thing noted from the head profiles is that the head loss in the erosion pipe is quite high resulting in minimal flow concentration near the pipe tip at x=60 m. This is due to the

soil permeability being an order of magnitude too high relative to the other sand characteristics in the analysis. As a result, the flow in and towards the pipe is much higher than it should be leading to the head profile shapes given. As this will magnify the approximation error due to the quadrilateral elements due to the increased flow, the results were deemed suitable for the purposes of this analysis.

Figure 6.6a shows that the element discretization influenced the resolution of the head profile for the solutions with linear pipe elements. However, the various element sizes resulted in nearly identical approximations of the pipe depth (Figure 6.6a). Figure 6.7 shows that both the head profile and the pipe depth are sensitive to element size using quadrilateral pipe elements due to the approximation error. In particular, the pipe depth and the head profile increasingly diverge from the 1D linear element approach as the element size is increased. This is due to the increasing approximation error as elements become larger. With decreasing element size, the quadrilateral solution converges to the 1D linear pipe element solution. As indicated by the results, the approximation error in the quadrilateral solution is minimal for the cases with element sizes of 0.5 m and 0.25 m. As such, the parallelepiped (and by extension parallelogram) approximations should not be used with elements larger than 0.5 m in order to avoid domain approximation errors due to the pipe domain being too large.

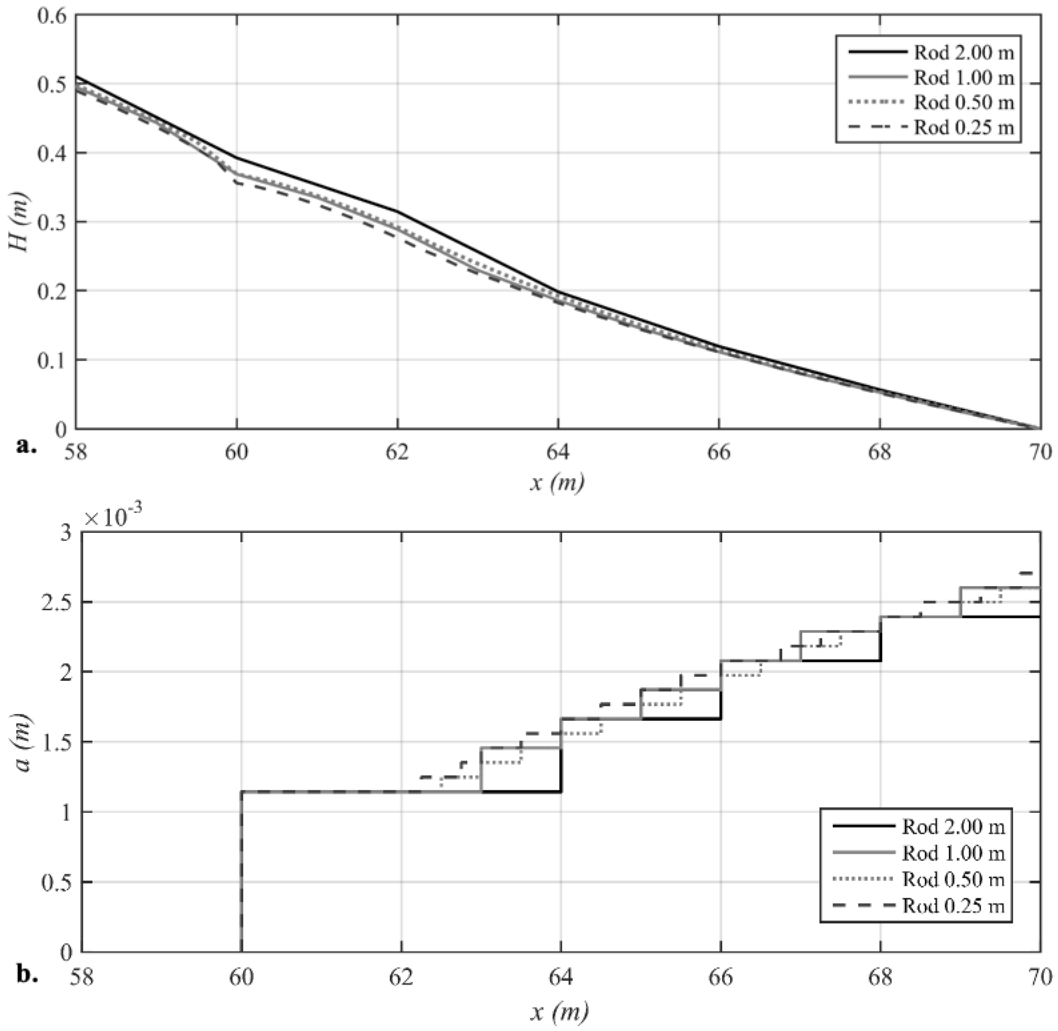

Figure 6.6. Head profile (a) and pipe depth (b) results obtained for the test problem using linear pipe elements.

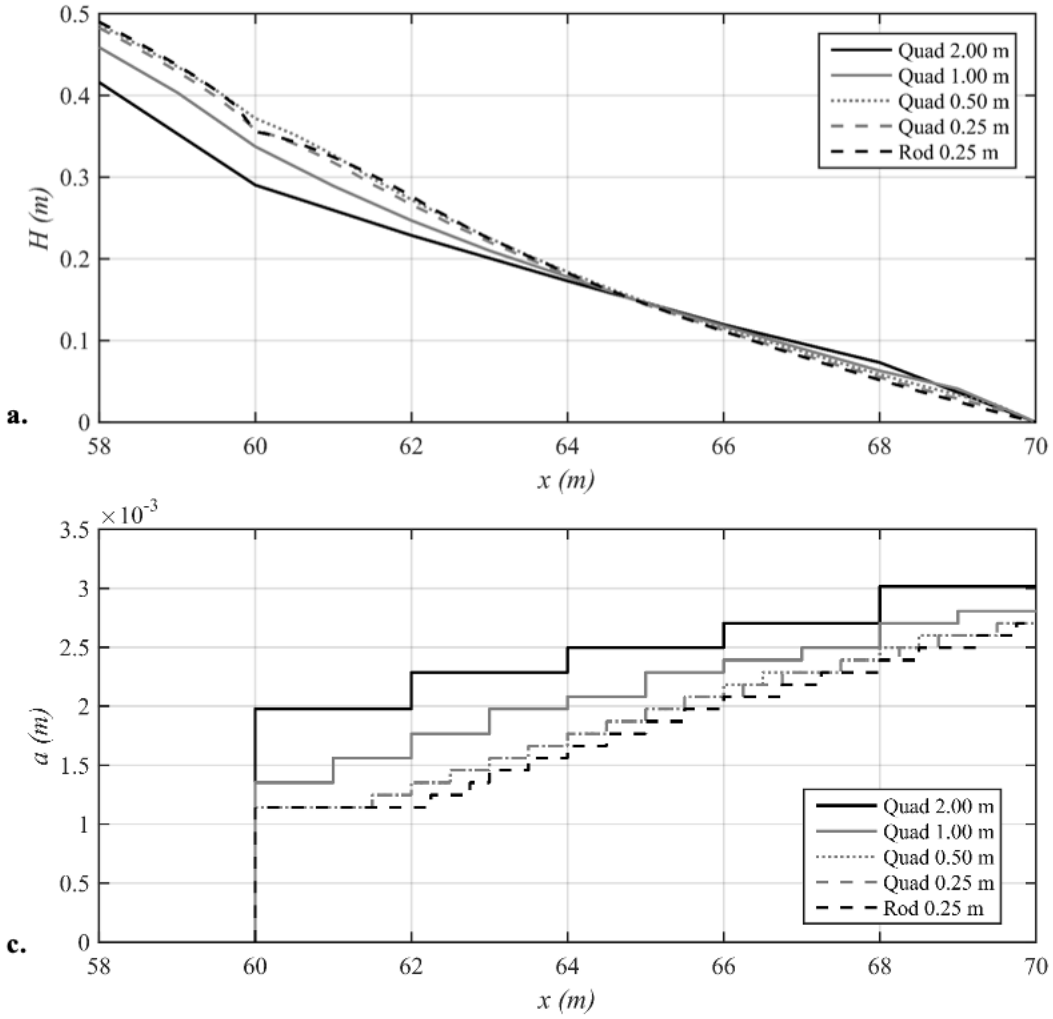

Figure 6.7. Head profile (a) and pipe depth (b) results obtained for the test problem using quadrilateral pipe elements.

CHAPTER 7

COMPARISON OF 2D AND 3D MODEL RESULTS

Based on a chapter published in *Internal Erosion in Earth Dams, Dikes, and Levees**

B.A. Robbins[1] and D.V. Griffiths[1]

In Chapter 5, the proposed steady-state analysis approach and concept of using the CSGF was validated through the use of three-dimensional models that closely approximated the actual geometry of the validation cases being assessed. The use of two-dimensional models has not yet been validated. The BEP process is a three-dimensional process, and it is not expected that two-dimensional models will accurately represent the hydraulics near the pipe. In order to demonstrate this, this chapter compares two-dimensional and three-dimensional results to highlight the differences in the solutions.

7.1 Comparison for a Single Pipe

As a starting point, a simple test problem was used to perform a direct comparison of two-dimensional plan view analysis and two-dimensional profile view analysis to the equivalent three-dimensional model being represented. The test problem illustrated in Figure 7.1 was used to perform an initial model comparison. The problem consists of a 10-m soil cube with constant head upstream and downstream boundary conditions. All other boundaries are no-flow boundaries. The pipe is initiated at the top-center location on the downstream face by changing a single element to a pipe element. An element size of 0.25 m was used in all analyses. Illustrations of the corresponding finite element meshes are shown in Figure 7.2 with the pipe progressed 6 m into the domain. All material properties used for the analyses are provided in

[1] Colorado School of Mines, Department of Civil and Environmental Engineering
*See Appendix C for permission and citation

Table 7.1. The value of i_{cs} was arbitrarily set to 0.1 (a value less than the average gradient of 0.2) to ensure that the pipe would progress completely through the domain. This was done as the focus of the investigation was on comparing the differences in the hydraulic solutions obtained from the three model formulations rather than evaluation of pipe progression.

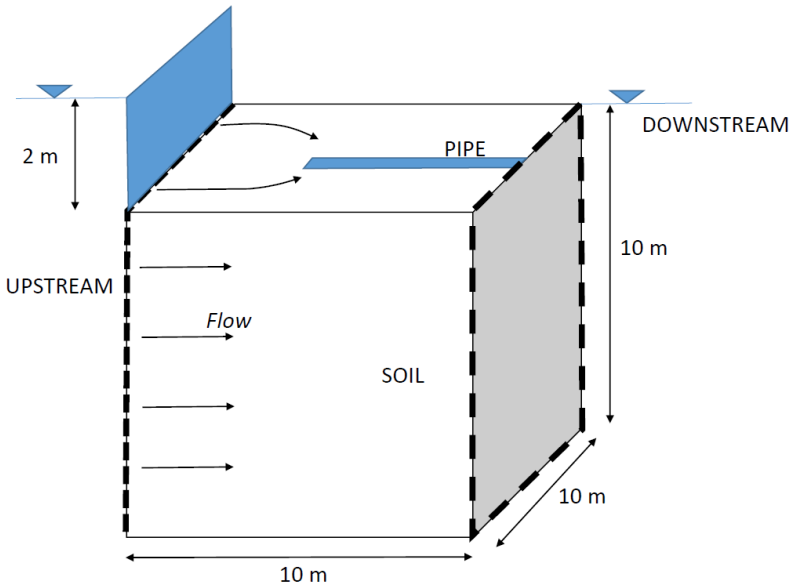

Figure 7.1. Simple test problem for model comparison.

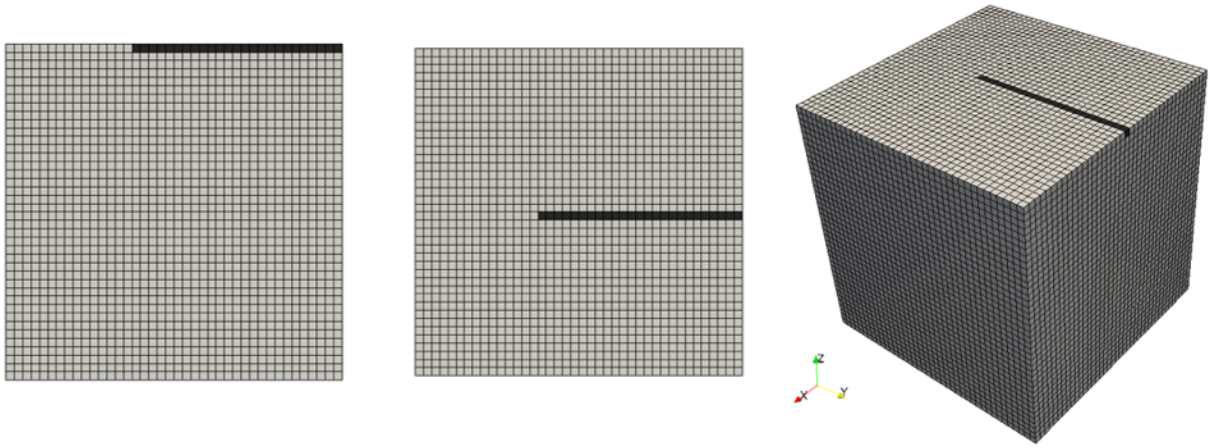

Figure 7.2. Meshes with pipe progressed 6 m shown for cross-sectional analyses, plan view analyses, and three dimensional analyses (from left to right).

Table 7.1. Material properties and boundary condition for BEP analyses.

d_{50} (mm)	k_h (m/s)	τ_c (Pa)	μ (Ns/m^2)	i_{cs}	ΔH (m)
0.2	1×10^{-5}	0.33	1×10^{-3}	0.10	2

The pipe was allowed to progress through the domain entirely. For each progression step, the head profile, nodal hydraulic gradients, and calculated pipe depth profile were examined. The step at which the pipe had progressed 6 m through the domain was chosen for comparison purposes as the pipe was sufficiently developed to see differences in the pipe hydraulic computations, but enough soil remained upstream to be able to examine upstream flow patterns. The flow nets for the 2D analyses are illustrated in Figure 7.3. The head profiles and pipe depth profiles along the centerline of the pipe are illustrated in Figure 7.4. It is readily observed that the head profiles in the pipe are quite similar for all three models. However, the head profile upstream of the pipe is much more non-linear in the three-dimensional model. This is due to the flow concentration that is able to be captured in three dimensions, which results in higher hydraulic gradients.

As the criterion for pipe progression is the secant gradient, a closer examination of the difference in the average, horizontal, hydraulic gradients upstream of the pipe was needed to fully understand the impacts of the model differences on analyses of pipe progression. To quantify this difference, a concentration factor was defined as

$$F_c = \frac{i_{s-3D}}{i_{s-2D}} \tag{7.1}$$

with i_{s-3D} and i_{s-2D} designating the horizontal secant gradient over one element immediately upstream of the pipe from the three-dimensional analyses and two dimensional analysis, respectively. A concentration factor was computed for both the cross-sectional analyses and the plan view analysis. The results are shown in Figure 7.5. When the pipe location is furthest

downstream, the value of F_c is 1.0 due to no flow concentration occurring into the pipe. As the pipe progresses upstream, the value of F_c increases due to the increasing amount of flow concentration. This indicates that the 2D analyses are not able to fully capture the degree of concentration observed in the 3D model.

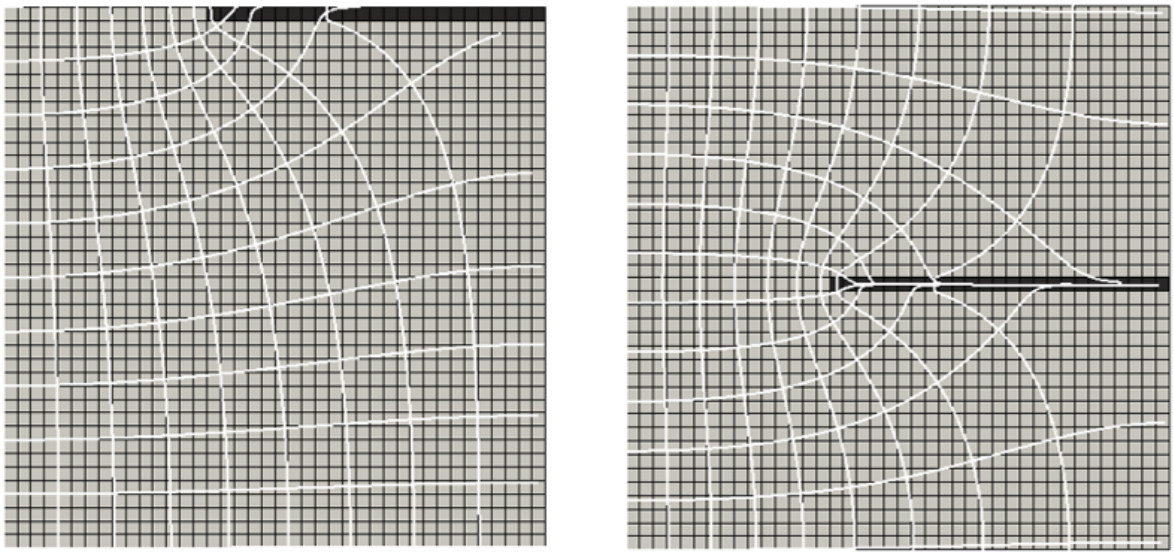

Figure 7.3. Flow nets with pipe progressed 6 m for cross-sectional analyses and plan view analyses.

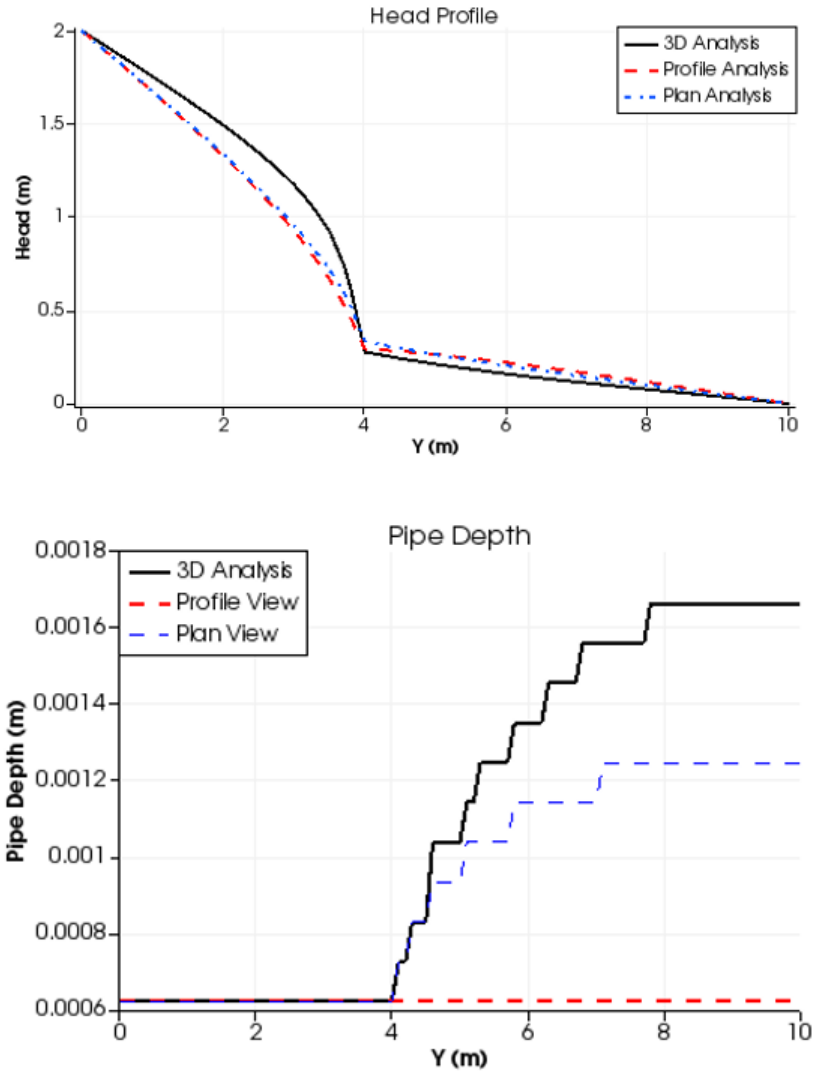

Figure 7.4. Head profile and pipe depth profile for all three models with the pipe progressed 6 m.

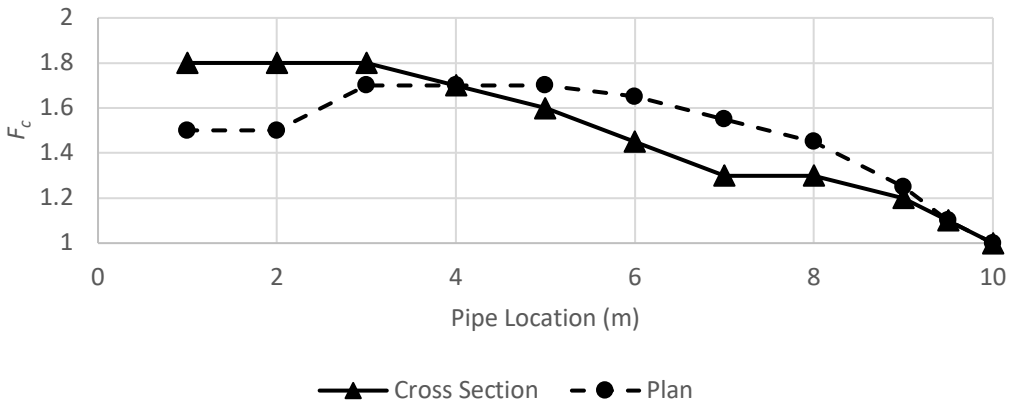

Figure 7.5. Gradient concentration factors as a function of pipe location.

This example analysis compared the results of two- and three-dimensional finite element models for piping. While the results indicate that 2D models are not able to fully capture the magnitude of hydraulic gradients upstream of the pipe, this initial analysis has been very limited in scope, and further research must be conducted. In particular, the following points should be carefully considered.

- The value of F_c increased as the pipe progressed. This may have in part been due to the constant head boundary conditions and small model domain.
- The F_c values presented should not be used until further research into the concentration factors is conducted for full scale levees at critical piping conditions. After further investigation, F_c values may be able to be used to correct 2D models to the equivalent 3D situation for assessing pipe progression using the CSGF.
- Existing two-dimensional models (e.g., Sellmeijer models) that have been calibrated to three-dimensional data may inherently include all necessary adjustments.
- Underprediction of the upstream gradient as observed in the 2D models may unconservatively predict BEP equilibrium if compared directly to the CSGF.

CHAPTER 8

ADAPTIVE MESH REFINEMENT

Based on a paper published in *Computers and Geotechnics**

B.A. Robbins[1] and D.V. Griffiths[1]

The domain approximation errors caused by representing the pipe by elements with either too small of an inflow area (line elements) or too large of an inflow area (oversized quadrilateral or hexahedral elements) results in significant errors in the hydraulic solution for the coupled groundwater-pipe flow. One means for overcoming the issue of oversized elements is too use adaptive meshing in the vicinity of the erosion pipe. The use of adaptive meshing permits using small elements to accurately represent the erosion pipe while also minimizing the number of elements required to solve the problem. In this chapter, a two-dimensional, auto-adaptive meshing algorithm is demonstrated for simulating pipe progression in plan view. While three-dimensional solutions are needed to fully represent the process (Chapter 7), the concept of adaptive meshing is significantly easier to visualize and demonstrate in two-dimensions. For this reason, the following sections demonstrate the concept in two-dimensions recognizing that the extension to three-dimensions is readily made.

8.1 Refinement techniques

As mentioned previously, the solution must be refined near the pipe to (1) obtain hydraulic gradient estimates over sufficiently small distances to assess pipe progression and (2) obtain

[1] Colorado School of Mines, Department of Civil and Environmental Engineering
*See Appendix C for permission and citation

elements small enough to represent the erosion pipe domain. A myriad of strategies exist for refining finite element solutions. The solution can be locally refined by decreasing the element size (h-refinement), increasing the polynomial order of the shape functions on select elements (p-refinement), redistributing nodes within an existing mesh (r-refinement), or any combination of the three approaches. Other strategies such as multigrid techniques may also be used to obtain locally refined solutions. For the present application, the author chose to use solely h-refinement as this approach yields a refined estimate of the solution surrounding the pipe while providing complete control over the element size being used to represent the pipe subdomain.

For h-refinement on structured, quadrilateral meshes, the easiest approach to implement is an element subdivision algorithm in which existing quadrilateral meshes are divided into four equally sized elements as illustrated in Figure 8.1a. This approach yields irregular meshes with "hanging nodes" that are not connected to neighboring elements. To obtain a continuous solution with hanging nodes, it is necessary to constrain the value of the solution at the hanging nodes as described by Rheinboldt and Mesztenyi (1980) or Bangerth et al. (2007). For the mesh in Figure 8.1a which has only 1 degree of irregularity, i.e., 1 hanging node permitted per edge, the solution at the hanging node is constrained to the average value of the neighboring nodes. Let h_i be the value of the solution at hanging node i as illustrated in Figure 8.1. The value of h_i is then simply constrained to the value

$$h_i = \frac{1}{2}\left(h_{c,1} + h_{c,2}\right) \tag{8.1}$$

where $h_{c,1}$ and $h_{c,2}$ are the values of the solution at the two constraining nodes neighboring the hanging node. This constraint can be enforced either by condensing the global system of equations if assembling the full matrices (Bangerth et al 2007), through a penalty approach (Smith and Griffiths 2004), or by enforcing the constraint within an iterative solver as suggested

by Sheu et al (1999). This third approach was taken in this study as an element-by-element preconditioned conjugate gradient solver was employed.

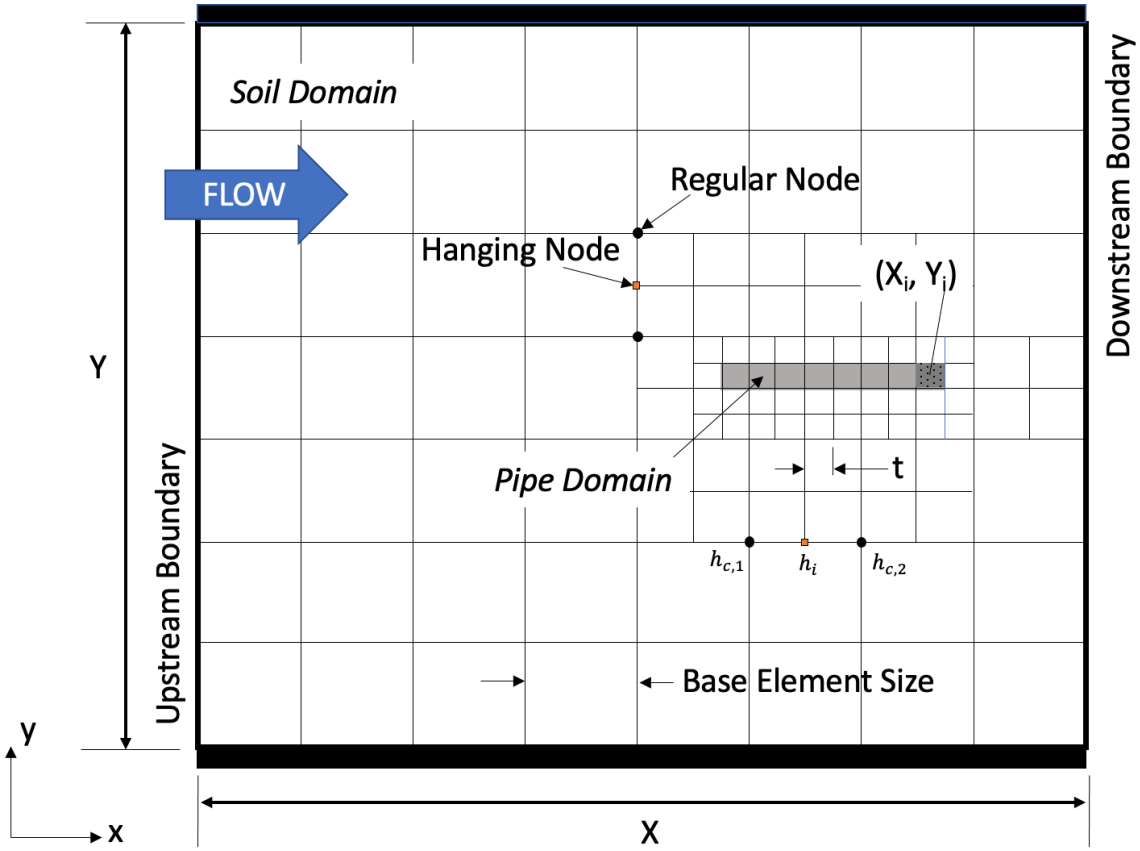

a.

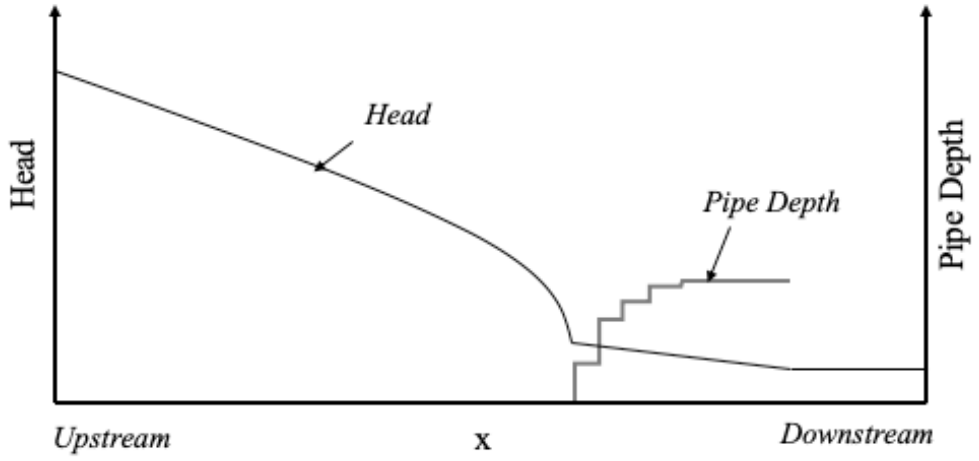

b.

Figure 8.1.(a.) Finite element discretization of x-y analysis plane for two-dimensional analysis of pipe progression and (b.) head and pipe depth profile along centerline of the erosion pipe.

For adaptive refinement of the solution, it is also necessary to specify criteria that define when and where the mesh is refined. Two criteria were used to specify local mesh refinement: (1) all elements adjacent to pipe elements were adapted until the element size was equal to or less than the target element size and (2) elements with an error estimator that was too large were also refined. The first criterion combined with only 1 degree of irregularity being permissible ensured a refined mesh in the vicinity of the erosion pipe. The second criterion allowed for additional refinement to be specified in areas with high hydraulic gradients to resolve the local hydraulic gradients near the pipe tip accurately. For this study, the Zienkiewicz and Zhu (1987) error indicator was calculated for the gradient field as the local hydraulic gradient was of primary interest. The error in the gradient field is defined as

$$e = i - \hat{i} \tag{8.2}$$

where $i = |\nabla h|$ is the exact solution, and $\hat{i} = \left| \nabla N_i h_i \right|$ is the approximate solution obtained from the finite element formulation. As the exact solution is unknown, an estimate $i \approx i^*$ is made following the averaging approach of Burkley and Bruch (1991) where

$$i^* = N_i i_i^* \tag{8.3}$$

The values of i_i^* at the FE nodes are calculated as the average value of all values of $\hat{i}$ at the nodes

$$i_i^* = \frac{1}{j} \sum_{j=1}^{n} \hat{i}_{i,j} \tag{8.4}$$

where $\hat{i}_{i,j}$ denotes the nodal value of $\hat{i}$ at node i obtained from elements $j = 1, \ldots, n$ that share node i. Figure 8.2 illustrates a situation where j=4 for node i. An indicator of the relative error in each element can then be estimated as

$$\eta_e = \frac{|e|}{|i^*|} = \frac{\left[\int_{\Omega_e} (e)^2 d\Omega_e\right]^2}{\left[\int_{\Omega_e} (i^*)^2 d\Omega_e\right]^2} \tag{8.5}$$

Limiting values of η_e can then be defined to obtain further refinement of the solution in areas of highest error.

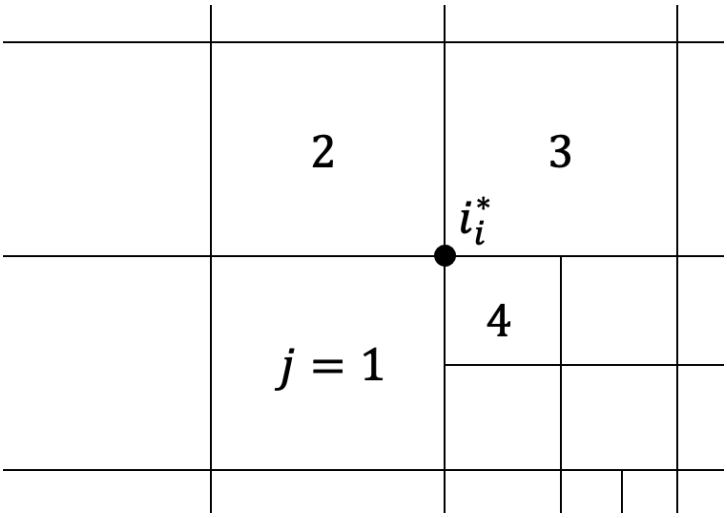

Figure 8.2. Example calculation of i_i^*.

8.2 Simulation algorithm

The simulation of pipe progression is still conducted in a piecewise, steady-state manner, but now with an additional step for refining the mesh. A diagram of the algorithm steps is provided in Figure 8.3. The mesh is initially refined to the target element size in the vicinity of the initiation point until the element containing the initiation point is smaller than the target element size. In this study, all mesh refinement was conducted using the SODA Fortran library described in Robbins and Griffiths (2020). The element containing the initiation point is

switched from the soil domain to the pipe domain, and the pipe depth in the initiation element is set to the initial value of $g_m d_{50}$. All soil elements adjacent to pipe elements are refined until they are equal in size to the pipe elements. Nominal initial boundary conditions are assigned, and Picard iterations over the pipe depth are conducted, increasing the depth by $d_{50}/2$ if $\tau > \tau_c$, until the sediment equilibrium condition of $\tau < \tau_c$ is satisfied in the pipe elements. Once the pipe depth is correct in all pipe elements, the error indicator is calculated, and elements are checked to see if further refinement is necessary. Once the mesh is adequately refined, the depth of the pipe elements is checked to see if the pipe will widen into neighboring elements. If the pipe is widened, the algorithm returns back to the Picard iteration loop over the pipe depth. Once the pipe widening has been checked and no further changes are needed, the magnitude of the hydraulic gradient in elements adjacent to the pipe is checked to see if the pipe can progress further. In the present study, only 1 soil element was switched to a pipe element during each progression step to ensure a single pipe path is obtained. A single pipe is preferred as it causes greater flow concentration thereby resulting in the most conservative analysis results. The element with $\max(i_s - i_{cs})$ was switched to a pipe element during each progression step. This process was repeated until $i_s < i_{cs}$ in all soil elements. Upon reaching equilibrium, the upstream head was increased, and the analysis was repeated until the pipe passed through the entire domain or the head on the upstream boundary reached a maximum value.

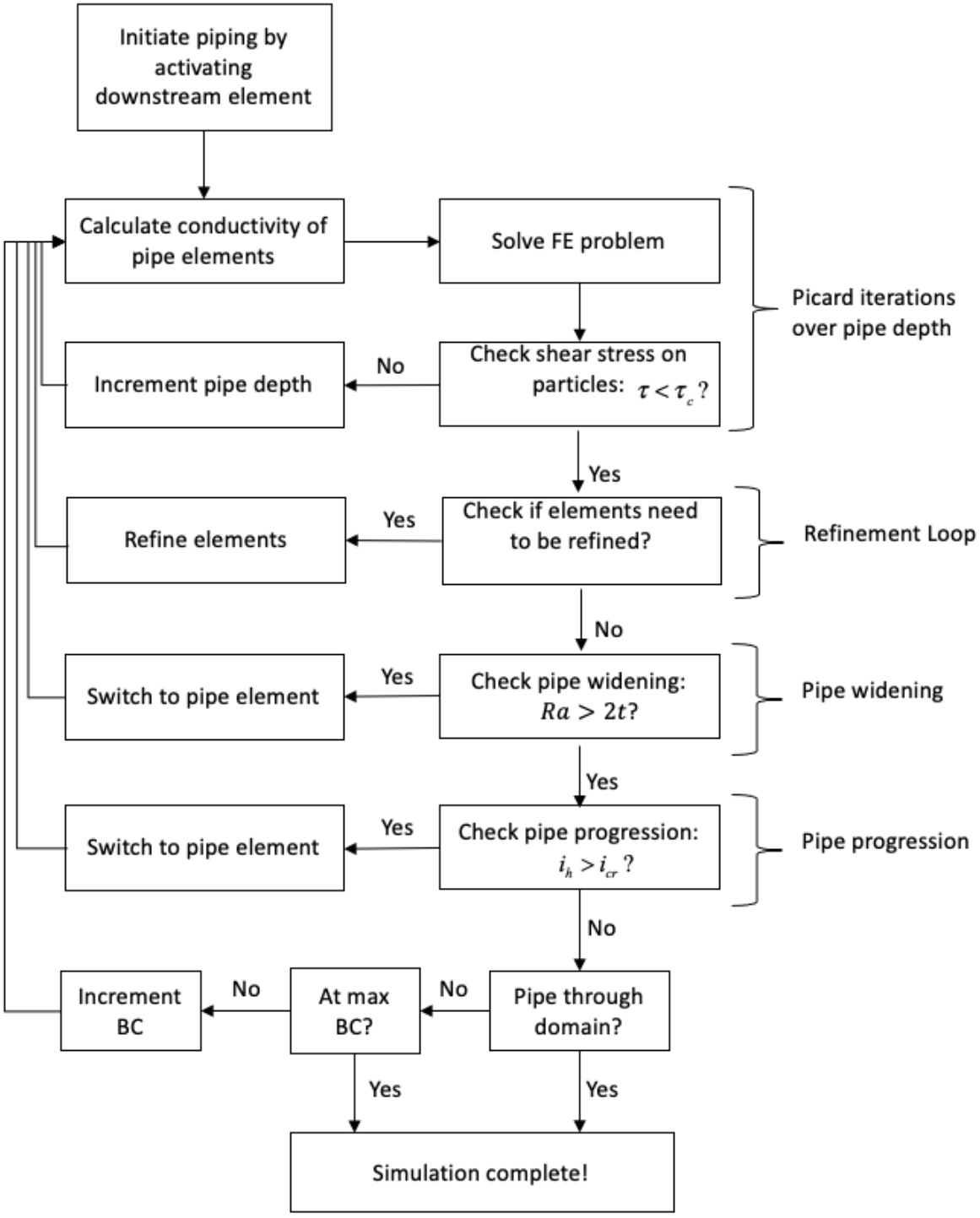

Figure 8.3. Diagram of revised simulation algorithm with adaptive meshing.

8.3 Example results

8.3.1 Levee Underseepage Example

A series of example analyses have been performed to demonstrate the analysis approach, assess the method repeatability, and demonstrate the result of the approximate depth correction factor introduced in Chapter 3. For the example analyses, consider the levee problem illustrated in Figure 8.4 for a case in which the embankment is 10 m in height with 3H:1V side slopes and a 5-m crest width. The base of the embankment is thus L_2 =65 m in width. Letting $L_1 = L_3 =$ 100 m, the total length of the analysis plane is L=265 m in length. Let us consider a domain that is 100 m in width (normal to the plane of Figure 8.4) such that the analysis plane is 265 m in length and 100 m in width. As fine sand is the primary material of concern for BEP, a fine sand with material properties shown in Table 8.1 is used for these example analyses. The hydraulic conductivity was selected based upon d_{50} =0.25 mm. The hydraulic shear stress was determined using equation 2.10. For all analyses conducted, the target element size was 0.2 m. The critical secant gradient, i_{cs}, was selected based on the measured values in Figure 4.6 over a distance of 0.2 m. The measurements in Figure 4.8 were for a sand with d_{50}=0.3 mm. While this sand had a slightly different grain diameter than that being represented, and the two-dimensional analysis may not equate precisely to the measured values, the measured values will be sufficient for demonstration purposes. Lastly, a pipe width-to-depth ratio of R=20 was selected for the pipe.

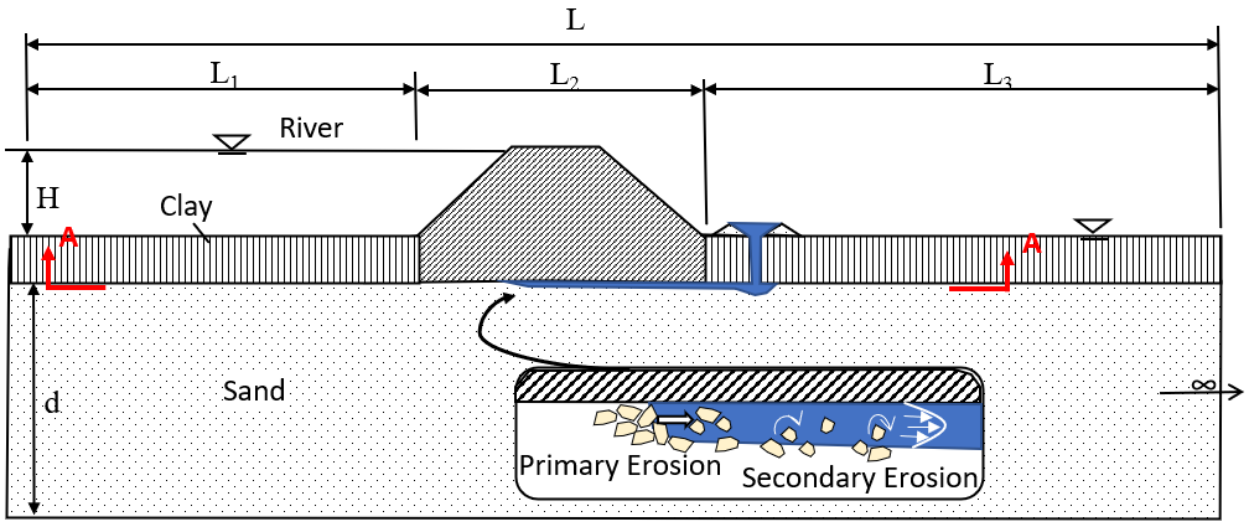

Figure 8.4. Illustration of example levee problem.

The downstream boundary condition is set to $h = 0$ while the upstream boundary condition is initialized to $h = 2.65$ m corresponding to an average hydraulic gradient across the domain of 0.01. When pipe equilibrium is reached, the upstream boundary condition is increased in 1% intervals until the pipe propagates through the entire domain.

The initiation point was arbitrarily selected to be 20 m downstream of the levee toe at an x-location of 185 m and a y-location of 50 m (center of domain). The initial, base element size was set to a value of 5.0 m, and the layer depth was initially set to 1.0 m (no depth correction). The flow in the pipe was initially simulated using only laminar flow assumptions (Equation 3.40) as this led to much faster calculations by eliminating the iteration on the friction factor f. As will be demonstrated in following sections, this assumption was reasonable for the layer depth of 1.0 m.

The resulting pipe path and calculated pipe depth for the main piping channel are illustrated in Figure 8.5. The relatively uniform mesh refinement along the pipe (Figure 8.5a) is obtained due to criterion 1 requiring all adjacent elements to be the same size as the pipe

elements. The additional refinement located downstream of the initiation point and in a few locations along the pipe is due to the calculated error indicator. Both refinement criteria can be adjusted to obtain varying levels of refinement.

The position of the pipe within the domain at equilibrium points is plotted as a function of the average hydraulic gradient applied across the entire domain in Figure 8.6. The pipe progresses with each increase in the upstream head until a critical value is reached. At this point, the pipe progresses continuously through the entire domain with no further increase in the upstream boundary conditions. This result is similar to results obtained by Sellmeijer (2006) and van Esch et al. (2013).

For this homogeneous case, the pipe should progress straight rather than meander as shown in Figure 8.5. Upon further inspection of the mesh near the upstream end of the erosion pipe (Figure 8.7), it was recognized that the pipe meandering was being caused by variations in the hydraulic gradient magnitude due to asymmetric mesh refinement around the pipe. As shown in Figure 8.7, one of the corner elements has a hydraulic gradient of 0.399, which is higher than the element directly in front of the pipe, due to the mesh refinement pattern that developed. Because of this, the pipe progresses to this corner element, activating both the corner element and element with a gradient of 0.379 to maintain edge connectivity of pipe elements. The result of this is the pipe progresses in sporadic directions based on the mesh refinement. To investigate the influence this may have on the results, two tests were run. First, three identical runs of the example problem were run to ensure the analysis approach is reproducible. Second, two additional runs of the example problem were run with the initiation point perturbed 10 m up and down in the y-direction to see if the critical value of the average hydraulic gradient is sensitive to

the pipe path taken. For the repeat runs, identical pipe patterns to the first run shown in Figure 8.5 were obtained in each case (Figure 8.6).

Table 8.1. Material properties for example analyses.

Property	Name	Value
k_x, k_y (m/s)	Hydraulic conductivity	1.0×10^{-5}
d_{50} (mm)	Grain size	2.5×10^{-4}
n	Initial pipe depth multiplier	3
i_{cs}	Critical secant gradient	0.30
τ_c (Pa)	Critical shear stress	0.25
ρ (kg/m^3)	Water density	1,000
μ (Ns/m^3)	Water dynamic viscosity	1.0×10^{-3}
R	Pipe width-to-depth ratio	20

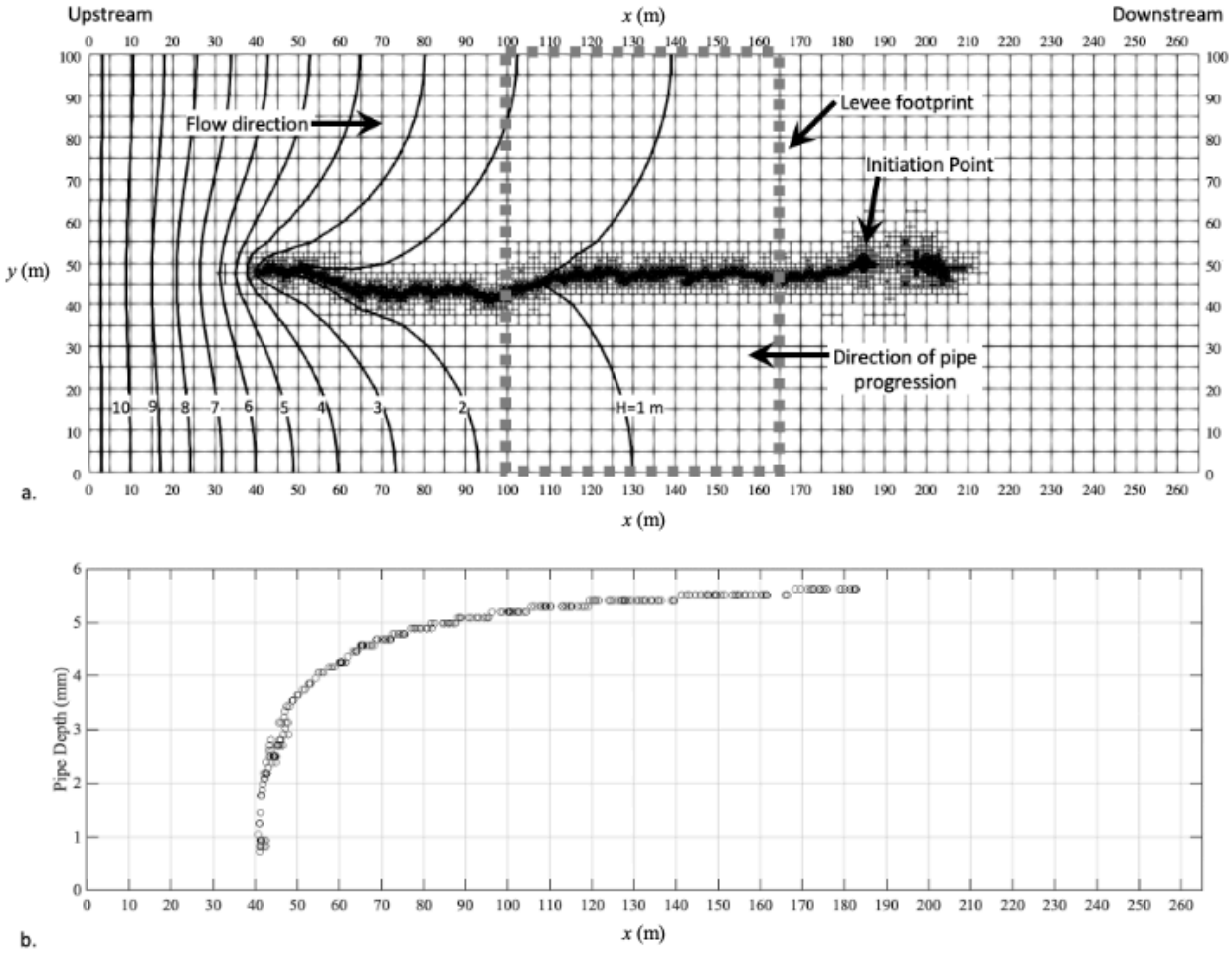

Figure 8.5. Results from plan view analysis of piping illustrating (a) the pipe path for example levee simulation with initiation point (185,50) and (b) corresponding depth of the erosion pipe.

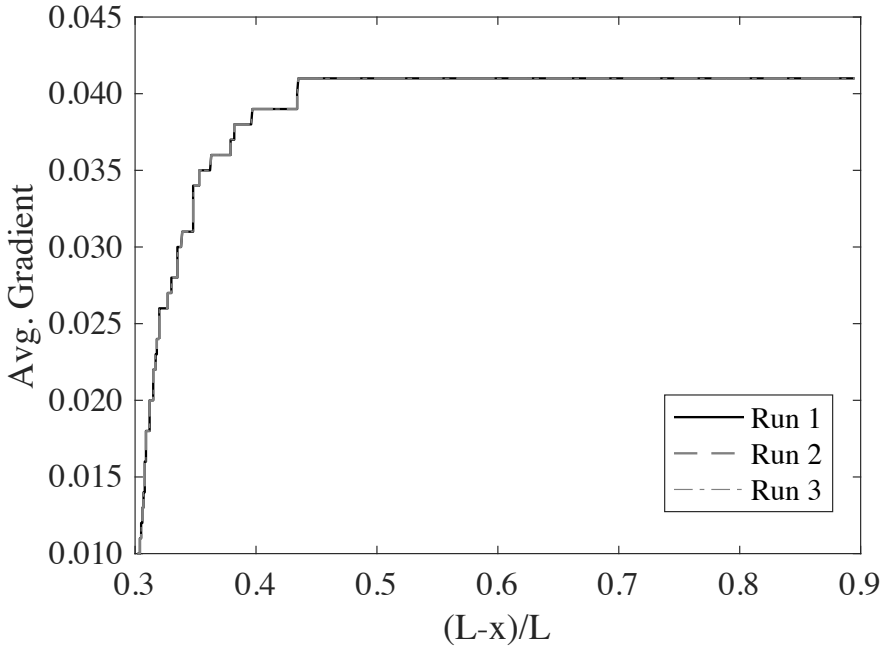

Figure 8.6. Normalized pipe location as a function of average hydraulic gradient.

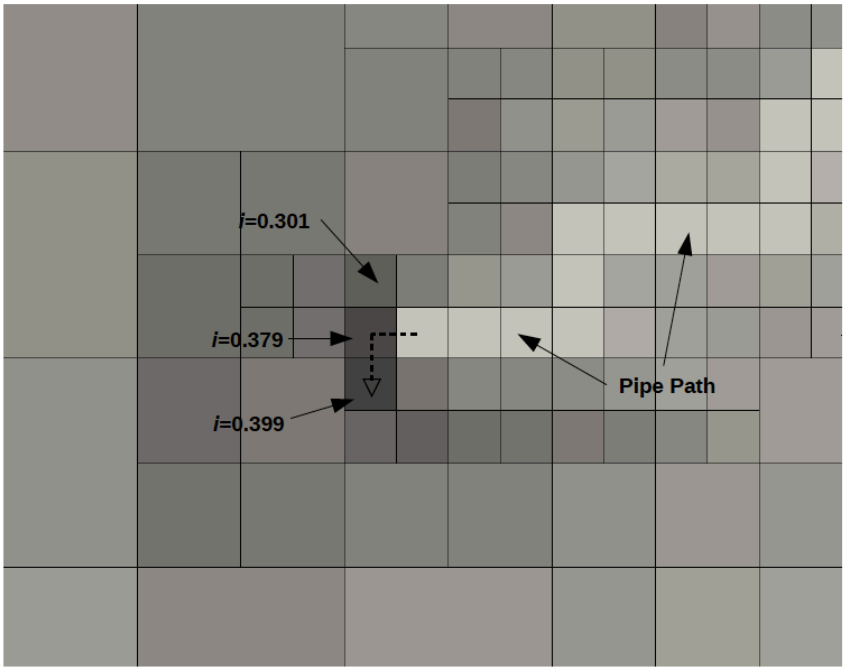

Figure 8.7. Asymmetrical refinement around the erosion pipe leading to pipe meandering.

The results obtained from the two additional runs with the initiation point perturbed are shown in Figures 8.8a and 8.8b. As seen from these figures, the resulting pipe paths obtained with the two different initiation points were different than the original pipe path illustrated in Figure 8.5. Additionally, minor differences in the pipe penetration curves (Figure 8.9) were also observed. However, despite these minor differences, the maximum value of the average hydraulic gradient required for full pipe progression (0.041) was identical for all three cases (Figure 8.9). This indicates that the critical, average, hydraulic gradient across the domain (or the critical upstream head) may not be sensitive to the exact pipe path taken, and the proposed adaptive meshing approach may be adequate for engineering purposes. Nevertheless, more work is needed to address the numerical meandering observed in these analyses to make the pipe paths follow the theoretically anticipated paths.

In addition to the runs discussed, the example analysis with the initiation point centered in the domain was also run with various sand layer thicknesses, D, to assess the performance of the depth correction factor proposed. Increasing D leads to increased flow in the erosion pipes and higher turbulence levels. As such, analyses were run (1) assuming solely laminar flow and (2) allowing either laminar or turbulent flow based upon the Reynolds number. This was done to also assess the influence of turbulent flow on piping calculations as the laminar flow assumption has often been made in the literature (van Esch et al 2013, Robbins and Griffiths 2018). The maximum value of the average hydraulic gradient required to cause the pipe to fully progress through the domain decreased as the aquifer depth increased for both flow assumptions (Figure 8.10a). Further, as the depth increased, the Reynolds number in the pipe increased (Figure 8.10b) such that the flow transitioned from laminar to turbulent flow at an aquifer depth of approximately 10m. For depths less than this, the flow was laminar due to the

low values of the Reynolds number computed when the pipe was at the critical pipe length (Figure 8.10). For greater depths, the flow was no longer laminar, and the analyses permitting turbulent flow yielded lower critical average gradients than the analysis conducted assuming solely laminar flow. However, the differences were relatively small (max difference of 0.002 in terms of average gradient, or 0.5 m across the 265m seepage length) and likely not of significant importance in a practical context. This suggests that laminar flow assumptions are adequate for the input parameter set considered in this study.

The decreasing critical average gradient computed with increasing values of D illustrated in Figure 8.10a is consistent with previous studies of Sellmeijer (1988, 2006) and Schmertmann (2000). To compare the results of this study to the results of previous studies, the piping rule of Sellmeijer et al. (2011) was compared to the results of the present study. Sellmeijer et al. (2011) found that the critical average gradient was related to the aquifer depth and length by the expression

$$\frac{H_c}{L_s} \propto 0.91\left(\frac{D}{L_s}\right)^{\frac{0.28}{\left(\frac{D}{L_s}\right)^{0.28}-1}+0.04} \tag{8.6}$$

where D denotes the depth of the aquifer, and L_s denotes the seepage length along the pipe path (185 m). Because this equation was calibrated to a series of experiments at different scales, it serves as a useful benchmark of the magnitude of the change in critical gradient due to changes in D and L_s. As sufficient data is not available to validate the depth correction using field case histories, comparing to Equation 8.6 was, in the author's view, the simplest means of evaluating the performance of the FE depth correction proposed in this study.

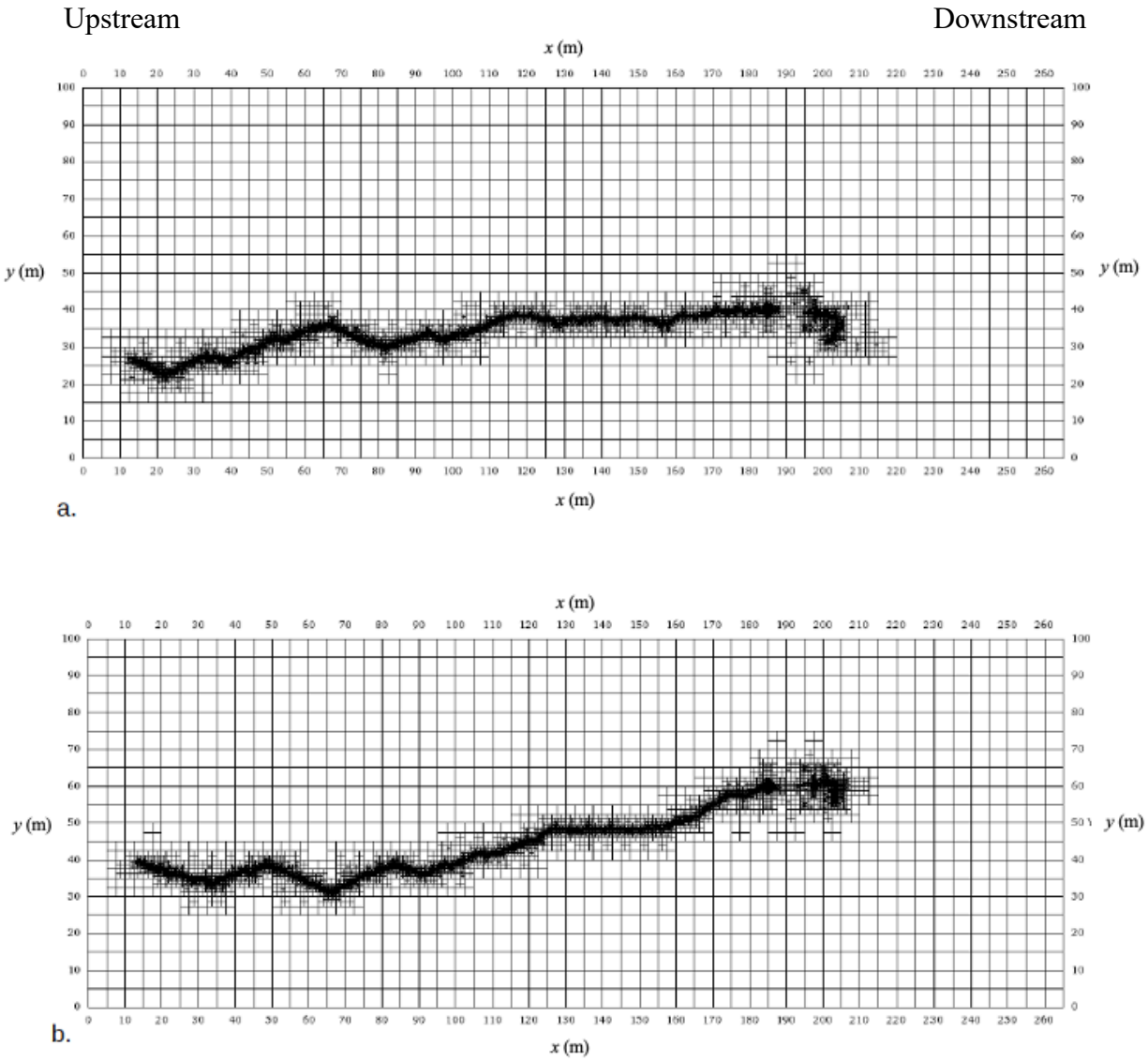

Figure 8.8. Resulting erosion pipe paths obtained for cases with the initiation point (a) perturbed down 10-m in the y-direction (185,40) and (b) perturbed up 10-m in the y-direction (185,60).

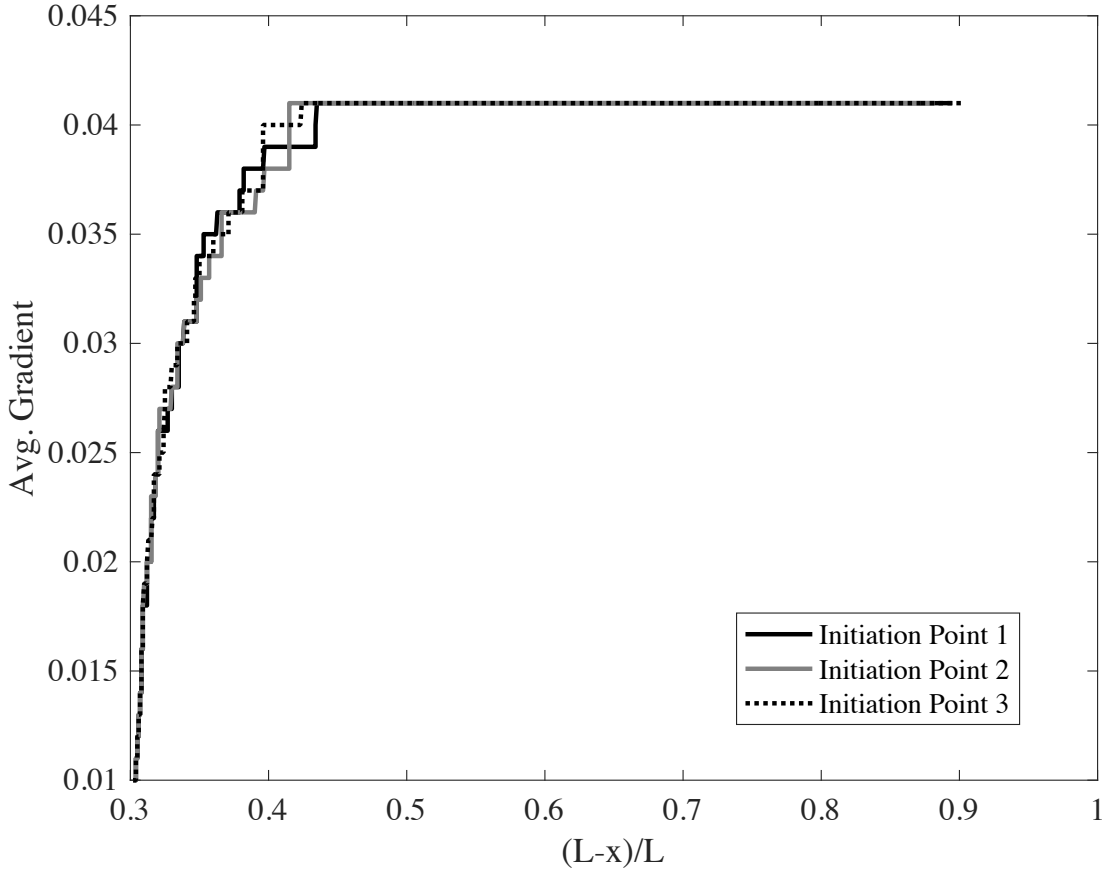

Figure 8.9. Pipe location curves for the original analysis (pt 1) and the analysis with the initiation point perturbed up and down (Pts 2 and 3).

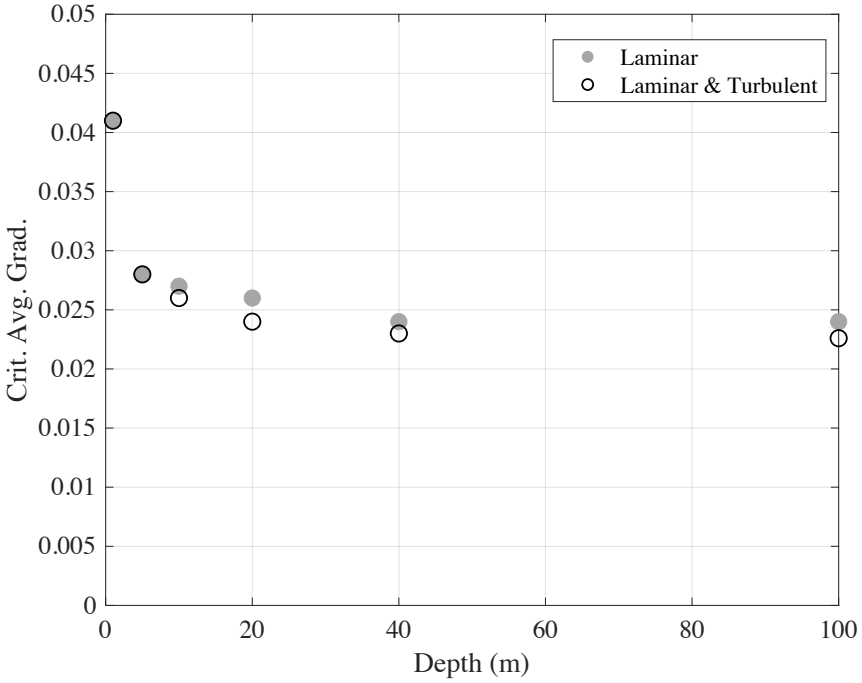

a.

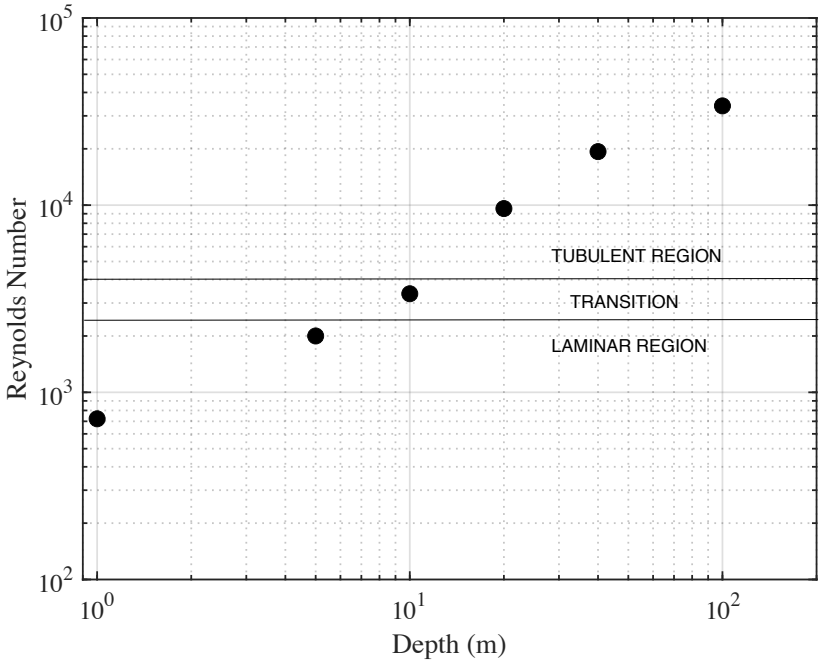

b.

Figure 8.10. Calculated (a) critical, average hydraulic gradient across the entire domain at pipe failure for laminar and turbulent flow assumptions and (b) maximum Reynolds number in turbulent simulations.

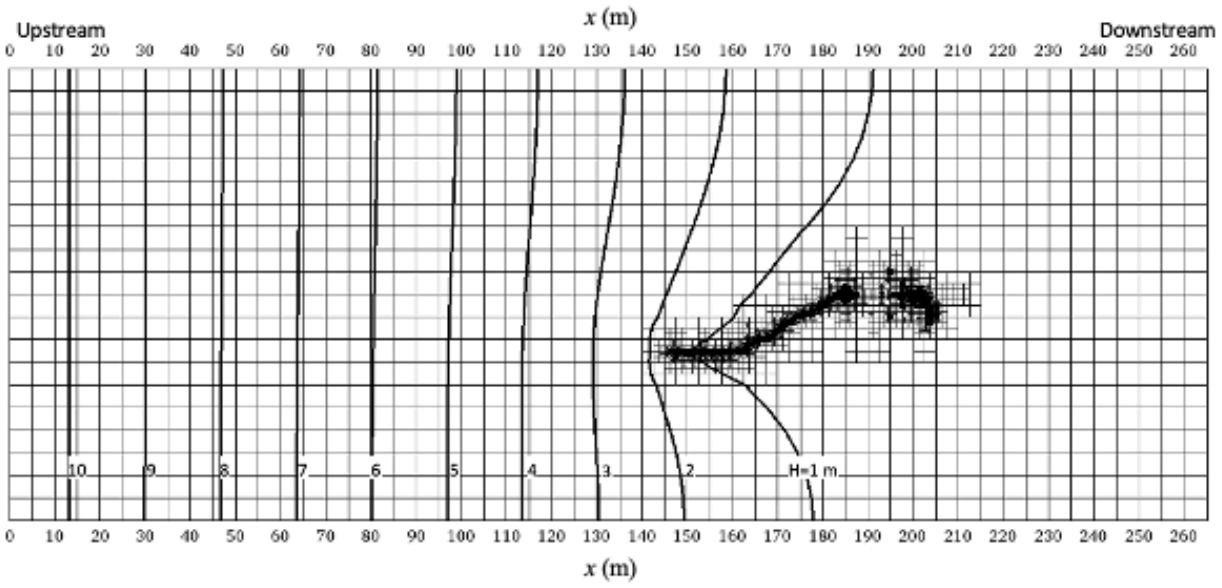

a.

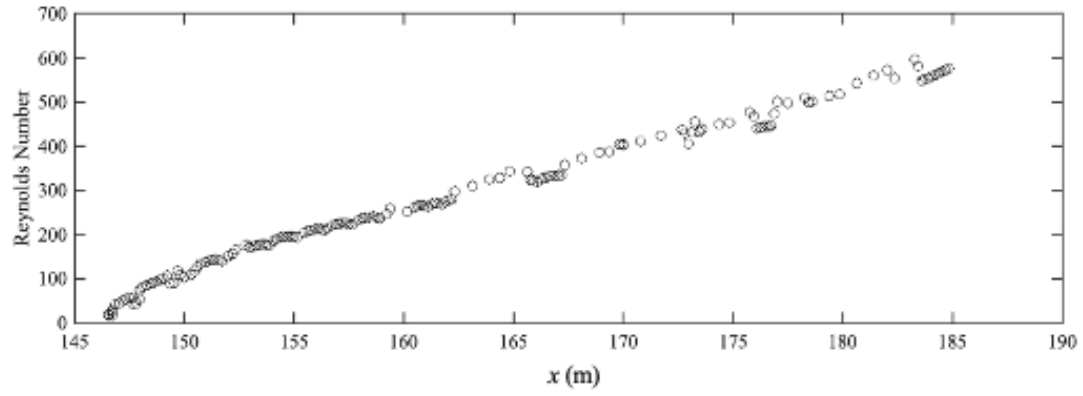

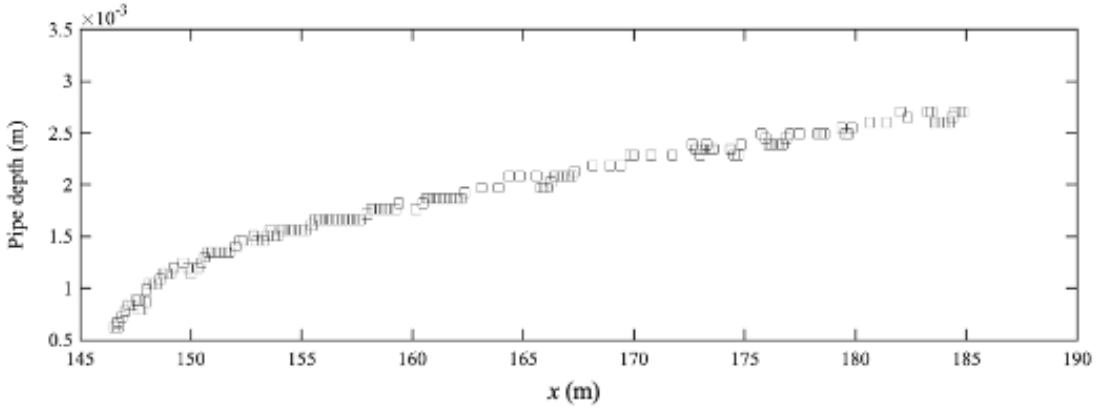

b.

Figure 8.11. Analysis results for turbulent flow with $d = 1$ m showing (a) pipe path at critical pipe length and (b) corresponding Reynolds number and pipe depth in the main pipe channel.

The results of this study can be compared to the results of Sellmeijer et al. (2011) by comparing the change in the critical, average hydraulic gradient across the domain (H_c/L) obtained for different aquifer depths to the trend predicted by Equation 8.6. This comparison was made by normalizing the modeled critical gradients to the case $D = 1$ m such that Equation 8.6 could be plotted normalized to Equation 8.6 for $D = 1$. The results of this comparison are shown in Figure 8.12. The reduction in H_c obtained with the depth correction as described for the FE calculations in this study yields a similar trend to that predicted by Equation 8.6. While the numerical calculations also yield a decreased value of H_c with increasing values of D, the magnitude of reduction obtained is not quite as large as predicted by Sellmeijer et al. 2011 for larger values of D. Nevertheless, for values of D ranging from 1 to 20 meters, the approximate depth correction method presented in this study may be sufficiently accurate for engineering practice.

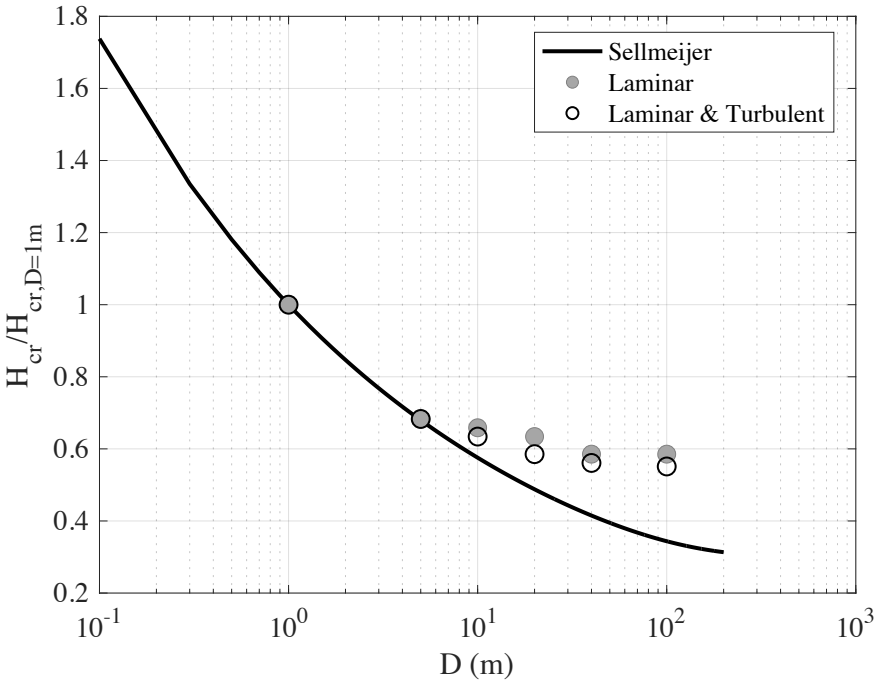

Figure 8.12. Influence of aquifer depth in the present FE model compared to the Sellmeijer theory.

8.3.2 Remedial Measure Example

Having demonstrated the use of adaptive meshing to evaluate BEP for field scale problems, the benefits of assessing BEP via finite elements can be demonstrated through an example problem comparing various remedial measures. Consider the same example levee problem analyzed in the previous section, but now with the following four analyses cases:

Case 1 – The base case consists of the uniform sand layer as previously described. This scenario is representative of the existing condition at a project being assessed for BEP potential. Case 1 is illustrated again in Figure 8.13a.

Case 2 – Consider a scenario where a cut-off wall extends partially through the domain as illustrated in Figure 8.13b. This scenario may occur near the end of a cut-off wall. The example analysis will show how this situation could potentially be assessed to determine how far a wall should be extended. It will also permit a relative comparison between a few scenarios.

Case 3 – Consider a case where relief wells were installed at x=200 m. In this case, the relief wells are 15 m downstream of the BEP initiation point. While wells are designed to prevent BEP altogether by limiting initiation of erosion, there are situations where wells become clogged over time or are under designed. In these cases, it may be of interest to assess what risk reduction the partially functioning wells provide if erosion is able to initiate. While the relief wells were represented by setting a constant head boundary of zero at nodes in this study, more sophisticated well representation could readily be incorporated that consider the relationship between outflow and total head associated with the wells.

Case 4 – Now consider the case where relief wells were installed 10 m downstream from the levee toe at x=170 m. In this case, the BEP initiation occurs 15 m downstream of the relief wells.

For all four cases, a simulation of BEP progression was conducted yielding the final pipe paths as shown in Figure 8.13. The head on the downstream boundary was set to zero, and the head at the initiation point was set to zero. The upstream head was gradually increased in steps, and the pipe progression was assessed using the algorithm previously described.

During each simulation, the relative pipe position (l_p/L_s) was recorded at each simulation step based upon the erosion pipe length (l_p) and the final length of the pipe path (L_s). By plotting the relative pipe position as a function of the applied upstream head (Figure 8.14), a pipe progression curve is generated. Consider the pipe progression curve for the base case with no remedial measures (Case 1) as shown in Figure 8.14. For this curve, it is readily seen that the critical head for pipe progression is 10.8 m. Once the upstream head reaches this level, the pipe progresses completely through the domain without any further increases in head. Further, the pipe progression curve illustrates that the critical pipe length occurs when the pipe has only progressed approximately 20 percent along the full erosion path. This information is useful when considering how likely it is that erosion would be detected in advance. That is, by considering how far a pipe may progress before reaching the critical head, the potential for instrumentation and monitoring to detect the erosion in early stages can be assessed.

By comparing the pipe progression curves for the four different cases, a few significant observations can be made. First, all remedial measures assessed result in an increase in the critical head required to cause failure. Intuitively, one may have expected Case 4 to actually

decrease the critical head due to the wells increasing the average gradient in the sand layer. This may be the case for closely spaced wells. However, in the scenario considered, the wells redirected water from the pipe tip to the well. This reduced the local gradient at the pipe tip and caused an increase in the critical head. Second, the position of the relief wells relative to the BEP initiation point is significant. The scenario with the wells downstream of the initiation point had a critical head of 12 m, whereas the scenario with the wells upstream of the initiation point was more resistant to BEP with a critical head of 14 m. This should be considered in designing well arrays. In addition to the pipe progression curves, the visualization of the pipe paths is a useful way to understand how BEP pipes will interact with remedial features and designs.

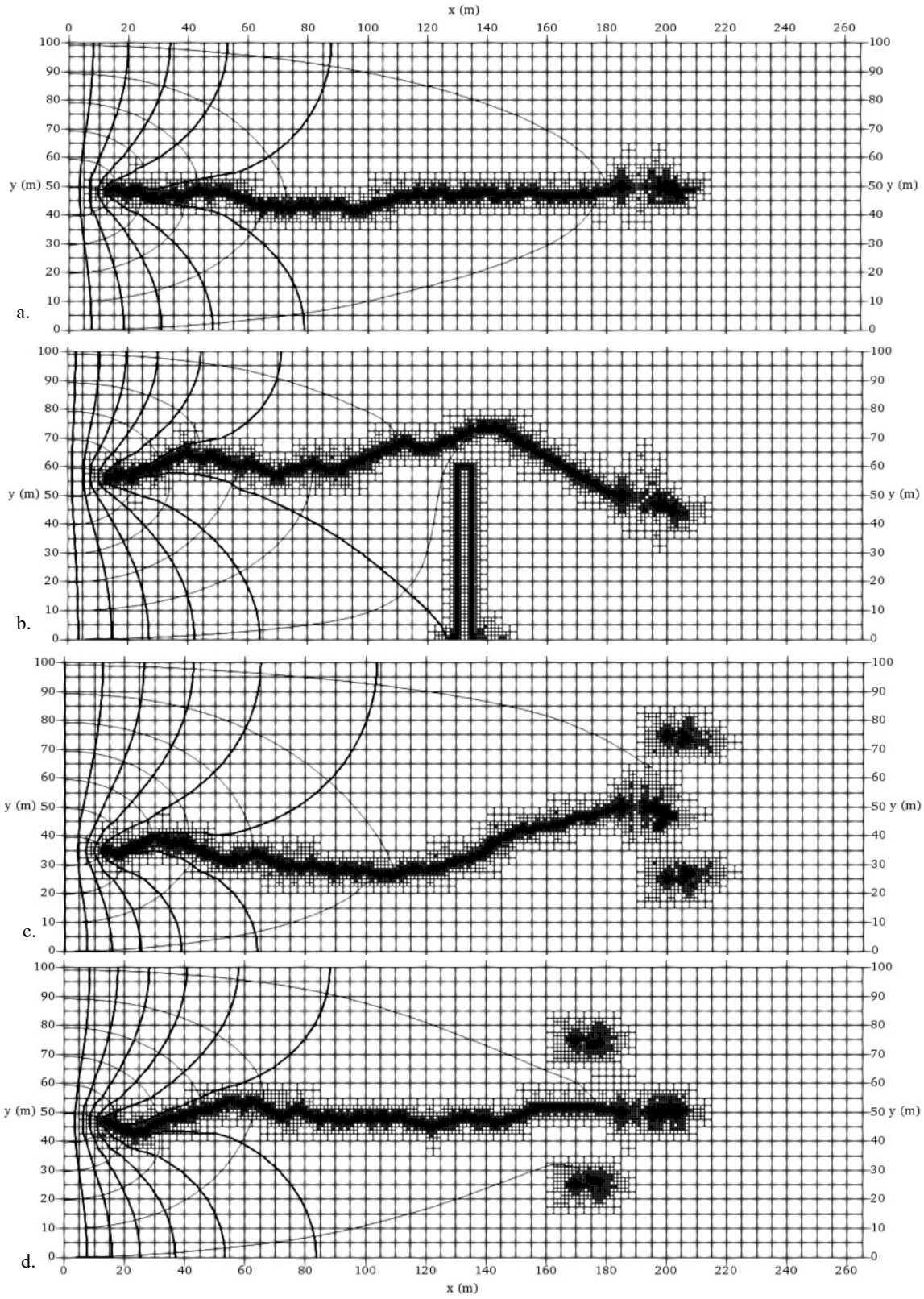

Figure 8.13. Final pipe paths for (a) Case 1, (b) Case 2, (c) Case 3, and (d) Case 4.

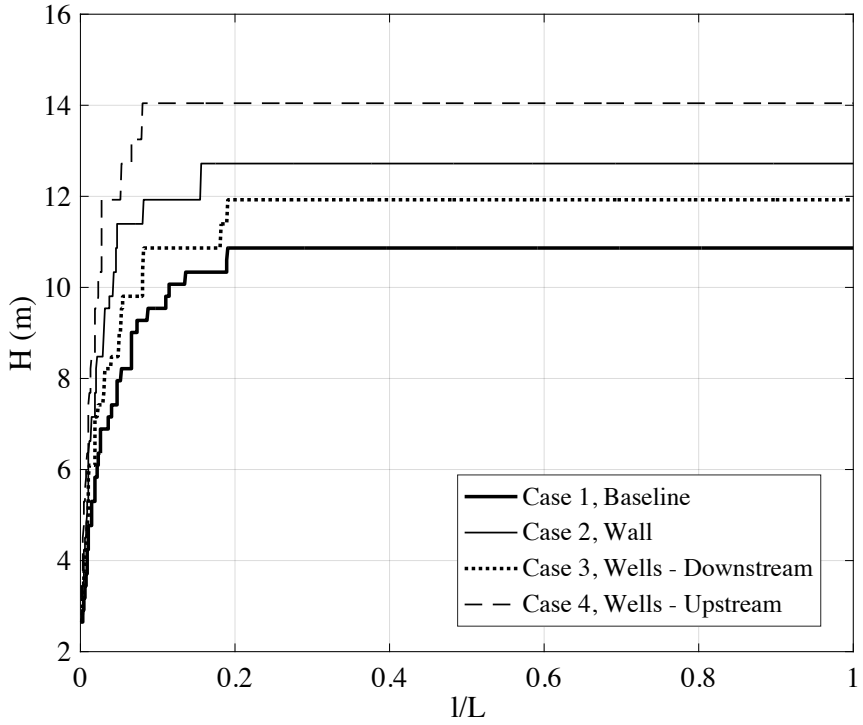

Figure 8.14. Relative pipe position as a function of head applied to the upstream boundary for the four cases assessed.

An example problem was used to demonstrate how the analysis approach can be used to assess the potential for BEP progression in various scenarios. The resulting visualizations of the BEP erosion path and corresponding pipe progression curves are valuable information for understanding BEP progression. Further, by comparing the resulting pipe progression curves for various designs, the relative robustness of remedial measures can be quantified. The proposed approach provides a step forward in the ability of dam engineers to quantitatively assess BEP risks and make informed decisions regarding structural modifications for risk mitigation.

CHAPTER 9

RANDOM FINITE ELEMENT ANALYSIS OF BACKWARD EROSION PIPING

Based on a paper published in *Computers and Geotechnics**

B.A. Robbins[1], D.V. Griffiths[1], and Gordon A. Fenton[2]

One factor that has been shown to greatly impact BEP progression is that of soil variability (Negrinelli et al., 2016; Methorst 2020). Through laboratory experiments on both uniform and layered soil deposits, Negrinelli et al. demonstrated that layered soils require up to 3 times more head differential to fail by BEP than uniform soils (Figure 9.1). This factor is not easily accounted for in the analysis of BEP, and the error of neglecting it is sufficiently large to limit the value of numerical methods that do not provide a means to account for soil variability. While some attempts at accounting for soil variability in BEP analysis have been made, these studies have either not explicitly simulated erosion (Liu et al. 2017), have simplified the erosion process (Kanning and Calle 2013), or have focused on other types of erosion (suffusion) that do not develop sequentially in the upstream direction (Liang et al. 2017).

Having developed finite element approaches for simulating BEP, the Random Finite Element Method (RFEM), developed by Griffiths and Fenton (1993) and Fenton and Griffiths (1993), can now be applied to the simulation of BEP in order to quantitatively assess how spatial variability in soil properties influences pipe progression. This chapter describes how the BEP finite element model can be used within an RFEM framework to assess the influence of spatial variability in both soil permeability and i_{cs} on the progression of BEP.

[1] Colorado School of Mines, Department of Civil and Environmental Engineering
[2] Dalhousie University, Department of Engineering Mathematics & Department of Civil and Resource Engineering
*See Appendix C for permissions and citation

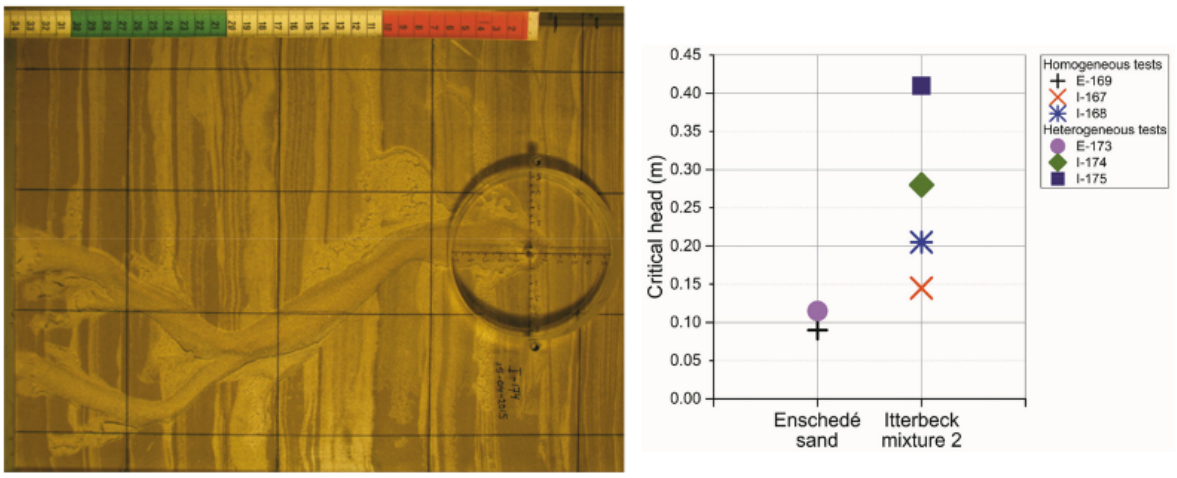

Figure 9.1. Influence of soil variability on critical head for BEP progression (Negrinelli et al., 2016).

9.1 Application of RFEM to BEP

RFEM is a combination of random field generation and finite element computations within a Monte-Carlo framework that is used to observe the influence of spatial variability in model properties on the statistics of model outputs. The results from RFEM analysis are useful for determining the sensitivity of model results to both the magnitude and patterns of spatial changes in model input properties, which in turn provides an indication of the probability of failure for various conditions. The following sections describe the random field generation, simulation of BEP progression through the random field, and Monte-Carlo simulation framework used to perform RFEM analysis of BEP progression in two dimensions (plan view).

9.1.1 Random Field Generation

The soil properties with the greatest influence on the pipe progression are the hydraulic conductivity of the soil and the critical hydraulic gradient for pipe progression (Schmertmann 2000; Sellmeijer et al. 2011). The hydraulic conductivity of the soil determines the magnitude of flow towards the pipe, and thus the pipe dimensions. The spatial variation of the hydraulic

conductivity also dictates the spatial distribution of hydraulic gradient in the soil. Both of these factors control the magnitude of the hydraulic gradients near the progressing pipe tip. Meanwhile, the resistance to pipe progression is dictated by the critical hydraulic gradient for pipe progression (i_{cs}). Therefore, the soil hydraulic conductivity and critical hydraulic gradient were both modeled as random fields for the RFEM analyses.

As both the hydraulic conductivity k_h and critical hydraulic gradient i_{cs} are related to the grain size distribution of the soil (e.g., Carrier 2003, Schmertmann 2000), it is necessary to allow the k_h-field and i_{cs}-field to be cross-correlated. For uniformly graded soils, both k_h and i_{cs} increase with increasing grain size, and the fields are positively correlated. For well graded soils, the hydraulic conductivity is controlled by the fine fraction of the gradation, while i_{cs} is controlled by the median grain size and overall coefficient of uniformity. Widening of the gradation to a larger range of particle sizes will decrease the particle diameter of the fine fraction (lowering k_h) while increasing the coefficient of uniformity and value of i_{cs} (Schmertmann 2000). In this scenario, the random fields will be negatively correlated. As such, both positive and negative correlations were considered herein.

For this study, both k_h and i_{cs} were treated as lognormally distributed random variables. A random field was generated for each soil property with spatial correlation lengths θ_x and θ_y as illustrated in Figure 9.2. The spatial correlation length defines the correlation in soil properties between points in the random field, with larger correlation lengths yielding more uniform soil properties over larger distances.

To generate the cross-correlated random fields for each soil property, the covariance matrix decomposition method was used (Fenton 1994; Fenton and Griffiths 2008). Two independent Gaussian random fields were generated using the Local Average Subdivision (LAS) method

(Fenton and Vanmarcke 1990) with specified correlation length $\theta = \theta_x = \theta_y$ and a Markov correlation function (Fenton and Griffiths 2008). The covariance decomposition method was then used to generate a third Gaussian field that had a specified correlation to the first field. The two correlated random fields were then transformed to the desired marginal distributions for each of the two soil properties of interest (k_h and i_{cs}).

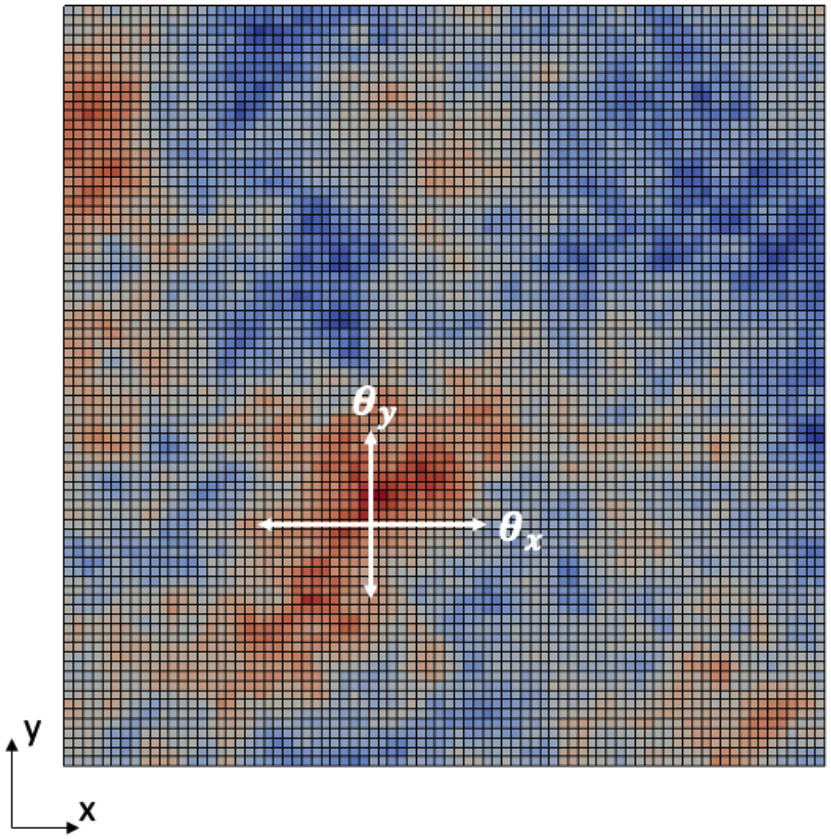

Figure 9.2. Random field of soil hydraulic conductivity with correlation lengths θ_x and θ_y in the x and y directions, repsectivley.

9.1.2 BEP Finite Element Analyses

Once the random fields for k_h and i_{cs} are generated, the progression of BEP through the random fields can be assessed just as before, except now every element has a distinct value of

both k_h and i_{cs} according to the random field values. Consider the simple example illustrated in Figure 9.3 of unidirectional flow through a random field. The top and bottom boundaries are no flow boundaries. The downstream boundary has a constant head of $h = 0$, whereas the upstream head is set to a nominal initial head of $h = h_i$. Erosion is initiated by switching a soil element to a pipe element at the center of the downstream boundary. BEP progression through the random field is then assessed using the plan view formulation and algorithm presented in Chapter 3. Each time equilibrium is reached, the upstream head is increased until the pipe progresses further. Throughout the simulation, the distance the pipe has progressed through the domain (l_p) and the total differential head across the sample ($H = h$-0) are recorded at each computational step. From this information, the normalized pipe progression curve (Figure 9.4a) can be generated. The pipe progression curve provides the degree of pipe penetration (l_p/L) through the domain as a function of the average hydraulic gradient (H/L). The critical average hydraulic gradient and critical pipe length are given by the point on the pipe progression curve when the maximum average hydraulic gradient is reached. Once this point is reached, the pipe progresses through the remainder of the domain without any further increase in head.

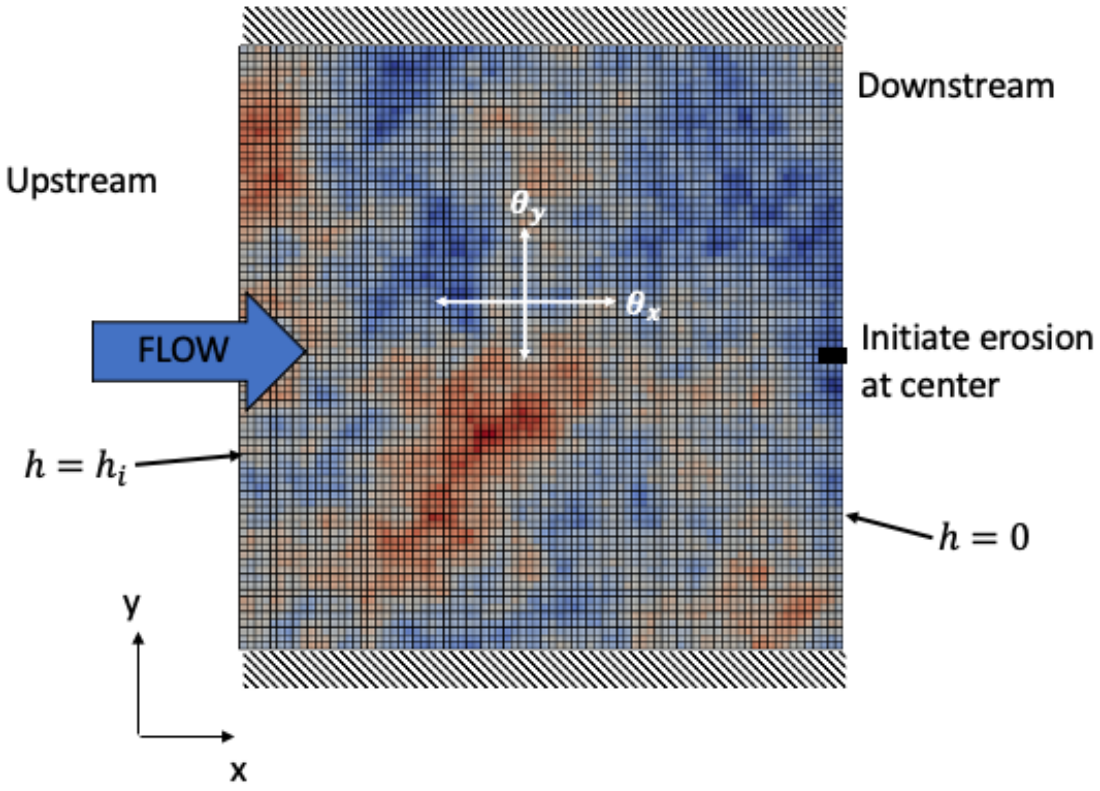

Figure 9.3. Initial conditions for simple BEP progression simulation in unidirectional flow.

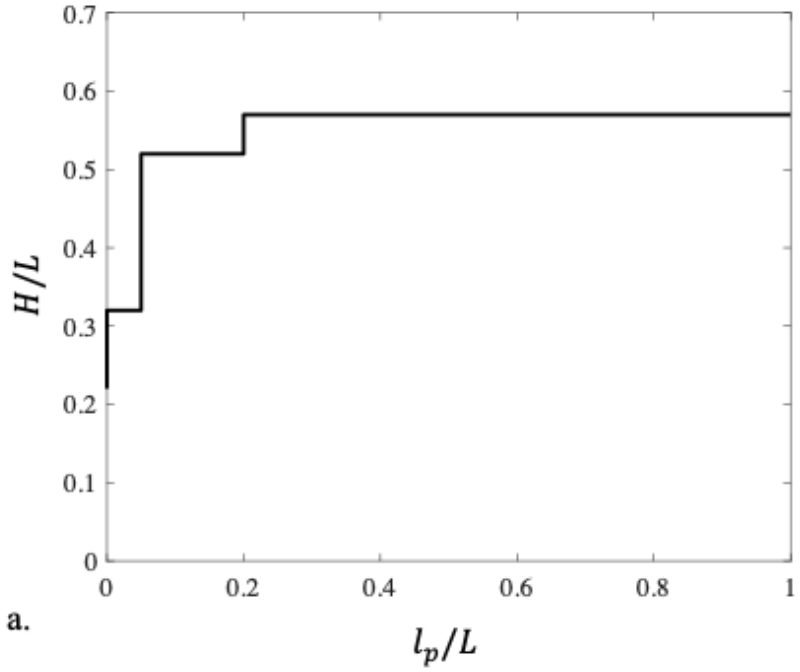

a.

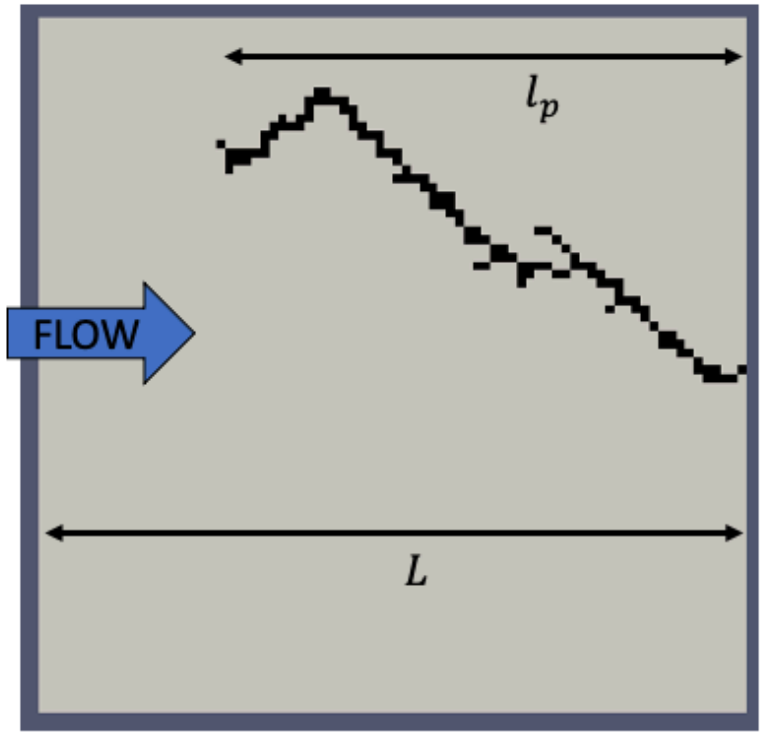

b.

Figure 9.4. Example (a) pipe progression curve and (b) pipe path for a single BEP simulation in a random k field.

9.1.3 Monte-Carlo Simulation

In RFEM analysis, it is necessary to perform Monte-Carlo simulations to generate meaningful and accurate statistics of output quantities of interest. For analysis of BEP, the critical average hydraulic gradient $(H/L)_{cr}$ is the quantity of interest. From the distribution of this quantity, the probability of BEP pipe progression through the analysis domain can be evaluated under various conditions.

The Monte-Carlo simulation loop follows the steps outlined in Figure 9.5. For each Monte-Carlo simulation, a new realization of the i_{cr} and k_h random fields is generated according to the specified random field parameters. The FEM analysis of the pipe progression is performed following the approach described in the previous section, resulting in a single pipe progression curve as illustrated in Figure 9.4a. The value of $(H/L)_{cr}$ for each simulation is determined by post processing the results to find the maximum value of (H/L) reached during the analysis. The $(H/L)_{cr}$ value from the simulation is stored, and this process is repeated for subsequent simulations until the distribution of $(H/L)_{cr}$ for the particular RFEM analysis has been adequately defined.

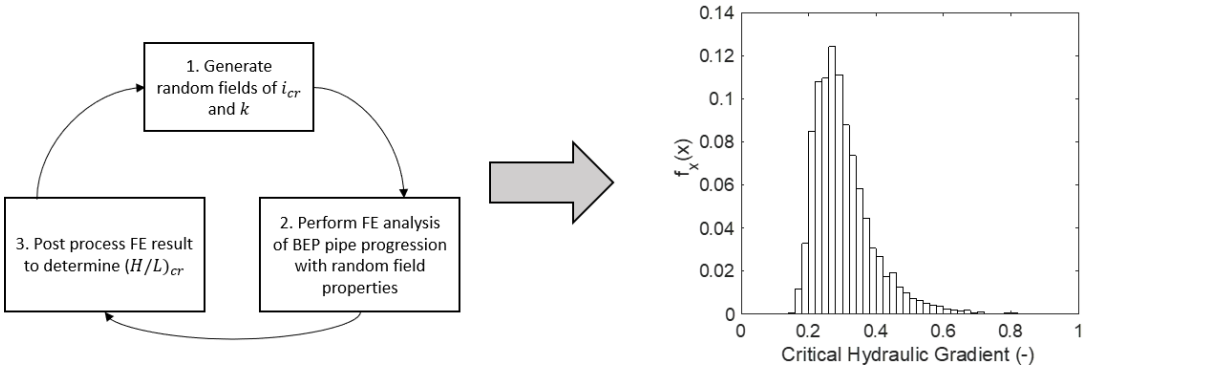

Figure 9.5. Illustration of Monte-Carlo analysis loop for BEP RFEM analysis.

9.2 Example Problem

A simple example problem was developed to illustrate the RFEM approach described in this study for a 10-m by 10-m domain as illustrated in Figure 9.6. The boundaries at y=0 and 10 m are no flow boundaries. The boundary at x=10 m is a constant head boundary with h=0 m. The boundary at x=0 m is the constant head, upstream boundary. An initial condition of h=0.1 m was assigned to the upstream boundary, and the head was increased each time the pipe reached equilibrium until the pipe progressed through the domain. For nearly all analyses conducted, the pipe was initiated at the center of the downstream boundary. For a few analyses, the pipe was allowed to initiate anywhere along the boundary to assess the influence of an unrestricted initiation location on the results.

An element size of 0.125 m was used such that the domain was a square with 80 elements in both the x- and y- directions for a total of 6400 elements. All elements were 4 node quadrilateral elements with linear shape functions.

Assumed soil properties, water properties, and random field characteristics for the example problem are listed in Table 9.1. The mean values of soil properties were selected to represent a fine-grained sand with a median grain size of d_{50}=0.2 mm. The mean hydraulic conductivity for a sand of this particle diameter is approximately $\mu_k = 1.0 \times 10^{-5}$ m/s (Van Beek 2015), and the critical shear stress has been shown to be τ_c=0.33 Pa (Van Beek et al. 2019). The mean value of the critical hydraulic gradient for pipe progression for fine sand is approximately μ_{ics}=0.3 (Robbins et al. 2018) when assessed over the distance of 1 element (0.125 m). In addition, values of μ_{ics}=1.0 and 3.0 were also considered to assess the influence of the critical hydraulic gradient magnitude on the results. The density (ρ) and dynamic viscosity (μ) of water were selected assuming a water temperature of 20 degrees Celsius.

While the mean properties for fine sand are well defined, less information on the spatial variability of these properties in the field is available, which may also be site specific. As such, a broad range of random field characteristics was assumed for this study to evaluate the general trends caused by random soil properties. All analyses considered were for isotropic random fields in which $\theta_x = \theta_y = \theta$. Five values of θ/L were considered in this study ranging from 0.05 to 1.0. For the hydraulic conductivity random field, k_h was assumed to be lognormally distributed with a mean of $\mu_k = 1 \times 10^{-5}$ m/s with five values of coefficient of variation (σ_k/μ_k) ranging from 0.25-3.0. To initially investigate the influence of randomness in only the hydraulic conductivity *k*, a set of analyses were conducted with a uniform, deterministic value of i_{cs}=0.3 (σ_{ics}=0.0). Subsequently, various i_{cs} random fields were considered with means 0.3, 1.0, and 3.0 and coefficients of variation for the critical gradient (σ_{ics}/μ_{ics}) of 0.16, 0.5, and 1.0. When random fields were also generated for the critical gradient, i_{cs} was also assumed to be lognormally distributed with the same spatial correlation length as the k_h-field. Values of correlation between the two random fields evaluated were ρ=-1, 0, and 1. These input parameters resulted in 25 different k_h-fields and 9 different i_{cs}-fields that were evaluated. Each of these combinations was re-evaluated for the 3 different correlation values resulting in 675 different input variable combinations. Considering the additional 25 scenarios with σ_{ics}=0.0, a total of 700 combinations of input parameters were evaluated, with a separate Monte-Carlo analysis being conducted for each scenario. A single, sample realization from one of the analysis scenarios is shown in Figure 9.7. While the result of a single realization does not yield meaningful information regarding $(H/L)_{cr}$, it does provide a nice illustration of the BEP behavior in random fields. It is readily seen that the pipe is meandering through the domain, searching for the path of least resistance. Further, the influence of the pipe on the groundwater

flow pattern can be seen from the flow net drawn in Figure 9.7a. The erosion pipe is capturing nearly all flow in the domain, and the hydraulic gradient is high near the upstream pipe tip as indicated by the closely spaced head contours. While the results of every realization could not be examined, some of the trends that will be presented in the distributions of $(H/L)_{cr}$ will best be explained in terms of some of these observed behaviors. The full distributions of results obtained from the RFEM analysis are presented and discussed in the next section.

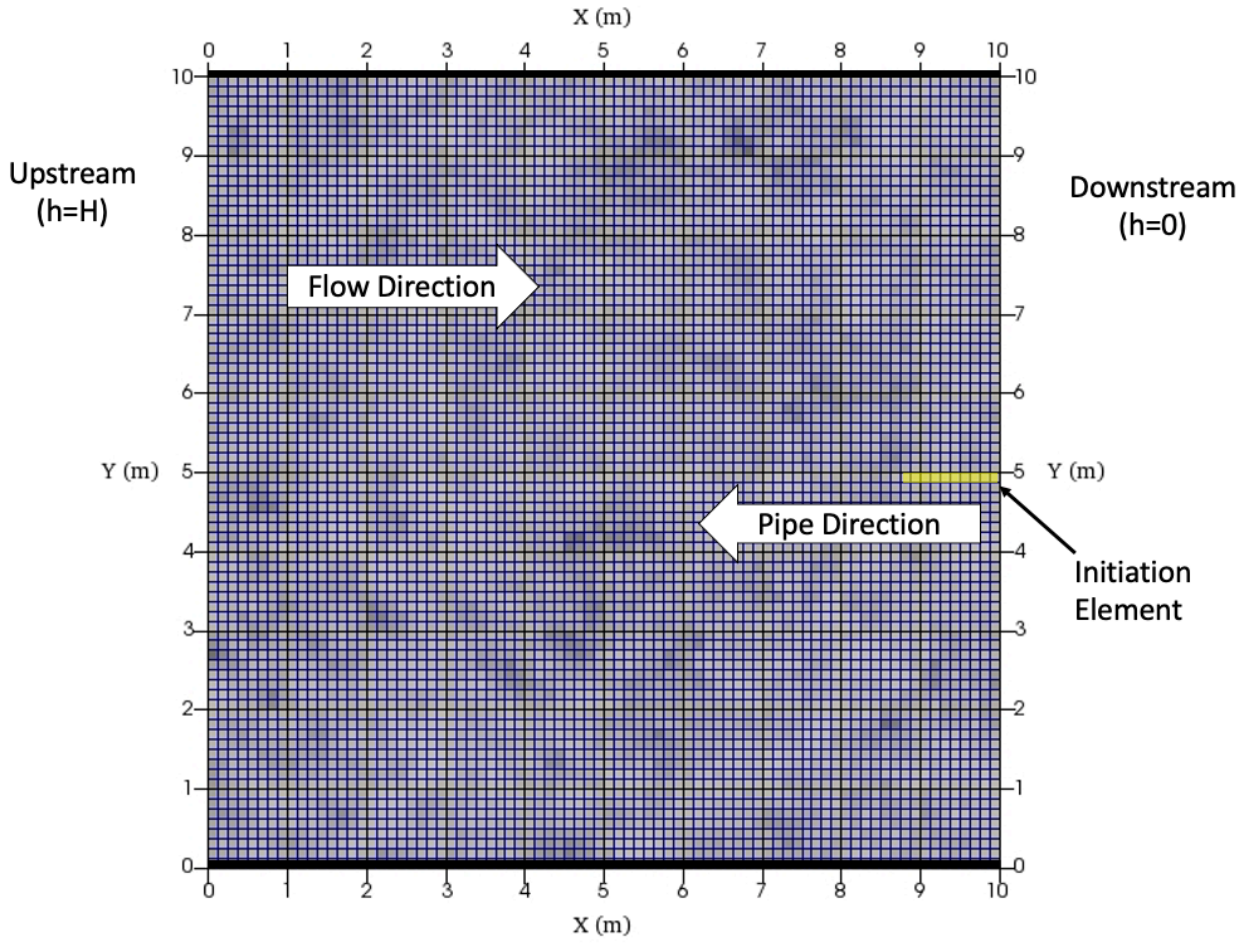

Figure 9.6. Example problem for RFEM analysis.

Table 9.1. Model inputs values for example problem.

Property	**Value**
d_{50} (mm)	0.2
μ_k (m/s)	1.0×10^{-5}
τ_c (Pa)	0.33
μ_{ics}	0.3, 1.0, 3.0
ρ (kg/m^3)	1,000
μ (Ns/m^2)	0.001
σ_k/μ_k	0.25, 0.5, 1.0, 2.0, 3.0
σ_{ics}/μ_{ics}	0.0, 0.16, 0.5, 1.0
θ/L	0.05, 0.10, 0.25, 0.50, 1.0
ρ	-1.0, 0.0, 1.0

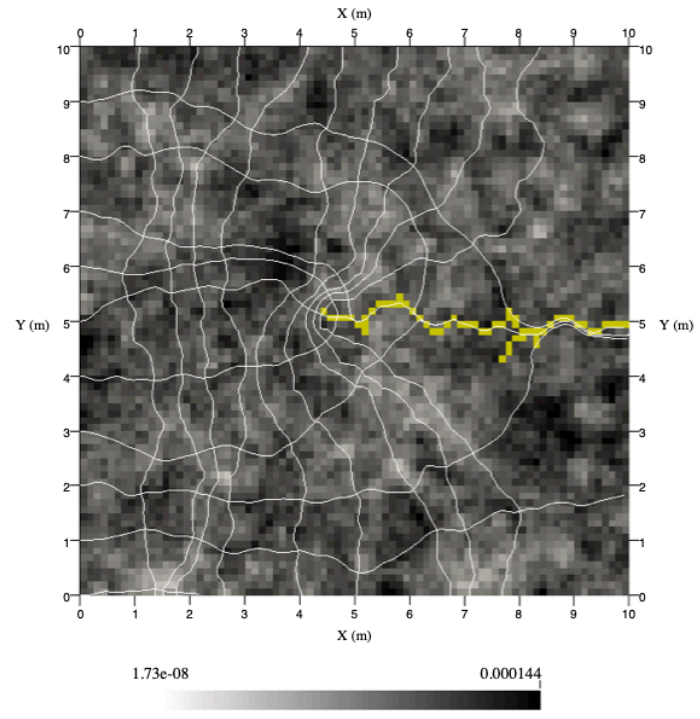

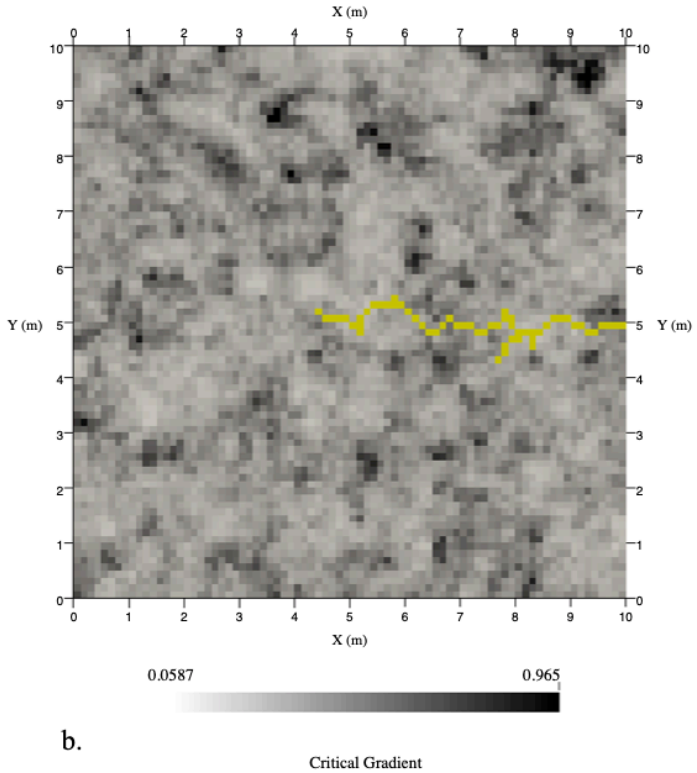

Figure 9.7. Example realization showing (a)k-field with head contours and pipe path and (b) i_{cs}-field with pipe path for scenario with σ_k/μ_k=3, μ_{ics}=0.3, σ_{ics}/μ_{ics}=0.5, ρ=0, and θ=0.5 m.

9.3 RFEM Analyses Results

The RFEM analyses were conducted on a Cray supercomputer using a program written in Fortran with OpenMPI. The supercomputer was used for this study due to the number of computations required. Each BEP finite element analysis consisted of 200-400 computational steps (for upstream head increments and pipe progression steps). The precise number of steps depended on the resistance of the soil to pipe progression, with more steps required for analyses requiring higher hydraulic gradients for progression of the pipe through the domain. At each step, the Picard iterations on the pipe depth also had to be performed such that the groundwater-pipe flow equation was solved approximately 1,000 times per BEP analysis. Considering the 700 combinations of input parameters, this study required that the groundwater-pipe flow equation be solved approximately 700,000 times per Monte-Carlo simulation that was conducted. As such, it was desired to minimize the number of simulations conducted to reduce the computational time required as much as possible. A discussion on the computational performance of the program and RFEM convergence is briefly presented prior to discussing the quantitative RFEM results.

All Monte-Carlo analyses were conducted on a Cray supercomputer at the U.S. Army Engineering Research and Development Center Supercomputing Resource Center named Onyx. The Onyx HPC is a Cray XC40/50 with 4,810 standard compute nodes. Each node has dual, 22-core Intel E5-2699v4 Broadwell processors with 2.8 GHz core speeds for a total of 44 cores per node. All of the analyses in this study were run on 10 nodes using 440 cores. An evaluation of the runtime was performed for the case with the highest coefficients of variation in both the k_h- and i_{cs}-fields. This case was used for timing as it was one of the longer simulations. As seen in Figure 9.8, the run time varied linearly with the simulation count due to the "embarrassingly" parallel nature of the RFEM simulation process.

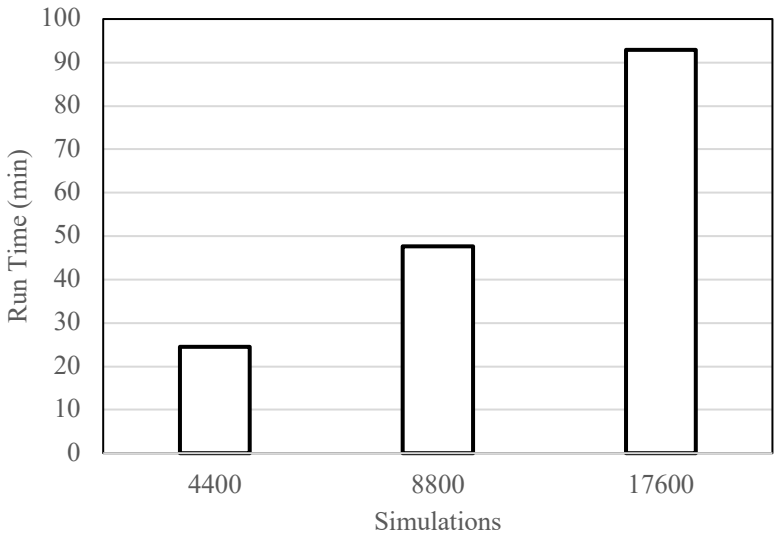

Figure 9.8. Runtimes for MPI Monte-Carlo simulations on 440 cores.

The convergence of the Monte-Carlo analysis was assessed by evaluating the mean and standard deviation of the critical gradient, $(H/L)_{cr}$, as the number of Monte-Carlo simulations increased. An example convergence plot for a case with high variance in the hydraulic conductivity random field is shown in Figure 9.9. The case with σ_k/μ_k=3.0 was selected for assessing convergence as the scenarios with the most variability converged the slowest. Additionally, as illustrated in Figure 9.9, the scenarios with the largest spatial correlation length (θ) converged the slowest. The analysis case with the smallest spatial correlation length converged rather quickly (less than 1,000) simulations. While the convergence of the standard deviation for the case of θ/L=1.0 in Figure 9.9b is not quite established by the time it reaches 4,400 simulations, it may be close enough for the purposes of this study in which only general trends in the critical gradient distributions are being assessed. The error in the estimated probability of failure (p_f) can be calculated with confidence level $(1-\alpha)$ as (Fenton and Griffiths, 2008)

$$e = \frac{z_{\alpha/2}}{\sqrt{\frac{n}{p_f(1-p_f)}}} \tag{9.1}$$

where $z_{\alpha/2}$ denotes the point on the normal distribution corresponding to $P[Z > z_{\alpha/2}] = \alpha/2$ and n is the number of Monte-Carlo simulations. For the case of n=4,400 and $p_f = 0.05$, e was estimated to be 0.005 with 90% confidence, or 10% error. This was deemed adequate for the purposes of the present study. As such, 4,400 simulations were selected as the number of Monte-Carlo simulations for use in the analysis to keep computational times to reasonable levels. As the error will increase with lower values of p_f, a value of $p_f = 0.05$ was the lowest probability on the distribution evaluated in the present study. The results of all analysis are discussed in the sections that follow, first focusing on trends due to hydraulic conductivity variability alone, followed by sections that discuss the influence of i_{cs} spatial variability and the erosion initiation location.

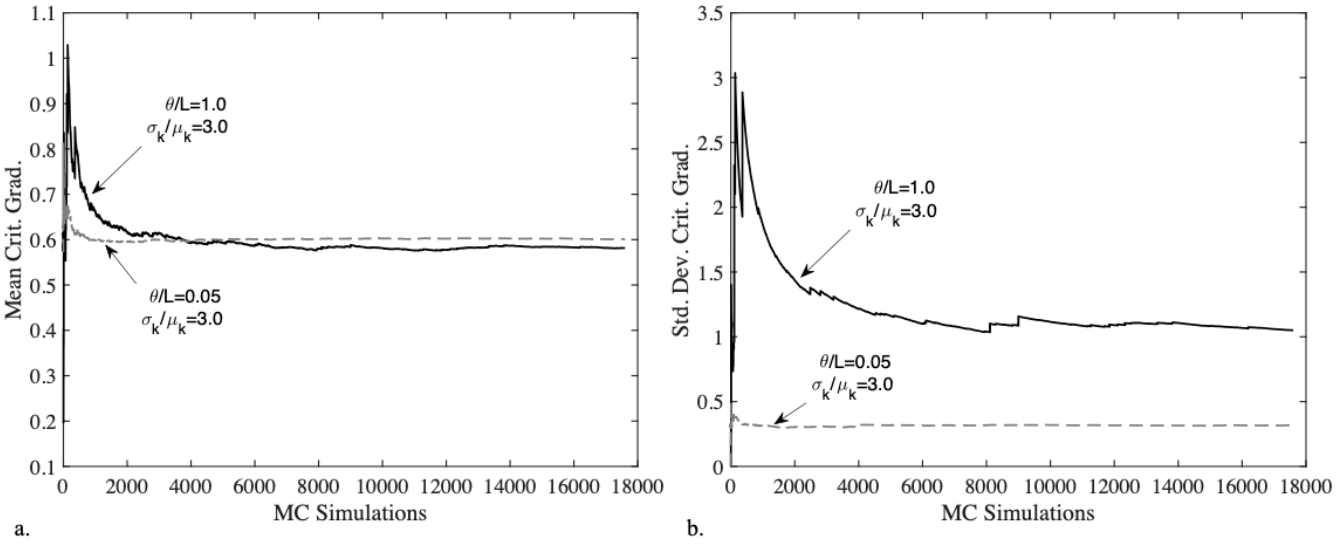

Figure 9-9. Convergence of the (a) mean and (b) standard deviation of the critical, average hydraulic gradient for case with μ_{ics}=0.3, σ_{ics}=0.3, and ρ=0.

9.3.1 Random k_h-field results

The 25 scenarios with hydraulic conductivity as the only random variable were run initially. To visualize the results, the empirical cumulative distribution function (CDF) of the $(H/L)_{cr}$ values obtained from the Monte-Carlo analysis was generated for each case. The five CDFs for the smallest and largest correlation lengths are illustrated in Figures 9.10a and 9.10b, respectively. The probability on the y-axis represents the percentage of Monte Carlo simulations that progressed to failure at or below the associated gradient value. This can be interpreted as the probability of failure.

From Figure 9.10, it is readily seen that increasing the coefficient of variation of the hydraulic conductivity random field causes the CDF to shift to the right. For low correlation lengths (Figure 9.10a), the entire CDF shifts to the right at all probability values. This indicates that any increase in variability leads to increasing resistance against piping if the correlation length is small relative to the analysis domain. For large correlation lengths (Figure 9.10b), increasing variability causes the low probability range of the CDF to shift to the left, meaning pipe progression becomes more likely. However, for large probability values, the distribution still tends to shift towards the right. The low probability value range (<10%) of the CDF is often of great interest for risk assessments as target failure probabilities are typically low. Therefore, to capture the trend observed for low probabilities, the value of the critical, average hydraulic gradient associated with p_f=5% was extracted from the CDFs for all 25 cases. Figure 9.11 illustrates the resulting trends in the critical, average hydraulic gradients associated with p_f=5% as a function of both θ and σ_k/μ_k. From these results, it is seen that for θ/L=0.05, 0.10, and 0.25, increasing σ_k/μ_k leads to an increase in the gradient associated with p_f=5% indicating that piping is less likely with increasing variance. For the larger correlation lengths, increasing σ_k/μ_k leads to smaller hydraulic gradients indicating that piping is more likely. Lastly,

regardless of the value of σ_k/μ_k, the hydraulic gradient required to cause failure decreases with increasing correlation length. The extent of this trend will be evaluated more thoroughly when discussing the results with random i_{cs} and random k_h fields.

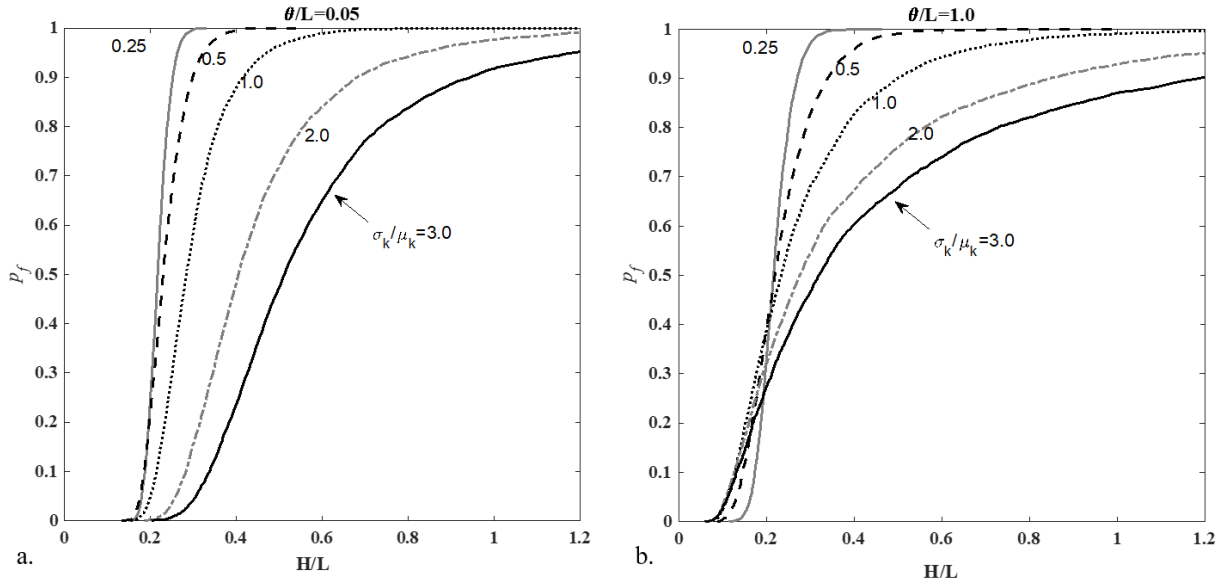

Figure 9.10. Cumulative distribution functions for $i_{cs} = 0.3$ with k as the only random variable for (a) smallest correlation length and (b) largest correlation length.

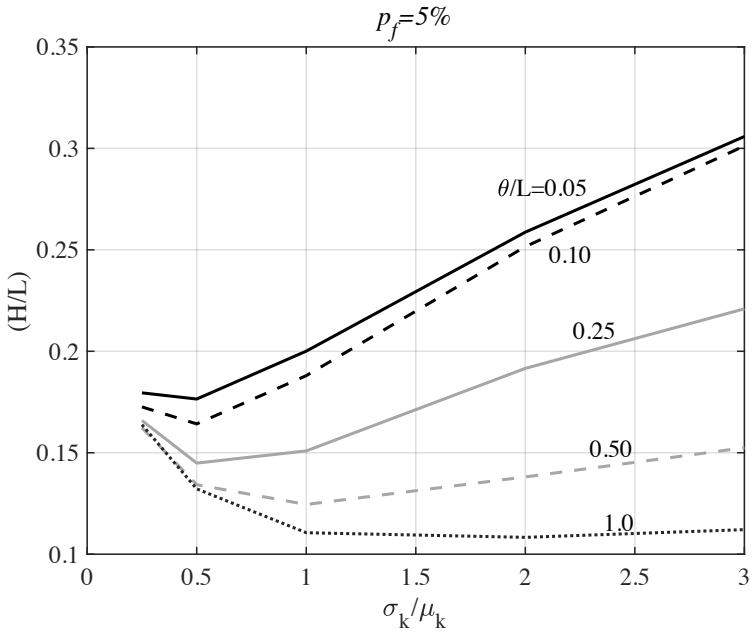

Figure 9.11. Influence of k_h coefficient of variation and θ on average hydraulic gradient associated with p(f)=5%.

9.3.2 Combined k_h-field and i_{cs}-field results

Each of the 25 scenarios with random hydraulic conductivity were repeated an additional 27 times to assess the combined influence of both spatially variable k_h and i_{cs}. The resulting CDFs of all 675 Monte-Carlo simulations were assessed graphically to evaluate trends. Two trends were observed universally in all of the results, as illustrated by the select CDFs for the extreme correlation lengths and hydraulic conductivity coefficients of variation shown in Figure 9.12. In all cases, as the coefficient of variation of i_{cs} increases, the CDF shifts to the left indicating that BEP progression is increasingly likely. This trend was exhibited in all of the scenarios. As might be expected, the second trend observed was that any increase in μ_{ics} leads to a direct increase in the hydraulic gradient required for pipe progression. This is readily seen in Figure 9.12 by comparing the CDFs for μ_{ics}=0.3 and μ_{ics}=1.0.

In addition to understanding the influence of i_{cs} on the results, it was also of interest to see if the gradient required to cause BEP failure still decreased with increasing correlation length. To assess this trend more thoroughly, a few additional analyses were also run for cases with larger values of θ. The trend in the hydraulic gradients associated with the 5%, 25%, 50%, 75%, and 95% failure probabilities for one particular case is illustrated in Figure 9.13. Just as before, the hydraulic gradient for p_f=5% decreases continually with increasing values of θ. This observation clearly highlights that large correlation lengths are the worst-case scenario when dealing with the low probability of failure range of the CDFs. Interestingly, for higher values of p_f, the highest value of hydraulic gradient required to achieve the given p_f value is associated with $0.5<\theta/L<1.0$.

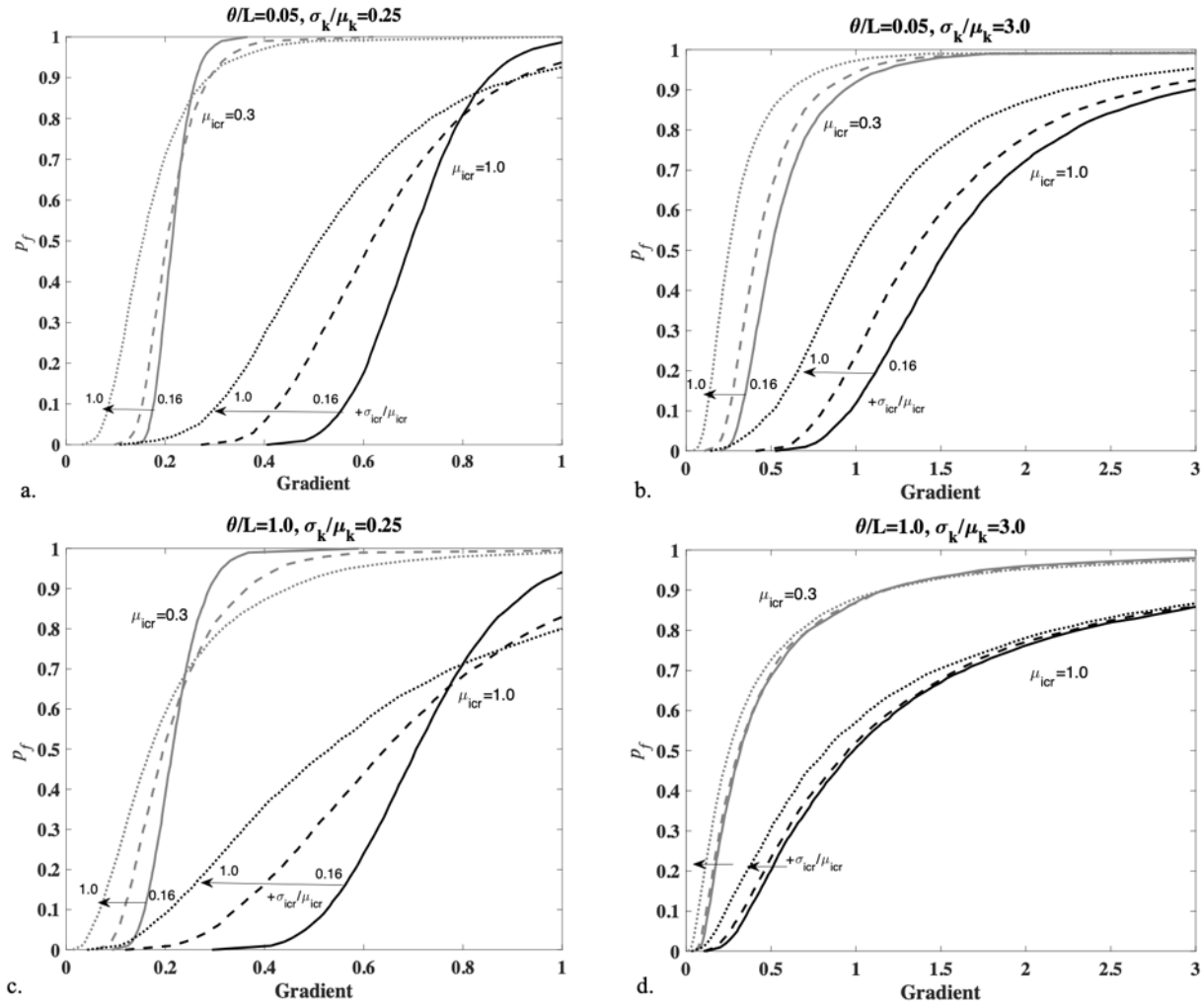

Figure 9.12. Influence of i_{cs} random field on probability of failure.

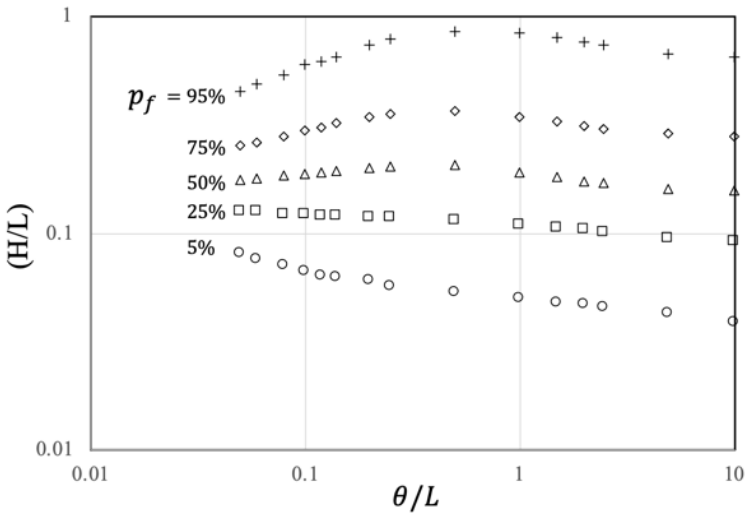

Figure 9.13. Influence of correlation length on failure probabilities for σ_k/μ_k=1, μ_{ics}=0.3, σ_{ics}=0.3, and ρ=1.

The influence of the correlation between the hydraulic conductivity field and the critical gradient field was also of interest. After evaluating the influence of ρ for all 675 scenarios, it was determined that two different trends were seen in the results as illustrated in Figure 9.14. For low values of σ_k and σ_{ics}, changing the value of ρ caused the distributions to cross over each other as indicated in Figure 9.14a. In this instance, ρ=-1 decreased the probability of BEP progression in the low probability arrange, and ρ=1 only slightly increased the probability of BEP progression in the low probability range. Once the value of σ_k/μ_k was equal to or greater than 0.5 or the value of σ_{ics}/μ_{ics} was greater than 0.16, the influence of ρ changed to that indicated in Figure 9.14b. In these cases, ρ simply shifted the CDF to the left or right, depending on the value of ρ. Values of ρ=-1 shifted the CDF to the left indicating that BEP was more likely, whereas values of ρ=1 shifted the CDF to the right indicating BEP progression was less likely.

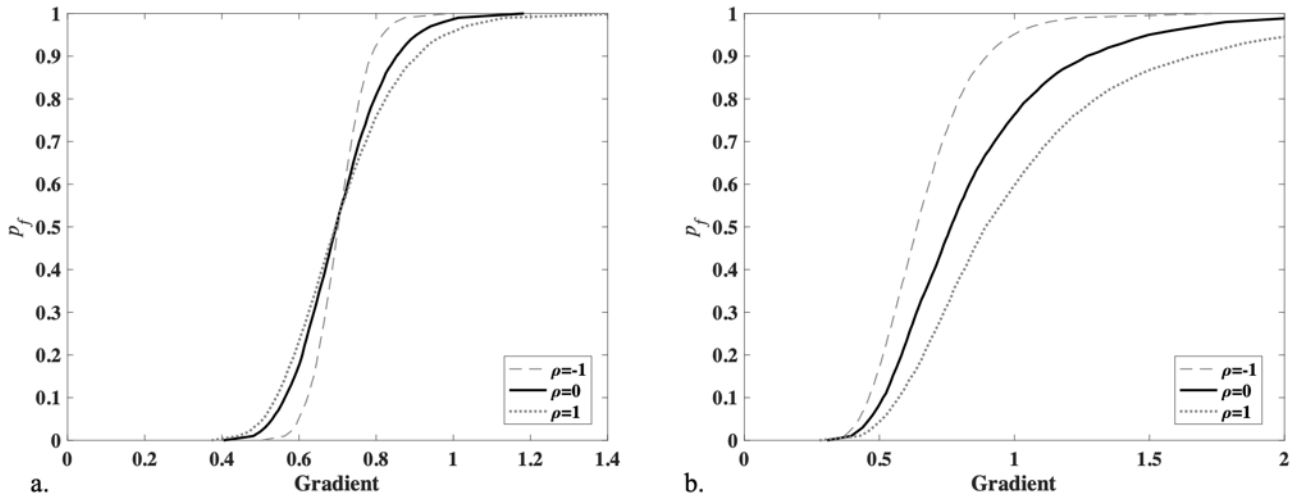

Figure 9.14. Influence of correlation between i_{cs}-field and k_h-field on critical gradient distribution for (a) $\mu_k = 10^{-5}$ m/s, σ_k/μ_k=0.25, θ/L=0.05, μ_{ics}=0.3, σ_{ics}=0.05 and (b) $\mu_k = 10^{-5}$ m/s, σ_k/μ_k=1.0, θ/L=0.05, μ_{ics}=1.0, σ_{ics}=0.5.

The previous presentation illustrated the general trends observed in the results obtained with both random k- and i_{cs}-fields; however, it was not possible to present the quantitative results obtained for all of the analysis conducted. To share the complete set of RFEM results with the interested reader, the resulting $(H/L)_{cr}$ distributions computed for each scenario were fitted to lognormal distributions (Figure 9.15). The mean ($\mu_{\ln((H/L)_{cr})}$) and standard deviation ($\sigma_{\ln((H/L)_{cr})}$) of the natural logarithm of $(H/L)_{cr}$ for the best fit distribution was determined for each scenario. A regression analysis was then performed to try and develop a reduced order model that predicted the resulting lognormal distribution of $(H/L)_{cr}$ as a function of the input variables σ_k/μ_k, θ/L, σ_{ics}/μ_{ics}, μ_{ics}, and ρ. The resulting equations developed for predicting $\mu_{\ln((H/L)_{cr})}$ and $\sigma_{\ln((H/L)_{cr})}$ are presented as Equations 9.2 and 9.3, respectively. The coefficient of determination was equal to 0.98 for Equation 9.2 and 0.88 for Equation 9.3.

$$\mu_{\ln((H/L)_{cr})} = -2.2001 + 0.337\frac{\sigma_k}{\mu_k} + 0.250\frac{\theta}{L} + 2.223\mu_{ics} - 0.084\frac{\sigma_{ics}}{\mu_{ics}} + 0.162\rho$$
$$- 0.018\left(\frac{\sigma_k}{\mu_k}\right)^2 - 0.361\left(\frac{\theta}{L}\right)^2 - 0.421\mu_{ics}^2 - 0.264\left(\frac{\sigma_{ics}}{\mu_{ics}}\right)^2 - 0.017\rho^2 \quad (9.2)$$

$$\sigma_{\ln((H/L)_{cr})} = -0.018 + 0.235\frac{\sigma_k}{\mu_k} + 1.007\frac{\theta}{L} + 0.012\mu_{ics} + 0.185\frac{\sigma_{ics}}{\mu_{ics}} + 0.105\rho$$
$$- 0.030\left(\frac{\sigma_k}{\mu_k}\right)^2 - 0.680\left(\frac{\theta}{L}\right)^2 - 0.003\mu_{ics}^2 + 0.133\left(\frac{\sigma_{ics}}{\mu_{ics}}\right)^2 - 0.012\rho^2 \quad (9.3)$$

Equation 9.2 and 9.3 can then be used to predict the lognormal distribution parameters that resulted from the RFEM analysis. To assess the model performance for low probability values, Equations 9.2 and 9.3 were used to predict the distributions for all scenarios evaluated. The value of (H/L) associated with p_f=5% obtained for each CDF using the predictive equations was then compared to the value obtained directly from the RFEM distributions (Figure 9.16). While the reduced order model provides a reasonable representation of the RFEM results, there are errors of up to $\pm$30% for many of the scenarios. As such, it is recommended that the reduced order model only be used for understanding the general trends of the RFEM analysis results pending further study

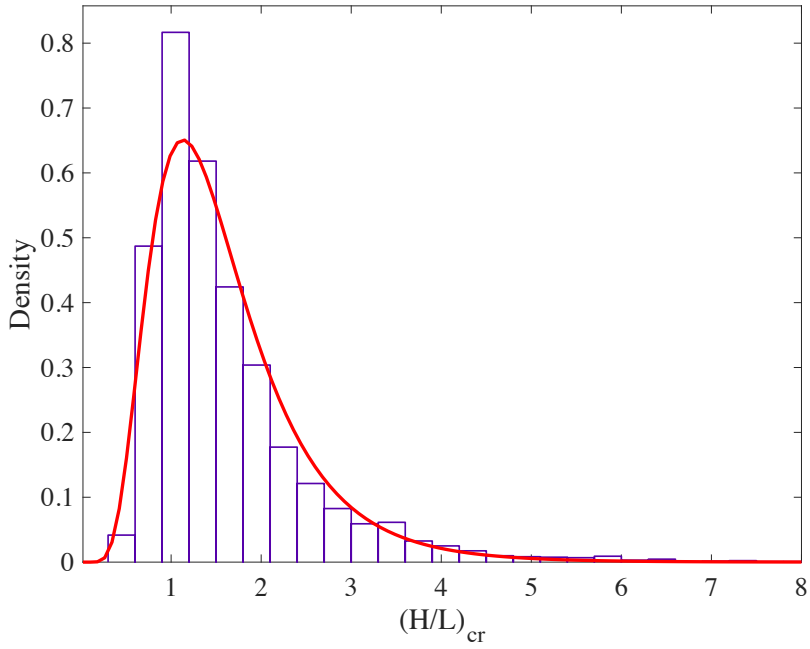

Figure 9.15. Fit of lognormal distribution to Monte-Carlo results for scenario with μ_{icr}=0.3, σ_{icr}=0.15, ρ=0.

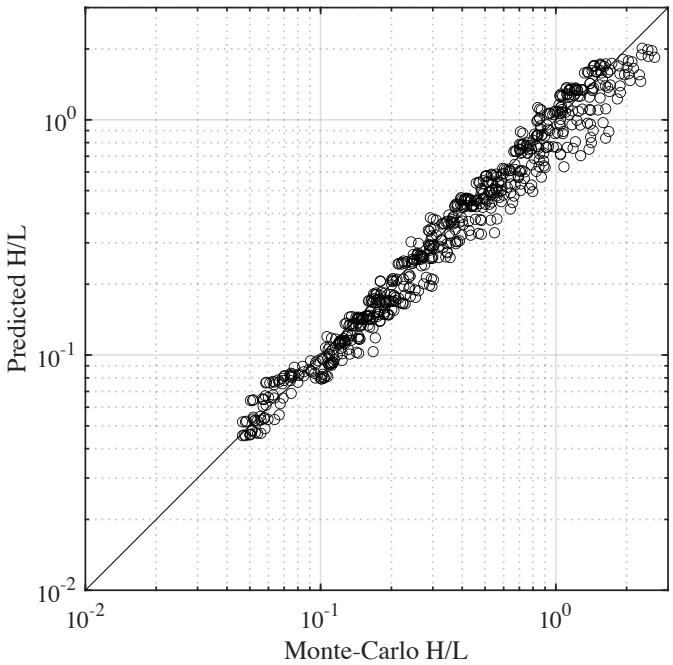

Figure 9.16. Predicted $(H/L)_{cr}$ from reduced order model compared to $(H/L)_{cr}$ from Monte-Carlo results for p_f=5%.

9.3.3 Influence of initiation condition

In addition to investigating the influence of random soil properties on the distribution of $(H/L)_{cr}$, a series of analysis was conducted to determine the influence of the initiation condition on the probability of pipe progression. For the analyses discussed thus far, the erosion was initiated from a single element at the center of the downstream boundary. A few additional analyses were conducted in which the erosion was allowed to begin from any point along the downstream boundary. This was accomplished by switching every element on the downstream boundary to a pipe element simultaneously.

The resulting distribution obtained with initiation permitted along the entire boundary is compared to the case with initiation at a single point in Figure 9.17 for one of the analysis cases. As seen, the CDF shifts to the left indicating that erosion is more likely when initiation can occur anywhere along the downstream boundary. Conceptually, this is explained by the fact that permitting initiation of erosion anywhere along the boundary ensures that the path of least resistance is followed during each realization. The low probability values of the CDF are for realizations in which the path of least resistance was already taken. Therefore, the lower portion of the CDF did not move. The upper portion of the CDF did shift, however, as the more resistant pipe paths followed when initiation was restricted to a single point were no longer followed. As a result, the hydraulic gradient required to cause piping decreased when erosion could be initiated anywhere on the boundary.

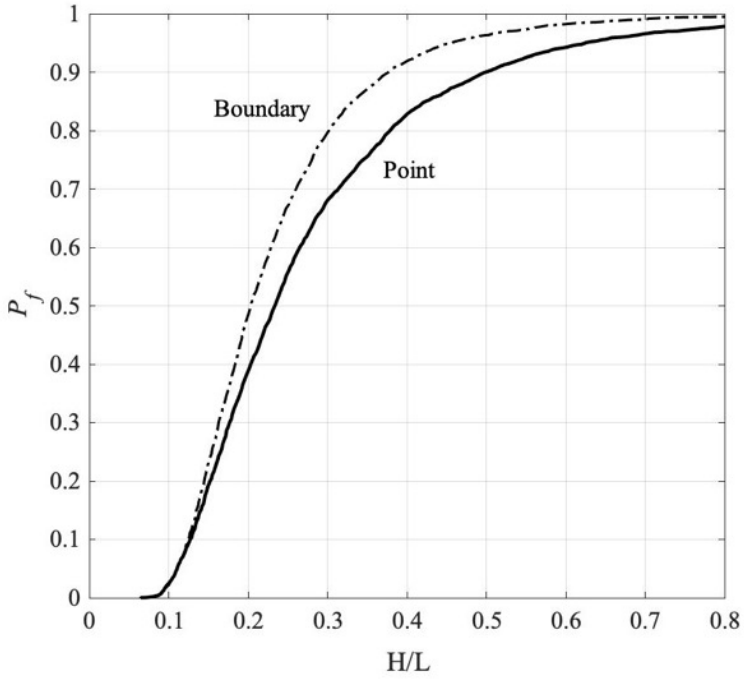

Figure 9.17. Influence of initiation condition on resulting CDF.

9.4 Conclusions regarding RFEM of BEP

Backward erosion piping is a potential cause of failure in earth dams and levees that has been shown to be sensitive to variability in soil properties. Numerical models for simulating piping developed to date have not included the option of statistically defined, spatially variable soil properties. This study developed and demonstrated a numerical approach for simulating BEP through spatially random soils using the Random Finite Element Method (RFEM). A finite element model for simulating BEP progression was used to simulate the progression of BEP erosion pipes through soils in which the hydraulic conductivity and critical hydraulic gradient for pipe progression were treated as random fields.

The results demonstrated that the probability of failure due to piping increases as the spatial correlation length increases. Additionally, any increase in hydraulic conductivity variance leads

to increased resistance against piping for cases with small spatial correlation lengths. However, if the spatial correlation length is large, increased variance in the hydraulic conductivity leads to an increased probability of failure in the range of typical target reliabilities commonly assessed for dams and levees. Any increase in the mean value of the critical hydraulic gradient for pipe progression decreased the probability of failure due to pipe progression. On the contrary, any increase in the variance of the critical hydraulic gradient distribution made piping failure more likely.

The resulting distributions from the 700+ scenarios for which RFEM analyses were conducted were fitted to lognormal distributions in an attempt to develop a predictive model for the mean and standard deviation of the average hydraulic gradient needed to produce a given probability of BEP failure. Results indicate that the reduced order model is capable of representing the qualitative trends, albeit with up to 30% error in some instances. As such, the reduced order model at this time should be used only as a guide for indicating probabilistic trends in the RFEM results. Further work is needed to develop more accurate predictive models that might avoid the need for extensive RFEM studies whenever a new problem is encountered.

Finally, the influence of the initiation condition on the probability of BEP progression was also evaluated by conducting analyses in which erosion was allowed to initiate from any location on the downstream boundary as opposed to just one centrally located position. The results of these analyses indicate that the probability of failure increases for scenarios with unrestricted initiation locations as the weakest erosion path is readily followed for these scenarios.

While this study illustrates how RFEM may be used for analysis of BEP progression, significant research is needed before these techniques can be used for reliability analysis of dams

and levees. In particular, the following limitations of the present study must be kept in mind when considering the results.

1. The two-dimensional, plan view formulation represents a 1-m thick sand bed. Further, the plan view calculations do not permit flow to pass below the pipe. In the field, a pipe may be only a few mm or cm in depth but passes through a sand bed of 10 m to 50 m in depth. As such, much of the flow in the real domain will not be conveyed towards this relatively small pipe, which may alter the influence the soil variability has on the results.
2. The pipe flow was assumed to be laminar. While this may be an appropriate assumption for fine sands (Robbins and Griffiths 2021), it may not be appropriate for higher k values present in some of the RFEM simulations with high σ_k.
3. BEP is a highly localized, three-dimensional, transient process that occurs over very large analysis domains (100 to 500 m). In this study, the process was assessed over a small, idealized domain with a simplified, two-dimensional, steady-state model to make the computational effort manageable.

Given these limitations, the results of this study should only be used in a qualitative manner to illustrate the general influence of spatial variability on the BEP process. Further research is needed to make RFEM suitable for assessing BEP in practice. In particular, research into the relationship between two dimensional and three dimensional analyses is needed to permit using two-dimensional analysis in a reliable fashion as three-dimensional analysis is likely too computationally intensive for performing RFEM analysis. Additionally, algorithmic development is needed in relation to adaptive mesh refinement strategies and techniques in random fields for reducing the cost of Monte-Carlo simulations of field scale problems. This will improve the ability to model localized phenomenon over larger problem domains. With these

improvements, it will become feasible to implement field scale models of BEP simulation for more realistic assessment of BEP progression, and to better understand some of the limitations imposed by the assumptions made in the present study.

CHAPTER 10

CONCLUSIONS AND RECOMMENDATIONS FOR FURTHER RESEARCH

This study has developed and validated a steady-state approach for prediction of backward erosion piping using the concept of the critical secant gradient function to predict pipe progression. As part of this, finite element models were developed in both two- and three-dimensions for simulating BEP progression using various approaches for discretizing the erosion pipe. Additionally, a laboratory test was developed for measuring the CSGF. The approach of using the CSGF in finite element models for predicting BEP progression was validated through hindcasting of five laboratory experiments with varying scale, configuration, and boundary geometries. Differences between two-and three-dimensional analyses were briefly investigated before demonstrating (1) efficient analysis of field scale problems using adaptive meshing and (2) inclusion of spatially variable soil properties via the random finite element method. The main contributions and practical implications of this research are summarized in the following sections before making recommendations for further research.

10.1 Main Contributions

The main contributions of this research are summarized in the following paragraphs.

1. The innovation of the critical secant gradient function (CSGF) as a new means of defining the criterion for pipe progression is the most significant and potentially transformative contribution of the present study. The remarkable agreement between theory, experimental measurements, and numerical predictions of behavior using the CSGF demonstrate both its validity and utility for predicting the progression of BEP.

2. The development of a laboratory test for measuring the CSGF provides engineers with a means of determining the input properties for numerical models of BEP progression.
3. The development and validation of finite element models for simulating pipe progression demonstrates that BEP can indeed be reliably predicted using physics-based models. This work also demonstrates that a steady-state model is capable of accurately predicting both the critical head for BEP failure and the general erosion behavior observed in experiments. This is a significant finding as it indicates that more complicated models may not be required to accurately simulate pipe progression.
4. This work also demonstrated that representing the pipe with one-dimensional, line elements results in 50-300% error in the hydraulic solution upstream of the pipe tip due to poor approximation of the pipe domain. This is a significant finding as most studies have used line elements to represent the pipe. The use of line elements will lead to significant errors in the predicted critical head at failure.
5. Similarly, the comparison between two- and three-dimensional models demonstrates that two-dimensional approximations of the BEP problem result in underprediction of the secant gradient at the pipe tip. Most studies have used two-dimensional analysis to date which is unconservative.
6. The field scale examples conducted with adaptive meshing demonstrated that the influence of turbulent flow conditions on the critical head may be negligible for fine sands. Additionally, the results with adaptive meshing demonstrated how to efficiently model BEP progression at the field scale. Adaptive mesh refinement is

essential for field scale problems as the pipe elements must be close in size to the actual pipe dimensions to prevent significant domain approximation error.

7. Lastly, as the first study to demonstrate random finite element modeling of BEP, this research provides a methodology for quantitatively evaluating the influence of spatially variable soil properties on the probability of failure due to BEP. The results demonstrate that spatial variations in the soil hydraulic conductivity and the critical secant gradient can have significant impacts on the probability of failure due to piping.

The contributions from this research provide a complete, theoretically sound framework for predicting BEP progression. The theory, laboratory tests, and numerical models developed in this research are all significant advancements to the body of knowledge. Through these advancements, the profession can more accurately assess and remediate flood risks associated with BEP resulting in a reduction in both economic damages and fatalities due to flooding.

10.2 Practical Implications

From a practical point of view, the findings of this research have several significant implications. First, one dimensional line elements should not be used to represent erosion pipes in models that base pipe progression on a primary erosion criterion at the pipe tip due to the large domain approximation errors exhibited. This is not an issue for models that base the progression on the flow in the pipe (e.g., Van Esch et al. 2013) as the line elements adequately described the pipe flow.

Second, because the two-dimensional analysis underestimated the gradients in front of the pipe, input parameters for two-dimensional models cannot be the same as those for three-dimensional models. Further research is needed in this area to fully understand the implications. For now, it is recommended that two-dimensional models be used with caution until it can be demonstrated precisely how the calculations relate to the full three-dimensional scenario.

Lastly, the three-dimensional models in conjunction with the measured CSGF values appear to provide an accurate means for prediction of BEP. These methods should begin to be implemented immediately for assessing failure probabilities due to BEP.

10.3 Recommendations for Further Research

While the developments in this study provide a significant step forward towards arriving at a predictive model for BEP progression, work remains to be done to fully develop and validate the approach for use in practice. In particular, the author recommends research be pursued as described below for the indicated topics.

1. *Approach Validation*: Further research should be undertaken to validate the use of the CSGF in numerical models for prediction of BEP progression. In particular, simulations of full-scale case histories should be undertaken to ensure realistic predictions are given at the field scale. In geotechnical engineering, approaches are typically validated against many case histories before gaining widespread use. This has not always been the case with internal erosion related developments due to the difficulty in obtaining case history data and the urgent need of assessment tools. If the proposed approach is used without further validation, it is highly recommended that the calculations be compared against the current Sellmeijer rule and Schmertmann method calculations to check the general reasonableness of predictions.

2. *CSGF Measurement*: As noted in Chapter 4, both the analytical CSGF expression and the cylindrical flume tests for measuring the CSGF are two-dimensional in nature. The CSGF analytical solution is derived from a two-dimensional conformal mapping solution, whereas the cylindrical experiment has limited flow towards the pipe in the third dimension due to the cylindrical shape of the sample. While the approach compared favorably to the measured CSGF values for 1 three-dimensional box shaped sample (Section 5.1), further validation of the analytical expression and cylinder CSGF measurements should be made via measurements from three-dimensional test conditions.

3. *Two-dimensional model validation*: More work is needed comparing two- and three-dimensional model results to fully understand the limitations and applications of two-dimensional modeling. In particular, the pseudo three-dimensional analysis via correction factors should be rigorously explored to determine to what degree the two-dimensional analysis replicate the trends observed in three-dimensional models.

4. *Adaptive mesh refinement and advanced techniques*: The adaptive meshing approach demonstrated in two dimensions should be extended to three dimensions to enable assessment of BEP progression via finite element analyses for field scale problems. Additionally, other advanced numerical techniques such as mutli-grid solvers, XFEM, and meshless techniques (RBF, point collocation, etc.) should be explored as options for efficiently solving the BEP progression problem at the field scale.

5. *Random field applications*: The RFEM simulations of BEP progression should be extended to three dimensions using conditioned random fields to enable (1) inclusion of correlation lengths in all three directions and (2) incorporation of available site data into probabilistic models of BEP progression. Additionally, adaptive meshing in random fields

should be pursued to permit efficient RFEM simulations to be conducted at the field scale. As the local average subdivision method used for random field generation is based on sequential subdivision of domains, it is naturally compatible with adaptive meshing.

CHAPTER 11

REFERENCES

Abdou, H., Emeriault, F., & Plé, O. (2020). New approach to describe hydro-mechanical phenomenon of suffusion: erosion, transport and deposition. *European Journal of Environmental and Civil Engineering*, 24(14), 2342–2360. https://doi.org/10.1080/19648189.2018.1505665

Aguilar-López, J. P., Warmink, J. J., Schielen, R. M. J., & Hulscher, S. J. M. H. (2016). Piping erosion safety assessment of flood defences founded over sewer pipes. *European Journal of Environmental and Civil Engineering*, 22(6), 707–735. https://doi.org/10.1080/19648189.2016.1217793

Akrami, S., Bezuijen, A., van Beek, V. M., Rosenbrand, E., Terwindt, J., & Förster, U. (2021). Analysis of development and depth of backward erosion pipes in the presence of a coarse sand barrier. *Acta Geotechnica*, 16, 381–397. https://doi.org/10.1007/s11440-020-01053-0

Allan, R. (2018). Backward Erosion Piping. PhD Thesis. Department of Civil and Environmental Engineering. University of New South Wales. https://doi.org/10.1002/9781118577165.ch3

Baker, C. (2018). USACE conducts first analysis of risk and benefits of USACE levees. *Flood Risk Management Newsletter* (Vol. 11). Washington, D.C.

Bangerth, W., Hartmann, R., & Kanschat, G. (2007). deal.II---A general-purpose object-oriented finite element library. *ACM Transactions on Mathematical Software*, *33*(4), 24-es. https://doi.org/10.1145/1268776.1268779.

Barendsen, L. (2020). *The effect of leakage on backward erosion piping: A modelling study in 2D and 3D*. Delft University of Technology.

Bennett, P. T. (1945). The Effect of Blankets on Seepage Through Pervious Foundations. *ASCE Transactions*, 215–252.

Bersan, S., Jommi, C., & Simonini, P. (2013). Applicability of the Fracture Flow Interface to the Analysis of Piping in Granular Material. In *COMSOL Conference* (pp. 1–8). Rotterdam, Netherlands.

Bezuijen, A., Akrami, S., van Beek, V., & Rosenbrand, E. (2021). On the Mechanism of Backward Erosion Piping in a CSB. In *ICSE10* (pp. 182–191). Washington, D.C.: ASCE.

Bligh, W. G. (1910). Dams, barrages and weirs on porous foundations. *Engineering Record*, 64(26), 708–710.

Bligh, W. G. (1915). Dams and Weirs. American Technical Society.

Bonelli, S. (2013). Erosion in geomechanics applied to dams and levees. (Stéphane Bonelli & F.

Nicot, Eds.). Hoboken, NJ, USA: John Wiley & Sons, Inc. https://doi.org/10.1002/9781118577165

Briaud, J. L., Govindasamy, A. V., & Shafii, I. (2017). Erosion charts for selected geomaterials. *Journal of geotechnical and geoenvironmental engineering*, 143(10), 04017072.

Brown, A. J. (2007). A framework for the Management of Risk from Internal Erosion Risk Analysis. In *Assessment of the Risk of Internal Erosion of Water Retaining Structures: Dams, Dykes and Levees* (EWGIE 2007) (pp. 255–266). Freising, Germany.

Brownlie, W. R., Brooks, N. H., & Irvine, J. (1981). Prediction of Flow Depth and Sediment Discharge in Open Channels. Report No. KH-R-43A., (November), 232.

Burkley, V. J., & Bruch, J. C. J. (1991). Adaptive error analysis in seepage problems. *International Journal for Numerical Methods in Engineering*, *31*, 1333–1356.

Callari, C., & Froiio, F. (2020). A hydromechanical finite element formulation for localized internal erosion in porous media, with application to backward piping in cofferdams. *International Journal for Multiscale Computational Engineering*, *18*(2), 181–197. https://doi.org/10.1615/IntJMultCompEng.2020031422

Cao, Z., Pender, G., & Meng, J. (2006). Explicit formulation of the shields diagram for incipient motion of sediment. *Journal of Hydraulic Engineering*, 132(10), 1097–1099. https://doi.org/10.1061/(ASCE)0733-9429(2006)132.

Carrier III, W. D. (2003). Goodbye, hazen; hello, kozeny-carman. *Journal of geotechnical and geoenvironmental engineering*, *129*(11), 1054-1056.

Casagrande, A. (1937). Seepage Through Dams. Journal of the New England Water Works Association, 51(2), 295–337.

Casagrande, A. (1950). Notes on the Design of Earth Dams. *Journal of the Boston Society of Civil Engineers*, 37(4), 231–255.

Cedergren, H. R. (1948). Use of Flow-Net in Earth Dam and Levee Design. In *Proceedings of the Second International Conference on Soil Mechanics and Foundation Engineering* (p. 7). Rotterdam, Netherlands.

Cengel Yunus, A., & Cimbala John, M. (2006). Fluid Mechanics: Fundamentals and Applications, McGraw-Hill.

Cividini, A., Bonomi, S., Vignati, G. C., & Gioda, G. (2009). Seepage-Induced Erosion in Granular Soil and Consequent Settlements. *International Journal of Geomechanics*, 9(4), 187–194. https://doi.org/10.1061/(asce)1532-3641(2009)9:4(187)

Cividini, A., & Gioda, G. (2004). Finite-Element Approach to the Erosion and Transport of Fine Particles in Granular Soils. *International Journal of Geomechanics*, 4(3), 191–198.

de Wit, J. M. (1984). Research report on sand boil model tests. Delft, Netherlands.

de Wit, J. M., Sellmeijer, J. B., & Penning, A. (1981). Laboratory Testing on Piping. In *10th International Conference on Soil Mechanics and Foundation Engineering* (pp. 517–520). Stockholm, Sweden.

Detournay, C., Tan, C., & Wu, B. (2006). Modeling the mechanism and rate of sand production using FLAC. In *4th International FLAC Symposium on Numerical Modeling in Geomechanics* (pp. 8–10). Minneapolis, Minnesota: Itasca Consulting Group.

Ding, L., Wu, M., Liu, C., Sun, D., & Yao, Q. L. (2007). Numerical simulation of dynamic development of piping in two-stratum dike foundations. *Water Resources and Hydropower Engineering*, 38(2), 36–39.

Dounias, G. T., & Bardanis, M. E. (2019). The failure of homogeneous dams by internal erosion—the case of Sparmos Dam, Greece. In *Sustainable and Safe Dams Around the World (ICOLD 2019),* p. 833–840). Tournier, Bennett, & Bibeau (Eds.), Ottawa, Canada: Canadian Dam Association. https://doi.org/10.1201/9780429319778-71

El Shamy, Usama, & Aydin, F. (2008). Multiscale Modeling of Flood-Induced Piping in River Levees. *Journal of Geotechnical and Geoenvironmental Engineering*, 134(9), 1385–1398. https://doi.org/10.1061/(ASCE)1090-0241(2008)134:9(1385)

Fannin, R.J., & Slangen, P. (2014). On the distinct phenomena of suffusion and suffosion. *Geotechnique Letters*, 4, 289–294.

Fannin, R Jonathan, Garner, S., & Crawford-flett, K. (2011). Case study of piping incidents at Coursier Dam , Canada. In *Internal Erosion in Embankment Dams and Their Foundations* (pp. 230–232). Brno, Czech Republic.

Fascetti, A., & Oskay, C. (2019). Dual random lattice modeling of backward erosion piping. *Computers and Geotechnics*, 105(May 2018), 265–276. https://doi.org/10.1016/j.compgeo.2018.08.018

Fell, R. (2011). Quantitative Risk Analysis of Internal Erosion of Dams and their Foundations-Some Practical Experience and Limitations . In *Internal Erosion in Embankment Dams and Their Foundations* (p. 210). Brno, Czech Republic.

Fell, R., & Fry, J.J. (Eds.). (2007). Internal Erosion of Dams and Their Foundations: Selected and Reviewed Papers from the workshop on Internal Erosion and Piping of Dams and their Foundations, Aussois, France, 25-27 April 2005. CRC Press, 2007.

Fenton, G.A. (1994). Error evaluation of three random field generators. *ASCE Journal of Engineering Mechanics*, 120(12), 2478-2497.

Fenton, G.A., & Griffiths, D.V. (1993). Statistics of block conductivity through a simple bounded stochastic medium. *Water Resources Research*, 29(6), 1825-1830.

Fenton, G.A, & Griffiths, D.V. (2008). Risk assessment in geotechnical engineering. New Jersey: John Wiley & Sons.

Fenton, G.A., & Vanmarcke, E.H. (1990). Simulation of random fields via local average subdivision. *ASCE Journal of Engineering Mechanics*, 116(8), 1733-1749.

FEMA. (1979). Federal Guidelines for Dam Safety. U.S. Department of Homeland Security, Federal Emergency Management Agency, Washington D.C.

FEMA. (2011). Filters for Embankment Dams. Federal Emergency Management Agency (FEMA), U.S. Department of Homeland Security, Washington D.C.

Foster, M., Fell, R., & Spannagle, M. (2000). The statistics of embankment dam failures and accidents. *Canadian Geotechnical Journal*, 37(5), 1000–1024. Retrieved from http://www.nrcresearchpress.com/doi/abs/10.1139/t00-030

Froiio, F., Callari, C., & Rotunno, A. F. (2019). A numerical experiment of backward erosion piping: kinematics and micromechanics. *Meccanica*, 54(14), 2099–2117. https://doi.org/10.1007/s11012-019-01071-7

Fry, J. J. (2009). Internal Erosion: the main ageing phenomena of hydraulic structures. In *Long Term Behavior of Dams* (pp. 50–55). Retrieved from http://lamp3.tu-graz.ac.at/~ltbd09/cms_new/papers/32345.pdf

Fry, J. J. (2016). Lessons on internal erosion in embankment dams from failures and physical models. In *Scour and Erosion (ICSE 2016),* 39–58. Oxford, UK. https://doi.org/10.1201/9781315375045-6

Fujisawa, K. (2016). Numerical analysis of backward erosion of soils by solving the Darcy-Brinkman Equations. In *Advances in Computational Fluid-Structure Interaction and Flow Simulation*. Bazilevs & K. Takizawa (Eds.), Springer International Publishing. https://doi.org/10.1007/978-3-319-40827-9

Fujisawa, K., Murakami, A., & Nishimura, S. (2010a). Numerical Analysis of the Erosion and the Transport of Fine Particles within Soils Leading to the Piping Phenomenon. *Soils and Foundations*, 50(4), 471–482.

Fujisawa, K., Murakami, A., & Nishimura, S. (2010b). Simultaneous Modeling of Internal Erosion and Deformation of Soil Structures. In *GeoShanghai 2010 International Conference* (pp. 71–78). Shanghai, China.

Fujisawa, K., Murakami, A., & Sakai, K. (2016). Numerical analysis of backward erosion by soil-water interface tracking. In *The 6th Japan-Korea Geotechnical Workshop* (pp. 84–87). Okayama, Japan.

Garcia Martinez, M. F., Marchi, M., Tonni, L., Gottardi, G., Bezuijen, A., & Rosso, A. (2017). Numerical simulation of the groundwater flow leading to sand boil reactivation in the Po River. In *EWGIE 2017* (pp. 79–87). Delft, The Netherlands.

Garcia Martinez, M. F., Gottardi, G., Marchi, M., & Tonni, L. (2019). On the reactivation of sand boils near the Po River major embankments. In *Geotechnical Research for Land Protection and Development*, Calvetti, F. Cotecchia, A. Galli, & C. Jommi (Eds.), pp. 328–337. Lecco, Italy: Springer. https://doi.org/10.1007/978-3-030-21359-6

Garner, S. J., & Fannin, R. J. (2010). Understanding internal erosion: a decade of research following a sinkhole event. *Hydropower & Dams*, 10(3), 93–98.

Griffith, W. (1913). The Stability of Weir Foundations on Sand and Soil Subject to Hydrostatic Pressure. *Minutes of the Proceedings of the Institution of Civil Engineers*, (197) 1914. Thomas Telford-ICE Virtual Library.

Griffiths, D.V., and Fenton, G.A. (1993). Seepage beneath water retaining structures founded on spatially random soil. *Géotechnique*, 43(4), 577-587.

Hagerty, D. J., & Curini, A. (2004). Impoundment Failure Seepage Analyses. *Environmental & Engineering Geoscience*, 10(1), 57–68.

Hanses, U. (1985). The mechanics of the development of erosion pipes in a layered substratum beneath dams. Technischen Universitat Berlin.

Harr, M. E. (1962). Groundwater and Seepage (1st ed.). New York, NY: McGraw-Hill Book Company.

Hattermann, F., Kundzewicz, Z., Huang, S., Vetter, T., Kron, W., Burghoff, O., Merz, B., Bronstert, A., Krysanova, V., Gerstengarbe, F., Werner, P., Hauf, Y. (2012). Flood Risk from a Holistic Perspective – Observed Changes in Germany. In *Changes in Flood Risk in Europe*, 1st edition, CRC Press.

Hill, R. (1963). Elastic properties of reinforced solids: some theortetical princples. *Journal of the Mechanics and Physics of Solids*, 11(5), 357-372.

Hoffmans, G. (2014). An Overview of Piping Models. In *ICSE7* (p. 17). Perth, Australia.

Hoffmans, G., & Van Rijn, L. (2018). Hydraulic approach for predicting piping in dikes. *Journal of Hydraulic Research*, 56(2), 268–281. https://doi.org/10.1080/00221686.2017.1315747

Hunter, G., Fell, R., & Topham, C. (2012). Backward Erosion Piping : What are the chances of that? In *ANCOLD* (pp. 1–9).

ICOLD. (2015). Bulletin 164 - Internal erosion of existing dams, levees and dikes, and their foundations. Volume 1: Internal erosion processes and engineering assessment (Vol. 1).

Jonkman, S.N., & Kelman, I. (2005). Deaths during the 1953 North Sea storm surge. In *Solutions to Coastal Disasters*, 749-758.

Kanning, W., & Calle, E. O. F. (2013). Derivation of a representative piping resistance parameter based on random field modelling of erosion paths. *Georisk*, 7(2), 99–109. https://doi.org/10.1080/17499518.2013.790735

Kaunda, R. B. (2015). A neural network assessment tool for estimating the potential for backward erosion in internal erosion studies. *Computers and Geotechnics*, 69, 1–6. https://doi.org/10.1016/j.compgeo.2015.04.010

Kleinberg, E. (6 April 2021). Halloween 1979: Reservoir breach at FPL plant unleashed a 10-foot wave on Indiantown. Palm Beach Post.

Knight, C., O'Sullivan, C., van Wachem, B., & Dini, D. (2020). Computing drag and interactions between fluid and polydisperse particles in saturated granular materials. *Computers and Geotechnics*, 117, 1–16. https://doi.org/10.1016/j.compgeo.2019.103210

Knoeff, J. G., Van Beek, V. M., & Förster, U. (2010). Observations of piping on the IJkdijk testdike in the Netherlands. In *EWGIE 2010* (pp. 1–10). Granada, Spain.

Kramer, R. (2014). *Piping Under Transient Conditions*. University of Twente.

Lane, E. W. (1935). Security from Under-Seepage Masonry Dams on Earth Foundations. *Transactions of ASCE*, 100(1), 1235–1272.

Liang, Y., & Chen, J. (2011). Mathematical Model for Piping Erosion Based on Fluid-Solid Interaction and Soils Structure. In *GSP 217: Advances in Unsaturated Soil, Geo-Hazard, and Geo-Environmental Engineering,* (pp. 109–116). Hunan, China. Retrieved from http://link.aip.org/link/?ASCECP/407/14/1

Liang, Y., Jim Yeh, T.-C., Wang, Y., Liu, M., Wang, J., & Hao, Y. (2017). Numerical simulation of backward erosion piping in heterogeneous fields. *Water Resources Research*, 53, 3246–3261. https://doi.org/10.1002/2013WR014979.

Liu, K., Vardon, P. J., Hicks, M. A., & Arnold, P. (2017). Combined effect of hysteresis and heterogeneity on the stability of an embankment under transient seepage. *Engineering Geology*, *219*, 140-150.

Lominé, F., Scholtès, L., Sibille, L., & Poullain, P. (2013). Modeling of fluid – solid interaction in granular media with coupled lattice Boltzmann / discrete element methods : application to piping erosion. *International Journal for Numerical and Analytical Methods in Geomechanics*, 37(December 2011), 577–596. https://doi.org/10.1002/nag

Mantz, P. A. (1977). Incipient transport of fine grains and flakes by fluids - Extended Shields diagram. *J. Hydr. Div.*, 103(HY6), 601–615.

Methorst, A. J. (2020). *Piping in sandy tidal deposits*. Delft University of Technology.

Miesel, D. (1978). Ruckschreitende Erosion unter bindiger Deckschicht. In *Vortrag Baugrundtagung*. Berlin, Germany.

Montalvo-Bartolomei, A. M., Robbins, B. A., & Murphy, J. (2018). Experimental Evaluation of Kovács ' Equations for Estimating Critical Gradients. ERDC/GSL TR-18-16, Geotechnical and Structures Laboratory. Vicksburg, MS: U.S. Army Corps of Engineers.

Mullens, A. (1999). The Sixty-Storey Crisis:The Story Behind BC Hydro's Worst Nightmare (WAC Bennett Dam). BCB, 26–31.

Muller-Kirchenbauer, H. (1978). Zum Zeitlichen Verlauf Der Ruckschreitenden Erosion in Geeschichtetem Untergrund unter Dammen Und Stauanlagen. In Beitrag Zum Talsperrensymposium. Munchen, Germany.

Muller-Kirchenbauer, H., Rankl, M., & Schlotzer, C. (1993). Mechanism for regressive erosion beneath dams and barrages. In *Filters in geotechnical and hydraulic engineering*, H. Brauns, M. Heibaum, & U. Schuler (Eds.), pp. 369–376. Rotterdam, Netherlands: Balkema.

Navin, M. P., & Shewbridge, S. (2017). Example of 2D Finite Element Analyses to Inform Backward Erosion Piping Evaluation of a Typical Levee Cross-Section. In *GSP 284: Geo-Risk 2017*, (pp. 32–45). Denver, CO. https://doi.org/10.1061/9780784480717.004

Negrinelli, G., van Beek, V. M., & Ranzi, R. (2016). Experimental and numerical investigation of backward erosion piping in heterogeneous sands. In *Scour and Erosion*, 12-15 September 2016, Oxford, UK.

Nikuradse, J. (1950). Laws of flow in rough pipes. Technical Memorandum 1292. National Advisory Committee for Aeronautics. Washinton D.C.

Ojha, C. S. P., Singh, V. P., & Adrian, D. D. (2001). Influence of Porosity on Piping Models of Levee Failure. *Journal of Geotechnical and Geoenvironmental Engineering*, 127(12), 1071–1074.

Ojha, C. S. P., Singh, V. P., & Adrian, D. D. (2003). Determination of Critical Head in Soil Piping. *Journal of Hydraulic Engineering*, 129(7), 511. https://doi.org/10.1061/(ASCE)0733-9429(2003)129:7(511)

Olsen, J. A. (2018). Investigating the role of grain size properties and the representative elementary volume of a soil in exit gradient computations for seepage analyses. MS Thesis. University of Colorado at Denver. https://doi.org/10.1192/bjp.111.479.1009-a.

Pietrus, T.J. (1981) An Experimental Investigation of Hydraulic Piping in Sand. MS Thesis. Department of Civil Engineering. University of Florida, Gainesville, FL.

Pol, J. C., van Klaveren, W., Kanning, W., van Beek, V. M., Robbins, B. A., & Jonkman, S. N. (2021a). Progression Rate of Backward Erosion Piping : Small Scale Experiments. In *ICSE10* (pp. 93–102). Washington, D.C.: ASCE.

Pol, J.C., Kanning, W., & Jonkman, S.N. (2021b). Temporal Development of Backward Erosion Piping in a Large-Scale Experiment. *Journal of Geotechnical and Geoenvironmental*

Engineering, 147(2), 04020168, https://doi.org//10.1061/(ASCE)GT.1943-5606.0002415.

Pol, J., Kanning, W., Van Beek, V.M., Robbins, B.A., Jonkman, S.N. (2022) Temporal evolution of backward erosion piping in small-scall experiments. *Acta Geotechnica*. https://doi.org/10.1007/s11440-022-01545-1 (In press)

Polanco, L., & Rice, J. D. (2014). A Reliability-Based Evaluation of the Effects of Geometry on Levee Underseepage Potential. *Geotechnical and Geological Engineering*, *32*(4), 807–820. https://doi.org/10.1007/s10706-014-9759-2

Polanco-Boulware, L., & Rice, J. D. (2016). Reliability-Based Three-Dimensional Assessment of Internal Erosion Potential due to Crevasse Splays. *Journal of Geotechnical and Geoenvironmental Engineering*, *143*(4), 1–12. https://doi.org/10.1061/(ASCE)GT.1943-5606.0001596

Rahimi, M., & Shafieezadeh, A. (2020). Coupled backward erosion piping and slope instability performance model for levees. *Transportation Geotechnics*, 24(April). https://doi.org/10.1016/j.trgeo.2020.100394

Rahimi, Mehrzad, Shafieezadeh, A., Wood, D., & Kubatko, E. J. (2021). A physics-based approach for predicting time-dependent progression length of backward erosion piping. *Canadian Geotechnical Journal*, 58(7), 995–1004. https://doi.org/10.1139/cgj-2019-0854

Reddy, J. N. (2004). *An introduction to the finite element method* (Vol. 1221). New York: McGraw-Hill.

Redlinger, C., Robbins, B. A., & Pabst, M. (2016). Filter Design : The Why , When , and Where. In *Dam Safety 2016* (Vol. 1, pp. 1–15). Philadelphia, PA: ASDSO.

Reisner, M. (1986). Cadillac Desert: The American West and Its Disappearing Water. Penguin Books. New York, NY.

Rheinboldt, W. C., & Mesztenyi, C. K. (1980). On a data structure for adaptive finite element mesh refinements. *ACM Transactions on Mathematical Software (TOMS)*, *6*(2), 166-187.

Rice, O. ., & Arthur, H. G. (1948). The most recent methods developed to avoid piping or blow-outs in dams. In *Third Congress on Large Dams* (pp. 917–927). Stockholm, Sweden.

Richards, K. S., & Reddy, K. R. (2007). Critical appraisal of piping phenomena in earth dams. *Bulletin of Engineering Geology and the Environment*, 66(4), 381–402. https://doi.org/10.1007/s10064-007-0095-0

Richards, K. S., & Reddy, K. R. (2014). Kinetic Energy Method for Predicting Initiation of Backward Erosion in Earthen Dams and Levees. *Environmental & Engineering Geoscience*, 20(1), 85–97.

Robbins, B. A. (2016). Numerical modeling of backward erosion piping. In *Proceedings of the 4th Itasca Symposium on Applied Numerical Modeling* (pp. 551–558). Lima, Peru: Itasca

Consulting Group.

Robbins, B. A., & Griffiths, D. V. (2018a). Internal Erosion of Embankments: A Review and Appraisal. In *Rocky Mountain Geo-Conference* (pp. 1–16). Denver, CO: American Society of Civil Engineers.

Robbins, B. A., & Griffiths, D. V. (2018b). Modelling of Backward Erosion Piping in Two- and Three- Dimensional Domains. In *Internal Erosion in Earth Dams, Dikes, and Levees* (Vol. 17, pp. 149–158). S. Bonelli, C. Jommi, & D. Sterpi (Eds.), Cham, Switzerland: Springer Nature Switzerland AG. https://doi.org/10.1007/978-3-319-99423-9

Robbins, B. A., & Griffiths, D. V. (2018c). A simplified finite element implementation of the Sellmeijer model for backward erosion piping. In C. et Al. (Ed.), *Numerical Methods in Geotechnical Engineering IX* (pp. 1213–1218). Porto, Portugal: Taylor and Francis Group, London.

Robbins, B. A., & Griffiths, D. V. (2021, May). SODA: A serial Fortran library for adaptation of structured meshes. In *International Conference of the International Association for Computer Methods and Advances in Geomechanics* (pp. 927-934). Springer, Cham.

Robbins, B. A., Griffiths, D. V., & Fenton, G. A. (2016). The Influence of Random Confining Layer Thickness on Levee Seepage Analysis. In *Rocky Mountain Geo-Conference* (pp. 1–13). Denver, CO: ASCE.

Robbins, B. A., Griffiths, D. V., & Fenton, G. A. (2021). Random finite element analysis of backward erosion piping. *Computers and Geotechnics*, 138, 1–14.

Robbins, B.A., Griffiths, D.V., Lucker, S.L., Van Beek, V.M., Rosenbrand, E. (2022) Prediction of backward erosion piping using critical secant gradient functions. *ASCE Journal of Geotechnical and Geoenviornmental Engineering*. (In review)

Robbins, B. A., Montalvo-Bartolomei, A. M., & Griffiths, D. V. (2020). Analyses of Backward Erosion Progression Rates from Small-Scale Flume Experiments. *Journal of Geotechnical and Geoenvironmental Engineering*, 146(9), 04020093. https://doi.org/10.1061/(asce)gt.1943-5606.0002338

Robbins, B. A., & Sharp, M. K. (2016). Incorporating uncertainty into Backward Erosion Piping risk assessments. In *3rd European Conference on Flood Risk Management* (Vol. 03007, pp. 1–6). Lyon, France. https://doi.org/10.1051/e3sconf/20160703007

Robbins, B. A., Stephens, I. J., Leavell, D. A., López-Soto, J. F., & Montalvo-Bartolomei, A. M. (2018). Laboratory piping tests on fine gravel. *Canadian Geotechnical Journal*, 12(February), 1–12.

Robbins, B. A., van Beek, V. M., Lopez-Soto, J., Montalvo-Bartolomei, A. M., & Murphy, J. (2018). A novel laboratory test for backward erosion piping. *International Journal of Physical Modelling in Geotechnics*, 18(5), 266–279.

Romeo, E., Royo, C., & Monzón, A. (2002). Improved explicit equations for estimation of the friction factor in rough and smooth pipes. *Chemical Engineering Journal*, 86(3), 369–374. https://doi.org/10.1016/S1385-8947(01)00254-6

Rosenbrand, E., & van Beek, V. M. (2021). Numerical simulation of a large-scale backward erosion piping experimenet in 2D and in 3D. In *ICSE10* (pp. 70–82). Washington, D.C.: ASCE.

Rosenbrand, Esther, van Beek, V., Koelewijn, A., Akrami, S., Förster, U., van Gerven, K., & Bezuijen, A. (2019). Scale effects in coarse sand barrier experiments. *Lecture Notes in Civil Engineering*, 17, 301–312. https://doi.org/10.1007/978-3-319-99423-9_27

Rosenbrand, Esther, van Beek, V. M., & Bezuijen, A. (2021). Numerical modelling of the resistance of the coarse sand barrier against backward erosion piping. *Géotechnique*, 1–10. https://doi.org/10.1680/jgeot.20.p.201

Rosenbrand, Esther, van Beek, V. M., Bezuijen, A., Akrami, S., Terwindt, J., Koelewijn, A. R., & Förster, U. (2020). Multi-scale experiments for a coarse sand barrier against backward erosion piping. *Géotechnique*, 1–11. https://doi.org/10.1680/jgeot.19.p.358

Rotunno, A. F., Callari, C., & Froiio, F. (2017). Computational Modeling of Backward Erosion Piping. In M. Fremond, F. Maceri, & G. Vairo (Eds.), *Models, Simulation, and Experimental Issues in Structural Mechanics* (Vol. 8, pp. 225–234). Springer. https://doi.org/10.1007/978-3-319-48884-4

Rotunno, A. F., Callari, C., & Froiio, F. (2019). A finite element method for localized erosion in porous media with applications to backward piping in levees. *International Journal for Numerical and Analytical Methods in Geomechanics*, 43(1), 293–316. https://doi.org/10.1002/nag.2864

Saliba, F., Nassar, R. B., Khoury, N., Maalouf, Y., Bou Nassar, R., Khoury, N., & Maalouf, Y. (2019). Internal Erosion and Piping Evolution in Earth Dams using an Iterative Approach. In *Geo-Congress 2019* (pp. 67–75). Philadelphia, PA: ASCE.

Savage, S., Douglas, K., Fell, R., Peirson, W., & Berndt, R. (2019). Modeling the Erosion and Swelling of the Sides of Transverse Cracks in Embankment Dams. *Journal of Geotechnical and Geoenvironmental Engineering*, 145(5), 04019015. https://doi.org/10.1061/(asce)gt.1943-5606.0002040

Schaefer, J. A., O'Leary, T. M., & Robbins, B. A. (2017). Assessing the Implications of Sand Boils for Backward Erosion Piping Risk. In *GSP 285: Geo-Risk 2017*. Denver, CO: ASCE. https://doi.org/10.1061/9780784480724.012

Schmertmann, J.H. (1981). Quantitative piping theory notes (unpublished).

Schmertmann, J. H. (2000). The No-Filter Factor of Safety Against Piping Through Sands. In F. Silva & E. J. Kavazanijian (Eds.), *Judgement and Innovation* (pp. 65–133). American Society of Civil Engineers.

Sherard, J.L. (1979) Sinkholes in dams of coarse, broadly graded soils. *13th Int. Congress on Large Dams*, New Delhi, Vol. 49.

Sellmeijer, J. B. (1988). On the mechanism of piping under impervious structures. PhD Thesis. Delft University of Technology.

Sellmeijer, J. B. (2006). Numerical computation of seepage erosion below dams (piping). In *International Conference on Scour and Erosion*. Amsterdam, The Netherlands.

Sellmeijer, J. B., Calle, E. O. F., & Sip, J. W. (1989). Influence of aquifer thickness on piping below dikes and dams. In *International Symposium on Analytical Evaluation of Dam Related Safety Problems* (pp. 357–366). Copenhagen, Denmark: International Commision on Large Dams.

Sellmeijer, J. B., & Koenders, M. A. (1991). A mathematical model for piping. *Applied Mathematical Modelling*, 15(11–12), 646–651. https://doi.org/10.1016/S0307-904X(09)81011-1

Sellmeijer, J. B., Lopez de la Cruz, J., van Beek, V. M., & Knoeff, H. (2011). Fine-tuning of the backward erosion piping model through small-scale , medium-scale and IJkdijk experiments. *European Journal of Environmental and Civil Engineering*, 15(8), 1139–1154. https://doi.org/10.3166/EJECE.15.1139-1154

Sherard, J. . (1979). Sinkholes in dams of coarse, broadly graded soils. In *ICOLD 1979*. New Delhi, India: ICOLD.

Sheu, T. W. H., Fang, C. C., & Tsai, S. F. (1999). Application of an element-by-element BiCGSTAB iterative solver to a monotonic finite element model. *Computers and Mathematics with Applications*, *37*(3), 57–70. https://doi.org/10.1016/S0898-1221(99)00046-2.

Shields, A. (1936). Anwendung der Aehnlichkeitsmechanik und der Turbulenzforschung auf die Geschiebebewegung. PhD Thesis. Technical University Berlin.

Silvis, F. (1991). Verificatie Piping Model: Proeven in de Deltagoot. Delft, The Netherlands: Waterloopkundig Laboratorium.

Smith, I.M. & Griffiths, D.V. (2004) Programming the Finite Element Method. John Wiley and Sons.

Stavropoulou, M., Papanastasiou, P., & Vardoulakis, I. (1998). Coupled Wellbore Erosion and Stability Analysis. *International Journal for Numerical and Analytical Methods in Geomechanics*, *22*(9), 749–769.

Tao, H. (2018). Numerical Modeling of Soil Internal Erosion Mechanism. PhD Thesis. The University of Akron.

Tao, H., & Tao, J. (2017). Numerical modeling and analysis of suffusion patterns for granular

soils. In *GSP 280: Geotechnical Frontiers 2017* (pp. 487–496). Orlando, Florida: ASCE. https://doi.org/10.1061/9780784480472.051

Terzaghi, K. (1922). Der Grundbruch an Stauwerken und seine Verhiitung. *Die Wasserkraft*, 17(24), 445–449.

Terzaghi, K. (1939). Soil mechanics: a new chapter in engineering science. J*ournal, Institution of Civil Engineers*, 12(7), 106 – 141.

Terzaghi, K. (1943), Theoretical Soil Mechanics, John Wiley & Sons, New York.

NY Times (4 Aug 1965). Danube damage put at $1Billion; Flood Estimates Incomplete – Slovaks Charge Laxity. *The New York Times*, New York, NY.

Townsend, F., Bloomquist, D., Shiau, J.-M., Martinez, R., & Rubin, H. (1988). Evaluation of filter criteria and thickness for mitigating piping in sands. Report for the U.S. Bureau of Reclamation. University of Florida, Gainseville, Florida.

Townsend, F., Schmertmann, J. H., Logan, T. J., Pietrus, T. J., & Wong, Y. W. (1981). An Analytical and Experimental Investigation of a Quantitative Theory for Piping in Sand. Report for the U.S. Bureau of Reclamation. University of Florida, Gainseville, Florida.

Townsend, F., & Shiau, J.-M. (1986). Analytical and experimental evaluation of piping and filter design for sands. Gainseville, Florida. Report for the U.S. Bureau of Reclamation. University of Florida, Gainseville, Florida.

Tran, D. K., Prime, N., Froiio, F., Callari, C., & Vincens, E. (2017). Numerical modelling of backward front propagation in piping erosion by DEM-LBM coupling. *European Journal of Environmental and Civil Engineering*, 21(7–8), 960–987. https://doi.org/10.1080/19648189.2016.1248794

Turnbull, W. J., & Mansur, C. I. (1961a). Construction and Maintenance of Control Measures. *Transactions of the American Society of Civil Engineers*, 126(1).

Turnbull, W. J., & Mansur, C. I. (1961b). Investigation of underseepage- Mississippi River Levees. *ASCE Transactions*, 126(1).

USACE and USBR. (2012). Internal Erosion Risks. In Best Practices in Risk Assessment for Dams and Levees (2012th ed.). Denver, CO: U.S. Army Corps of Engineers and U.S. Bureau of Reclamation.

USBR and USACE. (2010). Internal Erosion and Piping Risks for Embankments. In Best Practices in Risk Assessment for Dams and Levees (pp. 1–48). Denver, CO.

van Beek, V. M. (2015). Backward Erosion Piping: Initiation and Progression. PhD Thesis. Technische Universiteit Delft. https://doi.org/10.1007/s13398-014-0173-7.2

van Beek, V. M., Bezuijen, A., Sellmeijer, J. B., & Barends, F. B. J. (2014). Initiation of

backward erosion piping in uniform sands. *Geotechnique*, 64(12), 927–941.

van Beek, V. M., Knoeff, H., & Sellmeijer, J. B. (2011). Observations on the process of backward erosion piping in small-, medium- and fullscale experiments. *European Journal of Environmental and Civil Engineering*, 15(8), 1115–1137. https://doi.org/10.3166/ejece.15.1115-1137

van Beek, V. M., Koelewijn, A. R., Kruse, G. A. M., Sellmeijer, J. B., & Barends, F. (2008). Piping Phenomena in Heterogeneous Sands - Experiments and Simulations. In *International Conference on Scour and Erosion* (pp. 453–459). Tokyo, Japan.

van Beek, V. M., Koelewijn, A. R., Negrinelli, G., & Förster, U. (2015). A coarse sand barrier as an effective piping measure. In *Proceedings of the 19th International Conference on Soil Mechanics and Geotechnical Engineering* (pp. 1295–1298). Seoul, Korea.

van Beek, V. M., Yao, Q. L., & Van, M. A. (2013). Backward Erosion Piping Model Verification Using Cases in China and the Netherlands. In *Seventh International Conference on Case Histories in Geotechnical Engineering* (pp. 1–7). Chicago, IL.

van Beek, V. M., Robbins, B. A., Hoffmans, G., Bezuijen, A., & van Rijn, L. (2019). Use of incipient motion data for backward erosion piping models. *International Journal of Sediment Research*, 34(5), 401–408. https://doi.org/10.1016/j.ijsrc.2019.03.001

van Esch, J. M. (2013). Modeling Groundwater Flow and Piping under Dikes and Dams Model validation and verification. In *3rd International Symposium on Computational Geomechanics (ComGeo III)* (p. 9). Krakow, Poland

Van Esch, J. M., Sellmeijer, J. B., & Stolle, D. (2013). Modeling transient groundwater flow and piping under dikes and dams. In *3rd International Symposium on Computational Geomechanics (ComGeo III)* (p. 9). Krakow, Poland.

Vandenboer, K. (2019). A Study on the Mechanisms of Backward Erosion Piping. PhD Thesis. Ghent University.

Vandenboer, K., van Beek, V. M., & Bezuijen, A. (2013). 3D FEM Simulation of Groundwater Flow During Backward Erosion Piping. In *Fifth International Young Geotechnical Engineering Conference* (pp. 5–8).

Vandenboer, K., van Beek, V. M., & Bezuijen, A. (2014). 3D finite element method (FEM) simulation of groundwater flow during backward erosion piping. *Frontiers of Structural and Civil Engineering*, *8*(2), 160–166. https://doi.org/10.1007/s11709-014-0257-7

Wang, D., Fu, X., Jie, Y., Dong, W., & Hu, D. (2014). Simulation of pipe progression in a levee foundation with coupled seepage and pipe flow domains. *Soils and Foundations*, 54(5), 974–984. https://doi.org/10.1016/j.sandf.2014.09.003

Wang, Y., & Ni, X. (2013). Hydro-mechanical analysis of piping erosion based on similarity criterion at micro-level by PFC 3D. *European Journal of Environmental and Civil*

Engineering, 17(sup1), s187–s204. https://doi.org/10.1080/19648189.2013.834594

Wautier, A. (2018). Micro-inertial analysis of mechanical instability in granular materials with application to internal erosion. PhD Thesis. Aix-Marseille Universite.

Weijers, J., & Sellmeijer, J. B. (1993). A new model to deal with the piping mechanism. In *Filters in geotechnical and hydraulic engineering* (pp. 349–355). Rotterdam, Netherlands: Balkema, Rotterdam, The Netherlands.

WES. (1941). Investigation of filter requirements for underdrains. Vicksburg, MS.

WES. (1948). Laboratory Investigation of Filters for Enid and Grenada Dams. Vicksburg, MS.

WES. (1953). Filter Experiments and Design Criteria. U.S. Army Engineer Waterways Experiment Station, Corps of Engineers, Vicksburg, MS.

Wewer, M., Aguilar-López, J. P., Kok, M., & Bogaard, T. (2021). A transient backward erosion piping model based on laminar flow transport equations. *Computers and Geotechnics*, 132. https://doi.org/10.1016/j.compgeo.2020.103992

Wing, O. E. J., Lehman, W., Bates, P. D., Sampson, C. C., Quinn, N., Smith, A. M., … Kousky, C. (2020). Inequitable patterns of US flood risk in the Antrhopocene. *Nature Climate Change*. https://doi.org/10.1038/s41558-021-01265-6

White, C. M. (1940). The Equilibrium of Grains on the Bed of a Stream. *Proceedings of the Royal Society A: Mathematical, Physical and Engineering Sciences*, 174(958), 322–338. https://doi.org/10.1098/rspa.1940.0023

Wong, Y.W. (1981). Three dimensional finite element analysis of a quantitative piping theory. MS Thesis. Department of Civl Engineering. University of Floriday, Gainesville, FL.

Xiao, Y., Cao, H., & Luo, G. (2019). Experimental investigation of the backward erosion mechanism near the pipe tip. *Acta Geotechnica*, 14(3), 767–781. https://doi.org/10.1007/s11440-019-00779-w

Xiao, Y., Cao, H., Luo, G., & Zhai, C. (2020). Modelling seepage flow near the pipe tip. *Acta Geotechnica*, *15*(7), 1953–1966. https://doi.org/10.1007/s11440-019-00878-8

Xiong, H., Yin, Z. Y., Zhao, J., & Yang, Y. (2021). Investigating the effect of flow direction on suffusion and its impacts on gap-graded granular soils. *Acta Geotechnica*, 16(2), 399–419. https://doi.org/10.1007/s11440-020-01012-9

Yalin, M. S., & Karahan, E. (1979). Inception of sediment transport. *Journal of the Hydraulics Division*, 105(11), 1433–1443. Retrieved from http://cedb.asce.org/cgi/WWWdisplay.cgi?5014975

Yao, Q. L., Ding, L., Sun, D., Liu, C., & Zhang, Q. (2007). Experimental studies on piping in single- and two-stratum dike foundations. *Water Resources and Hydropower Engineering*,

38(2), 7.

Yin, Jianhua (1998). FE Modeling of Seepage in Embankment Soils with Piping Zone. *Chinese Journal of Rock Mechanics and Engineering*, 17(6), 679–686.

Zienkiewicz, O. C., & Zhu, J. Z. (1987). A simple error estimator and adaptive procedure for practical engineerng analysis. *International Journal for Numerical Methods in Engineering*, *24*(2), 337–357. https://doi.org/10.1002/nme.1620240206

Zhang, X. S., Wong, H., Leo, C. J., Bui, T. A., Wang, J. X., Sun, W. H., & Huang, Z. Q. (2012). A Thermodynamics-Based Model on the Internal Erosion of Earth Structures. *Geotechnical and Geological Engineering*, 31, 479–492. https://doi.org/10.1007/s10706-012-9600-8

Zhou, X., Jie, Y., & Li, G. (2012). Numerical simulation of the developing course of piping. *Computers and Geotechnics*, 44, 104–108. https://doi.org/10.1016/j.compgeo.2012.03.010

APPENDIX A

RELATED PUBLICATIONS BY B.A. ROBBINS

Journal Papers

Robbins, B.A., Griffiths, D.V., Lucker, S.L., Van Beek, V.M., Rosenbrand, E. (2022) Prediction of backward erosion piping using critical secant gradient functions. *ASCE Journal of Geotechnical and Geoenviornmental Engineering.* (In review)

Van Beek, V.M., Robbins, B.A., Rosenbrand, E., Van Esch, J. (2022) . 3D Modelling of Backward Erosion Piping Experiments. *Geomechanics for Energy and the Environment.* (In review)

Pol, J., Kanning, W., Van Beek, V.M., Robbins, B.A., Jonkman, S.N. (2022) Temporal evolution of backward erosion piping in small-scall experiments. *Acta Geotechnica.* *https://doi.org/10.1007/s11440-022-01545-1 (In press)*

Robbins, B.A., Van Beek, V.M., Pol, J.C., and Griffiths, D.V. (2022) Errors in finite element analysis of backward erosion piping. *Geomechanics for Energy and the Environment*. https://doi.org/10.1016/j.gete.2022.100331 (In press)

Robbins, B. A., Griffiths, D. V., & Fenton, G. A. (2021). Random finite element analysis of backward erosion piping. *Computers and Geotechnics*, *138*, 1–14.

Robbins, B. A., & Griffiths, D. V. (2021). A two-dimensional, adaptive finite element approach for simulation of backward erosion piping. *Computers and Geotechnics*, *129*, 103820. https://doi.org/10.1016/j.compgeo.2020.103820

Robbins, B. A., Montalvo-Bartolomei, A. M., & Griffiths, D. V. (2020). Analyses of Backward Erosion Progression Rates from Small-Scale Flume Experiments. *Journal of Geotechnical and Geoenvironmental Engineering*, *146*(9), 04020093. https://doi.org/10.1061/(asce)gt.1943-5606.0002338

van Beek, V. M., Robbins, B. A., Hoffmans, G., Bezuijen, A., & van Rijn, L. (2019). Use of incipient motion data for backward erosion piping models. *International Journal of Sediment Research*, *34*(5), 401–408. https://doi.org/10.1016/j.ijsrc.2019.03.001

Robbins, B. A., & Griffiths, D. V. (2019) A new fragment for seepage beneath impervious structures. *Géotechnique*, 69(2), 174-179. https://doi.org/10.1680/jgeot.17.P.209

Robbins, B. A., van Beek, V. M., Lopez-Soto, J., Montalvo-Bartolomei, A. M., & Murphy, J. (2018). A novel laboratory test for backward erosion piping. *International Journal of Physical Modelling in Geotechnics*, *18*(5), 266–279.

Robbins, B. A., Stephens, I. J., Leavell, D. A., López-Soto, J. F., & Montalvo-Bartolomei, A. M. (2018). Laboratory piping tests on fine gravel. *Canadian Geotechnical Journal*, *12*(February), 1–12.

Conference Papers

Robbins, B.A., Griffiths, D.V., & Fenton, G.A. (2022) Assessing piping risks by finite elements. *GSP 333: Proceedings of Geo-Congress 2022.* ASCE. March 20-23, Charlotte, North Carolina.

Robbins, B.A. & Griffiths, D.V. (2022) Analysis of backward erosion piping by critical secant gradient functions. *Proceedings of the 7th International Young Geotechnical Engineers Conference*, April 29 – May 1, Sydney, Australia.

Robbins, B.A. & Griffiths, D.V. (2022) Quantifying the performance of piping mitigation measures with two-dimensional, adaptive finite element analysis. *Proceedings of the 20th International Conference on Soil Mechanics and Geotechnical Engineering*. May 2-5, Sydney, Australia.

Robbins B.A., Griffiths D.V. (2021) SODA: A Serial Fortran Library for Adaptation of Structured Meshes. In: Barla M., Di Donna A., Sterpi D. (eds) Challenges and Innovations in Geomechanics. IACMAG 2021. Lecture Notes in Civil Engineering, vol 125. Springer, Cham. https://doi.org/10.1007/978-3-030-64514-4_101

Robbins, B. A., Griffiths, D. V., & Fenton, G. A. (2019). Influence of Spatially Variable Soil Permeability on Backward Erosion Piping. In *Proceedings of the 7th International Symposium on Geotechnical Safety and Risk (ISGSR) Proceedings of the 7th International Symposium on Geotechnical Safety and Risk (ISGSR)* (pp. 96–101). https://doi.org/10.3850/978-981-11-2725-0-bs2-cd

Robbins, B. A., & Griffiths, D. V. (2018). Modelling of Backward Erosion Piping in Two- and Three- Dimensional Domains. In S. Bonelli, C. Jommi, & D. Sterpi (Eds.), *Internal Erosion in Earth Dams, Dikes, and Levees* (Vol. 17, pp. 149–158). Cham, Switzerland: Springer Nature Switzerland AG. https://doi.org/10.1007/978-3-319-99423-9

Robbins, B. A., & Griffiths, D. V. (2018). A simplified finite element implementation of the Sellmeijer model for backward erosion piping. In C. et Al. (Ed.), *Numerical Methods in Geotechnical Engineering IX* (pp. 1213–1218). Porto, Portugal: Taylor and Francis Group, London.

Robbins, B. A., & Griffiths, D. V. (2018). Internal Erosion of Embankments: A Review and Appraisal. In *Rocky Mountain Geo-Conference* (pp. 1–16). Denver, CO: American Society of Civil Engineers.

Robbins, B. A., & van Beek, V. M. (2017). Physical measurements of the backward erosion piping. In *EWGIE* (pp. 29–37). Delft, The Netherlands.

Robbins, B. A. (2016). Numerical modeling of backward erosion piping. In *Proceedings of the 4th Itasca Symposium on Applied Numerical Modeling* (pp. 551–558). Lima, Peru: Itasca Consulting Group.

Robbins, B.A., Griffiths, D.V., & Fenton, G.A. (2016) The influence of random confining layer thickness on levee seepage analysis. *Rocky Mountain Geo-Conference 2016*, GPP 10, ASCE, Denver, CO.

APPENDIX B

SUMMARY OF STUDIES ON MODELING OF INTERNAL EROSION

Of the 950 papers reviewed as part of this research, there were 342 papers related to the prediction of internal erosion using some form of model. This included studies on numerical modeling, empirical or statistical modeling, or analytical modeling. The 342 papers on modeling of internal erosion are provided in Table B.3.

All papers were categorized using a classification system developed as part of this research. The classification system categorized the papers based on the type of internal erosion research (Table B.1) and the type of research study that was conducted (Table B.2). Every study was categorized using the tags for the classification system. It should be noted that a study may have more than one applicable tag for both the category of research and the type of study that was conducted. Additionally, for studies where it was not abundantly clear what type of internal erosion was being researched, the IE tag was applied as a generic tag. The tags assigned to each study are listed in the right column of Table B.3.

The number of studies that pursued either empirical (MES), analytical (MA), or numerical (MN) models is shown in Figure B.1. For this thesis, the primary area of focus was on the numerical studies. The distribution of numerical studies by study year is illustrated in Figure B.2. Further discussion of these studies was provided in Section 2.4 of this thesis.

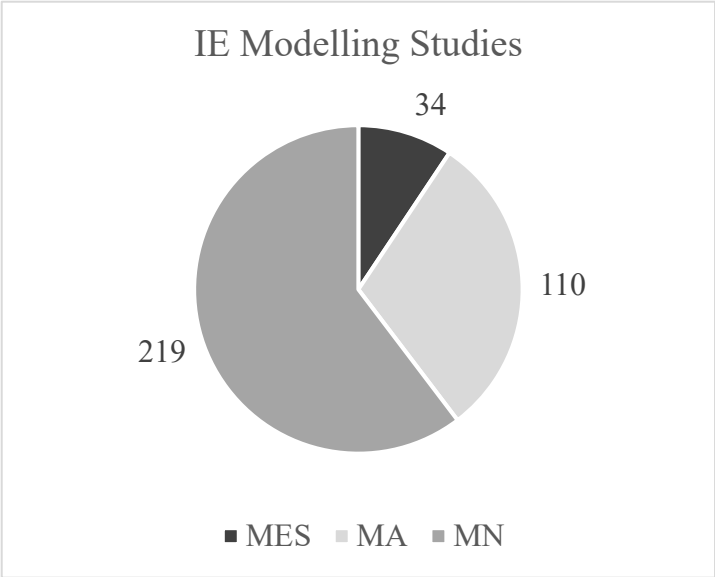

Figure B.1. Distribution of IE modeling studies by modeling approach.

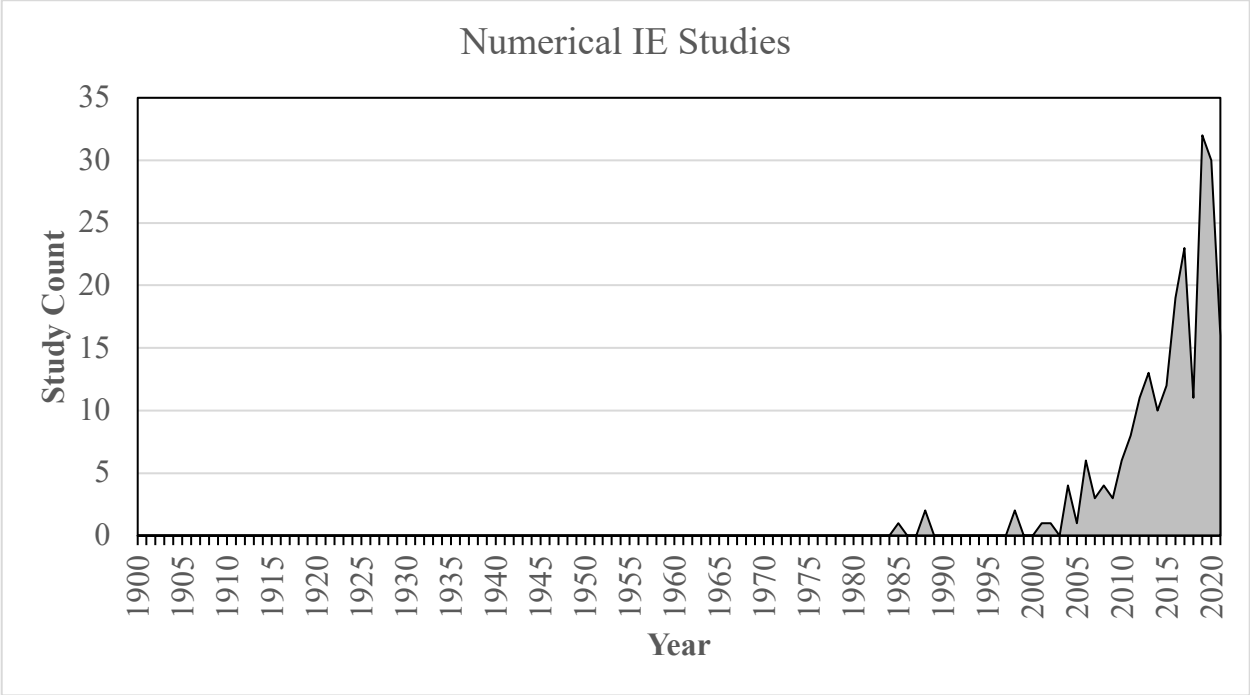

Figure B.2. Distribution of numerical modeling studies by year.

Table B.1. Category of IE Research

Type of IE Research	**Tag**
CLE	CLE
BEP	BEP
Internal Instability	II
Contact Erosion	CE
GBE/ Stoping	GBE/S
Internal Erosion	IE
Filter Research	F

Table B.2. Type of research study.

Type of Study	**Subcategory**	**Tag**
Observational	Experimental	OE
	Case History/Anecdotal	OC
Model Development	Empirical/Statistical	MES
	Analytical	MA
	Numerical	MN
Verification/Validation		VV
Monitoring & Sensing	Laboratory	MSL
	Field	MSF
	Numerical	MSN
Design Strategies		DS
Reviews		RV
Failure Intervention/ Emergency Ops		FI

Table B.3. Studies involving prediction of internal erosion through numerical models, empirical or statistical models, or analytical models.

Year	Author	Title	Publication Title	Study Tags
1910	Bligh, W.G.	Dams, barrages and weirs on porous foundations	Engineering Record	MES; IE
1914	Griffith, William	The Stability of Weir Foundations on Sand and Soil Subject to Hydrostatic Pressure	Minutes of the Proceedings of the Institution of Civil Engineers	DS; IE; MES
1915	Bligh, W.G.	Dams and Weirs		IE; MES; OC
1935	Lane, E.W.	Security from Under-Seepage Masonry Dams on Earth Foundations	Transactions of ASCE	MES; OC; IE
1956	USACE	Investigation of Underseepage and Its control, Lower Mississippi River Levees, Volume 1		BEP; DS; MES; OC
1956	USACE	Investigation of Underseepage, Mississippi River Levees, Alton to Gale, IL - Volume 1		BEP; DS; MES; OC
1961	Turnbull, W.J.; Mansur, C.I.	Investigation of underseepage- Mississippi River Levees	ASCE Transactions	BEP; MES; OC
1968	Lubochkov, E.A.	Calculation of the piping properties of cohesionless soils with the use of a nopiping analog	Gidrotechnicheskoe Stroitel'stvo	OE; II; MA
1977	Kälin, M	Hydraulic piping-theoretical and experimental findings	Canadian Geotechnical Journal	OE; MA; IE
1981	Townsend, FC; Schmertmann, John H; Logan, T.J.; Pietrus, T.J.; Wong, Y.W.	An Analytical and Experimental Investigation of a Quantitative Theory for Piping in Sand		BEP; MA; OE
1981	Kovacs, Gyorgy	The motion of grains in cohesionless loose clastic sediments		MA; IE
1985	Hanses, Ullrich	The mechanics of the development of erosion pipes in a layered substratum beneath dams		BEP; MN; OE; MA
1985	Kenney, T. C.; Lau, D.	Internal stability of granular filters	Canadian Geotechnical Journal	OE; II; MA
1987	Bezuijen, A.; Breteler, M. Klein; Bakker, K.J.	Design Criteria for Placed Block Revetments and Granular Filters	Second International Conference on Coastal and Port Engineering in Developing Countries	OE; MA; F; CE
1988	Srbulov, M	Estimation of Soil Internal Erosion Potential	Computers and Geotechnics	II; MA; MN
1988	Sellmeijer, J.B.	On the mechanism of piping under impervious structures		BEP; MA
1988	Howard, Alan D; McClane, Charles F	Erosion of Cohesionless Sediment by Groundwater Seepage	Water Resources Research	MN; MA; IE
1989	Sellmeijer, J.B.; Calle, E.O.F.; Sip, J.W.	Influence of aquifer thickness on piping below dikes and dams	International Symposium on Analytical Evaluation of Dam Related Safety Problems	BEP; MA
1989	Calle, E. O.F.	Probabilistic analysis of piping underneath water retaining structures	Proceedings of the International Conference on Soil Mechanics and Foundation Engineering	BEP; MA
1991	Sellmeijer, J.B.; Koenders, M.A.	A mathematical model for piping	Applied Mathematical Modelling	BEP; MA
1992	Van Rhee, C.; Bezuijen, A.	Influence of Seepage on Stability of Sandy Slope	Journal of Geotechnical Engineering	IE; MA; OE
1992	Koenders, M.A.; Sellmeijer, J.B.	Mathematical Model for Piping	Journal of Geotechnical Engineering	BEP; MA
1992	Wörman, A.; Olafsdottir, Ragnheidur	Erosion in a granular medium interface	Journal of Hydraulic Research	OE; MA; CE
1993	Weijers, JBA; Sellmeijer, J.B.	A new model to deal with the piping mechanism	Filters in geotechnical and hydraulic engineering	BEP; MA
1993	Aberg, B.	Washout of grains from filtered sand and gravel materials	Journal of Geotechnical Engineering	OE; II; MA

Table B.3 (continued)

Year	Author	Title	Publication Title	Study Tags
1993	Burenkova, V.V.	Assessment of suffosion in non-cohesive and graded soils	Filters in geotechnical and hydraulic engineering	OE; II; MA
1994	den Adel, H; Koenders, M.A.; Bakker, K J	The analysis of relaxed criteria for erosion-control filters	Canadian Geotechnical Journal	OE; MA; CE
1997	Peck, R.B.	The risk of the oddball	Reclamation workshop on risk of piping and internal erosion	MES; MA; IE; RV
1998	Stavropoulou, M; Papanastasiou, P; Vardoulakis, I	Coupled Wellbore Erosion and Stability Analysis	International Journal for Numerical and Analytical Methods in Geomechanics	MN; IE
1998	Jianhua, Yin	FE Modeling of Seepage in Embankment Soils with Piping Zone	Chinese Journal of Rock Mechanics and Engineering	BEP; MN
1999	Foster, Mark; Fell, Robin	Assessing Embankment Dam Filters That Do Not Satisfy Design Criteria	Journal of Geotechnical and Geoenvironmental Engineering	MES; IE; F
2000	Reddi, Lakshmi N.; Ming, Xiao; Hajra, Malay G.; Lee, In Mo	Permeability Reduction of Soil Filters due to Physical Clogging	Journal of Geotechnical and Geoenvironmental Engineering	F; MA; OE
2000	Schmertmann, John H	The No-Filter Factor of Safety Against Piping Through Sands	Judgement and Innovation	BEP; MA
2000	Foster, Mark; Fell, Robin; Spannagle, Matt	A method for assessing the relative likelihood of failure of embankment dams by piping	Canadian Geotechnical Journal	MES; IE
2000	Foster, M.; Fell, R.	Use of event trees to estimate the probability of failure of embankment dams by internal erosion and piping	Proceedings of the 20th ICOLD Congress	MES; MA; IE
2001	Fell, R.; Wan, C.F.; Cyganiewicz, J.; Foster, M.	The Time for Development and Detectability of Internal Erosion and Piping in Embankment Dams and their Foundations		CLE; MA; OE
2001	Ojha, C.S.P.; Singh, V.P.; Adrian, D.D.	Influence of Porosity on Piping Models of Levee Failure	Journal of Geotechnical and Geoenvironmental Engineering	BEP; MA
2001	Wörman, A.; Xu, S.	Stochastic Analysis of Internal Erosion in Soil Structures - Implications for Risk Assessments	Journal of Hydraulic Engineering	IE; MN
2001	Badv, K; Sargordi, F	The study of Piping in some hydraulic structures in Urmia region, Iran, using the PIPING model	15th International Conference on Soil Mechanics and Geotechnical Engineering	BEP; MA
2002	Popielski, Pawel; Stasierski, Jacek; Dluzewski, J.	Numerical model of suffusion in terms of finite element method	International Conference on Hydro-Science and Engineering Nr V Warsaw	II; MN
2003	Ozkan, Senda	Analytical Study on Flood Induced Seepage under River Levees		BEP; MA; RV
2003	Ojha, C. S. P.; Singh, V.P.; Adrian, D.D.	Determination of Critical Head in Soil Piping	Journal of Hydraulic Engineering	MA; IE
2003	Kakuturu, S.	Modeling and Experimental Investigations of Self-Healing or Progressive Erosion of Earth Dams		OE; MA; CLE
2004	Glynn, M. Eileen; Kuszmaul, Joel K.	Prediction of Piping Erosion Along Middle Mississippi River Levees–An Empirical Model (Sept 2004, Revised 2010)		BEP; MES; OC
2004	Cividini, Annamaria; Gioda, Giancarlo	Finite-Element Approach to the Erosion and Transport of Fine Particles in Granular Soils	International Journal of Geomechanics	MN; II
2004	Bui, H.N.; Song, C.; Fell, R.	Two and Three Dimensional Numverical Analysis of the Potential for Cracking of Embankment Dams During Construction		MN; IE; CLE
2004	Cai, F; Ugai, K	Seepage analysis of two case histories of piping induced by excavations in cohesionless soils	ICCI2004	MN; OC; IE
2004	Hagerty, D J; Curini, Andrea	Impoundment Failure Seepage Analyses	Environmental & Engineering Geoscience	MN; IE

Table B.3 (continued)

Year	Author	Title	Publication Title	Study Tags
2004	Fell, R; Wan, C F; Foster, M	Methods for Estimating the Probability of Failure of Embankment Dams By Internal Erosion and Piping - Piping through the embankment		MA; IE; CLE
2005	Bui, Hong Ngoc; Tandjiria, Vipman; Fell, Robin; Song, Chongmin; Khalili, Nasser	Two and Three Dimensional Numerical Analysis of the Potential for Cracking of Embankment Dams – Supplementary Report		MN; IE; CLE
2005	Fell, R; Wan, C F	Methods for Estimating the Probability of Failure of Embankment Dams By Internal Erosion and Piping in the Foundation and From Embankment To Foundation		MA; IE
2006	Sellmeijer, J.B.	Numerical computation of seepage erosion below dams (piping)	International Conference on Scour and Erosion	BEP; MN
2006	Detournay, C; Tan, C; Wu, B	Modeling the mechanism and rate of sand production using FLAC	4th International FLAC Symposium on Numerical Modeling in Geomechanics	BEP; IE; II; MN
2006	Vardoulakis, I	Sand-production and sand internal erosion : Continuum modeling		IE; MN
2006	Bonelli, S.; Brivois, O.; Borghi, R.; Benahmed, N.	On the modelling of piping erosion	C.R. Mecanique	CLE; MA; MN
2006	Chapuis, R P; Tournier, J P	Simple graphical methods to assess the risk of internal erosion	Proceedings of the 12th ICOLD Congress	II; MA
2006	Josef, Karl; Semar, O.; Witt, K.J.	Internal erosion – state of the art and an approach with percolation theory	ICSE3	MN; II; MA; RV
2006	Bonelli, S.; Brivois, O.	Piping Erosion : Modelling	EWGIE	MN; MA; CLE
2007	Ding, Liu-qian; Wu, Meng-xi; Liu, Chang-jun; Sun, Dong-ya; Yao, Q.L.	Numerical simulation of dynamic development of piping in two-stratum dike foundations	Water Resources and Hydropower Engineering	BEP; MN
2007	Steeb, H.; Stefan, Diebels; Vardoulakis, I	Modeling Internal Erosion in Porous Media	Geo-Denver 2007: New Peaks in Geotechics	MN; II
2007	Foster, M.A.	Application of no, excessive and continuing erosion criteria to existing dams	Internal Erosion in Embankment Dams and Their Foundations	MES; IE; F
2007	Benamar, A.; Elkawafi, A.; Alem, A.; Wang, H.	Clogging evaluation of permeable soil filters	Assessment of the Risk of Internal Erosion of Water Retaining Structures: Dams, Dykes and Levees (EWGIE 2007)	OE; MA; F
2007	Wörman, A; Saucke, U; Calle, E O F; Sellmeijer, J B; Koelewijn, A R	Probabilistic Aspects of Geomechanical Filter Design	Assessment of the Risk of Internal Erosion of Water Retaining Structures: Dams, Dykes and Levees (EWGIE 2007)	BEP; MA; F
2007	Sellmeijer, J B; Koelewijn, A R	Engineering tools for piping – neural networks created using FEM	Assessment of the Risk of Internal Erosion of Water Retaining Structures: Dams, Dykes and Levees (EWGIE 2007)	BEP; MN
2008	Fontana, Nicola	Experimental Analysis of Heaving Phenomena in Sandy Soils	Journal of Hydraulic Engineering	IE; MA; OE
2008	El Shamy, U; Aydin, Firat	Multiscale Modeling of Flood-Induced Piping in River Levees	Journal of Geotechnical and	BEP; MN
2008	Bonelli, S.; Marot, D.	On the modelling of internal soil erosion	International Association for Computer Methods and Advances in Geomechanics	II; MN
2008	van Beek, V.M.; Koelewijn, A. R.; Kruse, G A M; Sellmeijer, Hans; Barends, Frans	Piping Phenomena in Heterogeneous Sands - Experiments and Simulations	International Conference on Scour and Erosion	BEP; MN; OE; VV
2008	Feng, Chen; Drumm, Eric; Guiochon, Georges; Suzuki, Kiichi	Discrete Element Simulation of 1D Upward Seepage Flow with Particle-Fluid Interaction Using Coupled Open Source Software	International Association for Computer Methods and Advances in Geomechanics	MN; IE

Table B.3 (continued)

Year	Author	Title	Publication Title	Study Tags
2008	Wan, Chi Fai; Fell, Robin	Assessing the Potential of Internal Instability and Suffusion in Embankment Dams and Their Foundations	Journal of Geotechnical and Geoenvironmental Engineering	OE; II; MA
2009	Li, M.; Fannin, R.J.; Garner, S.J.	Application of a new criterion for assessing the susceptibility to internal erosion	CDA Annual Conference	MES; II
2009	Lachouette, D; Bonelli, S.; Golay, Frédéric; Seppecher, P	Numerical modeling of interfacial soil erosion	19eme Congres Francais de Mecanique	MN; IE; CLE
2009	Mehlhorn, Tobias; Prohaska, S; Slowik, Volker	Modelling and analysis of particle and pore structures in soils	Proceedings of the Workshop on Internal Erosion	MN; II
2009	Cividini, Annamaria; Bonomi, Simone; Vignati, Giulio C.; Gioda, Giancarlo	Seepage-Induced Erosion in Granular Soil and Consequent Settlements	International Journal of Geomechanics	MN; II
2009	Hendrix, Joshua M; Stark, T.D.	Predicting Underseepage of Masonry Dams	ASDSO Dam Safety	MES; IE
2010	Benamar, A.; Beaudoin, A.; Bennabi, A.	Experimental Study of Internal Erosion of Fine Grained Soils	ICSE5	II; MN; OE
2010	Scheuermann, A.; Steeb, H.; Kiefer, J	Internal erosion of granular materials - Identification of erodible fine particles as a basis for numerical calculations	9th HSTAM International Congress on Mechanics	II; MA; OE
2010	Fujisawa, K.; Murakami, Akira; Nishimura, S	Numerical Analysis of the Erosion and the Transport of Fine Particles within Soils Leading to the Piping Phenomenon	Soils and Foundations	II; MN
2010	Maeda, K.; Muir Wood, D.; Nukudani, E.	Modelling mechanical consequences of erosion	Géotechnique	II; MN
2010	Fujisawa, K.; Murakami, Akira; Nishimura, S	Simultaneous Modeling of Internal Erosion and Deformation of Soil Structures	GeoShanghai 2010 International Conference	MN; II
2010	Becker, C.; Kurzeja, P.; Steeb, H.	Modelling internal erosion of cohesionless soils using a microstructural parameter	PAMM	MN; II
2010	Zhou, J; Bai, YF	A Mathematical Model for Determination of the Critical Hydraulic Gradient in Soil Piping	GeoShanghai 2010 International Conference	OE; II; MA
2010	Golay, Frédéric; Bonelli, S.	Numerical modeling of suffusion as an interfacial erosion process	European Journal of Environmental and Civil Engineering	MN; II
2011	Salehi Sadaghiani, M.R.; Witt, K.J.	Variability of the grain size distribution of a soil related to suffusion	ISGSR	II; MA
2011	Liang, Y; Chen, J.	Mathematical Model for Piping Erosion Based on Fluid-Solid Interaction and Soils Structure	GSP 217: Advances in Unsaturated Soil, Geo-Hazard, and Geo-Environmental Engineering	MN; II
2011	Lopez de la Cruz, J; Calle, E.O.F.; Schweckendiek, T.	Calibration of Piping Assessment Models in the Netherlands	ISGSR 2011	BEP; MES; MA
2011	Frishfields, V.; Hellström, J.G.I.; Lundström, T.S.; Mattsson, H.	Fluid Flow Induced Internal Erosion within Porous Media : Modelling of the No Erosion Filter Test Experiment	Transport in Porous Media	MN; F
2011	Golay, Frédéric; Lachouette, D; Bonelli, S.; Seppecher, P	Numerical modelling of interfacial soil erosion with viscous incompressible flows	Computer Methods in Applied Mechanics and Engineering	MN; CLE
2011	Sari, H; Chareyre, B.; Catalano, E.; Philippe, P.; Vincens, E.	Investigation of internal erosion processes using a coupled DEM-Fluid method	PARTICLES 2011	MN; II
2011	Goltz, M; Etzer, T; Aufleger, M; Muckenthaler, P.	Assessing the Critical Seepage Velocity Causing Transport of Fine Particles in Embankment Dams and Their Foundation	Long Term Behavior of Dams	II; MA
2011	Ramírez, A.; González, J. L.; Carrillo, F.; Lopez, S.	Simulation of uncompressible fluid flow through a porous media	Internal Erosion in Embankment Dams and Their Foundations	MN; IE
2011	Sellmeijer, Hans; Lopez de la Cruz, J; van Beek, V.M.; Knoeff, Han	Fine-tuning of the backward erosion piping model through small-scale , medium-scale and IJkdijk experiments	European Journal of Environmental and Civil Engineering	BEP; MES; MA

Table B.3 (continued)

Year	Author	Title	Publication Title	Study Tags
2011	Bonelli, S.; Benahmed, N.	Piping flow erosion in water retaining structures	Internal Erosion in Embankment Dams and Their Foundations	MA; CLE
2011		Reliability assessment of internal erosion initiation Limit state method – the village of Troubky	Internal Erosion in Embankment Dams and Their Foundations	MA; IE
2011	Fannin, R J; Moffat, R M; Li, M	Internal instability : empirical and theoretical criteria for soils evaluation	Internal Erosion in Embankment Dams and Their Foundations	MES; IE
2011	Fell, R.	Quantitative Risk Analysis of Internal Erosion of Dams and their Foundations- Some Practical Experience and Limitations .	Internal Erosion in Embankment Dams and Their Foundations	MES; MA; IE
2011	Garner, Stephen	Proposed Development of a Fully Coupled Internal Erosion Model	Internal Erosion in Embankment Dams and Their Foundations	MN; II
2011	Hoffmans, Gijs; Verheij, Henk	Impact of turbulent groundwater flow in granular	Internal Erosion in Embankment Dams and Their Foundations	MA; F
2011	Navin, Michael P.; Vroman, Noah; Schwanz, N. T.; Farmer, Brian M.	Development of risk assessment methods with regard to internal erosion for corps of engineers levees	Internal Erosion in Embankment Dams and Their Foundations	BEP; MES
2011	Popielski, Pawel; Stasierski, Jacek; Dluzewski, J.	Numerical model of suffusion in terms of finite element method	Internal Erosion in Embankment Dams and Their Foundations	MN; II
2011	Shire, Thomas; Sullivan, Catherine O	Particle scale numerical modelling to develop insight into suffusion in granular filters	Internal Erosion in Embankment Dams and Their Foundations	MN; II
2011	Sjah, Jessica; Vincens, Eric	Calibration of an inverse method to compute the Constriction Size Distribution for granular filters Statistics on samples composed of spheres Creation of numerical samples of spheres	Internal Erosion in Embankment Dams and Their Foundations	MA; F
2012	Hicher, P.	Modelling the Behaviour of Soil Subjected to Internal Erosion	ICSE6	II; MN
2012	Rice, J.D.; Polanco, Lourdes	Reliability-based underseepage analysis in levees using a response surface-monte carlo simulation method	Journal of Geotechnical and Geoenvironmental Engineering	BEP; MN
2012	van Beek, V.M.; Yao, Q.L.; Van, M.A.; Barends, Frans	Validation of Sellmeijer's model for backward piping under dikes on multiple sand layers	ICSE6	BEP; MN; OE; VV
2012	Moraci, Nicola; Mandaglio, Maria Clorinda; Ielo, Domenico	A new theoretical method to evaluate the internal stability of granular soils	Canadian Geotechnical Journal	OE; II; MA
2012	Schaufler, A.; Becker, C.; Steeb, H.; Scheuermann, A.	A continuum model for infiltration problems	ICSE6	MN; II; F
2012	van Beek, V.M.	SBW Piping 5A: Model development for initiation of piping		BEP; OE; MA
2012	Moraci, Nicola; Mandaglio, Maria Clorinda; Lelo, Domenico	Reply to the discussion by Dallo and Wang on “A new theoretical method to evaluate the internal stability of granular soils”	Canadian Geotechnical Journal	MN; II
2012	Maeda, Kenichi; Muir Wood, D.; Kondo, Akihiko	Micro and macro modeling of internal erosion and scouring with fine particle dynamics	ICSE6	MN; OE; II
2012	Dallo, Yousif A.H.; Wang, Yuan	Discussion of "A new theoretical method to evaluate the internal stability of granular soils"	Canadian Geotechnical Journal	II; MA
2012	Moraci, Nicola; Mandaglio, Maria Clorinda; Ielo, Domenico	Corrigendum : A new theoretical method to evaluate the internal stability of granular soils	Canadian geotechnical journal	II; MA
2012	Reza, Mohamad; Salehi Sadaghiani, M.R.; Witt, K.J.; Jentsch, H	A Statistical Approach to Identify Mobile Particles of Widely Graded Soils	ICSE6	MN; II

Table B.3 (continued)

Year	Author	Title	Publication Title	Study Tags
2012	Ghafghazi, M.; Azhari, F.	A Simple Method for Estimating the Non-Structural Fines Content of Granular Materials	ICSE6	II; MA
2012	Kanning, W.	The weakest link - spatial variability in the piping failure mechanism of dikes		BEP; MN
2012	Uzuoka, Ryosuke; Ichiyama, Tomohiro; Mori, Tomohiro; Kazama, Motoki	Hydro-mechanical analysis of internal erosion with mass exchange between solid and water	ICSE6	MN; II
2012	Zhang, X. S.; Wong, H.; Leo, C. J.; Bui, T.A.; Wang, J. X.; Sun, W. H.; Huang, Z. Q.	A Thermodynamics-Based Model on the Internal Erosion of Earth Structures	Geotechnical and Geological Engineering	MN; II
2012	Zhou, Xiao-jie; Jie, Yu-xin; Li, Guang-xin	Numerical simulation of the developing course of piping	Computers and Geotechnics	BEP; MN
2012	Alamdari, N Zaki; Banihashemi, M; Mirghasemi, A	A numerical Modeling of Piping Phenomenon in Earth Dams	Engineering and Technology I	MA; CLE
2013	Shire, T.; O'Sullivan, C.	Micromechanical assessment of an internal stability criterion	Acta Geotechnica	II; MN
2013	Farahnak, Mojtaba; Soroush, Abbas; Tabatabaie Shourijeh, Piltan; Shafipour, Roozbeh	Stress transmission in internally unstable gap-graded soils using discrete element modeling	Powder Technology	II; MN
2013	Zou, Yu-Hua; Chen, Qun; Chen, Xiao-Qing; Cui, Peng	Discrete numerical modeling of particle transport in granular filters	Computers and Geotechnics	F; II; MN
2013	Li, Maoxin; Fannin, R.J.	Capillary Tube Model for Internal Stability of Cohesionless Soil	Journal of Geotechnical and Geoenvironmental Engineering	II; MA
2013	Xu, Tianhua; Zhang, Limin	Simulation of Piping in Earth Dams Due to Concentrated Leak Erosion	Geo-Congress 2013	MA; CLE
2013	Schaufler, A.; Becker, C.; Steeb, H.	Infiltration processes in cohesionless soils	ZAMM Zeitschrift fur Angewandte Mathematik und Mechanik	MN; II; F
2013	Luo, Y L	International Journal of Civil Engineering A continuum fluid-particle coupled piping model based on solute transport	International Journal of Civil Engineering	MN; II
2013	van Beek, V.M.; Yao, Q.L.; Van, M.A.	Backward Erosion Piping Model Verification Using Cases in China and the Netherlands	Seventh International Conference on Case Histories in Geotechnical Engineering	BEP; OC; MA; VV
2013	Van Esch, J.M.; Sellmeijer, J.B.; Stolle, D.	Modeling transient groundwater flow and piping under dikes and dams	3rd International Symposium on Computational Geomechanics (ComGeo III)	BEP; MN
2013	Lominé, F.; Scholtès, Luc; Sibille, L.; Poullain, P	Modeling of fluid – solid interaction in granular media with coupled lattice Boltzmann / discrete element methods : application to piping erosion	International Journal for Numerical and Analytical Methods in Geomechanics	MN; CLE
2013	Boukhemacha, Mohamed Amine; Bica, Ioan; Mezouar, Khoudir	New procedures to estimate soil erodibility properties from a hole erosion test record	Periodica Polytechnica Civil Engineering	MN; OE; CLE
2013	Kanning, W.; Calle, E.O.F.	Derivation of a representative piping resistance parameter based on random field modelling of erosion paths	Georisk	BEP; MN
2013	O'Leary, T.M.; Vroman, Noah; Williams, Carmen; Pabst, Mark	Critical Horizontal Gradients	Journal of Dam Safety	BEP; MA
2013	van Esch, J.M.	Modeling Groundwater Flow and Piping under Dikes and Dams Model validation and verification		BEP; MN

Table B.3 (continued)

Year	Author	Title	Publication Title	Study Tags
2013	Wang, Yuan; Ni, Xiao-dong	Hydro-mechanical analysis of piping erosion based on similarity criterion at micro-level by PFC 3D	European Journal of Environmental and Civil Engineering	BEP; MN; OE; II
2013	Bersan, S.; Jommi, Cristina; Simonini, Paolo	Applicability of the Fracture Flow Interface to the Analysis of Piping in Granular Material	COMSOL Conference	BEP; MN; RL
2013	Vandenboer, K.; van Beek, V.M.; Bezuijen, A.	3D FEM Simulation of Groundwater Flow During Backward Erosion Piping	Fifth International Young Geotechnical Engineering Conference	BEP; MN
2013	Benjasupattananan, Sittinan; Meehan, Christopher L.	Probability-Based Design for Levee Underseepage: Heaving vs. Piping Phenomena	Geo-Congress 2013	BEP; MA
2014	Wang, Da-yu; Fu, Xu-dong; Jie, Yu-xin; Dong, Wei-jie; Hu, Die	Simulation of pipe progression in a levee foundation with coupled seepage and pipe flow domains	Soils and Foundations	BEP; DS; MN; OE
2014	Seghir, A.; Benamar, A.; Wang, H.	Effects of Fine Particles on the Suffusion of Cohesionless Soils . Experiments and Modeling	Transport in Porous Media	II; MN; OE
2014	Rönnqvist, H.; Fannin, J.; Viklander, P.	On the use of empirical methods for assessment of filters in embankment dams	Geotechnique Letters	II; MES
2014	Polanco, Lourdes; Rice, J.D.	A Reliability-Based Evaluation of the Effects of Geometry on Levee Underseepage Potential	Geotechnical and Geological Engineering	BEP; MN
2014	Kramer, Renier	Piping Under Transient Conditions		BEP; MN
2014	Richards, K.S.; Reddy, K.R.	Kinetic Energy Method for Predicting Initiation of Backward Erosion in Earthen Dams and Levees	Environmental & Engineering Geoscience	BEP; II; MA; OE
2014	Schweckendiek, T.	On Reducing Piping Uncertainties: A Bayesian Decision Approach		BEP; MA
2014	Vazquez Borragan, M.A.	Modelling Internal Erosion Within An Embankment Dam Prior To Breaching		MN; OE; II
2014	Shire, T.; Hanley, K J; Fannin, R.J.	Fabric and Effective Stress Distribution in Internally Unstable Soils	Journal of Geotechnical and Geoenvironmental Engineering	MN; II; RV
2014	Xue, Xinhua; Yang, Xingguo; Chen, X I N; Chen, Xin	ESTIMATING PIPING POTENTIAL IN EARTH DAMS AND LEVEES USING GENERALIZED NEURAL NETWORKS	Acta Geotechnica Slovenica	MN; II; IE
2014	van Essen, H.M.; Kanning, W.; van Beek, V.M.	Research and Development of Flood Defense Assessment Tools for Piping in WTI 2017 - Report 12. Heterogeneity		BEP; MN; OE
2014	Yin, Z.Y.; Zhao, Jidong; Hicher, P.	A micromechanics-based model for sand-silt mixtures	International Journal of Solids and Structures	MN; II
2014	Moraci, Nicola; Mandaglio, MC; Ielo, D.	Analysis of the internal stability of granular soils using different methods	Canadian Geotechnical Journal	OE; II; MA
2014	Vandenboer, K.; van Beek, V.M.; Bezuijen, A.	3D finite element method (FEM) simulation of groundwater flow during backward erosion piping	Frontiers of Structural and Civil Engineering	BEP; MN
2015	Moffat, R.; Herrera, Paulo	Hydromechanical model for internal erosion and its relationship with the stress transmitted by the finer soil fraction	Acta Geotechnica	II; MA; OE
2015	Roscoe, Kathryn; Hanea, Anca	Bayesian networks in levee system reliability	12th International Conference on Applications of Statistics and Probability in Civil Engineering	BEP; MA
2015	Shire, T.; O'sullivan, C.; Fannin, R.J.; Hanley, K J	Use of discrete element modelling to assess the internal instability of dam filters	Proceedings of the XVI ECSMGE	II; MN
2015	Wang, Xiaoliang; Li, Jiachun	On the degradation of granular materials due to internal erosion	Acta Mechanica Sinica/Lixue Xuebao	II; MA; MN

Table B.3 (continued)

Year	Author	Title	Publication Title	Study Tags
2015	Lőrincz, Janos; Imre, Emöke; Fityus, Stephen; Trang, Phong; Tarnai, Tibor; Talata, István; Singh, V.P.	The Grading Entropy-based Criteria for Structural Stability of Granular Materials and Filters	Entropy	F; II; MA
2015	Kaunda, Rennie B.	A neural network assessment tool for estimating the potential for backward erosion in internal erosion studies	Computers and Geotechnics	BEP; MA; MN
2015	Bezuijen, A.	Critical vertical gradients in piping: A preliminary sensitivity study concerning the 0.3-D rule		BEP; MA
2015	Anderson, Scott; Ferguson, Keith	Examination of three-dimensional effects of internal erosion (IE) and piping processes in soil	USSD Annual Meeting and Conference	BEP; MN
2015	Tejada, I G; Sibille, L.; Chareyre, B.	Micromechanical modeling of internal erosion by suffusion in soils	Grenoble Geomechanics Group	MN; II
2015	Hoffmans, G.	Shields-Darcy model: Alternative piping model?		BEP; MA
2015	Kanning, W.; Bocovich, C.; Schweckendiek, T.; Mooney, M.A.	Incorporating Observations to Update the Piping Reliability Estimate of the Francis Levee	ISGSR 2015	BEP; MA
2015	Galindo-Torres, S. a.; Scheuermann, A.; Mühlhaus, H. B.; Williams, D. J.	A micro-mechanical approach for the study of contact erosion	Acta Geotechnica	MN; CE
2015	Melnikova, Natalia; Sloot, Peter; Jordan, David; Krzhizhanovskaya, Valeria	Numerical prediction of the IJkDijk trial embankment failure	Proceedings of the ICE - Geotechnical Engineering	BEP; MN
2015	Indraratna, B.; Israr, J.; Rujikiatkamjorn, C.	Geometrical Method for Evaluating the Internal Instability of Granular Filters Based on Constriction Size Distribution	Journal of Geotechnical and Geoenvironmental Engineering	OE; II; MA
2015	Muhlhaus, Hans; Gross, Lutz; Scheuermann, A.	Sand erosion as an internal boundary value problem	Acta Geotechnica	MN; II
2015	Ni, Xiao-dong; Wang, Yuan; Chen, Ke; Zhao, Shuai-long	Improved similarity criterion for seepage erosion using mesoscopic coupled PFC–CFD model	Journal of Central South University	MN; IE
2015	Farahnak Langroudi, Mojtaba; Soroush, Abbas; Tabatabaie Shourijeh, Piltan	A comparison of micromechanical assessments with internal stability / instability criteria for soils	Powder Technology	MN; II
2015	Sibille, L.; Lominé, F.; Poullain, P; Sail, Y.; Marot, D.	Internal erosion in granular media: direct numerical simulations and energy interpretation	Hydrological Processes	MN; CLE
2015	van Beek, V.M.; van Essen, H.M.; Vandenboer, K.; Bezuijen, A.	Developments in modelling of backward erosion piping	Géotechnique	BEP; MN; OE
2016	Rönnqvist, Hans; Viklander, Peter	A unified-plot approach for the assessment of internal erosion in embankment dams	International Journal of Geotechnical Engineering	II; MES; OE; RV
2016	Fujisawa, K.	Numerical analysis of backward erosion of soils by solving the Darcy-Brinkman Equations	Advances in Computational Fluid-Structure Interaction and Flow Simulation	BEP; MN
2016	Polanco-Boulware, Lourdes; Rice, J.D.	Reliability-Based Three-Dimensional Assessment of Internal Erosion Potential due to Crevasse Splays	Journal of Geotechnical and Geoenvironmental Engineering	BEP; MN
2016	Aboul Hosn, R.; Sibille, L.; Benahmed, N.; Chareyre, B.	A discrete numerical description of the mechanical response of soils subjected to degradation by suffusion	Scour and Erosion (ICSE 2016)	II; MN

Table B.3 (continued)

Year	Author	Title	Publication Title	Study Tags
2016	Winkler, P; Jentsch, H; Salehi Sadaghiani, M.R.; Witt, K.J.	Numerical investigation of the particle skeleton of widely graded soils prone to suffusion	Scour and Erosion (ICSE 2016)	II; MN
2016	Robbins, B.A.; Sharp, Michael K.	Incorporating uncertainty into Backward Erosion Piping risk assessments	3rd European Conference on Flood Risk Management	BEP; MA; MES; OE
2016	Abdelhamid, Yasser; El Shamy, Usama	Pore-Scale Modeling of Fine-Particle Migration in Granular Filters	International Journal of Geomechanics	F; MN
2016	Tejada, I G; Sibille, L.; Chareyre, B.; Vincens, E.	Numerical modeling of particle migration in granular soils	Scour and Erosion (ICSE 2016)	MN; II
2016	Robbins, B.A.	Numerical modeling of backward erosion piping	Proceedings of the 4th Itasca Symposium on Applied Numerical Modeling	BEP; MN
2016	Ahmed, C; Ahmed, B	Modeling of particles migration in porous media : Application to soil suffusion	Scour and Erosion (ICSE 2016)	MN; II
2016	Semmens, S.	An examination of the impact of the natural environment on levee sustainability		BEP; MES
2016	Robbins, B.A.; Griffiths, D.V.; Fenton, G.A.	The Influence of Random Confining Layer Thickness on Levee Seepage Analysis	Rocky Mountain Geo-Conference	BEP; MN
2016	Fujisawa, K.; Murakami, Akira; Sakai, Kotaro	Numerical analysis of backward erosion by soil-water interface tracking	The 6th Japan-Korea Geotechnical Workshop	BEP; MN
2016	Durand, E; Boulay, A	CARDigues : An integrated tool for levee system diagnosis and assessment	Scour and Erosion (ICSE 2016)	BEP; MA; RL
2016	Martinez, Maria Fernanda Garcia; Gragnano, Carmine Gerardo; Gottardi, G.; Marchi, M.; Tonni, Laura; Rosso, A.	Analysis of Underseepage Phenomena of River Po Embankments	Procedia Engineering	BEP; MN
2016	de Groot, J.	3D groundwater flow in heterogeneous subsurfaces underneath dikes		BEP; MN
2016	Papin, A A; Sibin, A	Model isothermal internal erosion of soil	Nonlinear Waves: Theory and New Apllications	MN; II; MA
2016	Sibille, L.; Marot, D.; Poullain, P; Lominé, F.	Phenomenological interpretation of internal erosion in granular soils from a discrete fluid-solid numerical model	8th International Conference on Scour and Erosion	MN; CLE
2016	Shire, T.; O'Sullivan, C.	Constriction size distributions of granular filters: a numerical study	Géotechnique	MN; F
2016	Rosenbrand, Esther	Validation piping module in DG Flow GUI		BEP; MN
2016	Abdoulaye Hama, N.; Ouahbi, T.; Taibi, S.; Souli, H.; Fleureau, J.M.; Pantet, A.	Analysis of mechanical behaviour and internal stability of granular materials using discrete element method	International Journal for Numerical and Analytical Methods in Geomechanics	MN; II
2016	Ferdos, Farzad	Internal Erosion Phenomena in Embankment Dams		MN; II; MSL; CLE
2016	Chetti, A.; Benamar, A.; Hazzab, A.	Modeling of Particle Migration in Porous Media: Application to Soil Suffusion	Transport in Porous Media	MN; OE; II
2016	Al-Hussaini, M.M.; Wahl, R.E.; Peters, J.F.; Holmes, T.L.	Seepage and Stability Analysis of Herbert Hoover Dike		BEP; OC; MA
2017	Tao, Junliang; Tao, Hui	Factors Affecting Piping Erosion Resistance : Revisited with a Numerical Modeling Approach	International Journal of Geomechanics ASCE	IE; MN
2017	Richards, Kevin S.; Kuo, Chun-Yi; Hockett, Rick B.; O'Neal, Troy S.; Patev, Robert C.	Simplified Length-Effect for Risk Assessment of Internal Erosion Moose Creek Dam, Alaska	GSP 285: Geo-Risk 2017	BEP; MA
2017	Wang, Min; Feng, Y. T.; Pande, G. N.; Chan, A. H.C.; Zuo, W. X.	Numerical modelling of fluid-induced soil erosion in granular filters using a coupled bonded particle lattice Boltzmann method	Computers and Geotechnics	F; MN

Table B.3 (continued)

Year	Author	Title	Publication Title	Study Tags
2017	Antoine, Wautier; Stéphane, Bonelli; François, Nicot	A micromechanical approach of suffusion based on a length scale analysis of the grain detachment and grain transport processes.	Powders and Grains 2017 - 8th International Conference on Micromechanics on Granular Media	II; MN
2017	Liang, Y; Jim Yeh, Tian-Chyi; Wang, Y; Liu, M.; Wang, J.; Hao, Yonghong	Numerical simulation of backward erosion piping in heterogeneous fields	Water Resources Research	BEP; II; MN
2017	Sibin, A	Numerical study of a mathematical model of internal erosion of soil	Journal of Physics: Conference Series 894 012085	IE; MN
2017	Garcia Martinez, M.F.; Marchi, M.; Tonni, Laura; Gottardi, G.; Bezuijen, A.; Rosso, A.	Numerical simulation of the groundwater flow leading to sand boil reactivation in the Po River	EWGIE 2017	BEP; MN
2017	Bezuijen, A.	The influence of the piping leakage length on the initiation of backward erosion piping	EWGIE 2017	BEP; MA
2017	Navin, Michael P.; Shewbridge, Scott	Example of 2D Finite Element Analyses to Inform Backward Erosion Piping Evaluation of a Typical Levee Cross-Section	GSP 284: Geo-Risk 2017	BEP; MN
2017	Kawano, K.; Shire, T.; O'sullivan, C.	Coupled DEM-CFD Analysis of the Initiation of Internal Instability in a Gap-Graded Granular Embankment Filter	Powders & Grains 2017	MN; II
2017	Bui, Ha H.; Nguyen, Giang	A coupled fluid-solid SPH approach to modelling flow through deformable porous media	International Journal of Solids and Structures	MN; IE
2017	Tao, Hui; Tao, Junliang	Numerical modeling and analysis of suffusion patterns for granular soils	GSP 280: Geotechnical Frontiers 2017	MN; II
2017	Aboul Hosn, R.	Suffusion and its effects on the mechanical behavior of granular soils : numerical and experimental		MN; OE; II
2017	Sibley, Heather M.; Vroman, Noah; Shewbridge, Scott	Quantitative Risk-Informed Design of Levees	GSP 284: Geo-Risk 2017	BEP; DS; MES; OC; MA
2017	Tao, Hui; Tao, Junliang	Quantitative analysis of piping erosion micro-mechanisms with coupled CFD and DEM method	Acta Geotechnica	BEP; MN; IE
2017	Ouahbi, T.; Hama, N Abdoulaye; Taibi, S.; Souli, H.; Fleureau, J.M.; Pantet, A.	Numerical Modeling of Suffusion by Discrete Element Method : A new internal stability criterion based on mechanical behaviour of eroded soil	Powders and Grains 2017	MN; II
2017	Su, Huaizhi; Fu, Zhaoqing; Gao, Ang; Wen, Zhiping	Particle Flow Code Method-Based Meso-scale Identification for Seepage Failure of Soil Levee	Transport in Porous Media	BEP; MN; RL
2017	Tran, D. K.; Prime, N.; Froiio, Francesco; Callari, Carlo; Vincens, E.	Numerical modelling of backward front propagation in piping erosion by DEM-LBM coupling	European Journal of Environmental and Civil Engineering	BEP; MN
2017	Gholampoor, Mohammad Hossein	Reliability analysis of internal erosion in embankment dam	3rd Nordic Rock Mechanics Symposium	MN; IE
2017	Rotunno, Andrea Francesco; Callari, Carlo; Froiio, Francesco	Computational Modeling of Backward Erosion Piping	Models, Simulation, and Experimental Issues in Structural Mechanics	BEP; MN
2017	Lee, Sangho; Lee, Samuel	Reliability Approach on Internal Erosion Risk Assessment of Earth Dam and Levee	GSP 285: Geo-Risk 2017	II; MA
2017	Polanco-Boulware, Lourdes	Reliability underseepage assessment of levees incorporating geomorphic features and length effects		BEP; MN
2017	Seblany, F.; Homberg, U.; Vincens, E.; Winkler, P; Witt, K.J.	Merging criteria for the definition of a local pore and the CSD computation of granular materials	EWGIE 2017	II; MA; F

Table B.3 (continued)

Year	Author	Title	Publication Title	Study Tags
2017	Yerro, A.; Rohe, Alexander; Soga, Kenichi	Modelling Internal Erosion with the Material Point Method	Procedia Engineering	MN; II
2017	van Beek, V.M.; Hoffmans, G.	Evaluation of Dutch backward erosion piping models and a future perspective	EWGIE 2017	BEP; MN; MA
2017	Huang, Zhe; Bai, Yuchuan; Xu, Haijue; Cao, Yufen; Hu, Xiao	A Theoretical Model to Predict the Critical Hydraulic Gradient for Soil Particle Movement under Two-Dimensional Seepage Flow	Water	MA; IE
2017	Yang, Jie; Yin, Z.Y.; Hicher, P.; Laouafa, Farid	A Finite Element Modeling of the Impact of Internal Erosion on the Stability of a Dike	Poromechanics VI	MN; II
2017	Liang, Yue; Jim Yeh, Tian-Chyi; Wang, Junjie; Liu, M.; Zha, Yuanyuan; Hao, Yonghong	An auto-adaptive moving mesh method for the numerical simulation of piping erosion	Computers and Geotechnics	MN; II
2017	Mansouri, M.; El Youssoufi, M. S.; Nicot, F.	Instabilities of a sand layer subjected to an upward water flow by a 2D coupled discrete element - Lattice Boltzmann hydromechanical model	Particles 2017	MN; IE
2018	Hoffmans, G.; Van Rijn, Leo	Hydraulic approach for predicting piping in dikes	Journal of Hydraulic Research	BEP; MA
2018	Robbins, B.A.; Griffiths, D.V.	Modelling of Backward Erosion Piping in Two- and Three- Dimensional Domains	Internal Erosion in Earth Dams, Dikes, and Levees	BEP; MN
2018	Robbins, B.A.; Griffiths, D.V.	A simplified finite element implementation of the Sellmeijer model for backward erosion piping	Numerical Methods in Geotechnical Engineering IX	BEP; MN
2018	Hekmatzadeh, Ali Akbar; Zarei, Farshad; Johari, Ali; Torabi Haghighi, Ali	Reliability analysis of stability against piping and sliding in diversion dams, considering four cutoff wall configurations	Computers and Geotechnics	BEP; MN
2018	Robbins, B.A.; Doughty, M.; Griffiths, D.V.	A Statistical Framework for Incorporating Sand Boil Observations in Levee Risk Analysis	Internal Erosion in Earth Dams, Dikes, and Levees	BEP; MES; OC
2018	Kawano, K.; Shire, T.; O'Sullivan, C.	Coupled particle-fluid simulations of the initiation of suffusion	Soils and Foundations	MN; II
2018	Wautier, A.	Micro-inertial analysis of mechanical instability in granular materials with application to internal erosion		MN; II
2018	Aboul Hosn, R.; Sibille, L.; Benahmed, N.; Chareyre, B.	A discrete numerical model involving partial fluid-solid coupling to describe suffusion effects in soils	Computers and Geotechnics	MN; II
2018	Khadka, Suraj	A numerical study of the coupled geomechanical processes in sinkholes		MN; GBE/S
2018	To, P.; Scheuermann, A.; Williams, D. J.	Quick assessment on susceptibility to suffusion of continuously graded soils by curvature of particle size distribution	Acta Geotechnica	MES; II
2018	Aguilar-López, Juan Pablo; Warmink, J. J.; Schielen, R. M J; Hulscher, S. J M H	Piping erosion safety assessment of flood defences founded over sewer pipes	European Journal of Environmental and Civil Engineering	BEP; MN
2018	Lendering, K.; Schweckendiek, T.; Kok, M.	Quantifying the failure probability of a canal levee	Georisk	BEP; MN; OC
2018	Tao, Hui	Numerical Modeling of Soil Internal Erosion Mechanism		MN; II; IE
2018	Allan Rebecca; Allan, Rebecca	Backward Erosion Piping		BEP; MN; OE; RV
2019	Robbins, B.A.; Griffiths, D.V.; Fenton, G.A.	Influence of Spatially Variable Soil Permeability on Backward Erosion Piping	Proceedings of the 7th International Symposium on Geotechnical Safety and Risk (ISGSR) Proceedings of the 7th International Symposium on Geotechnical Safety and Risk (ISGSR)	BEP; MN

Table B.3 (continued)

Year	Author	Title	Publication Title	Study Tags
2019	Luu, Li Hua; Noury, Gildas; Benseghier, Zeyd; Philippe, P.	Hydro-mechanical modeling of sinkhole occurrence processes in covered karst terrains during a flood	Engineering Geology	GBE/S; MN; OE
2019	Yang, Jie; Halatte, Verneuil	Hydro-mechanical modeling of internal erosion in dike	53 rd US ROCK MECHANICS / GEOMECHANICS SYMPOSIUM	II; MN
2019	Wei, Yuan; li Zhan, Mei; fu Huang, Qing; Sheng, Jinchang; Luo, Yulong; Zhou, Qing	Erosion probability model of base-soil particle migration into a granular filter under local flow	International Journal of Sediment Research	F; MN
2019	Zhong, C.	Study of Soil Behavior Subjected to An Internal Erosion Process		II; MN; OE
2019	Saliba, F.; Nassar, R.B.; Khoury, N.; Maalouf, Y.; Bou Nassar, R.; Khoury, N.; Maalouf, Y.	Internal Erosion and Piping Evolution in Earth Dams using an Iterative Approach	Geo-Congress 2019	BEP; MN
2019	Zhang, Lulu; Wu, Fang; Zhang, Hua; Zhang, Lei; Zhang, Jie	Influences of internal erosion on infiltration and slope stability	Bulletin of Engineering Geology and the Environment	II; MN
2019	Marijnissen, Richard; Kok, Matthijs; Kroeze, Carolien; Van Loon-Steensma, Jantsje	Re-evaluating safety risks of multifunctional dikes with a probabilistic risk framework	Natural Hazards and Earth System Sciences	BEP; MA
2019	Froiio, Francesco; Callari, Carlo; Rotunno, Andrea Francesco	A numerical experiment of backward erosion piping: kinematics and micromechanics	Meccanica	BEP; MN
2019	He, Ke; Fell, Robin; Song, Chongmin	Transverse cracking in embankment dams resulting from cross-valley differential settlements	European Journal of Environmental and Civil Engineering	MN; CLE
2019	Zhang, Fengshou; Li, Mengli; Peng, Ming; Chen, C.; Zhang, Limin	Three-dimensional DEM modeling of the stress–strain behavior for the gap-graded soils subjected to internal erosion	Acta Geotechnica	MN; II
2019	Gu, Dong Ming; Huang, Da; Liu, Han Long; Zhang, Wen Gang; Gao, Xue Cheng	A DEM-based approach for modeling the evolution process of seepage-induced erosion in clayey sand	Acta Geotechnica	MN; IE
2019	Rahimi, M.; Dehgani, N.; Shafieezadeh, A.	Probabilistic Lifecycle Cost Analysis of Levees against Backward Erosion	International Conference on Sustainable Infrastructure	BEP; MA
2019	Yang, Jie	Numerical analyses of the multi-physics problem of sinkholes in the vicinity of a dike or a linear		MN; OE; II
2019	Chetti, A.; Benamar, A.; Korichi, K.	Three-dimensional numerical model of internal erosion	European Journal of Environmental and Civil Engineering	MN; II
2019	Robbins, B.A.; Stephens, I.J.; van Beek, V.M.; Koelewijn, A. R.; Bezuijen, A.	Field measurements of sand boil hydraulics	Géotechnique	BEP; OC; MA
2019	Garcia Martinez, M.F.; Gottardi, G.; Marchi, M.; Tonni, Laura	On the reactivation of sand boils near the Po River major embankments	Geotechnical Research for Land Protection and Development	BEP; MN; OC
2019	Rahimi, M.; Dehgani, N.; Shafieezadeh, A.	Probabilistic Livecycle Cost Analysis of Levees against Backward Erosion	International Conference on Sustainable Infrastructure	BEP; MA
2019	Vandenboer, K.	A Study on the Mechanisms of Backward Erosion Piping		BEP; MN; OE
2019	Yang, Jie; Yin, Z.Y.; Laouafa, Farid; Hicher, P.	Modeling coupled erosion and filtration of fine particles in granular media	Acta Geotechnica	MN; II
2019	Fascetti, Alessandro; Oskay, Caglar	Dual random lattice modeling of backward erosion piping	Computers and Geotechnics	BEP; MN
2019	Kimoto, S; Akaki, T; Kodama, H	Numerical simulation of seepage failure by upward flow considering internal erosion	7th Asia-Pacific Conference on Unsaturated Soils	MN; IE

Table B.3 (continued)

Year	Author	Title	Publication Title	Study Tags
2019	Fascetti, Alessandro; Oskay, Caglar	Multiscale modeling of backward erosion piping in flood protection system infrastructure	Computer-Aided Civil and Infrastructure Engineering	BEP; MN
2019	Semmens, S.; Zhou, W.	Evaluation of environmental predictors for sand boil formation: Rhine–Meuse Delta, Netherlands	Environmental Earth Sciences	BEP; MES
2019	Hu, Zheng; Zhang, Yida; Yang, Zhongxuan	Suffusion-induced deformation and microstructural change of granular soils: a coupled CFD–DEM study	Acta Geotechnica	MN; II
2019	Zhang, Lingran; Gelet, Rachel; Marot, Didier; Smith, Marc; Konrad, Jean Marie	A method to assess the suffusion susceptibility of low permeability core soils in compacted dams based on construction data	European Journal of Environmental and Civil Engineering	MES; II
2019	Khoury, A.; Divo, E.; Kassab, A.; Kakuturu, S.; Reddi, L.	Meshless Modeling of Flow Dispersion and Progressive Piping in Poroelastic Levees	Fluids	BEP; MN; IE
2019	Bui, T.A.; Gelet, R.; Marot, D.	Modelling of internal erosion based on mixture theory: General framework and a case study of soil suffusion	International Journal for Numerical and Analytical Methods in Geomechanics	II; MA
2019	Liu, K.; Vardon, Phil; Hicks, Michael A.	Probabilistic Analysis of Seepage for Internal Stability of Earth Embankments	Environmental Geotechnics	MN; IE; NIE
2019	Rotunno, Andrea Francesco; Callari, Carlo; Froiio, Francesco	A finite element method for localized erosion in porous media with applications to backward piping in levees	International Journal for Numerical and Analytical Methods in Geomechanics	BEP; MN
2019	Giliberti, M. Daniela; Cirincione, Massimiliano; Cavagni, Alessandro	Impact of the use of 3D modeling on sand boil risk management	Lecture Notes in Civil Engineering	BEP; MN
2019	Polanco-Boulware, Lourdes; Rice, John	Reliability underseepage assessment of levees incorporating geomorphic features	Lecture Notes in Civil Engineering	BEP; MA
2019	Rotunno, Andrea Francesco; Callari, Carlo; Froiio, Francesco	A numerical approach for the analysis of piping erosion in hydraulic works	Lecture Notes in Civil Engineering	BEP; MN
2019	Rousseau, Quentin; Sciarra, Giulio; Gelet, Rachel; Marot, Didier	Constitutive modeling of a suffusive soil with porosity-dependent plasticity	Lecture Notes in Civil Engineering	MN; II
2019	Seblany, Feda; Vincens, Eric; Picault, Christophe	Simplified estimation of some main characteristics of pores and constrictions in granular materials	Lecture Notes in Civil Engineering	MA; F
2019	Takahashi, Akihiro; Kokaki, Hibiki; Maruyama, Takahiro; Horikoshi, Kazuki	Numerical and physical modelling of seepage-induced internal erosion around holes on permeable sheet pile	Lecture Notes in Civil Engineering	MN; OE; II
2019	Zhang, Lingran; Gelet, Rachel; Marot, Didier; Smith, Marc; Konrad, Jean Marie	Assessing suffusion susceptibility of soils by using construction data: Application to a compacted till dam core	Lecture Notes in Civil Engineering	MES; II
2019	Mandaglio, Maria Clorinda; Moraci, Nicola; Polimeni, Erika	Assessment of internal stability of granular soils by means of theoretical and laboratory methods	Lecture Notes in Civil Engineering	OE; II; MA
2019	Bezuijen, Adam; van Beek, Vera; Rosenbrand, Esther; Akrami, Sepideh	Analytical groundwater flow calculations for understanding the flow and erosion in a coarse sand barrier	Lecture Notes in Civil Engineering	BEP; DS; MA
2019	Bouziane, Abderrezak; Benamar, Ahmed; Tahakourt, Abdelkader	Finite element analysis of internal erosion effect on the stability of dikes	Lecture Notes in Civil Engineering	MN; II

Table B.3 (continued)

Year	Author	Title	Publication Title	Study Tags
2019	Federico, Francesco; Cesali, Chiara	A numerical procedure to simulate particle migration at the contact between different materials in earthfill dams	Lecture Notes in Civil Engineering	MN; II; F
2019	Garuti, Dario; Jommi, Cristina; Rijkers, Richard	The role of the hydraulic resistance of the river bed and the time dependent response of the foundation layers in the assessment of water defences for macrostability and piping	Lecture Notes in Civil Engineering	BEP; MN
2019	Yang, Jie; Yin, Z.Y.; Laouafa, Farid; Hicher, P.	Internal erosion in dike-on-foundation modeled by a coupled hydromechanical approach	International Journal for Numerical and Analytical Methods in Geomechanics	MN; II
2019	Yang, Jie; Yin, Z.Y.; Laouafa, Farid; Hicher, P.	Analysis of suffusion in cohesionless soils with randomly distributed porosity and fines content	Computers and Geotechnics	MN; II
2019	Savage, Steven; Douglas, Kurt; Fell, Robin; Peirson, William; Berndt, Richard	Modeling the Erosion and Swelling of the Sides of Transverse Cracks in Embankment Dams	Journal of Geotechnical and Geoenvironmental Engineering	MA; CLE
2020	García Martínez, María Fernanda; Tonni, Laura; Marchi, Michela; Tozzi, Simone; Gottardi, Guido	Numerical Tool for Prediction of Sand Boil Reactivations near River Embankments	Journal of Geotechnical and Geoenvironmental Engineering	BEP; MN
2020	Reed, Tomsen	Study of Levee Underseepage through Abandoned Channels and Point Bars on Curved Levee Sections Using the Response Surface-Monte Carlo Method		BEP; MA
2020	Abdou, Hashem; Emeriault, Fabrice; Plé, Olivier	New approach to describe hydro-mechanical phenomenon of suffusion: erosion, transport and deposition	European Journal of Environmental and Civil Engineering	II; MN; OE
2020	Yang, Jie; Yin, Z.Y.; Laouafa, Farid; Hicher, P.	Hydromechanical modeling of granular soils considering internal erosion	Canadian Geotechnical Journal	II; MA; MN; RL
2020	Hu, Z.; Yang, Z. X.; Zhang, Y. D.	CFD-DEM modeling of suffusion effect on undrained behavior of internally unstable soils	Computers and Geotechnics	II; MN
2020	Bouziane, Abderrezak; Benamar, Ahmed; Tahakourt, Abdelkader	Experimental and Numerical Investigation of Internal Erosion Effect on Shear Strength of Sandy Soils	Indian Geotechnical Journal	II; MN; OE
2020	Methorst, A J	Piping in sandy tidal deposits		BEP; MN; OE
2020	Murphy, J.; Yerro, A.; Soga, Kenichi	A new approach to simulate suffusion processes with MPM	Geo-Congress 2020 GSP 320	II; MN
2020	Xiao, Yingping; Cao, Hong; Luo, Guanyong; Zhai, Cong	Modelling seepage flow near the pipe tip	Acta Geotechnica	BEP; MA; OE
2020	Benseghier, Zeyd; Cuéllar, P; Luu, Li Hua; Bonelli, S.; Philippe, P.	A parallel GPU-based computational framework for the micromechanical analysis of geotechnical and erosion problems	Computers and Geotechnics	IE; MN
2020	Xiao, Qiong; Wang, Ji-peng	CFD–DEM Simulations of Seepage-Induced Erosion	Water (Switzerland)	II; MN
2020	Menad, K.; Missoum, H.; Bendani, K.	Geometrical method for assessing the internal stability against suffusion of cohesionless soils based on controlling constriction size	Innovative Infrastructure Solutions	II; MA; OE
2020	Nguyen, Thanh Trung; Indraratna, B.	A Coupled CFD–DEM Approach to Examine the Hydraulic Critical State of Soil under Increasing Hydraulic Gradient	International Journal of Geomechanics	IE; MN
2020	Pol, J.C.; van Beek, V.M.; Kanning, W.; Jonkman, S.N.; Van Beek, V.M.; Kanning, W.; Jonkman, S.N.	Progression Rate of Backward Erosion Piping in Laboratory Experiments and Reliability Analysis	7th International Symposium on Geotechnical Safety and Risk	BEP; MA; OE

Table B.3 (continued)

Year	Author	Title	Publication Title	Study Tags
2020	Zou, Yuhua; Chen, C.; Zhang, Limin	Simulating Progression of Internal Erosion in Gap-Graded Sandy Gravels Using Coupled CFD-DEM	International Journal of Geomechanics	II; MN
2020	Gu, Dongming; Liu, Hanlong; Huang, Da; Zhang, Wengang; Gao, Xuecheng	Development of a Modeling Method and Parametric Study of Seepage-Induced Erosion in Clayey Gravel	International Journal of Geomechanics	MN; II
2020	Tao, Yida	Improving the uplift model for the assessment of internal erosion		MA; IE
2020	Wang, Gang; Horikoshi, Kazuki; Takahashi, Akihiro	Effects of Internal Erosion on Parameters of Subloading Cam-Clay Model	Geotechnical and Geological Engineering	MN; OE; II
2020	Ming, P; Lu, J; Cai, X.; Liu, M.; Chen, X.	MULTI-PARTICLE MODEL OF THE CRITICAL HYDRAULIC GRADIENT FOR DIKE PIPING	Soil Mechanics and Foundation Engineering	BEP; OE; II; MA; IE
2020	Wang, Yu; Chai, Junrui; Xu, Zengguang; Qin, Yuan; Wang, Xin	Numerical Simulation of the Fluid – Solid Coupling	Water (Switzerland)	MN; OE; II
2020	Pirnia, Pouyan; Duhaime, François; Ethier, Yannic; Dubé, Jean Sébastien	Hierarchical multiscale numerical modelling of internal erosion with discrete and finite elements	Acta Geotechnica	MN; II
2020	Zhou, Wei; Ma, Qirui; Ma, Gang; Cao, Xuexing; Cheng, Yonggang	Microscopic investigation of internal erosion in binary mixtures via the coupled LBM-DEM method	Powder Technology	MN; II
2020	Knight, Chris; O'Sullivan, Catherine; van Wachem, Berend; Dini, Daniele	Computing drag and interactions between fluid and polydisperse particles in saturated granular materials	Computers and Geotechnics	MN; IE
2020	Zagema, Arjen	The Effects of Gravels on Piping		BEP; MN
2020	Zhou, Zongqing; Li, Zhuohui; Ranjith, Pathegama Gamage; Wen, Zhijie; Shi, Shaoshuai; Wei, Cheche	Numerical simulation of the influence of seepage direction on suffusion in granular soils	Arabian Journal of Geosciences	MN; II
2020	Semmens, S.	Geospatial and Logistic Regression Assessment of Factors Contributing to Backwards Erosion Piping		BEP; MES
2020	Liang, Dongfang; Zhao, Xuanyu; Soga, Kenichi	Simulation of overtopping and seepage induced dike failure using two-point MPM	Soils and Foundations	MN; IE
2020	Chapuis, R.P.; Saucier, Antoine	Assessing internal erosion with the modal decomposition method for grain size distribution curves	Acta Geotechnica	OE; II; MA
2020	Farshbaf Aghajani, Hamed; Shahbazi, Peyman; Salimi, Mohammad; Azimzadeh, Reza	The effect of a defective permeable zone inside the clay core of an earthfill dam with regard to the seepage aspect	SN Applied Sciences	MN; IE
2020	Rahimi, M.; Shafieezadeh, A.	Coupled backward erosion piping and slope instability performance model for levees	Transportation Geotechnics	BEP; MN
2020	Azadbakht, S.; Nouri, A.; Chan, D.	An analytical model for estimation of internal erosion rate	Geomechanics and Geoengineering	II; MA
2020	Barendsen, L	The effect of leakage on backward erosion piping: A modelling study in 2D and 3D		BEP; MN; MA
2020	Semmens, S.; Zhou, W.	Predicting backward erosion piping hazard, Lower Mississippi Valley, USA	Quarterly Journal of Engineering Geology and Hydrogeology	BEP; MES
2020	Liu, Yajing; Yin, Z.Y.; Wang, Li-Zhong; Hong, Yi	A coupled CFD-DEM investigation of internal erosion considering suspension flow	Canadian Geotechnical Journal	MN; II
2020	Callari, Carlo; Froiio, Francesco	A hydromechanical finite element formulation for localized internal erosion in porous media, with application to backward piping in cofferdams	International Journal for Multiscale Computational Engineering	BEP; MN

Table B.3 (continued)

Year	Author	Title	Publication Title	Study Tags
2020	Li, Zhuomin; Luo, Xianqi; Bi, Jinfeng; Shen, Hui	Numerical modelling of internal erosion process in gravel soils based on the percolation analytical method	Environmental Earth Sciences	MN; II; MA
2020	Hu, Zheng; Zhang, Yida; Yang, Zhongxuan	Suffusion-Induced Evolution of Mechanical and Microstructural Properties of Gap-Graded Soils Using CFD-DEM	Journal of Geotechnical and Geoenvironmental Engineering	MN; II
2020	Sakyi, Adu; Amoako-Yirenkyi, Peter; Dontwi, Isaac Kwame	A Rigorous Homogenization for a Two-Scale Convergence Approach to Piping Flow Erosion with Deposition in a Spatially Heterogeneous Soil	Journal of Advances in Mathematics and Computer Science	MN; II; MA
2020	Zhang, Fengshou; Wang, Tuo; Liu, Fang; Peng, Ming; Furtney, Jason; Zhang, Limin	Modeling of fluid-particle interaction by coupling the discrete element method with a dynamic fluid mesh: Implications to suffusion in gap-graded soils	Computers and Geotechnics	MN; II
2020	Ahmadi, M.; Shire, T.; Mehdizadeh, Amirhassan; Disfani, M.M.	DEM modelling to assess internal stability of gap-graded assemblies of spherical particles under various relative densities, fine contents and gap ratios	Computers and Geotechnics	MN; II
2021	Rossi, Nicola; Bačić, Mario; Kovačević, Meho Saša; Librić, Lovorka	Development of fragility curves for piping and slope stability of river levees	Water (Switzerland)	BEP; MA
2021	Wang, Xiukai; Tang, Yao; Huang, Bo; Hu, Tiantian; Ling, Daosheng	Review on numerical simulation of the internal soil erosion mechanisms using the discrete element method	Water (Switzerland)	IE; MN; RV
2021	Winkels, T. G.; Cohen, K. M.; Knaake, S. M.; Middelkoop, H.; Stouthamer, E.	Geological framework for assessing variability in subsurface piping parameters underneath dikes in the Rhine-Meuse delta, the Netherlands	Engineering Geology	BEP; MES
2021	Xiong, Hao; Wu, Han; Bao, Xiaohua; Fei, Jianbo	Investigating effect of particle shape on suffusion by CFD-DEM modeling	Construction and Building Materials	MN; II
2021	Wewer, Manuel; Aguilar-López, Juan Pablo; Kok, M.; Bogaard, Thom	A transient backward erosion piping model based on laminar flow transport equations	Computers and Geotechnics	BEP; MN
2021	Xue, Haibin; Dang, Faning; Li, Yanlong; Yin, Xiaotao; Lei, Man	Development of Piping Analysis Method for Embankment Including Time-Dependent Change in Permeability Coefficient	International Journal of Geomechanics	MN; II
2021	Robbins, B.A.; Griffiths, D.V.; Fenton, Gordon A.	Random finite element analysis of backward erosion piping	Computers and Geotechnics	BEP; MN
2021	Semmens, S.; Zhou, W.; Robbins, B.A.	Empirical Assessment of Backward Erosion Piping via Blanket Thickness, Lower Mississippi Valley	Natural Hazards Review	BEP; MES
2021	Bi, Jinfeng; Zhang, Haitao; Luo, Xianqi; Shen, Hui; Li, Zhuomin	Modeling of internal erosion using particle size as an extra dimension	Computers and Geotechnics	MN; II
2021	Rahimi, Mehrzad; Shafieezadeh, Abdollah; Wood, Dylan; Kubatko, Ethan J.	A physics-based approach for predicting time-dependent progression length of backward erosion piping	Canadian Geotechnical Journal	BEP; MN
2021	Robbins, B.A.; Griffiths, D.V.	A two-dimensional, adaptive finite element approach for simulation of backward erosion piping	Computers and Geotechnics	BEP; MN
2021	Yao, Qiuling; Ding, Liuqian; Zhang, Shunfu; Sun, Dongya; Liu, Changjun	Backward erosion piping mechanism and its size effect	ICSE10	BEP; MN; OE
2021	van Beek, V.; De la Loma Gonzalez, B. Rosenbrand, E.; Noordam, A.	Numerical Simulation of Erosion Lens Formation in 3D Geohydrological Environments	ICSE10	BEP; MN

Table B.3 (continued)

Year	Author	Title	Publication Title	Study Tags
2021	Sufian, Adnan; Knight, Chris; Sullivan, Catherine O; Wachem, Berend Van; Dini, Daniele	Modelling Internal Erosion in Gap-Graded Soils using Pore Network Models	ICSE10	MN; II
2021	Rosenbrand, E.; Wiersma, A.; Noordam, A.; van Beek, V.	Numerical analysis of backward erosion piping for two geological environments in the Netherlands	ICSE10	BEP; MN
2021	Rosenbrand, E.; van Beek, V.M.	Numerical simulation of a large-scale backward erosion piping experimenet in 2D and in 3D	ICSE10	BEP; MN
2021	Hoffmans, Gijs	Fundamentals of Laminar Flow In Pipes	ICSE10	BEP; MA; RV
2021	Federico, Francesco; Cesali, Chiara	Granulometric compatibility between different materials . Interpretation of empirical criteria through micro-mechanical modeling	ICSE10	MN; F
2021	Bessonov, Mikhail; Shire, Thomas	Effect of Pipe Shape on the Pressure Conditions in the Hole Erosion Test	ICSE10	MN; CLE
2021	Xiong, Hao; Yin, Z.Y.; Zhao, Jidong; Yang, Yi	Investigating the effect of flow direction on suffusion and its impacts on gap-graded granular soils	Acta Geotechnica	MN; II

APPENDIX C

COAUTHOR AND COPYRIGHT PERMISSIONS

C.1 Coauthor Permissions

Permission to include Chapter 5, Chapter 6, and Chapter 9 as part of this thesis has been obtained from coauthors who are not on the thesis committee. Emails containing the permission statements from coauthors may be found in the Supplemental File CoauthorPermissionsThesis2022.pdf.

C.2 Copyright permissions

Permissions to reuse all copyrighted materials are included in the supplemental file CopyrightReusePermissionsThesis2022.pdf. The following permissions are included in the supplemental file.

1. Permissions from Vera Van Beek for reuse of Figures 2.4, 2.10b, 2.16, 2.25, and 2.36 from the reference Van Beek (2015).
2. Permissions from Kristine Vandenboer for reuse of Figures 2.8, 2.12, 2.14, and 2.28 from the reference Vandenboer (2019).
3. Permissions from Rebecca Allan for reuse of Figures 2.10a, 2.13, 2.27, 2.37, 2.38, and 5.18 from the reference Allan (2018).
4. Permissions from Taylor and Francis for reuse of Figure 2.9 from the reference Mueller-Kirchenbauer et al., (1993) reference.
5. Permissions from ICE Publishing for reuse of Figures 2.17, 2.18, 2.26 from Robbins et al. (2018) reference.

6. Permissions from Springer-Verlag for reuse of Figures 2.19, 2.20, 2.21, and 2.22 from Xiao et al. (2020) reference.
7. Permissions from Hans Sellmeijer for reuse of Figure 2.29 from Sellmeijer (1988) and Figure 2.49 from Sellmeijer (2006).
8. Permissions from Elsevier for reuse of Figure 2.31 from Sellmeijer and Koenders (1991).
9. Permission from ASCE for reuse of Figures 2.32, 2.33, and 2.34 from Schmertmann (2000) reference.
10. Permission from Xudong Fu for reuse of Figure 2.52 from Wang et al. (2014).
11. Permission from ASCE for reuse of Figure 2.54 from Liang et al (2011).
12. Permission from John Wiley and Sons for reuse of Figure 2.55 from Liang et al. (2017).
13. Permission from John Wiley and Sons for reuse of Figures 2.56 and 2.57 from Rotunno et al. (2019).
14. Permission from ASCE for reuse of Figure 2.58 from El Shamy & Aydin (2008).
15. Permission from John Wiley and Sons for reuse of Figure 2.59a from Lomine et al. (2013).
16. Permissions from Elsevier to reprint Chapter 5 content from the reference Robbins et al. (2022).
17. Permissions from Elsevier to reprint Chapter 6 content from the reference Robbins et al. (2022).
18. Permissions from Springer International Publishing to reprint Chapter 7 content from the reference Robbins and Griffiths (2018).
19. Permission from Elsevier to reprint Chapter 8 content based on the reference Robbins and Griffiths (2021).

20. Permission from Elsevier to reprint Chapter 9 content based on the reference Robbins et al. (2021).